Two Aspects of Crystalline Topological Matter

Fractional Corner Charges with Fourfold Rotational Symmetry
and
Symmetry Indicator Invariants for Non-Hermitian Topological Materials

Pascal Marc Vecsei

Master Thesis
Condensed Matter Physics
Date: February 4, 2021

Department of Physics
University of Zurich

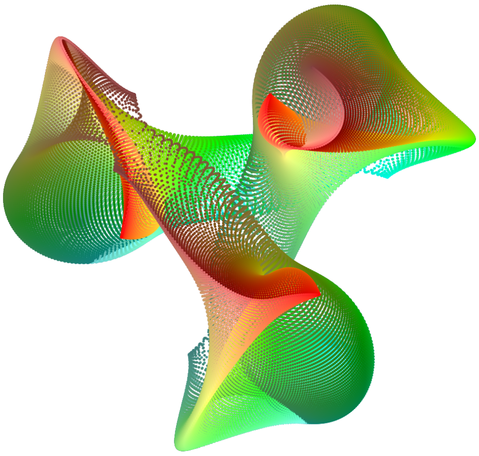

Supervisors:

Prof. Dr. Titus Neupert, Department of Physics, University of Zurich
Dr. Frank Schindler, Department of Physics, University of Zurich and Princeton Center for Theoretical Science, Princeton University
M. Michael Denner, Department of Physics, University of Zurich

Contents

I. General Introduction 4

II. Fractional Corner Charges with Fourfold Rotational Symmetry 9

- II.1. Abstract . . . 9
- II.2. Introduction . . . 9
  - II.2.1. Motivation . . . 10
  - II.2.2. Current State of Research . . . 10
  - II.2.3. Structure of Part II . . . 13
- II.3. Symmetries . . . 13
  - II.3.1. Space Group Symmetries . . . 13
  - II.3.2. Internal Symmetries . . . 14
- II.4. Models . . . 14
  - II.4.1. Models for Obstructed Atomic Limits . . . 14
  - II.4.2. Model for Double Topological Insulator with C_4 and TRS . . . 21
  - II.4.3. Random Perturbations . . . 22
- II.5. Wyckoff Positions and Symmetry Eigenvalues . . . 25
- II.6. Wilson Loops . . . 27
  - II.6.1. Effects of Symmetries on the Wilson Loop . . . 30
  - II.6.2. Wilson-Eigenvalues of Two TRS-Permuted Bands . . . 34
- II.7. Chern numbers . . . 36
- II.8. Methods Based on Parallel Transport . . . 37
  - II.8.1. Continuous Gauge on the Line $\overline{\mathbf{\Gamma M}}$, Ensuring Compatibility with C_4 Eigensectors in the Points $\mathbf{\Gamma}$, $\mathbf{M}$ . . . 37
  - II.8.2. Parallel Transport Method of Kooi, van Miert and Ortix . . . 40
- II.9. Projected Symmetric Operators and Their Band Structures . . . 42
  - II.9.1. Proof for the Existence of an $\mathring{\psi}_{\mathbf{k}}$ . . . 45
  - II.9.2. Proof of Smoothness and Symmetry of the Gauge . . . 46
  - II.9.3. Construction of PSOs Based on Symmetry Only . . . 50
  - II.9.4. Construction of SOs based on Wyckoff Positions . . . 73
  - II.9.5. Degeneracies . . . 79
- II.10. Outlook . . . 82
  - II.10.1. Non-Hermitian Topology with Star-Gaps . . . 82
  - II.10.2. PSO Method for Non-Hermitian Hamiltonians . . . 82
  - II.10.3. Winding of Wilson Loops in the Occupied Bands . . . 82
- II.11. Final Remarks . . . 83
- II.A. Explicit Constructive Proof for the Existence of a SO in a Case with TRS and C_4 Symmetry . . . 84
  - II.A.1. Smoothness and Gap . . . 84
  - II.A.2. Symmetries . . . 84

II.B. Explicit Proofs for the Block-(Off-)Diagonality of Sewing Matrices 85
  II.B.1. Lemmas 85
  II.B.2. Proof that the C_4 Sewing Matrix $\tilde{D}$ is Block-Diagonal 86
  II.B.3. Proof that the C_4 Sewing Matrix is Block-Diagonal 87
  II.B.4. Further Splitting of Pairs of Bands 90
II.C. Perturbation of $\mathring{\Psi}_{\mathbf{k}}$ Instead of $\mathring{\psi}_{\mathbf{k}}$ 91
II.D. Calculation of Wilson Loop in Occupied $\mathring{\Psi}$ Bands Without Diagonalisation . . 91
II.E. Matrices used 94

III. Symmetry Indicator Invariants for Non-Hermitian Topological Materials 96
III.1. Abstract 96
III.2. Introduction 96
III.3. General Properties of Non-Hermitian Systems 97
  III.3.1. Spectrum and Eigenspace of Non-Hermitian Systems 97
  III.3.2. Gaps in Non-Hermitian Systems 98
  III.3.3. Symmetries in Non-Hermitian Systems 99
III.4. One-Dimensional Systems 103
  III.4.1. (Pseudo-)Inversion Symmetry 104
III.5. Two-Dimensional Systems 106
  III.5.1. Hermitian Flattening and Rotational Symmetry 107
III.6. Three-Dimensional Systems 110
  III.6.1. Model of the Exceptional Topological Insulator 110
  III.6.2. Symmetry Indicators for w_{3D} and $w_{\mathrm{1D},j}$ 112
  III.6.3. Symmetry Indicators for Class AII 127
  III.6.4. Summary Table 141
III.7. Outlook 142
III.8. Final Remarks 142

IV. General Conclusion 143

I. General Introduction

In this thesis, two aspects of topological matter in presence of space group symmetries are treated. To introduce topological materials and to give context to the topics of this thesis, we start with a short historical overview.

Topological matter has become an increasingly prominent topic within condensed matter physics during the last few decades[1–13]. Topological condensed matter physics originally started with the discovery of the Quantum Hall Effect (QHE) by von Klitzing et al.[14]. They discovered that a two-dimensional electron gas in a strong magnetic field shows peculiar transport behaviour with their Hall conductivity quantised to discrete levels

$$\sigma_{xy} = \frac{Ne^2}{h}, \tag{I.1}$$

which are integer multiples of a combination of physical constants. This transport behaviour can be understood in terms of a discrete number of boundary modes, which can be understood by taking into consideration that electrons are forced onto circular (Larmor) orbits inside a strong magnetic field. Some of the orbits intersect the boundary and a skipping motion emerges, which yields a boundary mode. The integer quantity N corresponds to the number of delocalised boundary modes around the 2D sample.
A few years after the QHE, the fractional Quantum Hall Effect (FQHE) was discovered, in which the Hall conductivity can also take fractional quantities

$$\sigma_{xy} = \frac{pe^2}{qh}, \tag{I.2}$$

with the integers p and q. This state was explained by Laughlin[15] using the famous Laughlin wave function.

Subsequently it was realised that QHE-like states cannot only appear in presence of a magnetic field, but also without. This was dubbed the Quantum Anomalous Hall Effect (QAHE)[16, 17] or Chern insulator. The Hall voltage number N is then given as the TKNN invariant[18] of the bulk band structure. It was quite quickly realised that the TKNN invariant coincides with the Chern number, already known from the mathematical theory of fiber bundles[19]. This established a connection between the mathematical field of topology and the newly discovered physical phenomena. The Chern number can be expressed with the Berry phase (cf. Ref. [20, p. 368-393]), known from adiabatic processes[21]. The Chern number of a band is[1, 22]

$$n_m = \frac{1}{2\pi} \int d^2\mathbf{k} \mathcal{F}_m, \tag{I.3}$$

which is given in terms of the Berry flux $\mathcal{F}_m = \nabla \times \mathcal{A}_m$ and the Berry connection $\mathcal{A}_m = i \langle u_m | \nabla_{\mathbf{k}} | u_m \rangle$. These quantities can be evaluated with the Bloch wave functions $|u_m(\mathbf{k})\rangle$ as input. A Chern insulator was first experimentally observed by Chang et al.[23]. Both the Chern insulator and the QHE require broken time reversal symmetry (TRS).

One of the hallmark features of QHE and Chern insulator phases is the appearance of quantised edge currents around the sample. The number of these chiral boundary modes directly corresponds to the number N, the current flows around the sample unidirectionally. These edge states have the property that even if the surface is impure, they swerve any small obstacles and do not scatter back. The correspondence between a property of the bulk bands, the Chern number, and the surface states is called *bulk boundary correspondence.* Bulk boundary correspondence is a generic property of topological phases and the interesting properties of these surface states are one of the reasons for the high degree of interest in topological matter.

Afterwards, the research focus shifted to time reversal symmetry respecting systems. 2D topological systems with TRS were first studied by Kane and Mele[24]. They investigated graphene with symmetry-allowed spin-orbit coupling terms, and discovered that with certain terms a Quantum Spin Hall Effect (QSHE) appears. This means that along the edges there are protected helical currents. Helical currents are bidirectional currents protected against being scattered by surface impurities or obstructions.

The study of topology was then extended to even more symmetry classes, taking into consideration all types of internal symmetry: time reversal symmetry (TRS), particle hole symmetry (PHS) and chiral symmetry (CS). For PHS and TRS there is distinction between the case when the symmetry operator squares to -1 or to $+1$. Altand and Zirnbauer[25] developed a set of symmetry classes (dubbed AZ symmetry classes), which stem from the symmetry classes for the classification of random matrices. The symmetry classes and their corresponding internal symmetries are listed in Table I.1 on the left. A "0" entry means that the symmetry is not present, 1 (-1) means that it is present and the symmetry operators squares to 1 (-1), respectively. Depending on the symmetry class, a different topological classification space is present[26–30]. Table I.1 on the right-hand side shows the topological classification; this is called the *periodic table for topological insulators and superconductors*[27]. $\mathbb{Z}$ means that the topology has an integer classification. Anomalous QHE phases belong to class A in 2D, therefore the classification is $\mathbb{Z}$. $\mathbb{Z}_2$ means that one can distinguish two different phases, like for example in the QSHE case. One of the phases appearing in the periodic table of topological matter is the time reversal invariant 3D topological insulator (TI), which has gapless surface states and therefore conducts on the surface, but remains an insulator in the bulk[1]. To study models of topological phases relevant to experiments, tight-binding models are often used[31].

Later on Fu and Kane[32] discovered that many topological phases can be detected easily in presence of inversion symmetry by studying the inversion parities at high-symmetry points of the Brouillon zone (BZ). This concept, referred to as *symmetry indicator invariants*, was extended to other space groups and internal symmetry classes[33–41].

From a mathematical point of view, all these different topological classes represent a classification of the mappings from the Brouillon zone (BZ) torus $\mathbb{T}^d$ to the real numbers. This mapping is the band structure. The topology of such mappings can be studied using K-theory[29, 42–45]. Two Hamiltonians are regarded as topologically equivalent if they can be smoothly deformed into each other while respecting their symmetries at each point along the deformation path.

class	Internal Symmetry			Dimension			
	TRS	PHS	CS	0	1	2	3
A	0	0	0	$\mathbb{Z}$	0	$\mathbb{Z}$	0
AIII	0	0	1	0	$\mathbb{Z}$	0	$\mathbb{Z}$
AI	1	0	0	$\mathbb{Z}$	0	0	0
BDI	1	1	1	$\mathbb{Z}_2$	$\mathbb{Z}$	0	0
D	0	1	0	$\mathbb{Z}_2$	$\mathbb{Z}_2$	$\mathbb{Z}$	0
DIII	-1	1	1	0	$\mathbb{Z}_2$	$\mathbb{Z}_2$	$\mathbb{Z}$
AII	-1	0	0	$\mathbb{Z}$	0	$\mathbb{Z}_2$	$\mathbb{Z}_2$
CII	-1	-1	1	0	$\mathbb{Z}$	0	$\mathbb{Z}_2$
C	0	-1	0	0	0	$\mathbb{Z}$	0
CI	1	-1	1	0	0	0	$\mathbb{Z}$

Table I.1.: Altland-Zirnbauer symmetry classes and the tenfold classification of topological insulators and superconductors (reproduced from Ref. [26]).

Many aspects of topological matter can be understood in terms of Topological Quantum Field Theory[46, 47].

The classification of topological phases of matter was further extended by the introduction of the concept of Topological Crystalline Insulators (TCI). In addition to internal symmetries, TCIs are taking into consideration space group symmetries like inversion or rotational symmetries[48–57], which allow for a finer structuring of the space of Hamiltonians into topologically distinct classes. Such phases were demonstrated for instance in SnTe[58], $\mathrm{Pb}_{1-x}\mathrm{Sn}_x\mathrm{Se}$[59] and the $\mathrm{Ca}_2\mathrm{As}$ family[60]. Phases in which the topological surface states are protected by inversion symmetry only are referred to as axion insulators (AXI)[61–63]. Their behaviour can be described with Axion Electrodynamics[64].

Furthermore, topological superconductors have become a topic of high interest in the recent decades[9, 65–67]. Some topological superconductors possess Majorana boundary modes. These Majoranas are important for the development of topological quantum computers[68, 69], since they might offer a path forward to a fault-tolerant quantum computer. Topological superconductivity was, for instance, observed in thin $\mathrm{Bi}_2\mathrm{Te}_3$ films on a superconducting NbSe_2 substrate[69]. Without substrate, $\mathrm{Bi}_2\mathrm{Te}_3$ is an insulator, but by proximity to the superconducting substrate superconductivity is induced and it turns into a topological superconductor.

The zoo of different topological phases of matter was unified in 2017 with the discovery of Topological Quantum Chemistry (TQC)[7, 70–72]. TQC moves the focus away from a pure band structure point of view by taking into account the real space picture. It thereby establishes a connection to chemistry. Its main ingredient are the band structures that can arise from symmetry-respecting localised orbitals, referred to as *band representations* (BRs)[70, 73, 74]. All band representations can be decomposed into *elementary band representations* (EBRs), a finite set of fundamental phases with localisable electrons. By comparing the symmetry-allowed band structures in reciprocal space with the band structures arising from localised orbitals (BRs), one realises that not all band structures can arise from localised orbitals. The band structures that cannot arise from localised orbitals but are still symmetry-allowed are the topological phases previously discovered, like TI oder Chern insulator phases. Amongst the phases that correspond to a BR, there are so-called *obstructed atomic limits* (OALs). In OALs, the Wannier charge centres do not coincide with ionic positions, and corner charges can arise[75]. Furthermore, insulators whose bands become band representation under addition of trivial bands are called fragile topological insulators[76–79].

Wannier functions describe localised electrons in a crystal and have been intensely studied[45, 77, 80–84]. In topological materials, there is an obstruction to the construction of Wannier functions that are compatible all the symmetries. If a material corresponds to an atomic limit, e.g. an OAL, symmetric localised Wannier functions can be calculated.

In a similar context, the term *Higher-Order Topological Insulators* (HOTIs)[63, 85–88] was introduced. These are all topological insulators in which the difference between the dimensionality of the gapless boundary states and the dimensionality of the system is more than one. They require space group symmetries for the protection of their topological surface states and are closely related to the previously known multipole insulators[89–91]. In multipole insulators such surface states appear, too. They were, for example, implemented in microwave systems[92]. Higher-order topology was observed in bismuth[93] and is thought to appear in Twisted Bilayer Graphene (TBG)[94].

Another topic that has recently drawn more and more attention are non-Hermitian Hamiltonians and their topological classification[95–104]. Non-Hermitian Hamiltonians appear when studying systems with loss[105], resistance or when taking into consideration electronic interactions. The topological classification for these systems differs from the Hermitian case, and their boundary states are distinctly different[106–109]. Non-Hermitian HOTIs[110–113], non-Hermitian Chern insulators[114–117] and non-Hermitian SSH chains[118, 119] are also a topic of current interest. Non-Hermitian phases were experimentally implemented or proposed in topoelectric circuits[120–126], as well as in optical[127], cold-atom[88] and mechanical[128, 129] systems.

In this thesis, we shed light on two very specific aspects of crystalline topological matter.

In the first part of the thesis, corner charges in two-dimensional spin-orbit coupled crystals with fourfold rotational symmetry are discussed. In these crystals, there are several allowed band representations, and it is possible that the electronic system corresponds to an OAL, which means that the electrons are not centred at the ionic positions[75]. Until recently, there was no topological invariant to distinguish one of the allowed obstructed atomic limits, the case of two electrons on the corner of the real space unit cell (called $1b|_{\frac{3\pi}{4}} \oplus 1b|_{\frac{\pi}{4}}$), from the trivial atomic limit, in which the electrons are centred at the ionic position. In this OAL, all the known invariants (cf. Ref. [75]) were identical to the invariants for the trivial case ($1a \oplus 1a$). The problem of the non-existence of a topological invariant has been recently solved by Kooi et al.[130]. We present an alternative, more elegant way to calculate the gauge needed to evaluate their invariants. Furthermore, we describe a general method to calculate gauges with smooth projectors in which the symmetries act as permutations on the bands.

In the second part of this thesis, symmetry indicator invariants in the realm of non-Hermitian topological materials are described. Symmetry indicators are an easy way to analyse the topology of a system by calculating eigenvalues of symmetry operators in the occupied bands at high-symmetry points (HSPs) of the BZ. Unlike other invariants, which often require the evaluation of BZ integrals, symmetry indicators can be evaluated very speedily. In this part, the main focus are invariants for systems with a point gap that have been characterised using the $\nu_3 = w_{\mathrm{3D}}$ winding number for chiral systems in odd space dimensions. Furthermore, we present a symmetry indicator to detect the non-trivial phase of the $\mathbb{Z}_2$ classification in time reversal symmetric 3D non-Hermitian systems with point gap. In 2D with line gaps, we show that the allowed values for the Chern number can be constricted using the symmetry indicators already known for Hermitian systems.

II. Fractional Corner Charges with Fourfold Rotational Symmetry

> Still round the corner there may wait
> A new road or a secret gate
> And though I oft have passed them by
> A day will come at last when I
> Shall take the hidden paths that run
> West of the Moon, East of the Sun.
>
> *(J.R.R. Tolkien)*

II.1. Abstract

In this work, we describe and treat the problem of determining the band representation of Wannierisable 2D systems in Altland-Zirnbauer class AII. This work is based on previous work by Schindler et al.[75] and tries to completely classify the OALs in 2-dimensional systems with fourfold rotational and spin-$\frac{1}{2}$ time-reversal symmetry (TRS with $\mathcal{T}^2 = -1$). First, parallel transport methods are presented, including the recent discoveries by Kooi et al.[130], who solved the problem we also aspired to solve and provided invariants.

Furthermore, we present a versatile easy-to-implement method to calculate gauges with smooth projectors, with bloch wave functions $|u^n_{\mathbf{k}}\rangle$ on which the symmetry operators of crystalline and internal time reversal symmetry act as permutations. This means that any symmetry operator s maps $|u^n_{\mathbf{k}}\rangle$ onto a state $c\left|u^{\sigma(n)}_{S\mathbf{k}}\right\rangle$ at the symmetry transformed momentum $S\mathbf{k}$ times a factor c, where σ is a permutation.

This method, dubbed *projected symmetric operator (PSO)* method, extends on the previous *projected symmetry operator* method by Alexandradinata et al.[131] by allowing for the construction of gauges in which the permutations σ contain n-cycles, with $n > 2$. The invariants presented in the work by Kooi et al.[130] can be evaluated in a gauge calculated using the PSO method.

II.2. Introduction

In first part of this Master project, fractional corner charges in spin-orbit coupled 2D insulators with fourfold rotational (C_4) and time-reversal symmetry (TRS), represented by $\mathcal{T}$ with $\mathcal{T}^2 = -1$, are treated. These insulators belong to class AII in the periodic table of topological invariants (cf. Ref. [132]). As insulators without edge modes they are gapped both in the bulk and along the edges. This means that the dipole polarisation $\mathbf{P}$ vanishes, because otherwise the materials would exhibit metallic edges, which would conduct charge and keep the fractional corner charge from being well localised[133].

The topic of this work is to extend the topological invariants previously found by Schindler et al.[75] with an additional invariant to gain the ability to distinguish all atomic limits in this class. In order to allow for an easy calculation of these topological invariants, this work focuses on methods that only use the bloch wave functions $|u^n_{\mathbf{k}}\rangle$ as input.
The research question of this part was unexpectedly already answered by a publication that was published during the course of the work by Kooi et al.[130].

II.2.1. Motivation

In recent years, there has been increased interest in topological phases of matter. Topological materials could lead to interesting applications, including topological quantum computers. Recently, higher order topological insulators [89, 90, 93] (HOTIs) were discovered. HOTIs are a subgroup of the topological crystalline insulators (TCIs); TCIs require space group symmetries for the protection of their topological states. Unlike regular topological insulators, the difference between the dimensionality of the system, which is gapped in the bulk, and the gapless regions (e.g. surface, hinges) is more than one for HOTIs. As an example, a HOTI could be a 2D material with gapped bulk and hinges, but gapless modes on the corners.

In order to obtain a complete understanding of HOTIs and the materials that fall into this category, it is important to be able to use relatively easy to calculate quantities that indicate whether a compound is a HOTI or not. It is convenient to have methods that are based on the band structure, which is easily available for many compounds.

In this context, the concept of Topological Quantum Chemistry[7, 71] appeared a few years ago. The idea behind it is that that one can distinguish two types of phases:

1. Phases that are continuously connected to a phase with localised electrons (a so-called atomic limit). Their filled bands correspond to a band representation. We distinguish “regular” atomic limits in which the electrons are centred at the ionic positions, and obstructed atomic limits (OAL), in which the electrons are situated away from the ionic positions. OALs are topologically distinct from each other and the trivial atomic limit.
2. Strong and weak topological phases that cannot be deformed to an atomic limit without closing the bulk gap or breaking symmetries.

Furthermore, there exist so-called fragile topological phases, which have a description in terms of localised, symmetric Wannier functions, but only under addition of trivial bands[76–78].

This project is concerned with OALs in the case of spin-orbit coupled two-dimensional crystals with C_4 rotational symmetry.

II.2.2. Current State of Research

Benalcazar et al.[133] developed topological invariants and formulae for the evaluation of corner charges for C_n-symmetric 2D materials belonging to the class AI (spinless, time reversal symmetric (TRS), $\mathcal{T}^2 = +1$) in the periodic table of topological invariants. They furthermore found that for (fractional) corner charges to occurr, the bulk dipole polarisation $\mathbf{P}$ has

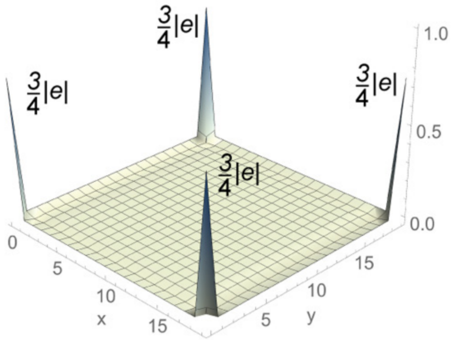

Figure II.1.: Visualisation of fractional $\frac{3}{4}e$ corner charges in a C_4-symmetric system, spinless case. Figure reproduced from Benalcazar, Li and Hughes[133].

Table II.1.: Electronic corner charge, polarisation and topological invariants for the different primitive generators for C_4-symmetric spinless systems[133].

primitive generator	$\left[X_1^{(2)}\right]$	$\left[M_1^{(4)}\right]$	$\left[M_2^{(4)}\right]$	$\mathbf{P}$	Q_{corner}
$h_{1b}^{(4)}$	-1	1	0	$\left(\frac{e}{2},\frac{e}{2}\right)$	$\frac{e}{4}$
$h_{2b}^{(4)}$	2	0	0	$(0,0)$	$\frac{e}{2}$
$h_{2c}^{(4)}$	1	1	-1	$\left(\frac{e}{2},\frac{e}{2}\right)$	0

to vanish. The corner charges, which are actually charges belonging to disjoint sectors connected by the involved symmetry, are exponentially localised on the corners. Figure II.1 shows a visualisation of corner charges on a C_4-symmetric lattice. Bancalcazar et al.[133] found a complete set of topological invariants using only symmetry indicator invariants, which can be calculated by determining the eigenvalues of the symmetry operators in the occupied bands at high symmetry points (HPSs) in the BZ. The invariants for the C_4 case are

$$\chi^{(4)} = \left\{ \left[X_1^{(2)}\right], \left[M_1^{(4)}\right], \left[M_2^{(4)}\right] \right\}. \tag{II.1}$$

Symmetry indicator invariants are described in section II.5. By evaluation for three different Hamiltonians that span all C_4-symmetric atomic limits, labeled by the Wyckoff position on which the electrons are localised, they obtained the results in table II.1.

Schindler et al.[75] developed topological invariants and formulae for the calculation of (fractional) corner charges for the case of spin-orbit coupled 2D insulators. These materials belong to the Altland-Zirnbauer class AII ($\mathcal{T}^2 = -1$). The topological invariants for C_4-symmetric systems in Ref. [75] are given by the Wilson loop invariant $\nu_{\mathbf{TX}}$, the nested Wilson loop invariant ν_x^π, and the symmetry indicator invariant $[M_1^{(4)}]$. For a definition of the different high symmetry points in the Brouillon zone of C_4 symmetric compounds, see Fig. II.2. The calculation of Wilson loop invariants and nested Wilson loops is described in section II.6, symmetry indicator invariants are treated in section II.5. These three invariants are not sufficient to distinguish all atomic limits that appear in C_4-symmetric systems, as can be seen in table II.2, where the values of the invariant for different atomic limits are listed[75]. In this table, different atomic limits are referred to as *elementary band representations*, which are basic bands

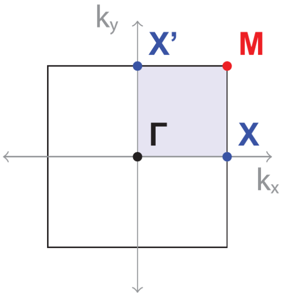

Figure II.2.: BZ of C_4 symmetric crystals. $\mathbf{\Gamma}$, $\mathbf{X}$, $\mathbf{X}'$, and $\mathbf{M}$ are the high symmetry points of the BZ. Figure reproduced from Ref. [75].

Table II.2.: EBRs, topological invariants and corner charges for C_4-symmetric systems. Table reproduced from Ref. [75].

C_4	$\nu_{\mathbf{TX}}$	ν_x^π	$[M_1^{(4)}]$	Q_c
$1a$	0	0	0	0
$1b\|_{\pm\frac{\pi}{4}}$	1	1	-1	1/2
$1b\|_{\pm\frac{3\pi}{4}}$	1	1	1	1/2
$2c$	1	0	0	0
$1b\|_{\pm\frac{\pi}{4}} \oplus 1b\|_{\pm\frac{3\pi}{4}}$	0	0	0	1

that span all the possible types of wannierisable bands that can appear. Because they can be wannierised in a symmetry-respecting way, each of the EBRs corresponds to a clear Wyckoff position. The maximal Wyckoff positions for a C_4-symmetric lattice are depicted in Fig. II.3. The corner charge can be obtained from considerations of cutting through Wannier centres at the corners of the material.

From this table, one sees that the trivial case $1a$ cannot be distinguished from the case $1b|_{\pm\frac{\pi}{4}} \oplus 1b|_{\pm\frac{3\pi}{4}}$ using solely the topological invariants proposed by Schindler et al. in Ref. [75]. Therefore the goal of the Master project presented in this thesis was originally to find an invariant that solves this problem. On the way there, smooth and symmetric gauges of the Bloch wave functions were studied in detail, which lead to a method to construct such gauges as a main result.

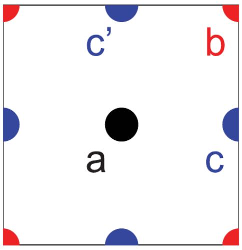

Figure II.3.: Real space unit cell and maximal Wyckoff positions of a C_4-symmetric 2D lattice. Figure reproduced from Ref. [75].

II.2.3. Structure of Part II

The first part of the thesis is structured as follows. In section II.3, space group symmetries are explained. Section II.4 gives the details of the models that are later on used as examples to show the methods presented. Later, in section II.5, the connection between localisation at Wyckoff positions and symmetry eigenvalues; as well as the *symmetry indicator invariants* following from it are explained. Section II.6 gives an overview over Wilson loops and a proof for an odd property in two-band subspaces in which the two bands are mapped onto each other by time-reversal. In section II.7, the first Chern number is quickly reviewed. Section II.8 describes parallel transport methods to construct symmetric and smooth gauges. There, the method developed by Kooi et al.[130] that solves the problem this project was supposed to solve is described. In section II.9, another method to construct symmetric gauges with smooth projectors, the *projected symmetric operator* method, is explained and examples are given. Section II.10 gives a short outlook to questions that might be of interest in the future.

II.3. Symmetries

In this section, the symmetries of Hamiltonians and their consequences for the eigenstates and the degeneracies of the energies are described. The results of Schindler et al.[75] and Bernevig and Hughes[10] are used.

II.3.1. Space Group Symmetries

The crystallographic symmetry of a translationally invariant system is given by the combination of the translation with other symmetries like rotation, screw-rotation, inversion, etc. In 2D, the space groups are referred to as wallpaper groups. They can have rotation, reflection and/or glide reflection symmetries. In this work, we are concerned with crystals with rotational symmetry as the only space group symmetry.

II.3.1.1. Translational Crystal Symmetry

Translational crystal symmetry allows, together with sufficiently weak interactions, the usage of a band structure description of the electronic system[134, 135][136, pp. 161-182]. If $\mathbf{G}$ is a vector of the reciprocal lattice, the crystal lattice in $\mathbf{k}$-space, then

$$H_{\mathbf{k}} = H_{\mathbf{k}+\mathbf{G}} \tag{II.2}$$

and

$$\left|u_{\mathbf{k}}^{(i)}\right\rangle = \left|u_{\mathbf{k}+\mathbf{G}}^{(i)}\right\rangle \quad \text{and} \quad E_{\mathbf{k}}^{(i)} = E_{\mathbf{k}+\mathbf{G}}^{(i)} \quad \text{for} \quad H_{\mathbf{k}}\left|u_{\mathbf{k}}^{(j)}\right\rangle = E_{\mathbf{k}}^{(j)}\left|u_{\mathbf{k}}^{(j)}\right\rangle . \tag{II.3}$$

These equalities are nothing but the periodicity of the electronic bands in the BZ. We can therefore equivalently say in 2D that $\mathbf{k} = (k_x, k_y) \in \mathbb{T}^2 = \mathbb{S}^1 \times \mathbb{S}^1$, where $\mathbb{T}^2$ is the two-torus, and $\mathbb{S}^1$ is the circle. The 2D BZ is a two-torus. A 3D Brouillon zone is a three-torus $\mathbb{T}^3 = \mathbb{S}^1 \times \mathbb{S}^1 \times \mathbb{S}^1$.

II.3.1.2. Rotational Symmetry

Rotational symmetry (C_n symmetry) is the symmetry under a rotation by an angle $\frac{2\pi}{n}$. The representation of rotational symmetry is given by a unitary operator r which acts on the Bloch wave function. If R is the rotation operator on the momentum vectors $\mathbf{k}$, then the effect of rotational symmetry on the Hamiltonian is expressed as

$$rH(\mathbf{k})r^\dagger = H(R\mathbf{k}), \qquad\qquad \text{with } r^\dagger = r^{-1}. \tag{II.4}$$

For spin-orbit coupled systems, r satisfies $r_n^n = -1$. If we have an eigenstate $\left|u_{\mathbf{k}}^{(i)}\right\rangle$ with eigenvalue $E_{\mathbf{k}}^{(i)}$ of $H(\mathbf{k})$, it follows that

$$H(R\mathbf{k})r\left|u_{\mathbf{k}}^{(i)}\right\rangle = rH(\mathbf{k})\left|u_{\mathbf{k}}^{(i)}\right\rangle = rE_k^{(i)}\left|u_{\mathbf{k}}^{(i)}\right\rangle = E_k^{(i)}r\left|u_{\mathbf{k}}^{(i)}\right\rangle. \tag{II.5}$$

This shows that $r\left|u_{\mathbf{k}}^{(i)}\right\rangle$ is an eigenstate of $H(R\mathbf{k})$ with eigenvalue $E_{\mathbf{k}}^{(i)}$; the band structure is C_n-symmetric.

II.3.2. Internal Symmetries

Time reversal symmetry (TRS), particle hole symmetry (PHS) and chiral symmetry (CS) are the possible internal symmetries of Hermitian Hamiltonians. The only relevant symmetry for this part of the thesis is TRS.

II.3.2.1. Time Reversal Symmetry

Time reversal describes the effects of flipping the arrow of time. In condensed matter physics, the main effect is to flip the spins. On the Bloch Hamiltonian TRS is given by

$$\mathcal{T}H(\mathbf{k})\mathcal{T}^{-1} = \tau H^*(\mathbf{k})\tau^\dagger = \tau H^T(\mathbf{k})\tau^\dagger = H(-\mathbf{k}), \tag{II.6}$$

with $\mathcal{T} = \tau K$, where τ is a unitary matrix and K is the complex conjugation. The inverse of $\mathcal{T}$ is given by

$$\mathcal{T}^{-1} = K\tau^\dagger. \tag{II.7}$$

The implication of TRS for the eigenstate $\left|u_{\mathbf{k}}^i\right\rangle$ with $H(\mathbf{k})\left|u_{\mathbf{k}}^i\right\rangle = E_{\mathbf{k}}^i\left|u_{\mathbf{k}}^i\right\rangle$ is that

$$H(-\mathbf{k})\mathcal{T}\left|u_{\mathbf{k}}^i\right\rangle = \mathcal{T}H(\mathbf{k})\left|u_{\mathbf{k}}^i\right\rangle = \mathcal{T}E_{\mathbf{k}}^i\left|u_{\mathbf{k}}^i\right\rangle = E_{\mathbf{k}}^i\mathcal{T}\left|u_{\mathbf{k}}^i\right\rangle. \tag{II.8}$$

This means that $\mathcal{T}\left|u_{\mathbf{k}}^i\right\rangle$ is an eigenstate of $H(-\mathbf{k})$ with eigenvalue $E_{\mathbf{k}}^i$.

II.4. Models

In this section, we will introduce the models used in the further sections of this part to exemplify proofs and to disprove other statements.

II.4.1. Models for Obstructed Atomic Limits

In this section, a number of models for OALs are introduced.

II.4.1.1. Models Without TRS

Benalcazar et al.[133] have proposed a number of primitive generators for the case without spin-orbit coupling in their paper about the *Quantization of fractional corner charge in C_n-symmetric higher-order topological crystalline insulators*[133]. These primitive generators span the space of all models whose occupied bands correspond to an atomic limit and respect the symmetries. Each of them corresponds to an EBR. Thus, it is sufficient to study these primitive generators to uncover the properties of OALs. The primitive generators are referred to as $h^{(n)}_{Zx}$, x is the Wyckoff position (cf. section II.5) at which the electrons are centred and n gives the type of rotational symmetry. Z gives the number of electrons. So, for example $h^{(4)}_{2b}$ means that it is the primitive generator for two electrons at the $1b$ Wyckoff position, with fourfold rotational symmetry.

Models corresponding to these generators can be transformed into models with spin-orbit coupling by doubling the model, see section II.4.1.2. For the convenience of the reader, these models, which are tight-binding models, are listed in the following.

Models with C_2 and/or C_4. First, the models with C_2 and/or C_4 symmetry are described.

The first tight-binding model we consider is the one corresponding to the primitive generator $h^{(4)}_{1b}$. It is therefore a C_4 symmetric model with one electron centred on the $1b$ position of the unit cell, for parameters $-1 < t_x = t_y < 1$. Its lattice with four sites per unit cell is depicted in Fig. II.4 a). The lines indicate hoppings with unit amplitude. In Fig. II.4c) its band structure along high-symmetry lines is shown. The model has one occupied and three unoccupied bands. In Figure II.4b) and d) the different OALs it can be in, depending on the parameters (t_x, t_y), are shown: In b) for C_2 with a general $t_x \neq t_y$, and in d) for C_4 with $t_x = t_y$. Its Hamiltonian is given by

$$H^{(2)}_1(\mathbf{k}, t_x, t_y) = \begin{pmatrix} 0 & e^{ik_x} & 0 & e^{ik_y} \\ e^{-ik_x} & 0 & e^{ik_y} & 0 \\ 0 & e^{-ik_y} & 0 & e^{-ik_x} \\ e^{-ik_y} & 0 & e^{ik_x} & 0 \end{pmatrix} + \begin{pmatrix} 0 & t_x & 0 & t_y \\ t_x & 0 & t_y & 0 \\ 0 & t_y & 0 & t_x \\ t_y & 0 & t_x & 0 \end{pmatrix}. \tag{II.9}$$

The representation of the C_4 rotation operator is

$$r_4 = \begin{pmatrix} 0 & 0 & 0 & 1 \\ 1 & 0 & 0 & 0 \\ 0 & 1 & 0 & 0 \\ 0 & 0 & 1 & 0 \end{pmatrix}. \tag{II.10}$$

and C_2 is represented as

$$r_2 = r_4^2. \tag{II.11}$$

The second model has a lattice depicted in Fig. II.5a). Its band structure is shown in Fig. II.5b). It has two occupied bands and two unoccupied bands, giving two electrons per unit cell, centred around the $1b$ position for $-1 < t_0 < 1$. This model corresponds to the case $1b \oplus 1b$ and will be of great interest to us in its spin-orbit coupled form. It corresponds to the primitive generator $h^{(4)}_{2b}$. Its Hamiltonian is given by

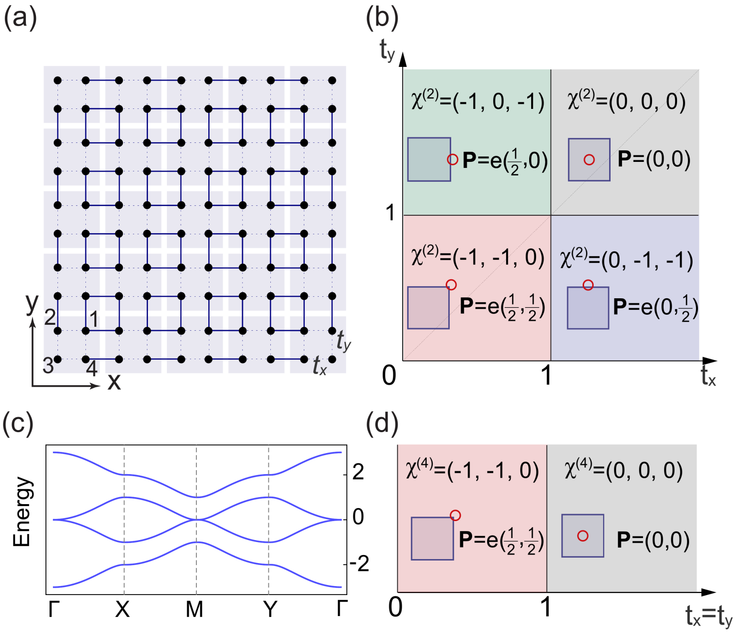

Figure II.4.: Lattice model $H_1^{(2)}$ by Benalcazar et al.[133]. This model corresponds to the primitive generator $h_{1b}^{(4)}$. Figure reproduced from Ref. [133].

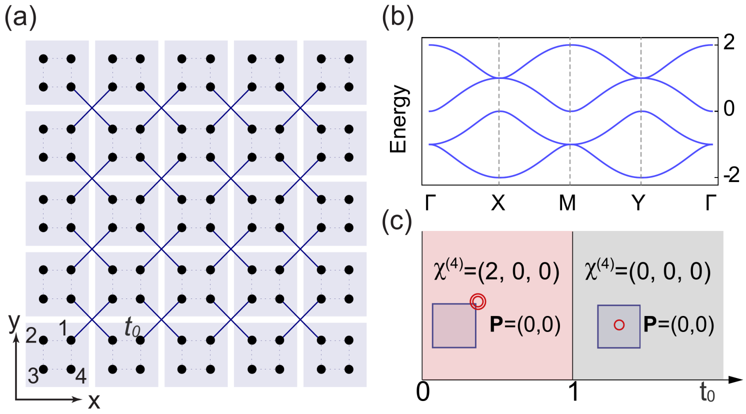

Figure II.5.: Lattice model $H_2^{(4)}$ by Benalcazar et al.[133]. This model corresponds to the primitive generator $h_{2b}^{(4)}$. Figure reproduced from Ref. [133].

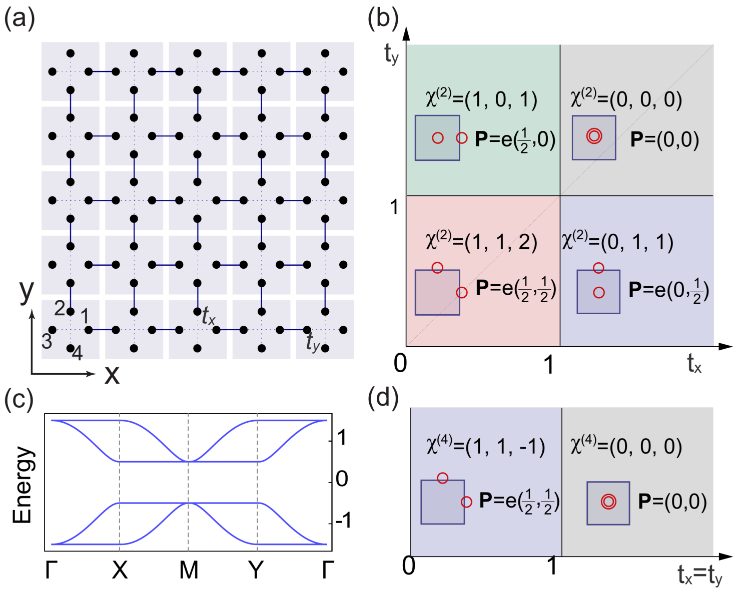

Figure II.6.: Lattice model $H_3^{(2)}$ by Benalcazar et al.[133]. This model corresponds to the primitive generator $h_{2c}^{(4)}$. Figure reproduced from Ref. [133].

$$H_2^{(4)}(\mathbf{k}, t_0) = \begin{pmatrix} 0 & t_0 & e^{i(k_x+k_y)} & t_0 \\ t_0 & 0 & t_0 & e^{-i(k_x-k_y)} \\ e^{-i(k_x+k_y)} & t_0 & 0 & t_0 \\ t_0 & e^{i(k_x-k_y)} & t_0 & 0 \end{pmatrix} \tag{II.12}$$

with the same representation of the rotation symmetry as in the model $H_1^{(2)}$, see eq. II.10.

The third lattice model for C_4-symmetric systems is $H_3^{(2)}$. For $t_x = t_y$, it is C_4-symmetric. It corresponds to the the primitive generator $h_{2c}^{(4)}$. The lattice is depicted in figure II.6a), its band structure in figure II.6c). It has two filled bands. The representation of C_4 is the same as before. The atomic limits for C_2 are depicted in II.6b), the ones for C_4 in figure II.6d). As can be seen, in the C_4 case, the electrons in the obstructed atomic limit only have a C_2 site symmetry group, which means that if we look at one of the sites on the side of the unit cell square, it is only mapped onto itself by C_2, taking into consideration lattice periodicity, not C_4. The Hamiltonian is

$$H_3^{(2)}(\mathbf{k}, t_x, t_y) = \begin{pmatrix} 0 & 0 & e^{ik_x} & 0 \\ 0 & 0 & 0 & e^{ik_y} \\ e^{-ik_x} & 0 & 0 & 0 \\ 0 & e^{-ik_y} & 0 & 0 \end{pmatrix} + \begin{pmatrix} 0 & 0 & t_x & 0 \\ 0 & 0 & 0 & t_y \\ t_x & 0 & 0 & 0 \\ 0 & t_y & 0 & 0 \end{pmatrix}. \tag{II.13}$$

The remaining primitive generator for C_2 is $h_{1d}^{(2)}$. The corresponding Hamiltonian is

$$H_4^{(2)}(\mathbf{k}, t_0) = \begin{pmatrix} 0 & t_0 + e^{-ik_y} \\ t_0 + e^{ik_y} & 0 \end{pmatrix} \tag{II.14}$$

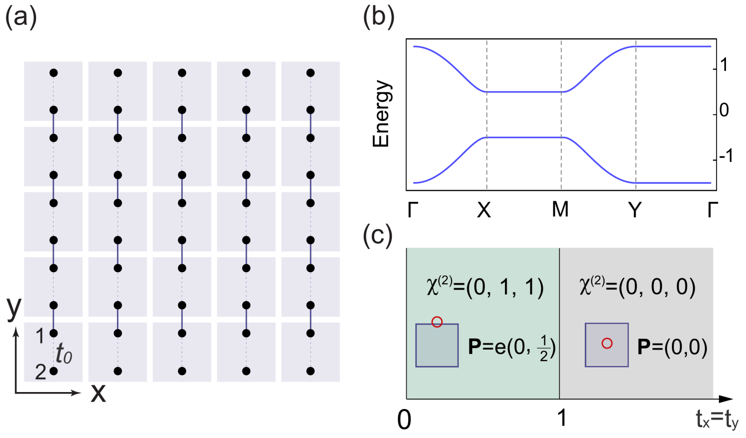

Figure II.7.: Lattice model $H_4^{(2)}$ by Benalcazar et al.[133]. This model corresponds to the primitive generator $h_{1d}^{(2)}$. Figure reproduced from Ref. [133].

with

$$r_2 = \sigma_x = \begin{pmatrix} 0 & 1 \\ 1 & 0 \end{pmatrix} \tag{II.15}$$

as representation of the C_2-symmetry. Its lattice model is shown in Figure II.7a), its band structure in Fig. II.7b), and its different atomic limits in Fig. II.7c). It is effectively an array of SSH models (cf. Ref. [137, p. 36-37] for the SSH model) stacked next to each other.

Models with C_3 and/or C_6. For the case of C_3 and C_6 symmetry, we look at a lattice with the two basis vectors

$$\mathbf{a}_1 = (1, 0) \text{ and } \mathbf{a}_2 = \left(\frac{1}{2}, \frac{\sqrt{3}}{2}\right) \tag{II.16}$$

and the third vector

$$\mathbf{a}_3 = \mathbf{a}_1 - \mathbf{a}_2. \tag{II.17}$$

The first tight-binding model for the C_6-case is $H_1^{(6)}$. It corresponds to the primitive generator $h_{4b}^{(6)}$ and has the Hamiltonian

$$H_1^{(6)}(\mathbf{k}, t_0) = \begin{pmatrix} 0 & t_0 & e^{i\mathbf{k}\cdot\mathbf{a}_2} & 0 & e^{-i\mathbf{k}\cdot\mathbf{a}_3} & t_0 \\ t_0 & 0 & t_0 & e^{-i\mathbf{k}\cdot a_3} & 0 & e^{-i\mathbf{k}\cdot\mathbf{a}_1} \\ e^{-i\mathbf{k}\cdot\mathbf{a}_2} & t_0 & 0 & t_0 & e^{-i\mathbf{k}\cdot\mathbf{a}_1} & 0 \\ 0 & e^{i\mathbf{k}\cdot\mathbf{a}_3} & t_0 & 0 & t_0 & e^{-i\mathbf{k}\cdot\mathbf{a}_2} \\ e^{i\mathbf{k}\cdot\mathbf{a}_3} & 0 & e^{i\mathbf{k}\cdot\mathbf{a}_1} & t_0 & 0 & t_0 \\ t_0 & e^{i\mathbf{k}\cdot\mathbf{a}_1} & 0 & e^{i\mathbf{k}\cdot\mathbf{a}_2} & t_0 & 0 \end{pmatrix}. \tag{II.18}$$

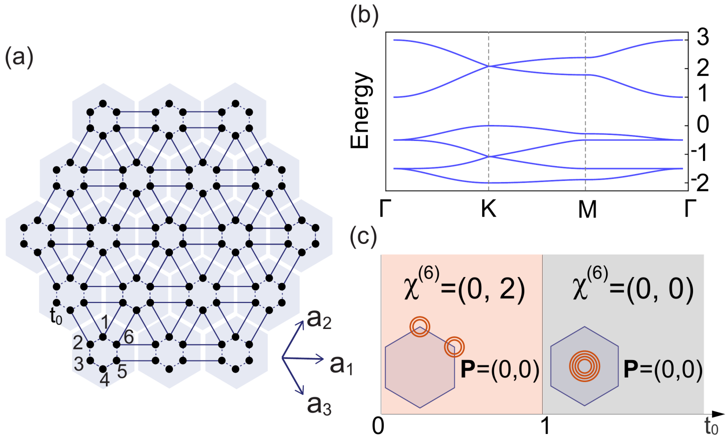

Figure II.8.: Lattice model $H_1^{(6)}$ by Benalcazar et al.[133]. This model corresponds to the primitive generator $h_{4b}^{(6)}$. Figure reproduced from Ref. [133].

The C_6 symmetry is represented by the constant matrix

$$\begin{pmatrix} 0 & 0 & 0 & 0 & 0 & 1 \\ 1 & 0 & 0 & 0 & 0 & 0 \\ 0 & 1 & 0 & 0 & 0 & 0 \\ 0 & 0 & 1 & 0 & 0 & 0 \\ 0 & 0 & 0 & 1 & 0 & 0 \\ 0 & 0 & 0 & 0 & 1 & 0 \end{pmatrix}. \tag{II.19}$$

The tight-binding model on the lattice is depicted in Fig. II.8a). Fig. II.8b) shows its band structure. There are four occupied bands and two unoccupied bands. Figure II.8c) shows the positions of the electrons in the atomic limits. The remaining symmetry for the individual electrons is a C_3 symmetry in the obstructed phase ($t_0 < 1$).

The second model with C_6 symmetry is $H_2^{(6)}$. Its tight-binding representation is depicted in Figure II.9a). It corresponds to the primitive generator $h_{3c}^{(6)}$. The tight-binding Hamiltonian is

$$H_2^{(6)}(\mathbf{k}, t_0) = \begin{pmatrix} 0 & t_0 & 0 & e^{i\mathbf{k}\cdot\mathbf{a}_2} & 0 & t_0 \\ t_0 & 0 & t_0 & 0 & e^{-i\mathbf{k}\cdot\mathbf{a}_3} & 0 \\ 0 & t_0 & 0 & t_0 & 0 & e^{-i\mathbf{k}\cdot\mathbf{a}_1} \\ e^{-i\mathbf{k}\cdot\mathbf{a}_2} & 0 & t_0 & 0 & t_0 & 0 \\ 0 & e^{i\mathbf{k}\cdot\mathbf{a}_3} & 0 & t_0 & 0 & t_0 \\ t_0 & 0 & e^{i\mathbf{k}\cdot\mathbf{a}_1} & 0 & t_0 & 0 \end{pmatrix} \tag{II.20}$$

and has three occupied bands. The site symmetry group in the obstructed phase ($t_0 < 1$) is C_2.

For C_3 symmetry, there are two different tight-binding models for the two generators. The first

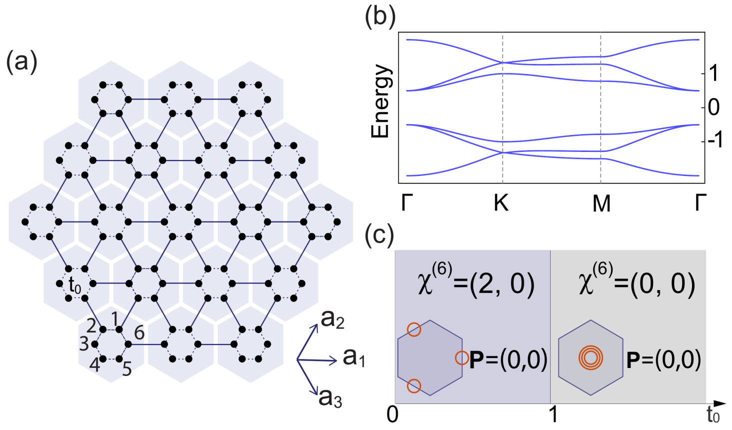

Figure II.9.: Lattice model $H_2^{(6)}$ by Benalcazar et al.[133]. This model corresponds to the primitive generator $h_{3c}^{(6)}$. Figure reproduced from Ref. [133].

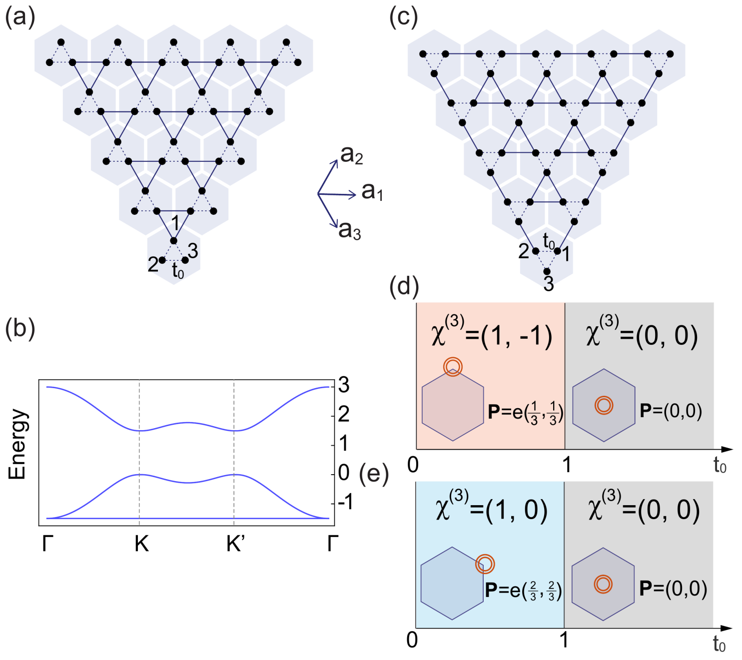

Figure II.10.: Lattice models $H_1^{(3)}$ and $H_2^{(3)}$ by Benalcazar et al.[133]. These model correspond to the primitive generators $h_{2b}^{(3)}$ and $h_{2c}^{(3)}$, respectively. Figure reproduced from Ref. [133].

model has the tight-binding representation depicted in Fig. II.10a) and has the Hamiltonian

$$H_1^{(3)}(\mathbf{k}, t_0) = \begin{pmatrix} 0 & t_0 + e^{i\mathbf{k}\cdot\mathbf{a}_2} & t_0 + e^{-i\mathbf{k}\cdot\mathbf{a}_3} \\ t_0 + e^{-i\mathbf{k}\cdot\mathbf{a}_2} & 0 & t_0 + e^{-i\mathbf{k}\cdot\mathbf{a}_1} \\ t_0 + e^{i\mathbf{k}\cdot\mathbf{a}_3} & t_0 + e^{i\mathbf{k}\cdot\mathbf{a}_1} & 0 \end{pmatrix}. \tag{II.21}$$

It corresponds to the primitive generator $h_{2b}^{(3)}$. The individual electrons have C_3 site symmetry group. The position of the electrons in the unit cell is shown in Fig. II.10d). The representation of C_3 is

$$r_3 = \begin{pmatrix} 0 & 0 & 1 \\ 1 & 0 & 0 \\ 0 & 1 & 0 \end{pmatrix}. \tag{II.22}$$

The second primitive generator of C_3 is $h_{2c}^{(3)}$. For this generator, we use the Hamiltonian

$$H_2^{(3)}(\mathbf{k}, t_0) = \begin{pmatrix} 0 & t_0 + e^{i\mathbf{k}\cdot\mathbf{a}_1} & t_0 + e^{i\mathbf{k}\cdot\mathbf{a}_2} \\ t_0 + e^{-i\mathbf{k}\cdot\mathbf{a}_1} & 0 & t_0 + e^{-i\mathbf{k}\cdot\mathbf{a}_3} \\ t_0 + e^{-i\mathbf{k}\cdot\mathbf{a}_2} & t_0 + e^{i\mathbf{k}\cdot\mathbf{a}_3} & 0 \end{pmatrix} \tag{II.23}$$

with the same representation of C_3 as before. The lattice model is shown in Fig. II.10c). The band structures of the two C_3 models are the same and shown in Fig. II.10b). Figure II.10e) shows the position of the electrons in the unit cell.

II.4.1.2. Adding TRS.

In order to add TRS, the Hamiltonians are doubled. For example in the case of $H_2^{(4)}$, we define the Hamiltonian as

$$H_{2\mathcal{T}}^{(4)}(\mathbf{k}) = \begin{pmatrix} H_2^{(4)}(\mathbf{k}) & 0 \\ 0 & H_2^{(4)}(\mathbf{k}) \end{pmatrix}. \tag{II.24}$$

This new Hamiltonian has twice as many bands and correspondingly one electron is replaced by one Kramers pair. The symmetries are rotational symmetry

$$r_{n\mathcal{T}} = e^{\frac{i\pi\sigma_z}{n}} \otimes r_n \tag{II.25}$$

and TRS

$$\mathcal{T} = i\sigma_y \otimes \mathbb{1}. \tag{II.26}$$

In the further sections of this part, $H_{n\mathcal{T}}^{(m)}$ will be referred to as $H_n^{(m)}$.

II.4.2. Model for Double Topological Insulator with C_4 and TRS

Furthermore, we use a model for a double topological insulator, developed by Song et al.[138]. It is also a C_4-symmetric model on a square lattice. It has a Hamiltonian given by

$$\begin{aligned} H(\mathbf{k}) = &-\frac{1}{2}(1 - \cos k_x - \cos k_y)\sigma_0 \otimes \sigma_z \otimes \sigma_0 - \frac{1}{2}\sin(k_x)\sigma_0 \otimes \sigma_x \otimes \sigma_x \\ &- \frac{1}{2}\sin(k_y)\sigma_0 \otimes \sigma_x \otimes \sigma_y - \frac{\Delta}{2}(\cos k_x - \cos k_y)\sigma_y \otimes \sigma_y \otimes \sigma_0. \end{aligned} \tag{II.27}$$

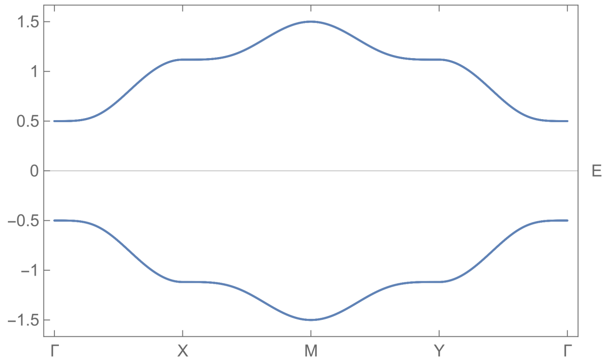

Figure II.11.: Band structure of the model by Song et al.[138]

This Hamiltonian has TRS and C_4 symmetry, which are represented by

$$\mathcal{T} = \mathbb{1}_4 \otimes i\sigma_y K \tag{II.28}$$

and

$$r_4 = \sigma_z \otimes \sigma_y \otimes e^{-\frac{i\pi\sigma_z}{4}}. \tag{II.29}$$

The band structure of this model is depicted in Fig. II.11. Unlike the previous models, its occupied bands do not correspond to a BR.

II.4.3. Random Perturbations

Random symmetry-respecting perturbations of a Hamiltonian $H_{\mathbf{k}}$ do not change the topological invariants, as long as the gap remains open. In section II.9, they are extensively used to construct useful gauges. One possibility to create a random perturbation is to start with a general random matrix-valued function defined on the torus $\mathbb{T}^2 = \{(k_x, k_y)\}$, then hermitise it, if Hermiticity is required, and to symmetrise it according to the needed symmetries (e.g. C_4 and TRS).

Random matrices on the torus (which are sufficiently well-behaved) can be represented as Fourier series

$$R(\mathbf{k}) = R(k_x, k_y) = \sum_{n_x \in \mathbb{Z}} \sum_{n_y \in \mathbb{Z}} \mathrm{RandMat}[\mathrm{N} \times \mathrm{N}](n_x, n_y) e^{i n_x k_x + i n_y k_y}, \tag{II.30}$$

where RandMat[N × N] are random complex matrices that are in general distinct for different values of (n_x, n_y). In principle, RandMat[N × N] can be drawn from any distribution, and an unlimited number of terms can be included. In practice, this is unnecessary and we only use a finite number of terms (e.g. $(n_x, n_y) = (0,0), (0,1), (1,0)$), which also resolves any otherwise occurring issues with divergences. For simplicity, we choose the real and imaginary parts of the components of RandMat[N × N] from a continuous uniform distribution on the interval $[-1, 1]$.

II.4.3.1. Random Perturbations with TRS and C_4 Symmetry

To get a random perturbation respecting C_4 and TRS, we start with a random matrix $R(\mathbf{k})$ and then symmetrise it in three steps. First, we hermitise the matrix, then we make it compatible

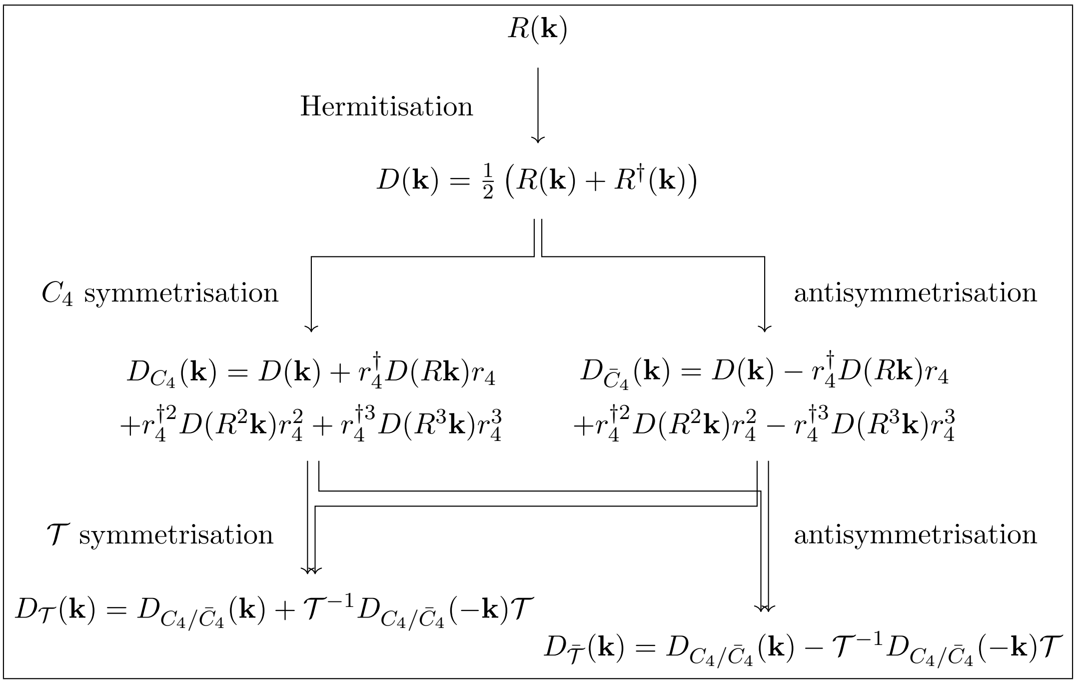

Figure II.12.: Symmetrisation procedure to get perturbations for the Hamiltonian or symmetric operators.

with C_4-symmetry. In the end, we ensure that it is TRS-symmetric. This symmetrisation procedure is depicted in Fig. II.12.

The hermitised perturbation is obtained as

$$D_{\text{herm}}(\mathbf{k}) = \frac{R(\mathbf{k}) + R(\mathbf{k})^\dagger}{2} \tag{II.31}$$

To make it C_4-symmetric, one proceeds as follows:

$$\begin{aligned} D_{\text{herm},C_4}(\mathbf{k}) = D_{\text{herm}}(\mathbf{k}) &+ r_4^\dagger D_{\text{herm}}(R_4\mathbf{k}) r_4 \\ &+ r_4^{\dagger 2} D_{\text{herm}}(R_4^2\mathbf{k}) r_4^2 + \left(r_4^\dagger\right)^3 D_{\text{herm}}(R_4^3\mathbf{k}) r_4^3. \end{aligned} \tag{II.32}$$

This is C_4-symmetric because

$$\begin{aligned} r_4 D_{\text{herm},C_4}(\mathbf{k}) r_4^\dagger &= r_4 r_4^{\dagger 4} D_{\text{herm}}(R_4^4\mathbf{k}) r_4^4 r_4^\dagger + r_4 r_4^\dagger D_{\text{herm}}(R_4\mathbf{k}) r_4 r_4^\dagger \\ &\quad + r_4 r_4^{\dagger 2} D_{\text{herm}}(R_4^2\mathbf{k}) r_4^2 r_4^\dagger + r_4 \left(r_4^\dagger\right)^3 D_{\text{herm}}(R_4^3\mathbf{k}) r_4^3 r_4^\dagger \\ &= D_{\text{herm}}(R_4\mathbf{k}) + r_4^\dagger D_{\text{herm}}(R_4 R_4\mathbf{k}) r_4 \\ &\quad + r_4^{\dagger 2} D_{\text{herm}}(R_4 R_4^2\mathbf{k}) r_4^2 + r_4^{\dagger 3} D_{\text{herm}}(R_4 R_4^3\mathbf{k}) r_4^3 = D_{\text{herm},C_4}(R_4\mathbf{k}). \end{aligned} \tag{II.33}$$

If one wants to ensure that

$$r_4 D_{\text{herm},\bar{C}_4}(\mathbf{k}) r_4^\dagger = -D_{\text{herm},\bar{C}_4}(R_4\mathbf{k}), \tag{II.34}$$

one can set

$$D_{\mathrm{herm},\bar{C}_4}(\mathbf{k}) = D_{\mathrm{herm}}(\mathbf{k}) - r_4^\dagger D_{\mathrm{herm}}(R_4\mathbf{k}) r_4 \\ + r_4^{\dagger 2} D_{\mathrm{herm}}(R_4^2\mathbf{k}) r_4^2 - \left(r_4^\dagger\right)^3 D_{\mathrm{herm}}(R_4^3\mathbf{k}) r_4^3. \quad \text{(II.35)}$$

As a last step, TRS is ensured by

$$D_{\mathrm{herm},\ C_4,\ \mathcal{T}}(\mathbf{k}) = D_{\mathrm{herm},C_4}(\mathbf{k}) + \mathcal{T}^{-1} D_{\mathrm{herm},C_4}(-\mathbf{k})\mathcal{T}. \quad \text{(II.36)}$$

If one wants an anticommutation with $\mathcal{T}$, one has to choose

$$D_{\mathrm{herm},\ C_4,\ \bar{\mathcal{T}}}(\mathbf{k}) = D_{\mathrm{herm},C_4}(\mathbf{k}) - \mathcal{T}^{-1} D_{\mathrm{herm},C_4}(-\mathbf{k})\mathcal{T}, \quad \text{(II.37)}$$

which ensures that

$$\mathcal{T} D_{\mathrm{herm},\ C_4,\ \bar{\mathcal{T}}}(\mathbf{k})\mathcal{T}^{-1} = -D_{\mathrm{herm},\ C_4,\ \bar{\mathcal{T}}}(-\mathbf{k}). \quad \text{(II.38)}$$

The further steps do not interfere with the earlier symmetrisation steps because $\mathcal{T}$ and space group symmetries commute and the prefactors $+1/-1$ are real. If some of the symmetries are broken, there are remaining symmetries. For example, in the case of $\bar{C}_4 \times \mathcal{T}$ what remains is a $C_2 \times \mathcal{T}$ symmetry, or in the case of $C_4 \times \bar{\mathcal{T}}$, the remaining symmetry is a C_4 symmetry. The anti-commutation-like behaviour under the broken symmetries can be useful to construct gauges in which symmetry operators act by exchanging bands.

II.4.3.2. Random Perturbations with C_2, C_3 and C_6 Symmetry

To get C_2-, C_3- and C_6-symmetric perturbation matrices, we start, as before, with a random matrix $R(\mathbf{k})$, and perform the Hermitisation step, if necessary. To enforce the space group symmetry, we then execute one of the following steps.
To obtain a C_2 symmetric matrix, one has to perform the symmetrisation step

$$D_{\mathrm{herm},C_2}(\mathbf{k}) = D_{\mathrm{herm}}(\mathbf{k}) + r_2^\dagger D_{\mathrm{herm}}(R_2\mathbf{k}) r_2, \quad \text{(II.39)}$$

for $\bar{C}_2$ it is

$$D_{\mathrm{herm},\bar{C}_2}(\mathbf{k}) = D_{\mathrm{herm}}(\mathbf{k}) - r_2^\dagger D_{\mathrm{herm}}(R_2\mathbf{k}) r_2. \quad \text{(II.40)}$$

For C_3 the step is

$$D_{\mathrm{herm},C_3}(\mathbf{k}) = D_{\mathrm{herm}}(\mathbf{k}) + r_3^\dagger D_{\mathrm{herm}}(R_3\mathbf{k}) r_3 + r_3^{\dagger 2} D_{\mathrm{herm}}(R_3^2\mathbf{k}) r_3^2. \quad \text{(II.41)}$$

For C_6 we get

$$D_{\mathrm{herm},C_6}(\mathbf{k}) = D_{\mathrm{herm}}(\mathbf{k}) + r_6^\dagger D_{\mathrm{herm}}(R_6\mathbf{k}) r_6 + r_6^{\dagger 2} D_{\mathrm{herm}}(R_6^2\mathbf{k}) r_6^2 \\ + r_6^{\dagger 3} D_{\mathrm{herm}}(R_6^3\mathbf{k}) r_6^3 + r_6^{\dagger 4} D_{\mathrm{herm}}(R_6^4\mathbf{k}) r_6^4 + r_6^{\dagger 5} D_{\mathrm{herm}}(R_6^5\mathbf{k}) r_6^5 \quad \text{(II.42)}$$

and for $\bar{C}_6$

$$D_{\mathrm{herm},C_6}(\mathbf{k}) = D_{\mathrm{herm}}(\mathbf{k}) - r_6^\dagger D_{\mathrm{herm}}(R_6\mathbf{k}) r_6 + r_6^{\dagger 2} D_{\mathrm{herm}}(R_6^2\mathbf{k}) r_6^2 \\ - r_6^{\dagger 3} D_{\mathrm{herm}}(R_6^3\mathbf{k}) r_6^3 + r_6^{\dagger 4} D_{\mathrm{herm}}(R_6^4\mathbf{k}) r_6^4 - r_6^{\dagger 5} D_{\mathrm{herm}}(R_6^5\mathbf{k}) r_6^5. \quad \text{(II.43)}$$

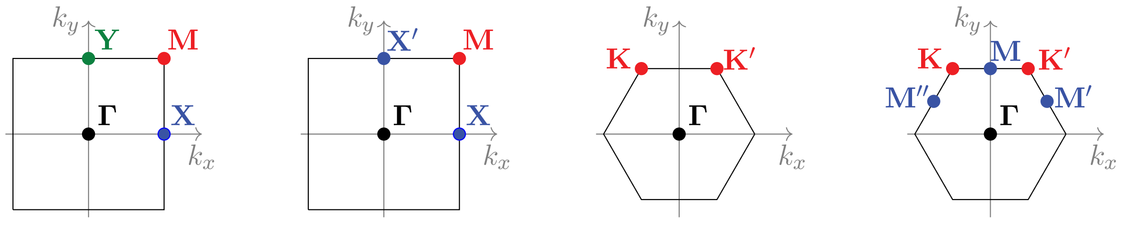

(a) C_2 (b) C_4 (c) C_3 (d) C_6

Figure II.13.: Brouillon zones of C_2-, C_4-, C_3- and C_6-symmetric systems with HSPs.

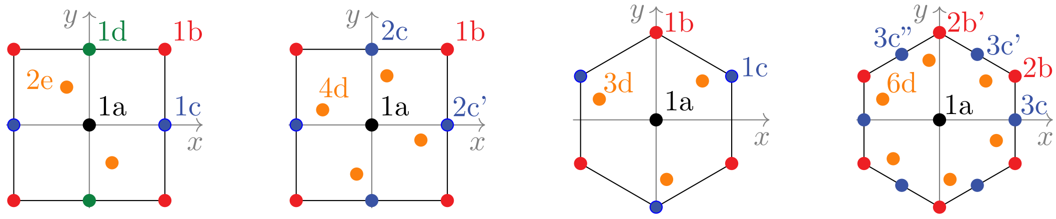

(a) C_2 (b) C_4 (c) C_3 (d) C_6

Figure II.14.: Wyckoff positions in C_2-, C_4-, C_3- and C_6-symmetric 2D unit cells. We indicate the maximal Wyckoff positions as well as the general Wyckoff position.

These types of perturbations or symmetric operators have some importance in the case of other wallpaper groups. When studying systems with C_6 or C_3, it can be useful to construct operators that break these symmetry. In the case $\bar{C}_6$ above, the symmetry we broke was C_2, but C_3 remained intact. To break C_3 symmetry one choses an operator with

$$r_3 D(\mathbf{k}) r_3^\dagger = e^{\frac{i2\pi}{3}} D(R_3\mathbf{k}). \tag{II.44}$$

Operators like these are extensively used in section II.9.3.2, their construction is discussed there.

II.5. Wyckoff Positions and Symmetry Eigenvalues

In this section, Wyckoff positions are described and we see how the knowledge about them can enable us to make statements about symmetry eigenvalues in the occupied bands at high-symmetry points (HSPs) in the BZ. Furthermore, symmetry indicator invariants will be described.

Every position in the real-space unit cell is a Wyckoff position, but with varying multiplicity. A Wyckoff position with multiplicity one has the property that it stays invariant under all symmetries. A Wyckoff position of multiplicity n has the property that there are n positions within the unit cell such that any of them is mapped onto another under symmetry transformations. The Wyckoff positions of 2D materials with C_2, C_3, C_4 and C_6 symmetry are depicted in Fig. II.14. The Wyckoff positions for a 2D material with C_4 symmetry are depicted in Fig. II.15. The figure shows all the different Wyckoff positions, beginning with 1a, which is the Wyckoff position at the centre of the unit cell. It remains at the same position under C_4

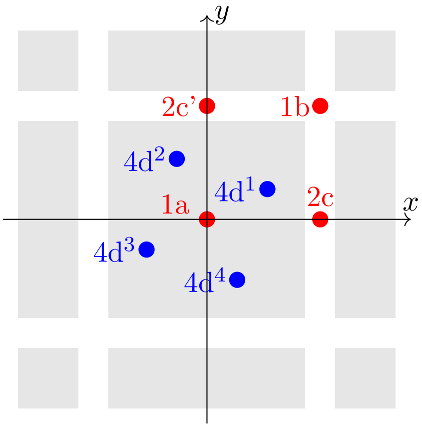

Figure II.15.: Wyckoff positions in quadratic system with C_4 symmetry. The positions 1a and 1b have multiplicity one. The position 2c has multiplicity two. The position 4d has multiplicity 4 and is the general Wyckoff position.

rotation. Position 1b is rotated by the C_4 rotation, but the new position is equivalent to the old one. In the case of 2c one needs to apply C_4 twice to get back to a position that is equivalent to the original position modulo lattice translations. Position 4d is the general Wyckoff position. One needs to apply C_4 four times to get back to the start. If the occupied bands correspond to a band representation, it is possible to construct a gauge in which the electronic charge is well-localised at Wyckoff positions (Wannierisation). In this case, the occupied can be grouped into groups of bands, each of which corresponding to an EBR. The electrons in each EBR are localised at a Wyckoff position, allowing us to make statements about symmetry eigenvalues at high symmetry positions in the BZ. The HSPs of the BZs of 2D systems with C_2, C_3, C_4 and C_6 symmetry are depicted in Fig. II.13. To make such statements, we use the fact that translation from an initial position $\mathbf{r}_i$ to a final position $\mathbf{r}_f$ adds the factor

$$e^{i\mathbf{k}\cdot(\mathbf{r}_f-\mathbf{r}_i)} \tag{II.45}$$

to the Bloch wave functions. So if the electrons of a band are localised at 1a, the r_4 eigenvalues at $\mathbf{\Gamma}$ and $\mathbf{M}$ are the same. If they are at 1b, the eigenvalues at $\mathbf{\Gamma}$ are multiplied with a factor of

$$e^{i\mathbf{k}\cdot(\mathbf{r}_f-\mathbf{r}_i)} = e^{i\begin{pmatrix}\pi\\\pi\end{pmatrix}\cdot\begin{pmatrix}-1\\0\end{pmatrix}} = e^{-i\pi} = -1$$

to obtain the eigenvalues at $\mathbf{M}$.

This means that the C_4 eigenvalues of a band well-localised at $1b$ change their sign when moving from $\mathbf{\Gamma}$ to $\mathbf{M}$. If that is not the case, it cannot correspond to a well-localised band at $1b$. If there are only two bands, and these bands have r_4 eigenvalues $e^{\pm i\pi/4}$ at $\mathbf{\Gamma}$, then these eigenvalues change to $e^{\pm i3\pi/4}$ at $\mathbf{M}$. This allows us to distinguish a phase with two electrons at 1a from the one with two electrons at 1b. To formalise, one defines the symmetry indicator invariant[75] as the difference between the number of $e^{i\pi/4}$ eigenvalues at $\mathbf{\Gamma}$ und $\mathbf{M}$ as

$$[M_1^{(4)}] = \#M_1^{(4)} - \#\Gamma_1^{(4)}, \tag{II.46}$$

where $\#T_1^4$ is the number rotational eigenvalues $e^{i\pi/4}$ within the occupied bands at the time-reversal invariant momentum (TRIM) $\mathbf{T}$. Corresponding formulae also exist for systems with other symmetries[75, 133].
A band inversion is a consequence of electronic centres being displaced from the centres of the unit cell or of non-Wannierisability of a band. If, like before, we are at Wyckoff position $1b$, we have seen that the eigenvalues change between $\mathbf{\Gamma}$ and $\mathbf{M}$. If we now have two bands, one with eigenvalues $e^{\pm i\pi/4}$ r_4 at $\mathbf{\Gamma}$, and a second one with eigenvalues $e^{\pm 3i\pi/4}$ r_4 at $\mathbf{\Gamma}$, then these bands exchange their r_4 eigenvalues when going from $\mathbf{\Gamma}$ to $\mathbf{M}$. This effect is called a band inversion.

II.6. Wilson Loops

Wilson loops are a way of characterizing the topology of a subspace of a vectorspace[139]. Intuitively, they express how the occupied space is deformed when moving on a path around the BZ torus. To first get a feeling for their meaning we examine the 1D Hamiltonians

$$\begin{aligned} H_1(k) = \left|v_k^1\right\rangle\left\langle v_k^1\right| - \left|u_k^1\right\rangle\left\langle u_k^1\right|, \text{ with } \left|u_k^1\right\rangle = \begin{pmatrix}\cos(k/2)\\ \sin(k/2)\end{pmatrix} \text{ and } \left|v_k^1\right\rangle = \begin{pmatrix}\sin(k/2)\\ -\cos(k/2)\end{pmatrix} \\ \text{and} \qquad\qquad\qquad\qquad\qquad\qquad\qquad\qquad \text{(II.47)} \\ H_2(k) = \left|v_k^2\right\rangle\left\langle v_k^2\right| - \left|u_k^2\right\rangle\left\langle u_k^2\right|, \text{ with } \left|u_k^2\right\rangle = \begin{pmatrix}\cos(k)\\ \sin(k)\end{pmatrix} \text{ and } \left|v_k^2\right\rangle = \begin{pmatrix}\sin(k)\\ -\cos(k)\end{pmatrix}. \end{aligned}$$

The Wilson loop is now constructed by starting with the occupied space at $k = 0$, and then stepwise projecting onto the occupied space while moving from $k = 0$ to $k = 2\pi$. This is done by applying $P_k = |u_k\rangle\langle u_k|$ at each step. This means that

$$W = \langle u_{2\pi=0}| \left(\prod_{i=0}^{N} |u_{k_i}\rangle\langle u_{k_i}|\right) |u_{2\pi=0}\rangle = \langle u_{2\pi=0}| \left(\prod_{i=0}^{N} P_{k_i}\right) |u_{2\pi=0}\rangle, \text{ with } k_i = \frac{i}{N}2\pi, \tag{II.48}$$

where we segmented the path into N steps. In this calculation it is imperative to choose a well-defined gauge, which means that it is BZ periodic. Evaluation of our two examples then yields

$$W_1 = -1 \text{ and } W_2 = +1. \tag{II.49}$$

This result is intuitive, because the projection in this case is equivalent to projectively rotating the initial vector around by an angle of π (2π) for H_1 (resp. H_2). The process of projecting around a circle is depicted in figure II.16.

Now, we can also observe that the two Hamiltonians have inversion symmetry

$$\mathcal{I}H_i(k)\mathcal{I}^\dagger = H_i(-k) \qquad \text{with } \mathcal{I} = \sigma_z = \begin{pmatrix}1 & \\ & -1\end{pmatrix}. \tag{II.50}$$

This symmetry has the consequence that

$$\begin{aligned} W^\dagger &= \left(\langle u_{2\pi=0}| \left(\prod_{i=0}^{N} |u_{k_i}\rangle\langle u_{k_i}|\right) |u_{2\pi=0}\rangle\right)^\dagger = \langle u_{2\pi=0}| \left(\prod_{i=N}^{0} |u_{k_i}\rangle\langle u_{k_i}|\right) |u_{2\pi=0}\rangle \\ &= \langle u_{2\pi=0}| \mathcal{I}^\dagger \left(\prod_{i=N}^{0} \mathcal{I}\,|u_{k_i}\rangle\langle u_{k_i}|\,\mathcal{I}^\dagger\right) \mathcal{I}\,|u_{2\pi=0}\rangle = \langle u_{2\pi=0}| \left(\prod_{i=0}^{N} |u_{k_i}\rangle\langle u_{k_i}|\right) |u_{2\pi=0}\rangle = W, \end{aligned} \tag{II.51}$$

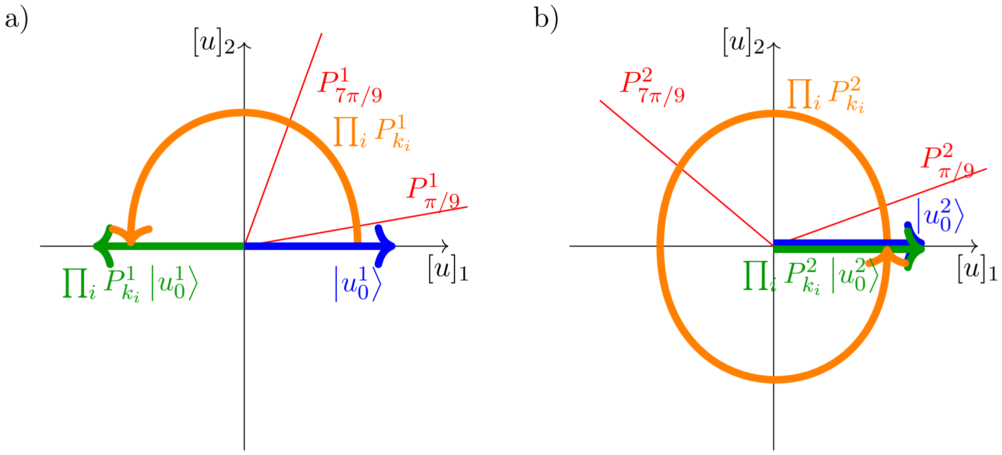

Figure II.16.: Graphical representation of the Wilson loops for H_1 and H_2. In panel a), the product of the projection operators for H_1 is represented by the orange arrow, which takes the blue state $\left|u^1_0\right\rangle$ and rotates it around, by projecting it into the spaces spanned by the projector P_{k_i}, until it is on the green arrow $\prod_i P_{k_i}\left|u^1_0\right\rangle$. The overlap of the green and the blue arrow is equal to W_1, and is here given by $W_1 = -1$. In panel b), the Wilson loop for H_2. The initial state is rotated once around on a circle such that the overlap is then $W_2 = +1$.

which then means that

$$W \in \mathbb{R}. \tag{II.52}$$

Because W is unitary, it further has absolute value 1. Then there cannot be a continuous transformation that respects $\mathcal{I}$ and can deform H_1 into H_2, because it is not possible to deviate from $W = -1$. In other words, H_1 and H_2 are topologically inequivalent. In this example, we have seen that Wilson loops allow, in some situations, especially when there are space group symmetries, to relatively simply classify Hamiltonians topologically. In the example above, we obtained a $\mathbb{Z}_2$ classification by distinguishing $W = +1$ from $W = -1$[1][2].

Next, we will write down the general formula for the Wilson loop, like described by Benalcazar et al.[89]. We begin with the definition of a Wilson line. To define a Wilson line, we look at a path $\mathcal{C}$ through the BZ $= \mathbb{T}^n$, given by a mapping $\mathcal{C} : t \in [0, 1] \to \mathbf{k}(t)$. We partition this path

---

[1] In the example above, we can also see the concept of an obstruction to defining a smooth gauge, which is in the next section II.7 detected by the Chern number in 2D. For this we interprete the Hamiltonian as describing physics that only allows real vectors (that's not the real world and has nothing to do with regular quantum mechanics.). The only allowed vectors are then in $\mathbb{R}^2$.
We immediately see that the projectors into the occupied band of $H_1(k)$ is smooth over BZ ring $\mathbb{T}^1 = \mathbb{S}^1$. If we now try to find a smooth gauge $\left|\tilde{u}^1_k\right\rangle$ we encounter a problem. If we arbitrarily start with $\left|\tilde{u}^1_0\right\rangle = (1,0)^T$, we have to set, to keep continuity, $\left|\tilde{u}^1_k\right\rangle = (\cos(k/2), \sin(k/2))^T$. This then implies that $(-1,0)^T = \left|\tilde{u}^1_{2\pi}\right\rangle \neq \left|\tilde{u}^1_0\right\rangle = (1,0)^T$. There is no smooth gauge over the whole BZ for this Hamiltonian, interpreted as a theory over real fiber bundles instead of complex fiber bundles.

[2] W can also be calculated using a symmetry indicator invariant, as

$$W = \prod_i^{N_{\text{occ}}} \lambda_i(0)\lambda_i(\pi), \tag{II.53}$$

with the inversion eigenvalues $\lambda_i(k)$ at the inversion-invariant momenta $k = 0$ and $k = \pi$[140].

into $M+1$ steps as $\mathbf{k}_i = \mathbf{k}(\frac{i}{M}), i \in \{0, ..., M\}$, and take the limit $M \to \infty$. The Wilson line is then given by

$$W_{mn} = \lim_{M\to\infty} \langle u^m_{\mathbf{k}_0}| \left(\prod_{i=0}^{M} P_{\mathbf{k}_i}\right) |u^n_{\mathbf{k}_M}\rangle = \lim_{M\to\infty} \langle u^m_{\mathbf{k}_0}| \left(\prod_{i=0}^{M} \left[\sum_{j=1}^{N_{\text{occ}}} \left|u^j_{\mathbf{k}_i}\right\rangle\left\langle u^j_{\mathbf{k}_i}\right|\right]\right) |u^n_{\mathbf{k}_M}\rangle, \tag{II.54}$$

where N_{occ} is the number of occupied bands, and $P_{\mathbf{k}_i}$ is the projector onto the occupied space at $\mathbf{k}_i$. W is a unitary matrix of shape $N_{\text{occ}} \times N_{\text{occ}}$. It is called a *Wilson loop* if and only if $\mathbf{k}(0) = \mathbf{k}(1)$ and $\left|u_{\mathbf{k}(0)}\right\rangle = \left|u_{\mathbf{k}(1)}\right\rangle$.
Often, especially when using a relatively small M, it is appropriate to use a Singular Value Decomposition (SVD) on the multiplying factors constituting the Wilson loop. For this sake, we define the overlap matrix F_i and its SVD as

$$[F_i]_{mn} = \left\langle u^m_{\mathbf{k}_i} \middle| u^n_{\mathbf{k}_{i+1}} \right\rangle \qquad\qquad F_i = U_i \Sigma_i V_i^\dagger, \tag{II.55}$$

with unitary matrices U_i and V_i and a diagonal matrix with nonnegative diagonal entries Σ_i. The unitary-projected overlap matrix is then given as

$$G_i = U_i V_i^\dagger \tag{II.56}$$

and allows us to calculate the Wilson loop as

$$W = \lim_{M\to\infty} \prod_{i=0}^{M-1} F_i = \lim_{M\to\infty} \prod_{i=0}^{M-1} G_i. \tag{II.57}$$

All the eigenvalues of W have absolute value 1 due to its unitarity. Therefore its eigenvalues are of form $e^{i\theta_j}$. We define the Wilson loop spectrum as the set of arguments θ_j of its eigenvalues. This means that if the Wilson loop eigenvalues are the set $\{e^{i\theta_j}\}$, then the Wilson loop spectrum is given by the set $\{\theta_j\}$.

It is sometimes useful to define the nested Wilson loop. Its calculation is described, for instance, by Benalcazar et al.[89, 90]. The procedure is to examine the set of Wilson loops along the paths $\mathcal{C}_l(t) = (2\pi l, 2\pi t)$, for a quadratic BZ, or $\mathcal{C}_l(t) = l\hat{\mathbf{k}}_1 + t\hat{\mathbf{k}}_2$ for an arbitrary BZ with reciprocal lattice vectors $\hat{\mathbf{k}}_{1/2}$ and $t, l \in \{0, 1\}$. This set of paths covers the whole BZ. Each Wilson loop W_l calculated along the path $\mathcal{C}_l$ is a unitary matrix on the occupied space at $\mathcal{C}_l(0)$. We can then look at the Wilson loop spectrum for all the $\mathcal{C}_l$. If its spectrum is gapped (like the spectrum in Fig. II.17b, keeping in mind that θ_j is only defined modulo 2π), we can define a “nested” Wilson loop. If the eigenvectors of W_l to the eigenvalue $e^{i\theta_j}$ are given by $\left|\nu^j_l\right\rangle$, we define a new basis

$$\left|w^j_l\right\rangle = \sum_{n=1}^{N_{\text{occ}}} \left[\nu^j_l\right]^n \left|u^n_{\mathcal{C}_l(0)}\right\rangle. \tag{II.58}$$

The gap in the Wilson loop spectrum allows us to group these vectors by their Wilson loop eigenvalues, for example getting an m-band subspace at each $\mathbf{k}_l = \mathcal{C}_l(0)$. The corresponding overlap matrices are then

$$\left[\tilde{F}_l\right]_{mn} = \langle w^m_{l+\Delta l} | w^n_l \rangle, \text{ with } \Delta l = \frac{1}{M}, \tag{II.59}$$

yielding the nested Wilson loop

$$\tilde{W} = \prod_{i=0}^{M-1} \tilde{G}_{i/M}, \tag{II.60}$$

where we used the unitary projection $\tilde{G}_j = \tilde{U}_j \tilde{V}_j^\dagger$ from the SVD $\tilde{F}_j = \tilde{U}_j \tilde{\Sigma}_j \tilde{V}_j^\dagger$. Another way to interprete the nested Wilson loop is in terms of the so-called Wilson loop Hamiltonian, as done, for instance, by Schindler et al.[75]. It is defined by the equation

$$\left[e^{iH_W(\mathcal{C}_j(0))}\right]_{mn} = \left\langle u^m_{\mathcal{C}_j(0)} \middle| W_j \middle| u^n_{\mathcal{C}_j(0)} \right\rangle. \tag{II.61}$$

The nested Wilson loop is then the Wilson loop of the Hamiltonian H_W, which is defined only along the line $\{\mathcal{C}_l(0) | l \in [0,1]\}$.

Often, when talking about the Wilson loop spectrum, what we're really talking about is the Wilson loop spectrum as function of l, or as function of the momentum in direction $C_1(0)$. This is then the set $\{\theta_j\}$ as function of l, or as function of one of the momenta. We calculate the Wilson loops in direction $\hat{\mathbf{k}}_2$ as function of k_1, with starting point $k_1\hat{\mathbf{k}}_1$. Then the Wilson loop spectrum as function of k_1 is the quantity which we then simply call the Wilson loop spectrum. The Wilson loop spectra of the models introduced in section II.4 are depicted in Fig. II.17.

Schindler et al.[75] use these Wilson loops to define invariants for spin-orbit coupled 2D systems. The first invariant is $\nu_{\mathbf{\Gamma k}}$ using the Wilson loop $W_{\mathbf{\Gamma k}}$ with the path from $\mathbf{\Gamma}$ to $\mathbf{k}$ and then back to $\mathbf{\Gamma}$ on the shortest path around the BZ torus. The invariant is evaluated as

$$\nu_{\mathbf{\Gamma k}} = -\frac{i}{\pi} \log \left(\prod_{\alpha=1,3,\dots,N-1} e^{i\theta_\alpha^{\mathbf{\Gamma k}}} \right) \bmod 2, \tag{II.62}$$

where the $e^{i\theta_\alpha^{\mathbf{\Gamma k}}}$ are the eigenvalues of the Wilson loop. The product runs only over odd αs to account for Kramers pairing. Secondly, Schindler et al.[75] define invariants stemming from nested Wilson loops, $\nu_{x,y}^{0,\pi}$, with the new gauge calculated using the Wilson bands pinned to 0 or π, respectively, at $j = 0, \frac{1}{2}$, with an analogous formula to eq. II.62. For example, in Fig. II.17d, no bands are pinned there, while in the spectrum in Fig. II.17b two bands are pinned at 0 and two at π. The set of paths $\mathcal{C}_j$ is given as $\mathcal{C}_j(i) = \hat{\mathbf{k}}_{\bar{l}} j + \hat{\mathbf{k}}_l i$, where $l = x, y$ and $\bar{l} = y, x$. To put it into other words: for ν_x we calculate all the Wilson loops W_x at fixed k_y with paths in k_x direction. Using these Wilson loops, we get a new gauge on the k_y axis, and then calculate the nested Wilson loop along the k_y axis. The eigenvalues of this nested Wilson loop are then used to evaluate eq. II.62. It is important to point out that this invariant is trivial if there are no bands with θ_j pinned to π or 0, respectively, at $j = 0, \frac{1}{2}$.

II.6.1. Effects of Symmetries on the Wilson Loop

In this section, the effect of internal and space group symmetries on the Wilson loop spectrum are discussed. This section is based on Schindler et al.[75], where the Wilson loop is represented as

$$w_\gamma = \prod_{\mathbf{k} \in \gamma} P(\mathbf{k}), \tag{II.63}$$

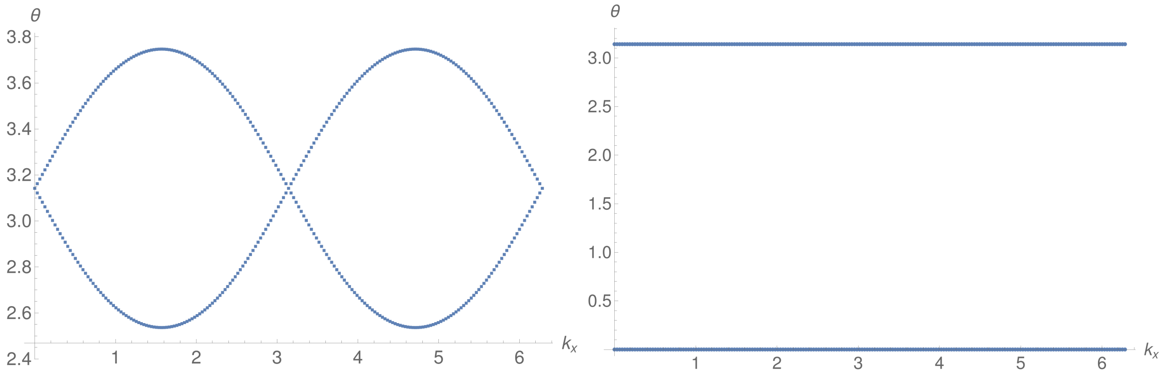

(a) Wilson loop spectrum W_y in k_y-direction of $H_2^{(4)}(\mathbf{k}, t = 0.2)$ as function of k_x (cf. section II.4.1).

(b) Wilson loop spectrum W_y in k_y-direction of $H_3^{(2)}(\mathbf{k}, t = 0.2)$ as function of k_x (cf. section II.4.1).

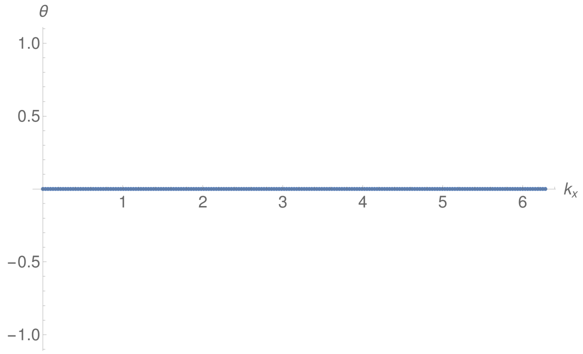

(c) Wilson loop spectrum W_y in k_y-direction of $H_3^{(2)}(\mathbf{k}, t = 1.2)$ as function of k_x (cf. section II.4.1).

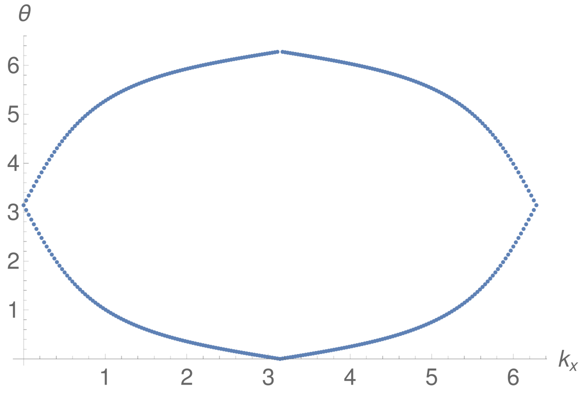

(d) Wilson loop spectrum W_y in k_y-direction of $H_{\text{double TI}}(\mathbf{k}, t = 0.0)$ as function of k_x (cf. section II.4.2).

Figure II.17.: Wilson loop spectra of the models used in this thesis. The Wilson loop spectra of models that correspond to an atomic limit do not show any winding in these examples (There are no counterexamples known up to date.). The model of a TI, $H_{\text{double TI}}$, shows a winding behaviour.

with the path γ and the projector into the occupied space $P(\mathbf{k})$ at momentum $\mathbf{k}$. We call this object w_γ. The Wilson loop including the encompassing vectors at the initial and final momentum $\mathbf{k}^*$ is then

$$W_\gamma^{mn} = \langle u^m_{\mathbf{k}^*} | w_\gamma | u^n_{\mathbf{k}^*} \rangle \,. \tag{II.64}$$

If crystallographic and/or internal symmetries are respected, this can have consequences for the Wilson loop spectrum.

TRS means for the projector at $\mathbf{k}$ that

$$\mathcal{T} P(\mathbf{k}) \mathcal{T}^{-1} = \tau K \sum_{m \in \text{occ}} |u^m_{\mathbf{k}}\rangle \langle u^m_{\mathbf{k}}| K \tau^\dagger = \sum_{m \in \text{occ}} |u^m_{-\mathbf{k}}\rangle \langle u^m_{-\mathbf{k}}| = P(-k), \tag{II.65}$$

which then implies

$$\begin{aligned} W_\gamma^{mn} = W_\gamma^{mn**} &= \left\langle u^m_{\mathbf{k}^*} \middle| \mathcal{T}^{-1}\mathcal{T} \prod_{\mathbf{k}\in\gamma} P(\mathbf{k}) \mathcal{T}^{-1}\mathcal{T} \middle| u^n_{\mathbf{k}^*} \right\rangle^{**} \\ &= \left\langle u^m_{\mathbf{k}^*} \middle| K\tau^\dagger \prod_{\mathbf{k}\in\gamma} P(-\mathbf{k}) \tau K \middle| u^n_{\mathbf{k}^*} \right\rangle^{**} = \left\langle u^n_{\mathbf{k}^*} \middle| \left(\tau^\dagger \prod_{\mathbf{k}\in\gamma} P(-\mathbf{k}) \tau \right)^{\dagger *} \middle| u^m_{\mathbf{k}^*} \right\rangle^{*} \\ &= \left\langle u^n_{\mathbf{k}^*} \middle| \left(\tau^\dagger \prod_{\mathbf{k}\in\gamma} P(\mathbf{k}) \tau \right)^{*} \middle| u^m_{\mathbf{k}^*} \right\rangle^{*} = \left\langle \tilde{u}^n_{\mathbf{k}^*} \middle| \prod_{\mathbf{k}\in\gamma} P(\mathbf{k}) \middle| \tilde{u}^m_{\mathbf{k}^*} \right\rangle = \tilde{W}_\gamma^{nm}, \end{aligned} \tag{II.66}$$

where we assumed that $\mathbf{k} \to -\mathbf{k}$ acts on γ by inversing its direction and that $\mathbf{k}^* = -\mathbf{k}^*$. Furthermore, $|\tilde{u}\rangle$ is in a different gauge than $|u\rangle$. Without loss of generality assuming that $|u\rangle$ is a gauge in which W is diagonal, we get

$$W_\gamma^{mm} = \tilde{W}_\gamma^{mm}, \tag{II.67}$$

where the left-hand side belongs to the eigenvector $|u^m_{\mathbf{k}^*}\rangle$ and the right-hand side to $|\tilde{u}^m_{\mathbf{k}^*}\rangle = \mathcal{T}\,|u^m_{\mathbf{k}^*}\rangle \perp |u^m_{\mathbf{k}^*}\rangle$ (cf. Eq. II.202). This shows that the Wilson loop spectrum at that point is degenerate.

Furthermore, for general paths, we observe that

$$W_\gamma^{mn} = \left\langle u^m_{\mathbf{k}^*} \middle| K\tau^\dagger \prod_{\mathbf{k}\in\gamma} P(-\mathbf{k}) \tau K \middle| u^n_{\mathbf{k}^*} \right\rangle = \left\langle \tilde{u}^m_{-\mathbf{k}^*} \middle| \prod_{\mathbf{k}\in\gamma} P(-\mathbf{k}) \middle| \tilde{u}^n_{-\mathbf{k}^*} \right\rangle^{*} = \tilde{W}_{\bar{\gamma}}^{mn*}, \tag{II.68}$$

where $\bar{\gamma}(t) = -\gamma(t)$. This also flips the orientation of the loop. To obtain a result that can be directly applied to Wilson loop spectra, we define $\hat{\gamma}(t) = \bar{\gamma}(1-t) = -\gamma(1-t)$. These BZ paths are depicted in Fig. II.18 for a case of quadratic BZ. Then we get

$$W_\gamma^{mn} = \left\langle u^n_{-\mathbf{k}^*} \middle| \prod_{\mathbf{k}\in\hat{\gamma}} P(\mathbf{k}) \middle| u^m_{-\mathbf{k}^*} \right\rangle = W_{\hat{\gamma}}^{nm}, \tag{II.69}$$

which implies that the Wilson loop spectrum of W have a TRS-type symmetry. This is because $W_\gamma = \tilde{W}_{\hat{\gamma}}^T$ and the fact that a matrix and its transpose have identical eigenvalues.

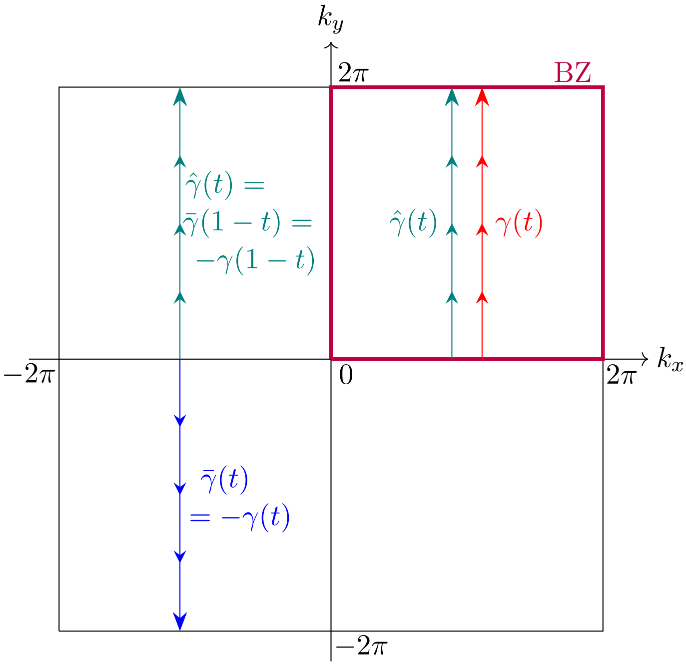

Figure II.18.: Brouillon zone with paths used in the arguments about the effects of symmetries on the Wilson loop spectrum. The Wilson loop spectrum is calculated using the paths in the upper right quadrant of the plot, which is the complete BZ.

Space Group Symmetries A space group symmetry (S, s) acts on the projector as

$$sP(\mathbf{k})s^\dagger = P(S\mathbf{k}), \tag{II.70}$$

if S is its action on the crystal momentum $\mathbf{k}$ and s is its representation in the space of Bloch wave functions.

This implies for the Wilson loop that if the symmetry projects a path back onto itself, but reversed, leaving the starting momentum $\mathbf{k}^*$ invariant, we find

$$\begin{aligned} W_\gamma^{mn} &= \left\langle u_{\mathbf{k}^*}^m \middle| s^\dagger s \prod_{\mathbf{k}\in\gamma} P(\mathbf{k}) s^\dagger s \middle| u_{\mathbf{k}^*}^n \right\rangle = \left\langle \tilde{u}_{\mathbf{k}^*}^m \middle| \prod_{\mathbf{k}\in\gamma} P(S\mathbf{k}) \middle| \tilde{u}_{\mathbf{k}^*}^n \right\rangle \\ &= \left\langle \tilde{u}_{\mathbf{k}^*}^n \middle| \prod_{\mathbf{k}\in\gamma} P(\mathbf{k}) \middle| \tilde{u}_{\mathbf{k}^*}^m \right\rangle^* = \tilde{W}_\gamma^{nm*}. \end{aligned} \tag{II.71}$$

This means that

$$W_\gamma = \tilde{W}_\gamma^\dagger \tag{II.72}$$

for paths starting and ending at TRIMs. Therefore the eigenvalues come in complex conjugate pairs if $S\mathbf{k}^* = \mathbf{k}^*$. For C_2 symmetry with $\hat{\gamma}(t) = -\gamma(1-t)$, we obtain

$$W_\gamma^{mn} = \left\langle \tilde{u}_{-\mathbf{k}^*}^m \middle| \prod_{\mathbf{k}\in\gamma} P(-\mathbf{k}) \middle| \tilde{u}_{-\mathbf{k}^*}^n \right\rangle = \left\langle \tilde{u}_{-\mathbf{k}^*}^n \middle| \prod_{\mathbf{k}\in\hat{\gamma}} P(\mathbf{k}) \middle| \tilde{u}_{-\mathbf{k}^*}^m \right\rangle^* = \tilde{W}_{\hat{\gamma}}^{nm*}, \tag{II.73}$$

which means that

$$W_\gamma = \tilde{W}^\dagger_{\hat{\gamma}}. \tag{II.74}$$

This property means that if $e^{i\theta}$ is an eigenvalue of the Wilson loop along γ, then $e^{-i\theta}$ must be an eigenvalue of the Wilson loop along $\hat{\gamma}$. This is a PHS-type symmetry of the Wilson loop spectrum.
Thus, if a system respects TRS and C_2 symmetry, its Wilson loop spectrum has a TRS-like symmetry and a PHS-like symmetry. PHS and TRS together imply that the Wilson loop spectrum has a chiral-like symmetry. This means that all Wilson loop eigenvalues come in complex conjugate pairs.

II.6.2. Wilson-Eigenvalues of Two TRS-Permuted Bands

This section is about a very specific two-band case. The two bands belong to a system with (at least) TRS and C_2 symmetry and are in a gauge such that the sewing matrices, defined by

$$D^{mn}_{\mathcal{T}\mathbf{k}} = \langle u^m_{-\mathbf{k}}|\mathcal{T}|u^n_{\mathbf{k}}\rangle \qquad \text{and} \qquad D^{mn}_{C_2\mathbf{k}} = \langle u^m_{R_2\mathbf{k}}|r_2|u^n_{\mathbf{k}}\rangle\,, \tag{II.75}$$

take the form

$$D_{\mathcal{T}} = \begin{pmatrix} & * \\ * & \end{pmatrix} \qquad \text{and} \qquad D_{C_2} = \begin{pmatrix} * & \\ & * \end{pmatrix}. \tag{II.76}$$

In this gauge r_2 maps the bands onto themselves and $\mathcal{T}$ maps between the two bands. Both symmetries act as permutations. The intuition behind this is that we are splitting a Kramers pair into two single electronic bands, each corresponding to a single electron per unit cell. The interesting observation is then that the Wilson loop spectrum calculated using the two bands is exactly the overlay of the two single-band Wilson loop spectra, calculated only using a single band each. An example for how this looks like can be seen in Figures II.31d and II.31e in section II.9. We prove that this is indeed the case. We label the two bands as $|u^1\rangle$ and $|u^2\rangle$.
First we have a look at the symmetries of these bands: We know that the 1-band Wilson loop is given by

$$W^1_1 = \prod_{i=N}^{1} \langle u^1_{i+1}|u^1_i\rangle = \langle u^1_{N+1}|u^1_N\rangle \cdots \langle u^1_2|u^1_1\rangle\,. \tag{II.77}$$

Due to how the symmetries act on the bands, we can express $|u^1_i\rangle$ as

$$|u^1_i\rangle = r_2\mathcal{T}\,|u^2_i\rangle = r_2\tau K\,|u^2_i\rangle \tag{II.78}$$

which then gives us

$$W^1_1 = \prod_{i=N}^{1} \langle u^1_{i+1}|u^1_i\rangle = \prod_{i=N}^{1} \left(\langle u^1_{i+1}|\right)^* \tau^\dagger r_2^\dagger r_2 \tau \left(|u^2_i\rangle\right)^* = \left(\prod_{i=N}^{1} \langle u^2_{i+1}|u^2_i\rangle\right)^* = W^{2*}_1. \tag{II.79}$$

This proves that the Wilson loop eigenvalue of one band is the complex conjugate of the Wilson loop eigenvalue of the other band. If we use the version of the Wilson loop given by Benalcazar et al.[90], with application of the SVD at each step, the Wilson loop eigenvalues are

$$W^1_1 = \prod_{i=N}^{1} \frac{\langle u^1_{i+1}|u^1_i\rangle}{|\langle u^1_{i+1}|u^1_i\rangle|} = W^{2*}_1. \tag{II.80}$$

To prove that these values are also eigenvalues of the 2-band Wilson loop, we use the form of the Wilson loop with the SVD. This form allows us to prove that the individual overlap matrices become diagonal after application of the SVD, assuming that $\left|u_i^2\right\rangle = r_2\mathcal{T}\left|u_i^1\right\rangle = r_2\tau\left|u_i^1\right\rangle^*$. The overlap matrix is given as

$$F = \begin{pmatrix} \left\langle u_{i+1}^1 \middle| u_i^1 \right\rangle & \left\langle u_{i+1}^1 \middle| u_i^2 \right\rangle \\ \left\langle u_{i+1}^2 \middle| u_i^1 \right\rangle & \left\langle u_{i+1}^2 \middle| u_i^2 \right\rangle \end{pmatrix} = \begin{pmatrix} \left\langle u_{i+1}^1 \middle| u_i^1 \right\rangle & \left\langle u_{i+1}^1 \right| r_2\tau \left(\left|u_i^1\right\rangle\right)^* \\ \left(\left\langle u_{i+1}^1 \right|\right)^* \tau^\dagger r_2^\dagger \left|u_i^1\right\rangle & \left(\left\langle u_{i+1}^1 \right|\right)^* \tau^\dagger r_2^\dagger r_2 \tau \left(\left|u_i^1\right\rangle\right)^* \end{pmatrix}$$
$$= \begin{pmatrix} \left\langle u_{i+1}^1 \middle| u_i^1 \right\rangle & \left\langle u_{i+1}^1 \middle| u_i^2 \right\rangle \\ \left(\left\langle u_{i+1}^1 \middle| u_i^2 \right\rangle\right)^* & \left(\left\langle u_{i+1}^1 \middle| u_i^1 \right\rangle\right)^* \end{pmatrix} = \begin{pmatrix} A & B \\ B^* & A^* \end{pmatrix}, \tag{II.81}$$

which holds for $Kr_2\tau\left|u_i^1\right\rangle^* = \tau^\dagger r_2^\dagger\left|u_i^1\right\rangle$, and where we defined $A = \left\langle u_{i+1}^1 \middle| u_i^1 \right\rangle$ and $B = \left\langle u_{i+1}^1 \middle| u_i^2 \right\rangle$. The former follows from

$$Kr_2\tau\left|u_i^1\right\rangle^* = \tau^\dagger r_2^\dagger\left|u_i^1\right\rangle \Leftrightarrow \left|u_i^1\right\rangle = r_2\tau K r_2\tau\left|u_i^1\right\rangle^* = r_2\mathcal{T}r_2\mathcal{T}\left|u_i^1\right\rangle = \mathcal{T}^2 r_2^2\left|u_i^1\right\rangle = \left|u_i^1\right\rangle \tag{II.82}$$

where we used that point group symmetry operators commute with TRS $[\mathcal{T}, \hat{r}_2] = 0$ [141, p. 14].

We then do an SVD of $F = U\Sigma V^\dagger$ in order to get $G = UV^\dagger$. G is one of the matrices that constitute the Wilson loop. Using Mathematica[142], we observe that the SVD is given by

$$\begin{aligned} U &= \frac{1}{\sqrt{2}}\begin{pmatrix} -\frac{B}{|B|} & \frac{B}{|B|} \\ \frac{A^*}{|A|} & \frac{A^*}{|A|} \end{pmatrix}, \\ \Sigma &= \begin{pmatrix} |A|-|B| & 0 \\ 0 & |A|+|B| \end{pmatrix}, \\ V^\dagger &= \frac{1}{\sqrt{2}}\begin{pmatrix} -\frac{B^*}{A^*}\frac{|A|}{|B|} & 1 \\ \frac{B^*}{A^*}\frac{|A|}{|B|} & 1 \end{pmatrix}. \end{aligned} \tag{II.83}$$

This fulfils the SVD property $F = U\Sigma V^\dagger$ and we find that

$$G = UV^\dagger = \begin{pmatrix} \frac{A}{|A|} & 0 \\ 0 & \frac{A^*}{|A^*|} \end{pmatrix} = \begin{pmatrix} \frac{\left\langle u_{i+1}^1 \middle| u_i^1 \right\rangle}{\left|\left\langle u_{i+1}^1 \middle| u_i^1 \right\rangle\right|} & 0 \\ 0 & \frac{\left\langle u_{i+1}^2 \middle| u_i^2 \right\rangle}{\left|\left\langle u_{i+1}^2 \middle| u_i^2 \right\rangle\right|} \end{pmatrix}, \tag{II.84}$$

which is independent of the choice of U, V[143, p. 42-45]. This then means that the Wilson loop is given by

$$W = \begin{pmatrix} \prod_{i=N}^{1} \frac{\left\langle u_{i+1}^1 \middle| u_i^1 \right\rangle}{\left|\left\langle u_{i+1}^1 \middle| u_i^1 \right\rangle\right|} & 0 \\ 0 & \prod_{i=N}^{1} \frac{\left\langle u_{i+1}^2 \middle| u_i^2 \right\rangle}{\left|\left\langle u_{i+1}^2 \middle| u_i^2 \right\rangle\right|} \end{pmatrix}. \tag{II.85}$$

Since the diagonal entries of this matrix are exactly the Wilson loop eigenvalues of 1-band Wilson loops in the form with SVD, this proves that the 2-band Wilson loop is decomposed into the 1-band Wilson loops. □

As Wilson loop eigenvalues are continuous and smooth throughout the BZ and the 1-band Wilson loop eigenvalues appear in complex conjugate pairs, therefore the 1-band Wilson loop eigenvalues exactly separate the two bands from each other, as seen, for instance, in Figures II.31d and II.31e.

II.7. Chern numbers

It is often useful to calculate a quantity known as Chern number, which is defined in even dimensions [26] as

$$\mathrm{Ch}_n = \frac{1}{n!}\left(\frac{i}{2\pi}\right)^n \int_{\mathrm{BZ}^d} \mathrm{Tr}(\mathcal{F}^n), \text{ where } n = \frac{d}{2} \text{ and } \mathcal{F} = d\mathcal{A} + \mathcal{A}^2 \tag{II.86}$$

in terms of the non-Abelian Berry connection

$$\mathcal{A}^{\alpha\beta}(\mathbf{k}) = \left\langle u^\alpha_{\mathbf{k}} \middle| du^\beta_{\mathbf{k}} \right\rangle = \left\langle u^\alpha_{\mathbf{k}} \middle| \nabla_{\mathbf{k}} u^\beta_{\mathbf{k}} \right\rangle \cdot d\mathbf{k}. \tag{II.87}$$

The first Chern number Ch_1 detects an obstruction to defining a smooth Bloch function over the BZ torus $\mathbb{T}^d$[144]. In the following, we will concentrate on the first Chern number Ch_1, which we call Chern number Q or C, omitting the "first". There are a few ways to calculate the Chern number.

Chern numbers for individual bands can be calculated as described by Asboth et al.[145, p. 23-28] for individual bands in a discretised BZ. The Chern number is then

$$Q = \frac{1}{2\pi} \sum_{nm} F_{nm} \tag{II.88}$$

with the plaquette phase factor

$$F_{nm} = -\arg\left(\langle u_{n,m}|u_{n+1,m}\rangle \langle u_{n+1,m}|u_{n+1,m+1}\rangle \langle u_{n+1,m+1}|u_{n,m+1}\rangle \langle u_{n,m+1}|u_{n,m}\rangle\right), \tag{II.89}$$

where the $|u_{n,m}\rangle$ are the eigenstates at $\mathbf{k}_{n,m}$, which form a grid over the BZ torus.

Another way to calculate the Chern number is to determine the total Wilson loop winding[137, p. 39-40]. For a quadratic 2D system, one looks at $W_y(k_x)$, the Wilson loop in k_y direction starting at $(k_x, 0)$. The total winding is given by

$$Q = \frac{1}{2\pi} \int dk_x \sum_i \theta_i = \frac{1}{2\pi \mathrm{i}} \int dk_x \ln\det W_y(k_x). \tag{II.90}$$

This quantity can be read off straight-forwardly by looking at the Wilson loop spectrum.

The Chern number of individual bands is linked to whether a set of bands is band representable. If all the symmetries of a 2D system in AZ class AI or AII act as permutations on the bands, i.e.

$$\left| u^{\sigma_s(n)}_{S\mathbf{k}} \right\rangle = s\,|u^n_{\mathbf{k}}\rangle, \text{ for all symmetries } (S, s), \tag{II.91}$$

where s is the action of the symmetry on the Bloch wave functions and S is its action on the momentum $\mathbf{k}$, and the Chern number of all the bands is 0, then the bands are a band representation[131][3].

---

[3] Explicitly, the theorem is given by Alexandradinata et al.[131] as

> **Crystallographic splitting theorem** Let P be a rank-N representation of G. P is a monomial BR of G if and only if there exists a splitting $P = \oplus_{j=1}^N P_j$ satisfying:
> (A) each P_j is analytic (throughout the Brillouin torus) and has trivial first Chern class, and
> (B) G acts as a permutation on $\{P_j\}_{j=1}^N$, i.e., for all $g \in G$, $g : P_j \to P_{\sigma_g(j)}$ with σ_g a permutation on $\{1, ..., N\}$.

Herein P is the projector into the occupied bands, and P_j are projectors into individual bands. G is the symmetry group of the crystal, which includes TRS. The distinction between monomial and non-monomial BRs does not exist in 2D, it only matters in cubic 3D systems. A single band has trivial first Chern class if and only if its Chern number Q vanishes.

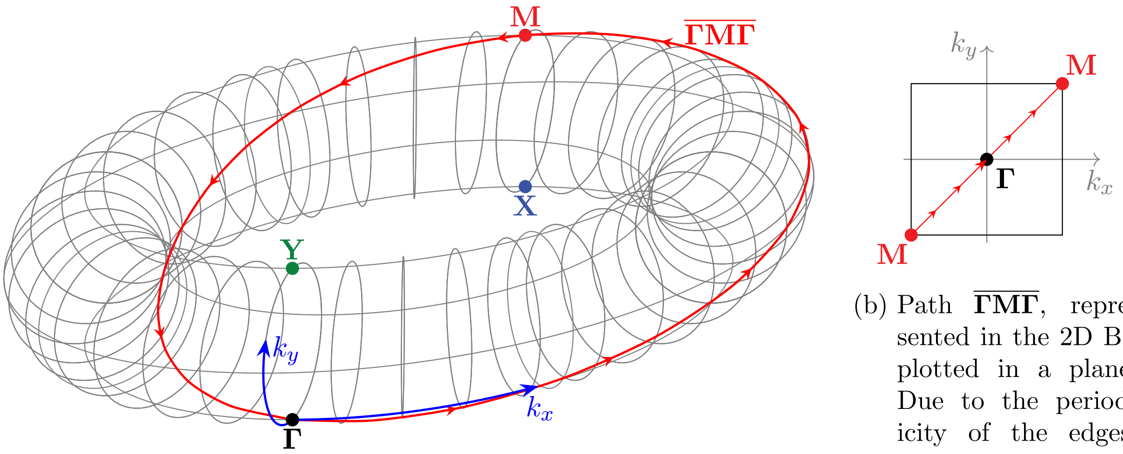

(a) Path $\overline{\mathbf{\Gamma M \Gamma}}$, showed on the 2D BZ represented as two-torus embedded in 3D. The path is showed in red, the blue arrows are the axes k_x and k_y.

(b) Path $\overline{\mathbf{\Gamma M \Gamma}}$, represented in the 2D BZ plotted in a plane. Due to the periodicity of the edges, the point **M** appears twice.

Figure II.19.: Path $\overline{\mathbf{\Gamma M \Gamma}}$ in the BZ.

II.8. Methods Based on Parallel Transport

Methods based on parallel transport are methods to construct a gauge fulfilling certain properties like smoothness by iteratively applying unitary transformations to Bloch wave functions. Such methods we first, at the beginning for 1D systems, developed by Soluyanov et al.[146]. Such gauges become significantly harder to calculate if in addition to smoothness symmetries have to be respected.

In principle, it would be advantageous to be able to construct a smooth and symmetric gauge over the whole BZ torus. This is a very difficult task that cannot be easily solved by parallel transport. If one already has a one-band subspace whose projector is smooth over the BZ, has trivial first Chern number and on which the symmetries act as permutations, it should be possible to construct such a smooth symmetric gauge by applying 2D parallel transport (cf. Ref. [146]) to the band. Such a symmetric gauge with analytic projectors can be constructed using the PSO method (see section II.9).

In the following, parallel transport methods are illustrated by a procedure to obtain a smooth gauge along the BZ line $\overline{\mathbf{\Gamma M \Gamma}}$. After that, the results by Kooi et al.[130] are described.

II.8.1. Continuous Gauge on the Line $\overline{\Gamma \mathrm{M}}$, Ensuring Compatibility with C_4 Eigensectors in the Points Γ, M

In this section, we describe a procedure to construct a smooth gauge on the line $\overline{\mathbf{\Gamma M \Gamma}}$ that coincides with eigenstates of r_4 at $\mathbf{\Gamma}$ and $\mathbf{M}$. The path is depicted in Fig. II.19. The idea behind this calculation is to test whether the eigenvalues of the Wilson loop along this path, taken only in the symmetry sector of some of the rotational C_4 eigenvalues, can serve as an invariant to distinguish the OAL $1b \oplus 1b$ from the trivial AL. The procedure consists of two steps:

1. Smooth states along the line are constructed.

2. The states are rotated to coincide with eigenstates of r_4 at $\mathbf{\Gamma}$ and $\mathbf{M}$.

II.8.1.1. Smooth States

We are treating a Hamiltonian $H(k_x, k_y)$ gapped along the line $\overline{\mathbf{\Gamma M \Gamma}}$ around the BZ torus. The eigenstates $|u^n_{\mathbf{k}}\rangle$ of H are split into those with energy below the energy gap, and those with energy above. To those below the gap, the procedure developed by Soluyanov and Vanderbilt [146] is applied (see also Ref. [52]). The resulting states $\left|\hat{u}^l_{\mathbf{k}}\right\rangle$ along the line $\overline{\mathbf{\Gamma M \Gamma}}$ are eigenstates of neither the Hamiltonian nor r_4.

The method works as follows. We require that the change of a state during one step of the discretisation is orthogonal to the state itself. This gauge is referred to as parallel transport gauge. To obtain such a gauge, the overlap matrix

$$L_{mn} = \left\langle u^m_{\mathbf{k}_j} \middle| u^n_{\mathbf{k}_{j+1}} \right\rangle \qquad m, n \in \{1, ..., N_{\text{occ}}\} \tag{II.92}$$

must be Hermititan with only positive eigenvalues. In order to ensure this we iterate along our discretised path, starting at $\mathbf{k} = \mathbf{0} = \mathbf{\Gamma}$, constructing new states at each step. At the point $\mathbf{\Gamma}$, the new states are identical to the old ones $|\check{u}^n_{\mathbf{0}}\rangle = |u^n_{\mathbf{0}}\rangle$. In each step we first calculate $L_{mn} = \left\langle \check{u}^m_{\mathbf{k}_j} \middle| u^n_{\mathbf{k}_{j+1}} \right\rangle$. In order to ensure Hermiticity and positive eigenvalues of the overlap matrix, we apply a SVD $L = V \Sigma W^\dagger$. We then define $\check{U} = W V^\dagger$. The transformed state at the next step is then given by

$$\left|\check{u}^n_{\mathbf{k}_{j+1}}\right\rangle = \sum_m^{N_{\text{occ}}} \check{U}_{mn} \left|u^m_{\mathbf{k}_{j+1}}\right\rangle . \tag{II.93}$$

The states $|\check{u}^n_{\mathbf{k}}\rangle$ are then smooth along the line from $\mathbf{\Gamma}$ to $\mathbf{M}$ to $\mathbf{\Gamma}$, but there can still be a jump from $\mathbf{\Gamma}(k_x = k_y = 2\pi)$ to $\mathbf{\Gamma}(k_x = k_y = 0)$. Next, we remove this jump. We observe that the states differ by the matrix

$$\Lambda_{mn} = \langle \check{u}^m_{2\pi} | \check{u}^n_0 \rangle \tag{II.94}$$

which has the property

$$|\check{u}^n_0\rangle = \sum_m^{N_{\text{occ}}} |\check{u}^m_{2\pi}\rangle \langle \check{u}^m_{2\pi} | \check{u}^n_0 \rangle = \sum_m^{N_{\text{occ}}} \Lambda_{mn} |\check{u}^m_{2\pi}\rangle . \tag{II.95}$$

Then we find a unitary S that diagonalises Λ, given by the normalised eigenvectors of Λ. By rotating all states by S, Λ becomes a diagonal matrix with entries $e^{i\phi_l}$ along the diagonal, which are the eigenvalues of Λ. This rotation by an angle has to be distributed over the whole range $\mathbf{k} = \mathbf{\Gamma} \to \mathbf{M} \to \mathbf{\Gamma}$. Therefore, we apply the transformation

$$\left|\hat{u}^l_{\mathbf{k}_j}\right\rangle = e^{i(j-1)\phi_l/M} \sum_m^{N_{\text{occ}}} S_{ml} \left|\check{u}^m_{\mathbf{k}_j}\right\rangle . \tag{II.96}$$

M is the number of discretisation steps along $\overline{\mathbf{\Gamma M \Gamma}}$. The states $\left|\hat{u}^l_{\mathbf{k}_j}\right\rangle$ are then smooth around the whole BZ torus along the line $\overline{\mathbf{\Gamma M \Gamma}}$. At each $\mathbf{k}_j$ they span the occupied subspace, but they are neither eigenstates of r_4 nor of $H(\mathbf{k}_j)$. In the next step, we ensure that the states coincide with eigenstates of r_4 at $\mathbf{\Gamma}$ and $\mathbf{M}$.

II.8.1.2. C_4 Compatibility

In order to calculate the Wilson loop in the sector that has rotational eigenvalues $e^{\pm i\pi/4}$, we apply a unitary rotation to all the states. This rotation is obtained as follows. We define the rotated states as

$$\left|\tilde{u}_k^n\right\rangle = \sum_m^{N_{\mathrm{occ}}} U_k^{mn} \left|\hat{u}_k^n\right\rangle . \tag{II.97}$$

We want to construct a U_k^{mn} such that $\left|\tilde{u}_k^1\right\rangle$ and $\left|\tilde{u}_k^2\right\rangle$ span the eigenspace of r_4 with the r_4-eigenvalues $e^{\pm \mathrm{i}\pi/4}$ at the points $\mathbf{\Gamma}$ and $\mathbf{M}$. This means that they are orthogonal to the eigenspace of $e^{\pm 3\mathrm{i}\pi/4}$. We refer to the 4 r_4-eigenstates with eigenvalues $e^{\pm \mathrm{i}\pi/4}$ ($e^{\pm 3\mathrm{i}\pi/4}$) as $\left|r_i^+\right\rangle$ ($\left|r_i^-\right\rangle$), respectively. The needed orthogonality leads to the equations

$$\begin{aligned}
&\left\langle r_i^+\right| \sum_m U_k^{m1} \left|\hat{u}_k^m\right\rangle = 0 = \sum_m U_k^{m2} \left\langle r_i^+ \middle| \hat{u}_k^m\right\rangle , && \text{(4 equations)}\\
&\left\langle r_i^-\right| \sum_m U_k^{m3} \left|\hat{u}_k^m\right\rangle = 0 = \left\langle r_i^-\right| \sum_m U_k^{m4} \left|\hat{u}_k^m\right\rangle . && \text{(4 equations)}
\end{aligned} \tag{II.98}$$

These equations are understood as equations for the components of U_k^{mn}. Writing out the first equation, we get

$$U_k^{11} \left\langle r_i^+ \middle| \hat{u}_k^1\right\rangle + U_k^{21} \left\langle r_i^+ \middle| \hat{u}_k^2\right\rangle + U_k^{31} \left\langle r_i^+ \middle| \hat{u}_k^3\right\rangle + U_k^{41} \left\langle r_i^+ \middle| \hat{u}_k^4\right\rangle = 0 \tag{II.99}$$

for each i. This is equivalent to a column of U_k being an element of

$$\mathrm{Ker}\left(T_{ij} = \left\{\left\langle r_i^+ \middle| \hat{u}_k^j\right\rangle\right\}\right) = \{v_1, v_2\} . \tag{II.100}$$

We orthonormalise these vectors to make U unitary. The second equation in Eq. II.98 again gives us two vectors $\{w_1, w_2\}$. U is then given as

$$U = (v_1, v_2, w_1, w_2) , \tag{II.101}$$

where the vectors are understood as column vectors.
Applying this procedure gives us two matrices $U_{\mathbf{\Gamma}}$ and $U_{\mathbf{M}}$, which transform gauge $\left|\hat{u}_k^m\right\rangle$ such that the symmetry sectors become clear (the first two of the eigenvectors $\left|\tilde{u}_k^l\right\rangle$ belong to the sector of $e^{\pm \mathrm{i}\pi/4}$ at $\mathbf{k} = \mathbf{\Gamma}, \mathbf{M}$).

Another way to find the matrices $U_{\mathbf{\Gamma}}$, $U_{\mathbf{M}}$ that allow to distinguish the different eigensectors of r_4 is to diagonalise r_4 in the space spanned by the vectors $\left|\hat{u}_k^l\right\rangle$. This is done by first defining the basis transformation matrix $\hat{S} = (\hat{u}_{\mathbf{k}}^1, \cdots, \hat{u}_{\mathbf{k}}^{N_{\mathrm{occ}}}, u_{\mathbf{k}}^{N_{\mathrm{occ}}+1}, \cdots, u_{\mathbf{k}}^N)$, where the vectors are understood as column vectors and the vectors $\left|u_{\mathbf{k}}^{N_{\mathrm{occ}}+1,\ldots,N}\right\rangle$ are the original unfilled eigenstates. r_4 with respect to the basis of $\hat{u}$ is then given by

$$r_4^b = \hat{S}^{-1} \cdot r_4 \cdot \hat{S}. \tag{II.102}$$

If r_4^b has block-diagonal form with a block r_4^{occ} of size $N_{\mathrm{occ}} \times N_{\mathrm{occ}}$ at the left top, we can diagonalise r_4 in the subspace of occupied states. If we denote the eigenvectors of r_4^{occ} by $w_1, \ldots, w_{\mathrm{occ}}$, then the matrix $U_{\mathbf{k}}$ is given as $(w_{\sigma(1)}, \ldots, w_{\sigma(N_{\mathrm{occ}})})$, where the w_i are understood as column vectors and σ is an arbitrary permutation that can be used to sort the vectors

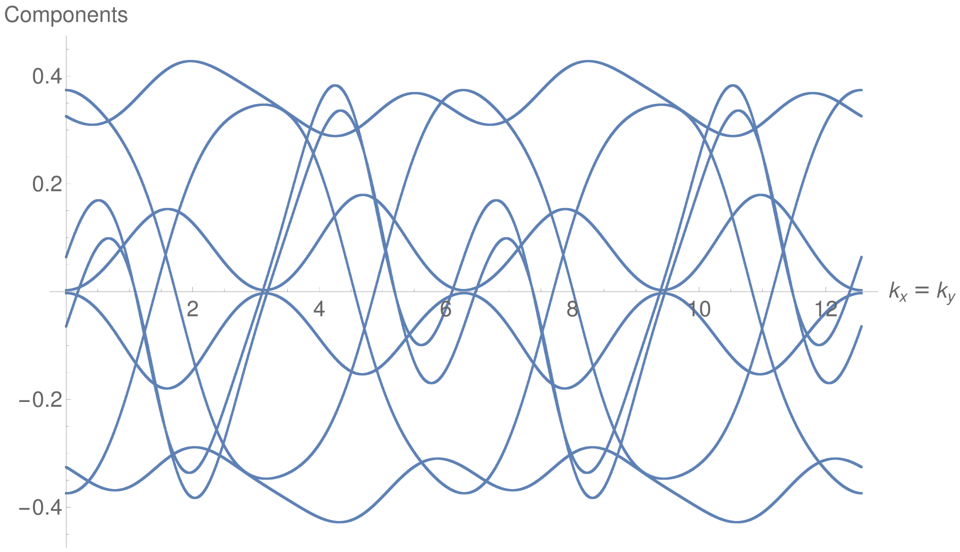

Figure II.20.: Components of a smooth vector along the line $\overline{\mathbf{\Gamma M \Gamma M \Gamma}}$.

according to the eigenvalues of r_4.

In order to keep smoothness, these two independent unitary matrices at the momenta $\mathbf{\Gamma}$, $\mathbf{M}$ must be connected in a smooth unitary way. This is done by defining the continuous transformation

$$U(t) = U_{\mathbf{\Gamma}} \exp\left(t \log\left(U_{\mathbf{\Gamma}}^{-1} U_{\mathbf{M}}\right)\right). \tag{II.103}$$

$U(t)$ fulfills $U(0) = U_{\mathbf{\Gamma}}$ and $U(1) = U_{\mathbf{M}}$. We then use $t = \frac{1}{2}\left(1 - \cos(k_x = k_y)\right)$. This gives us a continuous interpolation from $\mathbf{\Gamma}$ to $\mathbf{M}$ and further back to $\mathbf{\Gamma}$, and thereby continuous states that are in a specific C_4-sector at $\mathbf{\Gamma}$ and $\mathbf{M}$. In the end, the overlap matrices $\tilde{L}_{mn} = \left\langle \tilde{u}^m_{\mathbf{k}_j} \middle| \tilde{u}^n_{\mathbf{k}_{j+1}} \right\rangle$ are not Hermitian anymore and have slightly imaginary eigenvalues. Still the states remain continuous, since they were continuous after the smoothing of the states, and all the following transformations were smooth too.
Figure II.20 depicts the real part of all the components of one smoothed vector along the line $\overline{\mathbf{\Gamma M \Gamma M \Gamma}}$. The graph clearly shows that the components are smooth along the whole line.

The Wilson loop calculated along the line $\overline{\mathbf{\Gamma M \Gamma}}$ in only one of the symmetry sectors does not allow a distinction between the the phase $1b \oplus 1b$ and $1a \oplus 1a$.

II.8.2. Parallel Transport Method of Kooi, van Miert and Ortix

In a recent publication, Kooi, van Miert and Ortix[130] describe a set of invariants that allows for a full classification of OALs in C_n-symmetric systems in AZ class AII (spinfull systems with $\mathcal{T}^2 = -1$). They call them *partial real-space invariants*. These invariants are based on the invariants previously developed for spinless systems by van Miert and Ortix[86], but work for spinfull systems as well. The idea is to split the bands into two smooth and symmetric subspaces which are mapped to each other by $\mathcal{T}$. In a second step they ease this condition such that they get a quantity that can be calculated using straight-forward parallel transport techniques.

We first describe the invariants that are used when having such a smooth and symmetric gauge. The gauge that is used to calculate the invariants has the properties that the $\mathcal{T}$ sewing matrix

$$B^{mn}_{\mathbf{k}} = \langle u^m_{-\mathbf{k}}|\mathcal{T}|u^n_{\mathbf{k}}\rangle \qquad D_{\mathcal{T},\mathbf{k}} = B_{\mathbf{k}} = \begin{pmatrix} 0 & * \\ * & 0 \end{pmatrix} \tag{II.104}$$

is block-off-diagonal. This means that effectively, the two spin-components get separated. The C_n-sewing matrix is block-diagonal as

$$D^{mn}_{\mathbf{k}} = \langle u^m_{R_n\mathbf{k}}|r_n|u^n_{\mathbf{k}}\rangle \qquad D_{C_n,\mathbf{k}} = D_{\mathbf{k}} = \begin{pmatrix} * & 0 \\ 0 & * \end{pmatrix}. \tag{II.105}$$

Such a gauge is very non-trivial to construct if there is non-negligible spin orbit coupling, still we are able to calculate it directly using the *Projected Symmetric Operator* method described in section II.9. In the following, we list the invariants, as given in Table I in Ref. [130]. The invariants for C_2-symmetric systems are given by

$$\begin{aligned}
\nu^I_{1a} &= \frac{1}{2}C^I + \Gamma^I_i + \frac{1}{2}\left[\Gamma^I_{-i} - X^I_{-i} - Y^I_{-i} - M^I_{-i}\right], \\
\nu^I_{1b} &= \frac{1}{2}C^I - \frac{1}{2}\left[\Gamma^I_{-i} - X^I_{-i} + Y^I_{-i} - M^I_{-i}\right], \\
\nu^I_{1c} &= \frac{1}{2}C^I - \frac{1}{2}\left[\Gamma^I_{-i} + X^I_{-i} - Y^I_{-i} - M^I_{-i}\right], \\
\nu^I_{1d} &= \frac{1}{2}C^I - \frac{1}{2}\left[\Gamma^I_{-i} - X^I_{-i} - Y^I_{-i} + M^I_{-i}\right],
\end{aligned} \tag{II.106}$$

where C^I is the first Chern number in the first $\mathcal{T}$-sector and A^I_α are the multiplicities of the symmetry eigenvalue α at A in the same sector. One way to calculate C^I is to evaluate

$$\frac{1}{2}C^I = \frac{1}{2\pi}\oint_{\partial\mathrm{EBZ}} d\mathbf{q}\cdot\mathrm{Tr}\left(\mathbf{A}^I(\mathbf{q})\right). \tag{II.107}$$

Other methods are described in the section about Chern numbers II.7.

The invariants for C_4 systems are given by

$$\begin{aligned}
\nu^I_{1a} =& -\frac{1}{2}C^I + \Big(-3\Gamma^I_{e^{i\pi/4}} - \frac{3}{2}\Gamma^I_{e^{3i\pi/4}} - \Gamma^I_{e^{-3i\pi/4}} - \frac{3}{2}\Gamma^I_{e^{-i\pi/4}} \\
&+ \frac{3}{2}M^I_{e^{3i\pi/4}} + 2M^I_{e^{-3i\pi/4}} + \frac{3}{2}M^I_{e^{-i\pi/4}} + X^I_{-i}\Big), \\
\nu^I_{1b} =& -\frac{1}{2}C^I + \Big(\frac{3}{2}\Gamma^I_{e^{3i\pi/4}} + 2\Gamma^I_{e^{-3i\pi/4}} + \frac{3}{2}\Gamma^I_{e^{-i\pi/4}} - \frac{1}{2}M^I_{e^{3i\pi/4}} \\
&- 2M^I_{e^{-3i\pi/4}} - \frac{1}{2}M^I_{e^{-i\pi/4}} - X^I_{-i}\Big), \\
\nu^I_{2c} =& +\frac{1}{2}C^I + \frac{1}{2}\Big(\Gamma^I_{e^{3i\pi/4}} + \Gamma^I_{e^{-i\pi/4}} - M^I_{e^{3i\pi/4}} - M^I_{e^{-i\pi/4}}\Big).
\end{aligned} \tag{II.108}$$

The invariants for C_6 systems are given by

$$\begin{aligned}
\nu^I_{1a} =& -\frac{1}{2}C^I + \Big(-5\Gamma^I_{e^{i\pi/6}} - \frac{5}{2}\Gamma^I_{e^{i\pi/2}} - \Gamma^I_{e^{i5\pi/6}} - \frac{1}{2}\Gamma^I_{e^{-i5\pi/6}} \\
&- \Gamma^I_{e^{-i\pi/2}} - \frac{5}{2}\Gamma^I_{e^{-i\pi/6}} + \frac{3}{2}M^I_{-i} + 2K^I_{-1} + 2K^I_{e^{-i\pi/3}}\Big), \\
\nu^I_{2b} =& C^I + \Big(\Gamma^I_{e^{i\pi/2}} + \Gamma^I_{e^{i5\pi/6}} + \Gamma^I_{e^{-i\pi/2}} + \Gamma^I_{e^{-i\pi/6}} - K^I_{-1} - K^I_{e^{-i\pi/3}}\Big), \\
\nu^I_{3c} =& \frac{1}{2}C^I + \frac{1}{2}\Big(\Gamma^I_{e^{i\pi/2}} + \Gamma^I_{e^{-i5\pi/6}} + \Gamma^I_{e^{-i\pi/6}} - M^I_{-i}\Big).
\end{aligned} \tag{II.109}$$

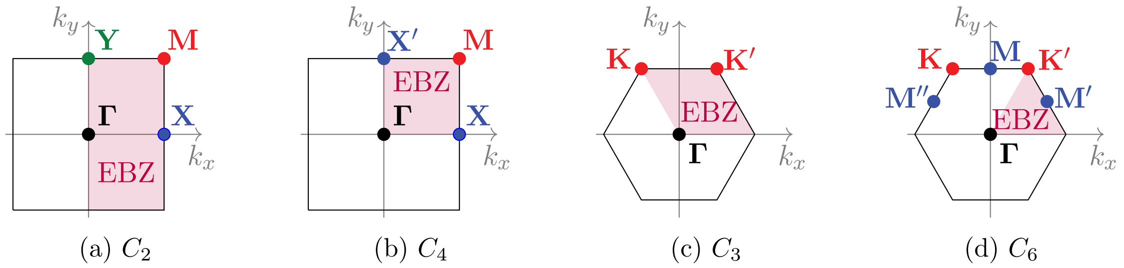

(a) C_2 (b) C_4 (c) C_3 (d) C_6

Figure II.21.: The effective BZ (EBZ) defined by Kooi et al.[130] to calculate invariants, for C_2, C_4, C_3 and C_6-symmetric systems.

These invariants allow for a complete classification of the atomic limits, so they solve our problem. On page 63, we discuss a method to construct such a gauge.

II.8.2.1. The Parallel Transport Method

Kooi et al.[130] also developed a method to evaluate the invariants given in the previous chapter without having to calculate a gauge that is smooth and symmetric over the whole BZ torus. They define the effective BZ (EBZ), which is the subregion of the BZ such that by the action of C_n one gets the whole BZ (e.g. $(0,\pi)^2 \in \text{BZ} = (-\pi,\pi)^2$ for C_4). The EBZs for rotationally symmetric 2D systems are depicted in Fig. II.21. The procedure then consists of calculating a $C_2\mathcal{T}$-symmetric smooth gauge $\chi(\vec{q})$ within the EBZ and a C_2- & TRS-symmetric smooth gauge $\Psi(\vec{q})$ along the edge ∂EBZ. The gauge $\Psi(\vec{q})$ is then used to calculate the multiplicities of the rotation eigenvalues and the partial Berry phase $\oint_{\partial\text{EBZ}} d\vec{q}\cdot\text{Tr}(\vec{A}^I(\vec{q}))$. The gauge $\chi(\vec{q})$ is used to calculate a $\mathbb{Z}_2$ or $\mathbb{Z}$ winding number $W(U|_{\partial\text{EBZ}})$ of the overlap-matrix $U(\vec{q}) = \langle\chi(\vec{q})|\Psi(\vec{q})\rangle$ along ∂EBZ. The invariants then need to be adjusted to take this winding number into consideration, like in the example

$$\nu^I_{1a} = \frac{1}{2\pi}\oint_{\partial\text{EBZ}} d\vec{q}\cdot\text{Tr}\left(\vec{A}^I(\vec{q})\right) + W(U|_{\partial\text{EBZ}}) + \Gamma^I_i + \frac{1}{2}\left[\Gamma^I_{-i} - X^I_{-i} - Y^I_{-i} - M^I_{-i}\right]. \quad \text{(II.110)}$$

We refrain from going into the details of this procedure, which can be found in the methods section of Ref. [130].

II.9. Projected Symmetric Operators and Their Band Structures

Often, when wanting to calculate topological invariants and making statements about whether a set of bands corresponds to a band representation, it is necessary to calculate gauges with specific properties, like block-diagonality of sewing matrices of certain symmetries and smoothness of the projectors of the gauge. This is often done using parallel transport techniques[130, 146, 147](cf. section II.8). Here, we present a method, very similar to the *projected symmetry method* proposed by Alexandradinata et al.[131], to calculate such gauges without having to use parallel transport. The obtained gauges have smooth projectors throughout the BZ and the symmetries act in a well defined way on the Bloch wave functions, for example by permuting the bands. We expect the method, to which we refer as *projected symmetric operator method*, to be applicable to all wallpaper groups for Hermitian Hamiltonians in AZ classes A, AI and AII, though due to time-constraints this was not tested thoroughly.

To construct the gauges, we define a smooth matrix-valued function $\mathring{\psi} : \mathbf{k} \to \mathring{\psi}_{\mathbf{k}}$, called *symmetric operator (SO)*, such that $\mathring{\psi}_{\mathbf{k}}$ has well-defined bahaviour under the symmetry transformations and carries the periodicity of the lattice. The projected symmetric operator (PSO) is then defined as

$$\mathring{\Psi}^{mn}_{\mathbf{k}} = \left\langle u^m_{\mathbf{k}} \middle| \mathring{\psi}_{\mathbf{k}} \middle| u^n_{\mathbf{k}} \right\rangle , \qquad \text{for } m, n \in \{1, ..., N_{\text{occ}}\}. \tag{II.111}$$

We know that if the spectrum of $\mathring{\Psi}_{\mathbf{k}}$ is gapped, we can construct a smooth symmetric gauge by looking at the eigenvectors $\vec{v}_{\mathbf{k},n}$ of $\mathring{\Psi}_{\mathbf{k}}$ (of $WV^\dagger$ with $\mathring{\Psi}_{\mathbf{k}} = W\Sigma V^\dagger$ the SVD of $\mathring{\Psi}_{\mathbf{k}}$) and using them to construct a new gauge $|b^n_{\mathbf{k}}\rangle = \sum_m v^m_{\mathbf{k},n} |u^m_{\mathbf{k}}\rangle$, for a Hermitian (non-Hermitian) $\mathring{\psi}$, respectively.
In general, the symmetries carried by the SO are

1. Lattice periodicity
$$\mathring{\psi}_{\mathbf{k}} = \mathring{\psi}_{\mathbf{k}+\mathbf{G}}, \tag{II.112}$$
with $\mathbf{G}$ as a vector in the reciprocal lattice. This symmetry must be fulfilled to guarantee smoothness of the gauge.

2. Hermiticity
$$\mathring{\psi}_{\mathbf{k}} = \mathring{\psi}^\dagger_{\mathbf{k}} \tag{II.113}$$
need not be necessarily fulfilled, but it makes calculations in most cases much easier, because then the eigenvalues of the projected symmetric operator $\mathring{\Psi}_{\mathbf{k}}$ are real and a gap can be defined in the usual Hermitian way. If Hermiticity is not given, one has to look at (star) line gaps in the complex plane instead, defined below.

3. Unitary (space group) symmetries
$$s_i \mathring{\psi}_{\mathbf{k}} s_i^\dagger = e^{\frac{2\pi i m}{n}} \mathring{\psi}_{S\mathbf{k}}. \tag{II.114}$$
The prefactor $e^{\frac{2\pi i m}{n}}$ allows for tuning which type of band-permutation one gets by applying this SO. If $\mathring{\psi}_{\mathbf{k}}$ is Hermitian, only ±1 are allowed because then $s\mathring{\psi}_{\mathbf{k}} s^\dagger = e^{i\alpha}\mathring{\psi}_{S\mathbf{k}} \implies s\mathring{\psi}^\dagger_{\mathbf{k}} s^\dagger = e^{-i\alpha}\mathring{\psi}^\dagger_{S\mathbf{k}} \implies e^{i\alpha} = e^{-i\alpha} \implies e^{i\alpha} = \pm 1$. $+1$ (-1) means that the corresponding sewing matrix becomes block-(off-)diagonal, respectively. A complex prefactor $e^{\frac{2\pi i m}{n}}$ allows for the construction of n-cycle permutations.

4. Anti-Unitary (internal) symmetries
$$\mathfrak{s}_j \mathring{\psi}^T_{\mathbf{k}} \mathfrak{s}^\dagger_j = \pm\mathring{\psi}_{-\mathbf{k}} \tag{II.115}$$
are relevant for TRS, which connects occupied bands at $\mathbf{k}$ with other occupied bands at $-\mathbf{k}$. If $\mathring{\psi}_{\mathbf{k}}$ is Hermitian, such anti-unitary symmetries can equivalently be expressed as
$$\mathfrak{s}_j \mathcal{K} \mathring{\psi}_{\mathbf{k}} \mathcal{K} \mathfrak{s}^\dagger_j = \pm\mathring{\psi}_{-\mathbf{k}}, \tag{II.116}$$
where $\mathcal{K}$ is the complex conjugation. There are no internal symmetries that correspond to permutation cycles of more than 2-cycles, therefore ± as a prefactor in sufficient. If

we have time reversal with complex conjugation $\mathcal{T} = \tau\mathcal{K}$ and a space group symmetry s with prefactor $e^{i\alpha}$, then

$$\left.\begin{aligned} s\mathcal{T}\mathring{\psi}_{\mathbf{k}}\mathcal{T}^{-1}s^{\dagger} &= s\left(\pm\mathring{\psi}_{-\mathbf{k}}\right)s^{\dagger} = \pm e^{i\alpha}\mathring{\psi}_{-S\mathbf{k}} \\ \mathcal{T}s\mathring{\psi}_{\mathbf{k}}s^{\dagger}\mathcal{T}^{-1} &= \tau\mathcal{K}e^{i\alpha}\mathring{\psi}_{S\mathbf{k}}K\tau^{\dagger} = \pm e^{-i\alpha}\mathring{\psi}_{-S\mathbf{k}} \end{aligned}\right\} \implies e^{i\alpha} = \pm 1 \in \mathbb{R}. \tag{II.117}$$

This is the reason why we define the anti-unitary symmetry using the transpose in equation II.115.

As an example, in the case of $s = r_4$, one might use $\mathring{\psi}_{\mathbf{k}} = r_4 + r_4^{\dagger}$ with $\pm\sqrt{2}$ as eigenvalues at $\boldsymbol{\Gamma}$ and $\mathbf{M}$.
The PSO is given by

$$\mathring{\Psi}_{\mathbf{k}}^{mn} = \left\langle u_{\mathbf{k}}^{m}\middle|\mathring{\psi}_{\mathbf{k}}\middle|u_{\mathbf{k}}^{n}\right\rangle. \tag{II.118}$$

If $\mathring{\psi}_{\mathbf{k}}$ is Hermitian, $\mathring{\Psi}_{\mathbf{k}}$ is Hermitian as well, because

$$\mathring{\Psi}_{\mathbf{k}}^{mn*} = \left(\left\langle u_{\mathbf{k}}^{m}\middle|\mathring{\psi}_{\mathbf{k}}\middle|u_{\mathbf{k}}^{n}\right\rangle\right)^{*} = \left\langle u_{\mathbf{k}}^{n}\middle|\mathring{\psi}_{\mathbf{k}}^{\dagger}\middle|u_{\mathbf{k}}^{m}\right\rangle = \left\langle u_{\mathbf{k}}^{n}\middle|\mathring{\psi}_{\mathbf{k}}\middle|u_{\mathbf{k}}^{m}\right\rangle = \mathring{\Psi}_{\mathbf{k}}^{nm}. \tag{II.119}$$

If $\mathring{\psi}_{\mathbf{k}}$ is Hermitian, we solve the eigenvalue problem of $\mathring{\Psi}$

$$\mathring{\Psi}_{\mathbf{k}}\vec{v}_{\mathbf{k},n} = \kappa_{\mathbf{k},n}\vec{v}_{\mathbf{k},n} \tag{II.120}$$

and then define the new gauge using the eigenvectors $\vec{v}_{\mathbf{k},n}$ as

$$\left|b_{\mathbf{k}}^{n}\right\rangle = \sum_{m} v_{\mathbf{k},n}^{m}\left|u_{\mathbf{k}}^{m}\right\rangle. \tag{II.121}$$

If $\mathring{\psi}_{\mathbf{k}}$ is non-Hermitian, we instead look at the SVD of $\mathring{\Psi}_{\mathbf{k}}$

$$\mathring{\Psi}_{\mathbf{k}} = W\Sigma V^{\dagger}, \tag{II.122}$$

then solve the eigenvalue problem of the unitary projected matrix

$$\mathring{\Psi}_{\mathbf{k}}' = WV^{\dagger} \tag{II.123}$$

and finally define the new gauge again as in equation II.120 and II.121.

For projectors of the new gauge to be smooth, we require that the spectrum of $\mathring{\Psi}_{\mathbf{k}}$ is gapped. This means that in the Hermitian case we require an overall real gap, in the non-Hermitian case we require a “star”-gap with a multiplicity corresponding to the type of cycle we want to construct. These different gaps are depicted in figure II.22.

Overall, two important proofs need to be provided to use this method:

1. Proof for the existence of a $\mathring{\psi}_{\mathbf{k}}$ that fulfils these properties if the occupied bands correspond to a band representation (see section II.9.1).
2. Proof that the subspaces spanned by $\left|b_{\mathbf{k}}^{n}\right\rangle$ represent a smooth symmetric gauge, where smooth is understood in a projector-sense (the projectors are smooth in $\mathbf{k}$, not the vectors themselves, see section II.9.2).

Furthermore, we need to check the compatibility of symmetries.

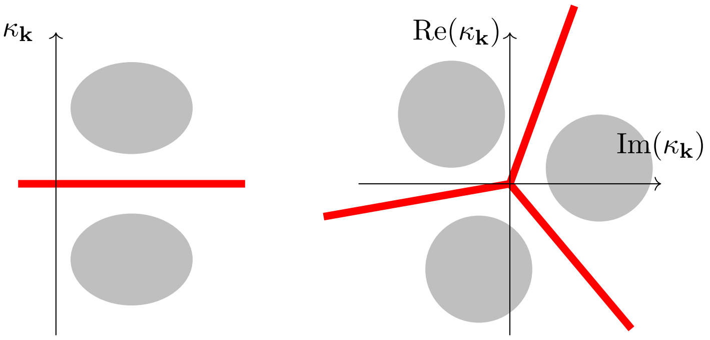

Figure II.22.: Types of gaps that can be useful. The gray areas represent the areas in which the eigenvalues of $\mathring{\Psi}_{\mathbf{k}}$ lie. On the left a Hermitian $\mathring{\Psi}$ with a usual gap known from Hermitian physics. On the right a non-Hermitian $\mathring{\Psi}_{\mathbf{k}}$ to get three-cycles, with the corresponding 3-star gap, is showed.

II.9.1. Proof for the Existence of an $\mathring{\psi}_{\mathbf{k}}$

To prove that a $\mathring{\psi}_{\mathbf{k}}$ with such properties exists, we first invoke the Crystallographic Splitting Theorem[131], which leads to a gauge $\left|u^i_{\mathbf{k}}\right\rangle$ consisting of single bands that are analytic throughout the BZ and on which the symmetries act as permutations. This only works if the occupied bands correspond to a BR. We then construct our SO as a sum over projectors with prefactors

$$\beta_{\mathbf{k}} = \sum_{i=1}^{N_{\mathrm{occ}}} \gamma_i \left|u^i_{\mathbf{k}}\right\rangle\!\left\langle u^i_{\mathbf{k}}\right| . \tag{II.124}$$

The γ_i have to be chosen such that a gap appears (e.g. $\pm\sqrt{2}$). If the symmetry s acts as the permutation $\sigma : i \to j$ $\Big($ i.e. $s\left|u^i_{\mathbf{k}}\right\rangle = \left|u^{\sigma(i)}_{S\mathbf{k}}\right\rangle\Big)$ on the bands, then its action on $\beta_{\mathbf{k}}$ is

$$\begin{aligned} s\beta_{\mathbf{k}}s^\dagger &= \sum_{i=1}^{N_{\mathrm{occ}}} \gamma_i \left|u^{\sigma(i)}_{S\mathbf{k}}\right\rangle\!\left\langle u^{\sigma(i)}_{S\mathbf{k}}\right| = \sum_{i=1}^{N_{\mathrm{occ}}} \gamma_{\sigma^{-1}(i)} \left|u^i_{S\mathbf{k}}\right\rangle\!\left\langle u^i_{S\mathbf{k}}\right| \\ &= \sum_{i=1}^{N_{\mathrm{occ}}} \frac{\gamma_{\sigma^{-1}(i)}}{\gamma_i} \gamma_i \left|u^i_{S\mathbf{k}}\right\rangle\!\left\langle u^i_{S\mathbf{k}}\right| = \frac{\gamma_{\sigma^{-1}(i)}}{\gamma_i}\beta_{S\mathbf{k}}, \end{aligned} \tag{II.125}$$

where we assumed that the condition

$$\frac{\gamma_{\sigma^{-1}(i)}}{\gamma_i} = \text{const.} \qquad \forall i \tag{II.126}$$

is fulfilled. This is one of the conditions for a well defined SO. Next, we turn to the anti-unitary symmetry $\mathfrak{s}$. This symmetry also acts as a permutation $\tilde{\sigma} : i \to j$ (i.e. $\mathfrak{s}\mathcal{K}\left|u^i_{\mathbf{k}}\right\rangle = \left|u^{\tilde{\sigma}(i)}_{-\mathbf{k}}\right\rangle$) on the occupied bands. Its action on $\beta_{\mathbf{k}}$ is then

$$\begin{aligned} \mathfrak{s}\beta^T_{\mathbf{k}}\mathfrak{s}^\dagger &= \left(\mathfrak{s}\beta^*_{\mathbf{k}}\mathfrak{s}^\dagger\right)^\dagger = \left(\mathfrak{s}\sum_{i=1}^{N_{\mathrm{occ}}} \gamma_i^* \left(\left|u^i_{\mathbf{k}}\right\rangle\right)^* \left(\left\langle u^i_{\mathbf{k}}\right|\right)^* \mathfrak{s}^\dagger\right)^\dagger = \left(\sum_{i=1}^{N_{\mathrm{occ}}} \gamma_i^* \left|u^{\tilde{\sigma}(i)}_{-\mathbf{k}}\right\rangle\!\left\langle u^{\tilde{\sigma}(i)}_{-\mathbf{k}}\right|\right)^\dagger \\ &= \left(\sum_{i=1}^{N_{\mathrm{occ}}} \gamma^*_{\tilde{\sigma}^{-1}(i)} \left|u^i_{-\mathbf{k}}\right\rangle\!\left\langle u^i_{-\mathbf{k}}\right|\right)^\dagger = \sum_{i=1}^{N_{\mathrm{occ}}} \gamma_{\tilde{\sigma}^{-1}(i)} \left|u^i_{-\mathbf{k}}\right\rangle\!\left\langle u^i_{-\mathbf{k}}\right| = \frac{\gamma_{\tilde{\sigma}^{-1}(i)}}{\gamma_i}\beta_{-\mathbf{k}}, \end{aligned} \tag{II.127}$$

where we assumed again that the condition

$$\frac{\gamma_{\tilde{\sigma}^{-1}(i)}}{\gamma_i} = \text{const.} \qquad \forall i \tag{II.128}$$

is fulfilled. This condition is the necessary condition for a well-defined SO.
The condition for Hermiticity of $\beta_\mathbf{k}$ is that

$$\gamma_i \in \mathbb{R} \qquad \forall i, \tag{II.129}$$

because then we have that

$$\beta_\mathbf{k}^\dagger = \left(\sum_{i=1}^{N_\mathrm{occ}} \gamma_i \left|u_\mathbf{k}^i\right\rangle\!\left\langle u_\mathbf{k}^i\right| \right)^\dagger = \sum_{i=1}^{N_\mathrm{occ}} \gamma_i^* \left|u_\mathbf{k}^i\right\rangle\!\left\langle u_\mathbf{k}^i\right| = \beta_\mathbf{k}. \tag{II.130}$$

Now one chooses the parameters γ_i such that the intended properties of $\beta_\mathbf{k}$ follow. Consequently to get 1- (and 2-)cycles one assigns $\gamma = \pm 1$ such that $\gamma_i = \gamma_{\sigma(i)}$ $(-\gamma_{\sigma(i)})$ and there is a gap, respectively. For n-cycles, one assigns $\gamma_i = e^{m\frac{2\pi i}{n}}, m \in \{0, ..., n-1\}$. This ensures that the condition is fulfilled. The continuity and lattice periodicity follows from $\left|u_\mathbf{k}^i\right\rangle$ having these properties. We are allowed to use this smooth gauge without loss of generality of the statement because the symmetric gauge vectors $\left|b_\mathbf{k}^i\right\rangle$ are independent of the gauge $\left|u_\mathbf{k}^j\right\rangle$ (cf. section II.9.2.2).

In practice, if one has a BR that can be decomposed into EBRs as BR $= \mathrm{EBR}_1 \oplus \mathrm{EBR}_2 \oplus \mathrm{EBR}_3 \oplus ...$, one would first split the EBRs from each other with a $\mathring{\psi}$ that decomposes the occupied bands into bundles of bands, each of which forming an EBR. This works because the permutations act on the smooth gauge obtained by the Crystallographic Splitting Theorem[131] only by cycling within the EBRs. Each of these EBRs can then be further decomposed, possibly with need to break symmetries, by applying further $\mathring{\psi}$s with corresponding prefactors γ_i.

In Appendix II.A we show explicitly how to construct such an operator for a case with TRS and C_4 symmetry.

II.9.2. Proof of Smoothness and Symmetry of the Gauge

In this section, we prove the smoothness and the symmetry properties of the gauge spanned by $|b_\mathbf{k}^n\rangle$. We want to prove the following statements:

1. The $|b_\mathbf{k}^n\rangle$ are independent of the choice of the gauge for $|u_\mathbf{k}^n\rangle$.
2. The $|b_\mathbf{k}^n\rangle$ are an orthonormal set that spans the subspace of the occupied bands.
3. The subspaces of the occupied subspaces corresponding to different sides of gaps are smooth. This does not mean that the $|b_\mathbf{k}^n\rangle$ are smooth, but only that the space that is spanned by the vectors on the same side of the gap is smooth. In other words, the projectors are smooth.
4. The sewing matrix $\tilde{D}_\mathbf{k}^{mn} = \langle b_{R\mathbf{k}}^m | r | b_\mathbf{k}^n \rangle$ corresponds to the intended type of permutation (e.g. block-diagonality, three-cycle) for a unitary symmetry s.

5. The sewing matrix $\tilde{D}^{mn}_{\mathbf{k}} = \langle b^m_{-\mathbf{k}} | \mathfrak{s}\mathcal{K} | b^n_{\mathbf{k}} \rangle$ corresponds to the intended permutation (it is either block-diagonal or block-off-diagonal, corresponding to the eigenvalues).

In this section, we make usage of Appendix A from Schindler et al. [75]. Proofs for block-(off-)diagonality of sewing matrices that proceed in analogy to this work can be found in Appendix II.B.

II.9.2.1. Orthonormality

The orthonormality of the $|b^n_{\mathbf{k}}\rangle$ follows from

$$\langle b^{\tilde{n}}_{\mathbf{k}} | b^n_{\mathbf{k}} \rangle = \sum_{\tilde{m}m} v^{\tilde{m}*}_{\mathbf{k},\tilde{n}} \langle u^{\tilde{m}}_{\mathbf{k}} | u^m_{\mathbf{k}} \rangle v^m_{\mathbf{k},n} = \sum_m v^{m*}_{\mathbf{k},\tilde{n}} v^m_{\mathbf{k},n} = \langle v_{\mathbf{k},\tilde{n}} | v_{\mathbf{k},n} \rangle = \delta_{\tilde{n}n}, \tag{II.131}$$

for which we used the orthonormality of the eigenvectors of $\mathring{\Psi}$ ($\mathring{\Psi}'$) in the Hermitian (non-Hermitian) case.

II.9.2.2. Gauge Independence

We prove that $|b^n_{\mathbf{k}}\rangle$ does not depend on the gauge of the vectors $|u^n_{\mathbf{k}}\rangle$. We suppress the parameter $\mathbf{k}$ in the notation in this section. Using the notation

$$u = \begin{pmatrix} -- & \vec{u}_1 & -- \\ -- & \vec{u}_2 & -- \\ ... & ... & ... \\ -- & \vec{u}_{N_{\mathrm{occ}}} & -- \end{pmatrix} \tag{II.132}$$

we can write $\mathring{\Psi}$ as

$$\mathring{\Psi} = u^* \mathring{\psi} u^T. \tag{II.133}$$

We apply a unitary transformation U to $|\tilde{u}^n\rangle = \sum_m U_{mn} |u^m\rangle$. If v is an eigenvector of $\mathring{\Psi}$, then we get that the vector

$$\tilde{v} = U^\dagger v \tag{II.134}$$

is an eigenvector of

$$\tilde{\mathring{\Psi}} = (U^T u)^* \mathring{\psi} (U^T u)^T = U^\dagger u^* \mathring{\psi} u^T U = U^\dagger \mathring{\Psi} U \tag{II.135}$$

with eigenvalue κ, because

$$\tilde{\mathring{\Psi}} \tilde{v} = \tilde{\mathring{\Psi}} U^\dagger v = U^\dagger \mathring{\Psi} U U^\dagger v = U^\dagger \mathring{\Psi} v = \kappa U^\dagger v = \kappa \tilde{v}. \tag{II.136}$$

We use this to look at

$$\left| \tilde{b}^n \right\rangle = \sum_m \tilde{v}^m_n |\tilde{u}^m\rangle. \tag{II.137}$$

We rewrite it as follows

$$\left| \tilde{b}^n \right\rangle = \sum_m \tilde{v}^m_n |\tilde{u}^m\rangle = \sum_m \left(\sum_p \left(U^\dagger \right)_{mp} v^p_n \right) \left(U_{lm} \left| u^l \right\rangle \right) = \sum_{lp} (UU^\dagger)_{lp} v^p_n \left| u^l \right\rangle$$

$$= \sum_{lp} \delta_{lp} v_n^p \left| u^l \right\rangle = \sum_{l} v_n^l \left| u^l \right\rangle = \left| b^n \right\rangle \tag{II.138}$$

This shows that the $|b^n_{\mathbf{k}}\rangle$ are independent of the gauge of the occupied subspace.
For the non-Hermitian case, we instead look at the SVD of $\mathring{\Psi} = W\Sigma V^\dagger$ and at $\mathring{\Psi}' = WV^\dagger$. We then get a new SVD

$$\tilde{\mathring{\Psi}} = U^\dagger \mathring{\Psi} U = U^\dagger W \Sigma V^\dagger U = \tilde{W} \Sigma \tilde{V}^\dagger \tag{II.139}$$

with $\tilde{V} = U^\dagger V$ and $\tilde{W} = U^\dagger W$, which are both unitary because the composition of unitary matrices is unitary. This then gives

$$\tilde{\mathring{\Psi}}' = U^\dagger W V^\dagger U \implies \tilde{\mathring{\Psi}}' = U^\dagger \mathring{\Psi}' U. \tag{II.140}$$

According to the arguments above in equations II.135 to II.138, this now implies that the vectors $|b^n\rangle$ are gauge-independent.

II.9.2.3. Smoothness of the Gauge

Using that the $|b^n_{\mathbf{k}}\rangle$ are independent of the gauge of the $|u^n_{\mathbf{k}}\rangle$ we can assume, without loss of generality, that the $|u^n_{\mathbf{k}}\rangle$ are already in a locally smooth gauge[4]. This implies that $\mathring{\Psi}^{mn}_{\mathbf{k}}$ is smooth as well, because it consists of multipications of smooth quantities. This then implies that the $\vec{v}_{\mathbf{k},n}$ span smooth subspaces above and below the gap (see Alexandradinata et al.[131], Refs. [148–151]). Since the space spanned by the $\langle \{ \vec{v}_{\mathbf{k},n} \mid \kappa_{\mathbf{k},n} > \kappa_{\text{gap}} \} \rangle$ is smooth, the space spanned by the back-transformations, $|b^n_{\mathbf{k}}\rangle = \sum_m v^m_{\mathbf{k},n} |u^m_{\mathbf{k}}\rangle$, is smooth as well, using the fact that our $|u^n_{\mathbf{k}}\rangle$ are smooth. Due to the gauge-independence of the $|b^n_{\mathbf{k}}\rangle$ this generalises to all possible gauges of $|u^n_{\mathbf{k}}\rangle$.

If we are in the non-Hermitian case and are looking at $\mathring{\Psi}' = WV^\dagger$, we additionally have to prove that the mapping $f : \mathring{\Psi} \to \mathring{\Psi}'$ is smooth. The fact that this mapping is a well-defined function comes from the uniqueness of the polar decomposition. The unitary projection can equivalently be written in terms of a polar decomposition of the matrix

$$\mathring{\Psi}_{\mathbf{k}} = W_{\mathbf{k}} \Sigma_{\mathbf{k}} V^\dagger_{\mathbf{k}} = \underbrace{W_{\mathbf{k}} \Sigma_{\mathbf{k}} W^\dagger_{\mathbf{k}}}_{P_{\mathbf{k}}} \underbrace{W_{\mathbf{k}} V^\dagger_{\mathbf{k}}}_{U_{\mathbf{k}}}. \tag{II.141}$$

The polar decomposition is unique for invertible matrices[143, pp. 42-45]. Therefore, the mapping $\mathring{\Psi}_{\mathbf{k}} \to \mathring{\Psi}'_{\mathbf{k}}$ is well-defined, whenever all its eigenvalues are nonvanishing. Furthermore, since

$$P_{\mathbf{k}} = \left(\mathring{\Psi}^\dagger_{\mathbf{k}} \mathring{\Psi}_{\mathbf{k}} \right)^{1/2} \tag{II.142}$$

is a smooth function of $\mathbf{k}$ and the inverse does not impede differentiability away from 0, the mapping f is smooth.
Another way to see is that we know that W and V are given by the eigenvectors of $\mathring{\Psi}^\dagger \mathring{\Psi}$ and $\mathring{\Psi} \mathring{\Psi}^\dagger$, respectively[152, pp. 91-120], which means, together with the fact that $WV^\dagger$ is independent of the chosen SVD, that f is indeed smooth.

---

[4] It is in general not possible to choose a globally smooth gauge, the impossibility to choose such a gauge is detected by a nonzero first Chern number. Still, for the sake of this argument, it is sufficient to look at a small open region around every momentum. All these regions can then be patched together, keeping in mind that the new gauge is independent of the original gauge.

II.9.2.4. Proof of Permutation-Likeness of Sewing Matrices

We assume that the $\mathring{\Psi}$ has the symmetries

$$s_j \mathring{\psi}_{\mathbf{k}} s_j^\dagger = e^{\frac{2\pi i m}{n}} \mathring{\psi}_{S\mathbf{k}} \tag{II.143}$$

and

$$\mathfrak{s}_i \mathring{\psi}^T_{\mathbf{k}} \mathfrak{s}_i^\dagger = \pm \mathring{\psi}_{-\mathbf{k}}. \tag{II.144}$$

The second line corresponds to a anti-unitary symmetry, expressed with the transpose instead of the complex conjugation.

Hermitian case If $\mathring{\psi}_{\mathbf{k}}$ is Hermitian, it is possible to simply use the eigenvector decomposition of $\mathring{\Psi}_{\mathbf{k}}$. In this case $e^{\frac{2\pi i m}{n}} \in \{+1, -1\}$. Because of the Hermiticity of $\mathring{\Psi}$, we know that

$$\mathring{\Psi}_{\mathbf{k}} = V_{\mathbf{k}} D_{\mathbf{k}} V_{\mathbf{k}}^\dagger, \tag{II.145}$$

with a diagonal matrix $D_{\mathbf{k}}$ and a unitary matrix $V_{\mathbf{k}}$. Furthermore, we know that the occupied eigenspace at $S\mathbf{k}$ is spanned by $|u^n_{S\mathbf{k}}\rangle = s\,|u^n_{\mathbf{k}}\rangle$. This does not lead to a loss of generality of the argument, because the vectors $|b^n_{\mathbf{k}}\rangle$ are gauge-independent. As before, we have $\mathring{\Psi}_{\mathbf{k}} = u^*_{\mathbf{k}} \mathring{\psi}_{\mathbf{k}} u^T_{\mathbf{k}}$. This implies for $S\mathbf{k}$ that

$$\mathring{\Psi}_{S\mathbf{k}} = u^*_{S\mathbf{k}} \mathring{\psi}_{S\mathbf{k}} u^T_{S\mathbf{k}} = u^*_{\mathbf{k}} s^\dagger e^{-\frac{2\pi i m}{n}} s \mathring{\psi}_{\mathbf{k}} s^\dagger s u^T_{\mathbf{k}} = e^{-\frac{2\pi i m}{n}} \mathring{\Psi}_{\mathbf{k}} \tag{II.146}$$

using that $u_{S\mathbf{k}} = u_{\mathbf{k}} s^T$. This now implies that if $\vec{v}_{\mathbf{k},n}$ is an eigenvector of $\mathring{\Psi}_{\mathbf{k}}$ with eigenvalue $\kappa_{\mathbf{k},n}$, it is also an eigenvector of $\mathring{\Psi}_{S\mathbf{k}}$ with eigenvalue $e^{-\frac{2\pi i m}{n}} \kappa_{\mathbf{k},n}$. If we have a set of orthogonal eigenvectors $\vec{v}_{\mathbf{k},n}$ and the correspoding set $|b^n_{\mathbf{k}}\rangle$, then this implies that a vector $\vec{v}_{\mathbf{k},n}$ can only be nonorthogonal to vectors $\vec{v}_{S\mathbf{k},m}$ with eigenvalue $e^{-\frac{2\pi i m}{n}} \kappa_{\mathbf{k},n}$. This proves the that the sewing matrix for the $|b^n_{\mathbf{k}}\rangle$ looks like a permutation (at least up to blocks of the size of the number of bands grouped together by gaps.).

Next, the anti-unitary symmetry $\mathfrak{s}$ is treated. In this case (e.g. TRS), the occupied space at $-\mathbf{k}$ is spanned by $\left|u^n_{-\mathbf{k}}\right\rangle = \mathfrak{s}K\,|u^n_{\mathbf{k}}\rangle$. Then

$$\begin{aligned}\mathring{\Psi}_{-\mathbf{k}} = u^*_{-\mathbf{k}} \mathring{\psi}_{-\mathbf{k}} u^T_{-\mathbf{k}} &= \pm \left(u^*_{\mathbf{k}} \mathfrak{s}^T\right)^* \mathfrak{s} \mathring{\psi}^*_{\mathbf{k}} \mathfrak{s}^\dagger \left(u^*_{\mathbf{k}} \mathfrak{s}^T\right)^T \\ &= \pm u_{\mathbf{k}} \mathfrak{s}^\dagger \mathfrak{s} \mathring{\psi}^*_{\mathbf{k}} \mathfrak{s}^\dagger \mathfrak{s} u^\dagger_{\mathbf{k}} = \pm u_{\mathbf{k}} \mathring{\psi}^*_{\mathbf{k}} u^\dagger_{\mathbf{k}} = \pm \left(u^*_{\mathbf{k}} \mathring{\psi}_{\mathbf{k}} u^T_{\mathbf{k}}\right)^* = \pm \mathring{\Psi}^*_{\mathbf{k}}.\end{aligned} \tag{II.147}$$

If $\mathring{\Psi}_{\mathbf{k}}$ has the eigenvector $v_{\mathbf{k},n}$ with eigenvalue $\kappa_{\mathbf{k},n}$, $\mathring{\Psi}_{-\mathbf{k}}$ has the eigenvector $v^*_{\mathbf{k},n}$ with eigenvalue $\pm\kappa^*_{\mathbf{k},n}$. This implies for the corresponding vector $|b^n_{\mathbf{k}}\rangle$ and the sewing matrix that

$$D^{mn}_{\mathbf{k}} = \left\langle b^m_{-\mathbf{k}} \middle| \mathfrak{s}K \middle| b^n_{\mathbf{k}} \right\rangle = \sum_{ji} v^j_{\mathbf{k},m} v^{i*}_{\mathbf{k},n} \left\langle u^j_{-\mathbf{k}} \middle| \mathfrak{s}K \middle| u^i_{\mathbf{k}} \right\rangle = \sum_{ji} v^j_{\mathbf{k},m} v^{i*}_{\mathbf{k},n} \delta_{ij} = \delta_{mn}. \tag{II.148}$$

This holds as long as the eigenvalues are nondegenerate. Due to the existence of a gap throughout the BZ, the sewing matrix is then block-(off-)diagonal, taking into consideration the ordering of the $\left|b^m_{-\mathbf{k}}\right\rangle$.

Non-Hermitian case Unitary symmetries work in exactly the same way as they do in the Hermitian case. For antiunitary symmetries, we have to look at the version of the symmetry with the transpose instead of the complex conjugation. Here

$$\begin{aligned}\mathring{\Psi}_{-\mathbf{k}} = u^*_{-\mathbf{k}}\mathring{\psi}_{-\mathbf{k}}u^T_{-\mathbf{k}} &= \pm\left(u^*_{\mathbf{k}}\mathfrak{s}^T\right)^* \mathfrak{s}\mathring{\psi}^T_{\mathbf{k}}\mathfrak{s}^\dagger \left(u^*_{\mathbf{k}}\mathfrak{s}^T\right)^T \\ &= \pm u_{\mathbf{k}}\mathfrak{s}^\dagger\mathfrak{s}\mathring{\psi}^T_{\mathbf{k}}\mathfrak{s}^\dagger\mathfrak{s}u^\dagger_{\mathbf{k}} = \pm u_{\mathbf{k}}\mathring{\psi}^T_{\mathbf{k}}u^\dagger_{\mathbf{k}} = \left(u^*_{\mathbf{k}}\mathring{\psi}_{\mathbf{k}}u^T_{\mathbf{k}}\right)^T = \pm\mathring{\Psi}^T_{\mathbf{k}} = \pm\mathring{\Psi}^{*\dagger}_{\mathbf{k}}. \qquad \text{(II.149)}\end{aligned}$$

Lemma (Biorthogonality)[153, p. 239]: If $\mathring{\Psi}\left|v\right\rangle = \kappa\left|v\right\rangle$ and $\mathring{\Psi}^\dagger\left|w\right\rangle = \lambda\left|w\right\rangle$ then

$$\kappa\left\langle w|v\right\rangle = \left\langle w\middle|\mathring{\Psi}\middle|v\right\rangle = \left\langle\mathring{\Psi}w\middle|v\right\rangle = \lambda^*\left\langle w|v\right\rangle \implies \left(\kappa-\lambda^*\right)\left\langle w|v\right\rangle = 0. \qquad \text{(II.150)}$$

If $\vec{w}_{\mathbf{k},m}$ is a left eigenvector of $\mathring{\Psi}_{\mathbf{k}}$, which means that $\mathring{\Psi}^\dagger_{\mathbf{k}}\vec{w}_{\mathbf{k},m} = \lambda_{\mathbf{k},m}\vec{w}_{\mathbf{k},m}$, then $\vec{w}^*_{\mathbf{k},m}$ is an eigenvector of $\mathring{\Psi}_{-\mathbf{k}}$ with eigenvalue $\kappa_{-\mathbf{k},m} = \pm\lambda^*_{\mathbf{k},m}$. The sewing matrix is given by

$$\begin{aligned}D^{mn}_{\mathbf{k}} = \left\langle b^m_{-\mathbf{k}}\middle|\mathfrak{s}K\middle|b^n_{\mathbf{k}}\right\rangle &= \sum_{ji} w^j_{\mathbf{k},m}v^{i*}_{\mathbf{k},n}\left\langle u^j_{-\mathbf{k}}\middle|\mathfrak{s}K\middle|u^i_{\mathbf{k}}\right\rangle \\ &= \sum_{ji} w^j_{\mathbf{k},m}v^{i*}_{\mathbf{k},n}\delta_{ij} = \left(\sum_i w^{i*}_{\mathbf{k},m}v^i_{\mathbf{k},n}\right)^* = 0 \text{ if } \pm\kappa_{-\mathbf{k},m} = \lambda^*_{\mathbf{k},m} \neq \kappa_{\mathbf{k},n}. \qquad \text{(II.151)}\end{aligned}$$

This proves that the sewing matrix has block-off-diagonal form for $-$ and a block-diagonal form for $+$.

II.9.3. Construction of PSOs Based on Symmetry Only

In this section, we will describe how to construct SOs and how the corresponding band structures look like. This section describes an easy method to construct SOs that is based solely on using symmetries and does not rely on defining real space operators. Still, the effects of real space symmetries on band structures are taken into consideration, by considering the appearance of band inversions.

We start this discussion with the case that motivated this thesis: the obstructed atomic limits of two-dimensional C_4-symmetric materials in Altland-Zirnbauer class AII ($\mathcal{T}^2 = -1$). In the second part of the section C_3- and C_6-symmetric Hamiltonians that require non-Hermitian SOs are treated.

The application of the PSO method is shown in several examples.

II.9.3.1. Case with TRS and C_4 Symmetry

This chapter mainly deals with the models by Benalcazar et al.[133] (cf. section II.4.1) for OALs that are C_4 symmetric and the model by Song et al.[138] (cf. section II.4.2). For the models by Benalcazar et al.[133] we look at the doubled models with TRS. The models are defined on a 2D quadratic lattice. They have TRS and C_4 symmetry and are lattice periodic. In these models the use of non-Hermitian $\mathring{\psi}$s is not necessary to arrive at single bands. The r_4 eigenvalues at the TRIMs $\mathbf{\Gamma}$ and $\mathbf{M}$ are either $e^{\pm i\pi/4}$ or $e^{\pm 3i\pi/4}$. The most straightforward way to separate these four bands with different eigenvalues to twice two bands with specific real parts of their rotational eigenvalues is to use the operator

$$\mathring{\psi}_{\mathbf{k}} = r_4 + r_4^\dagger. \qquad \text{(II.152)}$$

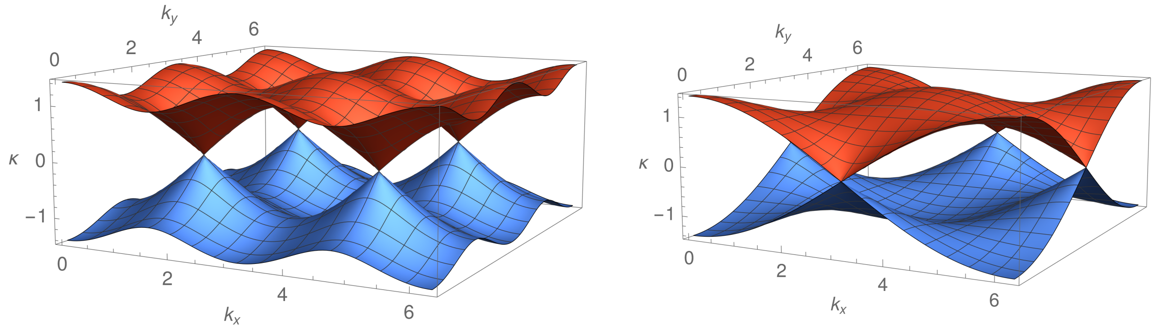

(a) $\mathring{\Psi}$ band structure of the model $H_2^{(4)}(\mathbf{k}, t = 0)$ (corresponding to the primitive generator $h_{2b}^{(4)}$, Benalcazar et al.[133]) at $t = 0$. We can clearly see four Dirac-like doubly generate points halfway between the TRIMs $\mathbf{\Gamma} = (0, 0)$ and $\mathbf{M} = (\pi, \pi)$.

(b) $\mathring{\Psi}$ band structure of the model $H_3^{(2)}(\mathbf{k}, t = 0)$ (corresponding to the primitive generator $h_{2c}^{(4)}$, Benalcazar et al.[133]) at $t = 0$. We can clearly see two Dirac-like doubly generate points at $\mathbf{X}$ and $\mathbf{Y}$.

Figure II.23.: $\mathring{\Psi}$ band structures calculated using $\mathring{\psi} = r_4 + r_4^\dagger$ for two different models.

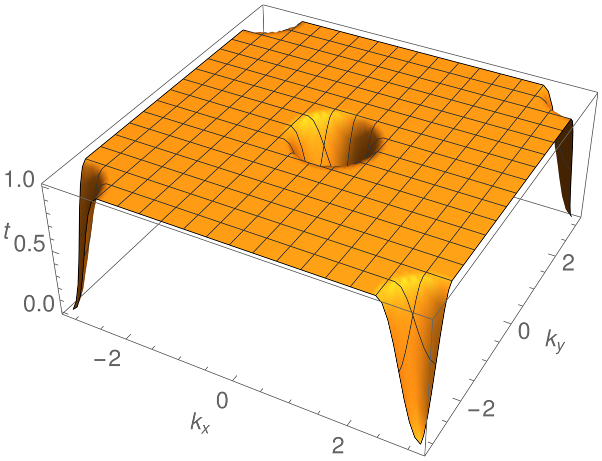

Figure II.24.: A typical function $t_{\mathbf{k}}$ with r_4 symmetry.

This matrix satisfies the symmetry requirements

$$\begin{aligned} r_4 \mathring{\psi}_{\mathbf{k}} r_4^\dagger &= \mathring{\psi}_{R_4 \mathbf{k}}, \\ \tau \mathring{\psi}_{\mathbf{k}}^T \tau^\dagger &= \mathring{\psi}_{-\mathbf{k}}, \\ \mathring{\psi}_{\mathbf{k}}^\dagger &= \mathring{\psi}_{\mathbf{k}}. \end{aligned} \tag{II.153}$$

If the spectrum of the corresponding PSO $\mathring{\Psi}$ is gapped, the two pairs of bands correspond to specific eigenvalues. The compatibility with Wyckoff position $1a$ can be seen from the fact that for $1a$, the r_4 eigenvalues at $\mathbf{\Gamma}$ and $\mathbf{M}$ are the same as for a Wannierised band centred at $1a$. The same applies also for the bands obtained using this operator: we always project into positive (negative) real part of the r_4 eigenvalue for the upper (lower) band, respectively. This is compatible with a BR corresponding to the Wyckoff position $1a$. If we instead wanted a $\mathring{\psi}$ compatible with $1b$, we would have to build a $\mathring{\psi}$ that takes the band inversion into account.

Using this $\mathring{\psi} = r_4 + r_4^\dagger$, a gapless spectrum can often be gapped out simply by using

$$\mathring{\psi}_{\mathbf{k}} = r_4 + r_4^\dagger + t_{\mathbf{k}}\alpha \tag{II.154}$$

with a symmetrised constant matrix α (fulfilling the same symmetry requirements as $\mathring{\psi}_{\mathbf{k}}$ in equation II.153), where $t_{\mathbf{k}}$ is a smooth function with values in $[0,1]$. This $t_{\mathbf{k}}$ is 0 at $\mathbf{\Gamma}$ and $\mathbf{M}$ and also respects r_4 symmetry. An example for a $t_{\mathbf{k}}$ is the function depicted in Fig. II.24. It is 0 at $\mathbf{\Gamma}$ and $\mathbf{M}$, away from there it goes up to 1 in the shape of a $\cos(4|\mathbf{k}|)$ and plateaus at the first ridge of the cosine. It is continuous and once differentiable. Due to the discretisation, the lack of higher order differentiability does not impede the application of smoothness arguments. Appendix II.C deals with the question whether it is possible to perturb $\mathring{\Psi}_{\mathbf{k}}$ instead of $\mathring{\psi}_{\mathbf{k}}$. It is hardly possible.

In the following we look at the examples. We start with the two tight-binding Hamiltonians $H_2^{(4)}(\mathbf{k})$ (primitive generator $h_{2b}^{(4)}$) and $H_3^{(2)}(\mathbf{k})$ (primitive generator $h_{2c}^{(4)}$) at $t = 0$. The $\mathring{\Psi}$ band structures of the models using $\mathring{\psi} = r_4 + r_4^\dagger$ are depicted in figure II.23a and II.23b (We refer to the eigenvalues of $\mathring{\Psi}_{\mathbf{k}}$ as function of $\mathbf{k}$ as "$\mathring{\Psi}$ band structure". The upper (lower) band of $\mathring{\Psi}_{\mathbf{k}}$ is then called the upper (lower) $\mathring{\Psi}$ band.). Both of these band structures have double degeneracies between the upper and the lower band. For $H_2^{(4)}(\mathbf{k})$, these degeneracies are halfway between $\mathbf{\Gamma}$ and $\mathbf{M}$. For $H_3^{(2)}(\mathbf{k})$ they are at $\mathbf{X}$ and $\mathbf{Y}$. Since the $\mathring{\Psi}$ band structure is gapless, the corresponding gauge is neither symmetric throughout the BZ nor are its projectors smooth. This makes it necessary to add a small perturbation to gap it out, like described in equation II.154. The perturbation that leads to the appearance of a gap is in both cases given by

$$\alpha_{\mathrm{ok}} = \sigma_0 \otimes \sigma_1 \otimes \sigma_0. \tag{II.155}$$

The other combinations of Pauli matrices do not lead to any gap appearance. The conditions under which such degeneracies can be gapped out are discussed in detail in section II.9.5, where we show that only double degeneracies can be gapped out. Single degeneracies always remain closed, but can be moved through the BZ by applying perturbations. The $\mathring{\Psi}$ band structure calculated with a perturbed $\mathring{\psi}$ is shown in Fig. II.25a (II.26a); in Fig. II.25b (II.26b) the Wilson spectra in the lower and upper $\mathring{\Psi}$ band are shown, for $H_2^{(4)}(\mathbf{k}, t = 0)$ (resp. $H_3^{(2)}(\mathbf{k}, t = 0)$). Appendix II.D deals with the question whether the Wilson loop spectra depicted in Figures II.25b and II.26b can also be calculated without diagonalising $\mathring{\Psi}_{\mathbf{k}}$ by instead modifying how the Wilson loop is calculated.

The type of $\mathring{\psi}$ we used here leads to block-diagonal sewing matrices of the form

$$D_{\mathcal{T}} = \begin{pmatrix} * & \\ & * \end{pmatrix} \text{ and } D_{r_4} = \begin{pmatrix} * & \\ & * \end{pmatrix}. \tag{II.156}$$

We are interested in distinguishing the case $h_{2b}^{(4)}$ with two Kramers pairs at the Wyckoff position $1b$ from the cases with electrons centred at $2c$ or $1a$. The question is whether this is easily possible. Looking only at Figure II.25b, one might think that this type of double winding could be a clear signal of the h_{2b} OAL. While we do know that the winding for a $\mathring{\psi}$ of the type we used, projecting both at $\mathbf{M}$ and at $\mathbf{\Gamma}$ into the same eigenvalues, must be non-trivial, the Wilson loop spectrum does not necessarily show the double winding behaviour. In Fig. II.27, we show an example of a Hamiltonian that corresponds to the same atomic limit (also $h_{2b}^{(4)}$) but shows a different winding pattern. This pattern with a fourfold winding appearing in

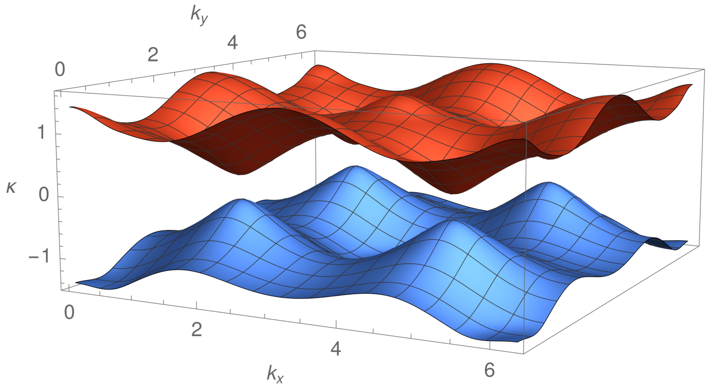

(a) $\mathring{\Psi}$ band structure of the model $H_2^{(4)}(\mathbf{k}, t=0)$ (corresponding to the primitive generator $h_{2b}^{(4)}$, Benalcazar et al.[133]). The Dirac-like cones, visible in Fig. II.23a, are gapped out using a small perturbation.

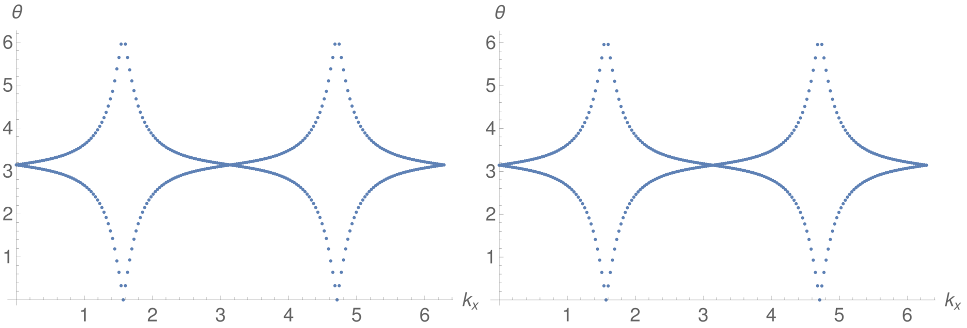

(b) Wilson loop spectrum in lower (left) and upper (right) $\mathring{\Psi}$ bands. We can see a double winding that cannot be trivialised within the symmetry constraints.

Figure II.25.: $\mathring{\Psi}$ band structures and Wilson loop spectra for $H_2^{(4)}(\mathbf{k}, t=0)$, perturbed $\mathring{\psi}$.

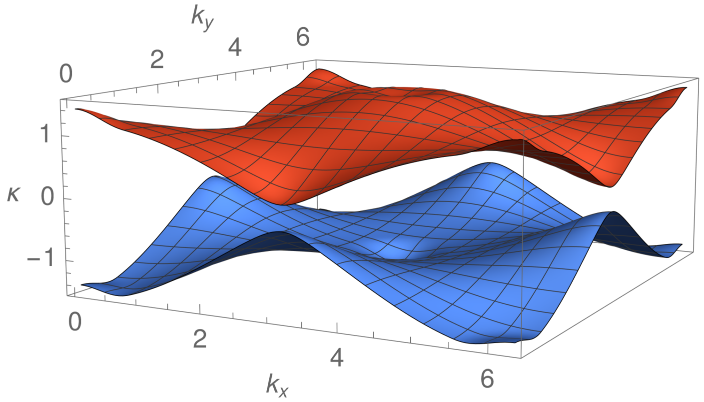

(a) $\mathring{\Psi}$ band structure of the model $H_3^{(2)}(\mathbf{k}, t = 0)$ (corresponding to the primitive generator $h_{2c}^{(4)}$, Benalcazar et al.[133]). The Dirac-like cones, visible in Fig. II.23a, are gapped out using a small perturbation.

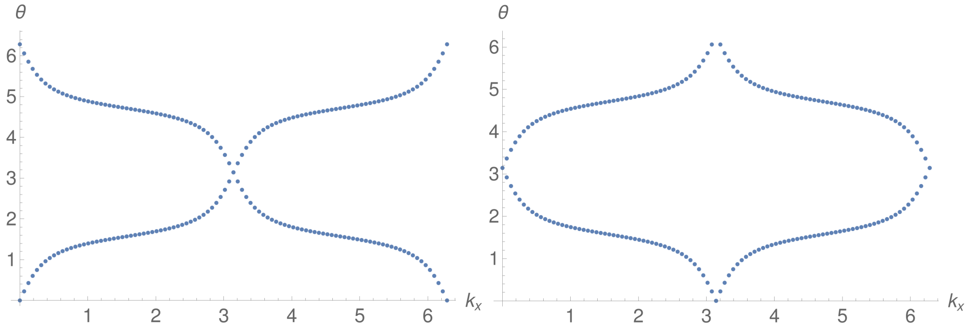

(b) Wilson loop spectrum in lower (left) and upper (right) $\mathring{\Psi}$ bands. We can see a winding that cannot be trivialised within the symmetry constraints.

Figure II.26.: $\mathring{\Psi}$ band structures and Wilson loop spectra for $H_3^{(2)}(\mathbf{k}, t = 0)$, perturbed $\mathring{\psi}$.

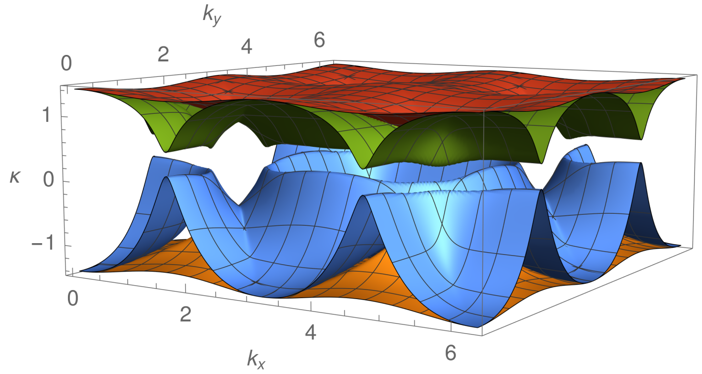

(a) $\mathring{\Psi}$ band structure of the model $H_2^{(4)}(\mathbf{k}, t = -0.2) + \frac{4}{5}\alpha_{4\text{ fold}}$ (corresponding to the primitive generator $h_{2b}^{(4)}$, Benalcazar et al.[133]). The $\mathring{\Psi}$ band structure is gapped.

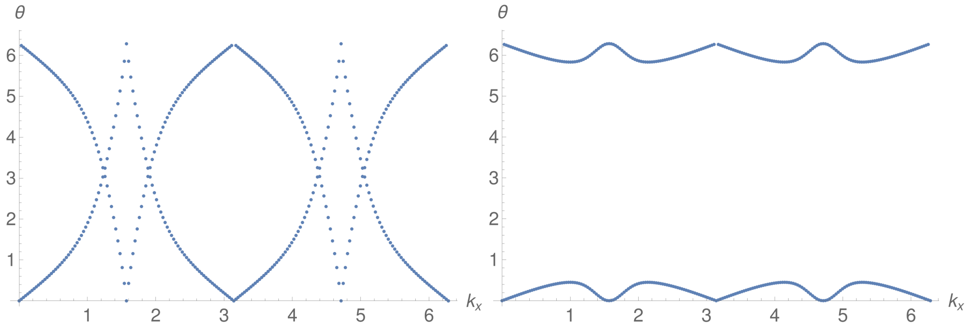

(b) Wilson loop spectrum in lower (left) and upper (right) $\mathring{\Psi}$ bands. We can see a trivial winding in the upper $\mathring{\Psi}$ bands and a fourfold winding in the lower bands.

Figure II.27.: $\mathring{\Psi}$ band structures and Wilson loop spectra. Here $H = H_2^{(4)}(\mathbf{k}, t = -0.2) + \frac{4}{5}\alpha_{4\text{ fold}}$, for $\alpha_{4\text{ fold}}$ see appendix II.E, Eq. II.257. The $\mathring{\Psi}$ band structure is calculated with $\mathring{\psi}_{\mathbf{k}} = r_4 + r_4^\dagger$.

the lower $\mathring{\Psi}$ bands and no winding at all in the upper $\mathring{\Psi}$ bands can be achieved by adding a constant perturbation $\frac{4}{5}\alpha_{4\text{ fold}}$, given in appendix II.E, equation II.257, to the Hamiltonian $H_2^{(4)}(\mathbf{k}, t = -0.2)$. Furthermore, we observe that the Wilson loop spectrum for $k_x = 0, \pi$ is not pinned to π anymore, which means that this property is not a topological invariant. In this example, $\mathring{\psi} = r_4 + r_4^\dagger$ was used.

Furthermore, it is enlightening to study the system $H(\mathbf{k}) = H_2^{(4)}(\mathbf{k}, t = 0.2) + \alpha_{\text{matadd}}$ with α_{matadd} given in appendix II.E, equation II.259. This system shows double winding in the upper and the lower $\mathring{\Psi}$ bands for $\mathring{\psi} = r_4 + r_4^\dagger$, but it can be driven to show the the combination of fourfold and no winding by using $\mathring{\psi}_{\mathbf{k}} = H(\mathbf{k})$. The $\mathring{\Psi}$ band structure and the Wilson spectrum for $\mathring{\psi} = r_4 + r_4^\dagger$ are depicted in Fig. II.29, for $\mathring{\psi}_{\mathbf{k}} = H(\mathbf{k})$ in Fig. II.28. Using this system, we can see that the transition from one type of winding behaviour to the other can also happen by changing $\mathring{\psi}_{\mathbf{k}}$.

In the numerics, it can be clearly seen that the transitions between different types of winding behaviour happen by gap closures. The gaps between the upper and lower $\mathring{\Psi}$ bands close at a

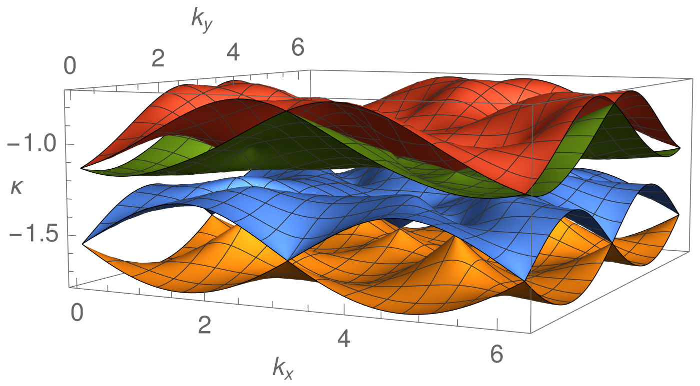

(a) $\mathring{\Psi}$ band structure of the model $H_2^{(4)}(\mathbf{k}, t = 0.2) + \alpha_{\text{matadd}}$ (corresponding to the primitive generator $h_{2b}^{(4)}$, Benalcazar et al.[133]).

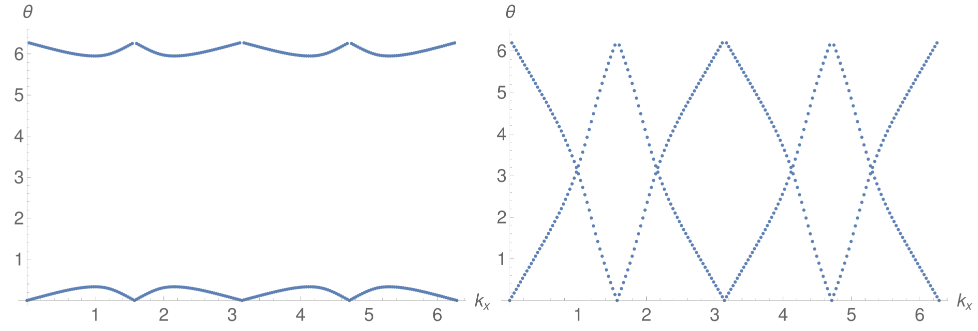

(b) Wilson loop spectrum in lower (left) and upper (right) $\mathring{\Psi}$ bands. We can see a double winding that cannot be trivialised within the symmetry constraints.

Figure II.28.: $\mathring{\Psi}$ band structures and Wilson loop spectra for $H_2^{(4)}(t = 0.2) + \frac{4}{5}\alpha_{\text{matadd}}$. $\mathring{\psi}_{\mathbf{k}} = H_2^{(4)}(\mathbf{k}, t = 0.2) + \alpha_{\text{matadd}}$

point in the BZ. The appearing degeneracies are always at least double, because single degeneracies cannot be gapped out. The double degeneracies are split from each other, then moved separately through the BZ and finally merged with other single degeneracies, to be gapped out. $\mathring{\psi}$s in which only single degeneracies appear, like those appearing when moving from one type of winding to the other, cannot be gapped out using infinitesimaly small perturbations; they require a certain strength of perturbation, because the single degeneracies must be moved through the BZ to gap them out. The properties of degeneracies are explained more in detail in chapter II.9.5.

Another system also studied in this section is the system described by Song et al.[138](cf. section II.4.2). Its Hamiltonian is given in equation II.27. Its $\mathring{\Psi}$ band structure for $t = 0$ and $\mathring{\psi}_{\mathbf{k}} = r_4 + r_4^\dagger$ is depicted in Fig. II.30a and its Wilson spectra in the upper and lower $\mathring{\Psi}$ band are shown in Fig. II.30b. This system is a double TI and does not correspond to an atomic limit.

Next, we observe that the gauges can be further split. To this end, we split each of the 2-band

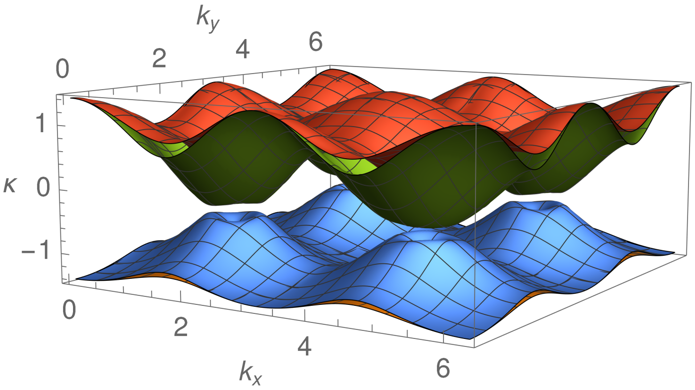

(a) $\mathring{\Psi}$ band structure of the model $H_2^{(4)}(\mathbf{k}, t = 0.2) + \alpha_{\text{matadd}}$ (corresponding to the primitive generator $h_{2b}^{(4)}$, Benalcazar et al.[133]).

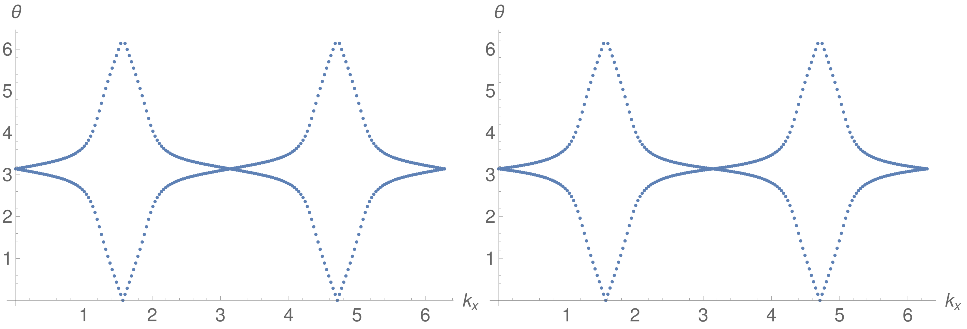

(b) Wilson loop spectrum in lower (left) and upper (right) $\mathring{\Psi}$ bands. We can see a fourfold winding that cannot be trivialised within the symmetry constraints in the upper $\mathring{\Psi}$ bands.

Figure II.29.: $\mathring{\Psi}$ band structures and Wilson loop spectra for $H_2^{(4)}(t = 0.2) + \alpha_{\text{matadd}}$ using $\mathring{\psi} = r_4 + r_4^\dagger$.

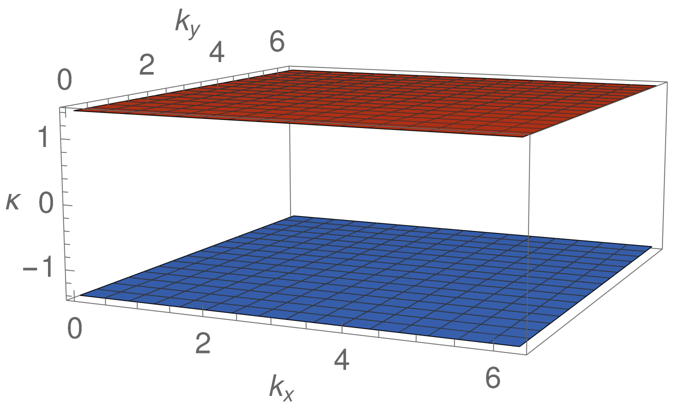

(a) $\mathring{\Psi}$ band structure of the model $H_{\text{double TI}}(\mathbf{k}, t = 0.0)$ (a double TI) (Song et al.[138]).

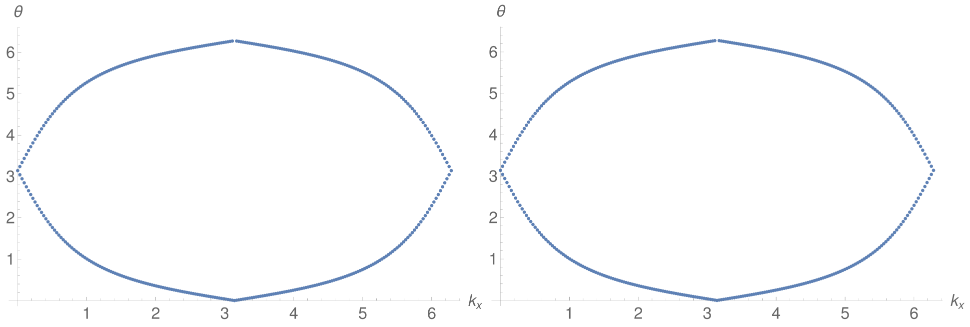

(b) Wilson loop spectrum in lower (left) and upper (right) $\mathring{\Psi}$ bands. We can see a single winding that cannot be trivialised within the symmetry constraints.

Figure II.30.: $\mathring{\Psi}$ band structures and Wilson loop spectra for $H_{\text{double TI}}$.

subspaces further using a $\tilde{\mathring{\psi}}$ with the properties

$$\begin{aligned} \tilde{\mathring{\psi}}_{\mathbf{k}} &= \tilde{\mathring{\psi}}^{\dagger}_{\mathbf{k}}, \\ r_4 \tilde{\mathring{\psi}}_{\mathbf{k}} r_4^{\dagger} &= \tilde{\mathring{\psi}}_{R_4\mathbf{k}}, \\ \mathcal{T} \tilde{\mathring{\psi}}_{\mathbf{k}} \mathcal{T}^{-1} &= -\tilde{\mathring{\psi}}_{-\mathbf{k}}. \end{aligned} \tag{II.157}$$

Intuitively, the idea behind it is to split the up- from the down-spin electrons. In this gauge ($|b^1_{\mathbf{k}}\rangle$, $|b^2_{\mathbf{k}}\rangle$), $\mathcal{T}$ maps one band to the other. This follows directly from the proof for the permutation-likeness of sewing matrices (cf. section II.9.2.4). For such gauges it can be shown that, if, like here, C_2 is present as well, the superimposed Wilson spectra of the one-bands subspaces give exactly the Wilson loop spectrum of the 2-band subspace (cf. section II.6.2). In Fig. II.31 and II.32, we show two different gauge-constructions for the case of $H_{\mathbf{k}} = H_2^{(4)}(\mathbf{k}, t = 0)$. One of the constructions (Fig. II.32) is like the previous one, only with the second the split added to get single-band subspaces. This means that $\mathring{\psi}_{\mathbf{k}} = r_4 + r_4^{\dagger} + t_{\mathbf{k}} \alpha_{\text{ok}}$. The other construction (Fig. II.31) is the case of $\mathring{\psi} = (r_4 + r_4^{\dagger})(1 + \cos k_x + \cos k_y) + t_{\mathbf{k}}\beta$, where β is the matrix in equation II.258 in appendix II.E. This $\mathring{\psi}$ corresponds to a projection into subspaces that change r_4 eigenvalues from $\mathbf{\Gamma}$ to $\mathbf{M}$, which is then compatible with the Wyckoff position $1b$, to which the Hamiltonian corresponds. This becomes evident from the fact that bands with positive eigenvalues κ of $\mathring{\Psi}$ change from having a positive real part of the r_4 eigenvalues to a negative one. This represents the band inversion of bands with Wannier centres localised at the $1b$ Wyckoff position. Therefore, the expected effect is that there is no winding. No winding in the Wilson spectrum of the single band subspaces corresponds to zero first Chern number. We obtain a gauge with vanishing Chern numbers and symmetries that act as permutations on the bands. Consequently, according to the Crystallographic Splitting Theorem, the occupied bands are a band representation[131].

Both in Fig II.31 and II.32, we show the splitting of the lower two $\mathring{\Psi}$ bands using the second $\tilde{\mathring{\Psi}}$ with the properties described in equation II.157.

Next, we look at the case when the electrons are situated at the positions $2c$ and $2c'$. In this case, it is impossible to find a $\mathring{\psi}_{\mathbf{k}}$ respecting C_4 symmetry such that the Wilson loop spectra of the final single bands do not wind. Instead, we construct a gauge such that the symmetries of the site symmetry group of the single electrons are respected and the remaining symmetries act by exchanging bands. To construct such a gauge, we use two consecutive splits, the first one with a matrix respecting

$$\begin{aligned} \mathring{\psi}_{\mathbf{k}} &= \mathring{\psi}^{\dagger}_{\mathbf{k}}, \\ r_4 \mathring{\psi}_{\mathbf{k}} r_4^{\dagger} &= -\mathring{\psi}_{R_4\mathbf{k}}, \\ \mathcal{T} \mathring{\psi}_{\mathbf{k}} \mathcal{T}^{-1} &= \mathring{\psi}_{-\mathbf{k}}, \end{aligned} \tag{II.158}$$

the second split is achieved using a matrix respecting

$$\begin{aligned} \tilde{\mathring{\psi}}_{\mathbf{k}} &= \tilde{\mathring{\psi}}^{\dagger}_{\mathbf{k}}, \\ r_4 \tilde{\mathring{\psi}}_{\mathbf{k}} r_4^{\dagger} &= -\tilde{\mathring{\psi}}_{R_4\mathbf{k}}, \\ \mathcal{T} \tilde{\mathring{\psi}}_{\mathbf{k}} \mathcal{T}^{-1} &= -\tilde{\mathring{\psi}}_{-\mathbf{k}}. \end{aligned} \tag{II.159}$$

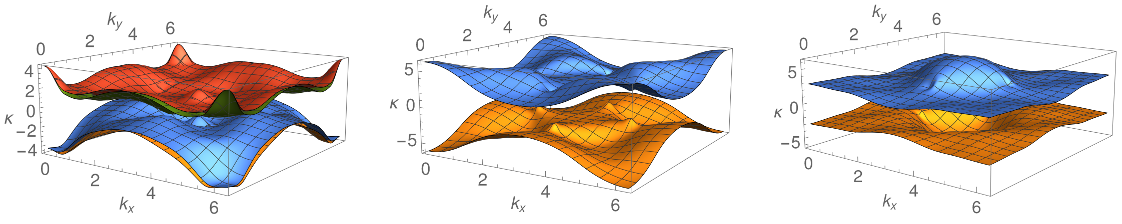

(a) $\mathring{\Psi}$ band structure of the model $H_2^{(4)}(\mathbf{k}, t = 0)$. Split to two two-band spaces using $\mathring{\psi}$ corresponding to Wyckoff position $1b$.

(b) $\tilde{\mathring{\Psi}}$ band structure within the lower two bands using a random $\mathring{\psi}$.

(c) $\tilde{\mathring{\Psi}}$ band structure within the upper two bands using the same random $\mathring{\psi}$.

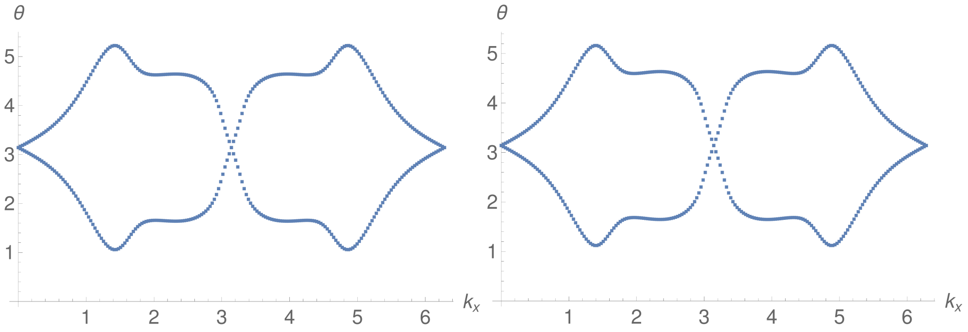

(d) Wilson loop spectrum in lower (left) and upper (right) $\mathring{\Psi}$ bands. We see no winding.

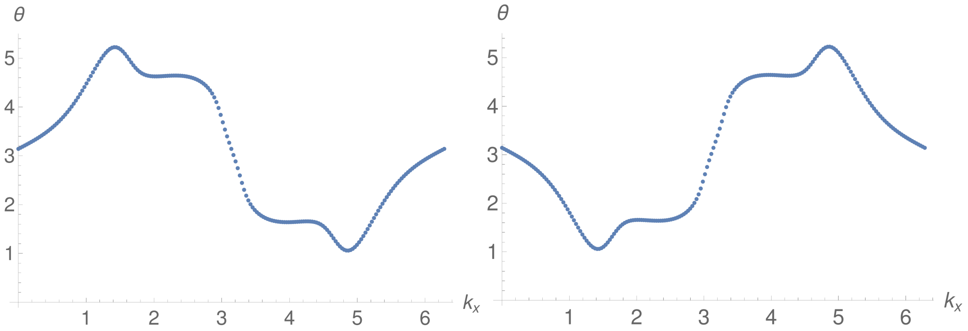

(e) Wilson loop spectrum in lower (left) and upper (right) $\tilde{\mathring{\Psi}}$ bands within the lower $\mathring{\Psi}$ band. Both bands have vanishing Chern number.

Figure II.31.: $\mathring{\Psi}$ band structures and Wilson loop spectra for $H_2^{(4)}(\mathbf{k}, t = 0)$, calculated using $\mathring{\psi} = (r_4 + r_4^{\dagger})(1 + \cos k_x + \cos k_y) + t_{\mathbf{k}}\beta$.

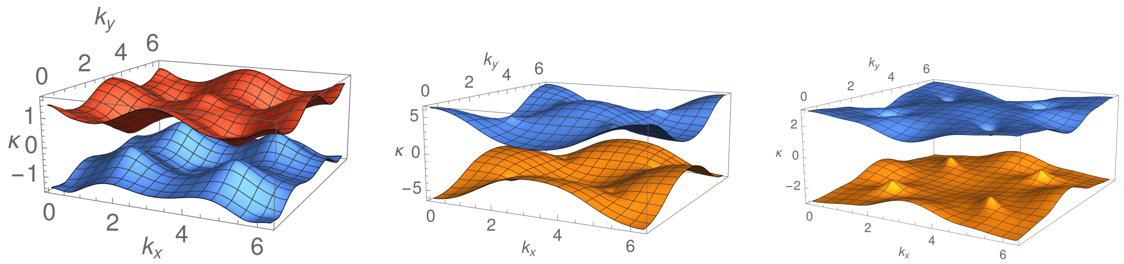

(a) $\mathring{\Psi}$ band structure of the model $H_2^{(4)}(\mathbf{k}, t=0)$. Split to two two-band spaces using $\mathring{\psi}$ corresponding to Wyckoff position $1a$.

(b) $\tilde{\mathring{\Psi}}$ band structure within the lower two bands using a random $\mathring{\psi}$.

(c) $\tilde{\mathring{\Psi}}$ band structure within the upper two bands using the same random $\mathring{\psi}$.

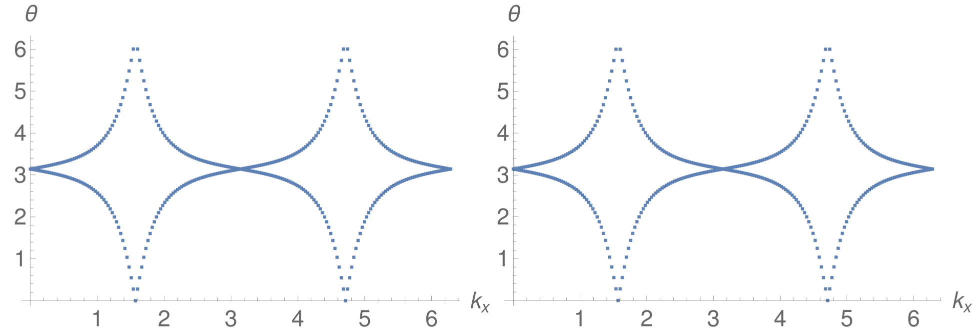

(d) Wilson loop spectrum in lower (left) and upper (right) $\mathring{\Psi}$ bands. We can see a double winding that cannot be trivialised within the symmetry constraints.

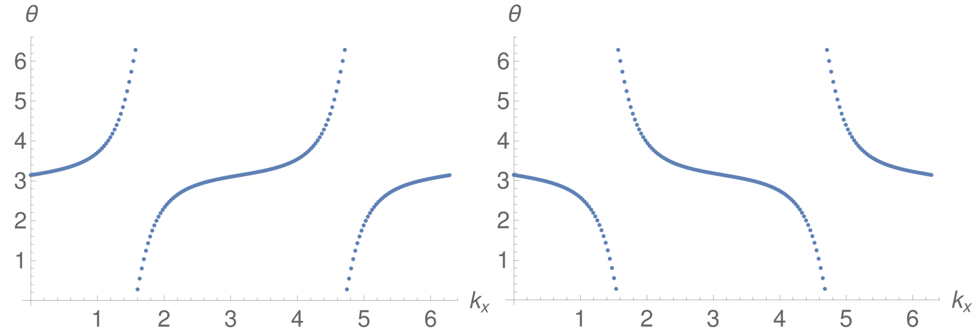

(e) Wilson loop spectrum in lower (left) and upper (right) $\tilde{\mathring{\Psi}}$ bands within the lower $\mathring{\Psi}$ band. The bands both have non-zero first Chern number $C = \pm 2$.

Figure II.32.: $\mathring{\Psi}$ band structures and Wilson loop spectra for $H_2^{(4)}(\mathbf{k}, t=0)$ using $\mathring{\psi}_{\mathbf{k}} = (r_4 + r_4^\dagger) + t_{\mathbf{k}} \sigma_0 \otimes \sigma_1 \otimes \sigma_0$.

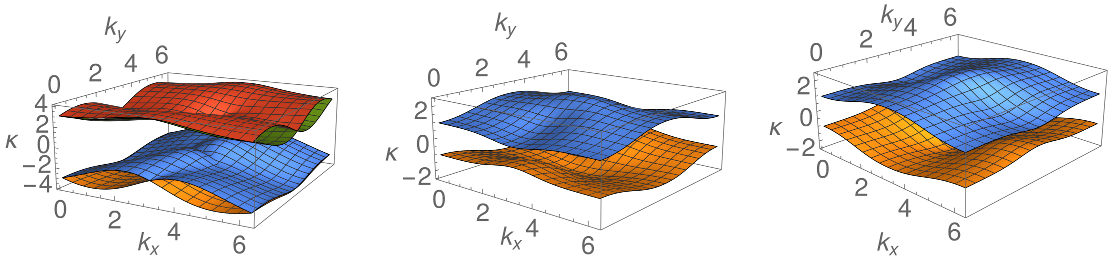

(a) $\mathring{\Psi}$ band structure of the model $H_3^{(2)}(\mathbf{k}, t = 0.2)$. Split to two 2-band-spaces using $\mathring{\psi}_{\mathbf{k}}$ corresponding to Wyckoff position $2c$.

(b) $\tilde{\mathring{\Psi}}$ band structure within the lower two bands using a random $\mathring{\psi}$.

(c) $\tilde{\mathring{\Psi}}$ band structure within the lower two bands using the same random $\mathring{\psi}$.

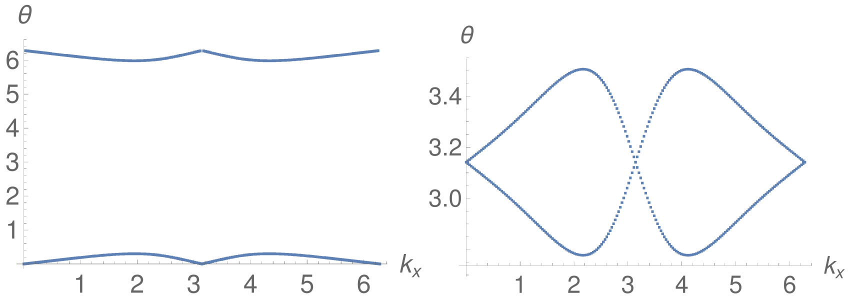

(d) Wilson loop spectrum in lower (left) and upper (right) $\mathring{\Psi}$ bands. We can see no winding.

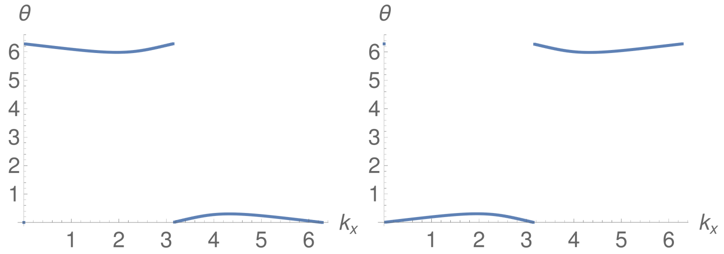

(e) Wilson loop spectrum in lower (left) and upper (right) $\tilde{\mathring{\Psi}}$ bands within the lower $\mathring{\Psi}$ band. These bands have zero first Chern number.

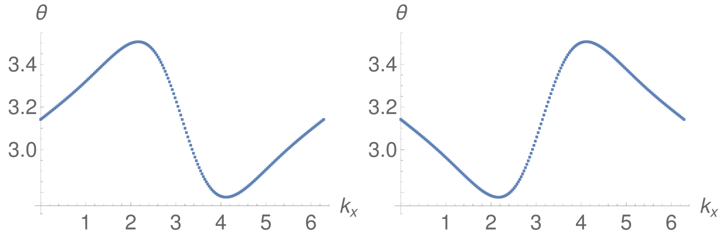

(f) Wilson loop spectrum in the lower (left) and upper (right) bands within the upper $\mathring{\Psi}$ band. These bands have zero first Chern number.

Figure II.33.: $\mathring{\Psi}$ band structures and Wilson loop spectra for $H_3^{(2)}(\mathbf{k}, t = 0.2)$ using a $\mathring{\psi}_{\mathbf{k}}$ that is compatible with Wyckoff position $2c$.

The constant matrix used as $\mathring{\psi}_{\mathbf{k}}$ for the first split is the matrix in eq. II.260, appendix II.E. The $\mathring{\Psi}$ band structure is shown in figure II.33a. The constant matrix used for the second split can be found in equation II.261, appendix II.E. The $\mathring{\Psi}$ band structures within the lower and upper $\mathring{\Psi}$ (first split) bands are shown in figures II.33b and II.33c. This gauge corresponds to the sewing matrices

$$D_{C_4} = \begin{pmatrix} & & * & \\ & & & * \\ * & & & \\ & * & & \end{pmatrix}, \qquad D_{\mathcal{T}} = \begin{pmatrix} & * & & \\ * & & & \\ & & & * \\ & & * & \end{pmatrix}. \tag{II.160}$$

The Wilson loop spectra both in the two-band subspaces after the first split and in the individual bands after the second split are depicted in Figures II.33d, and Figures II.33e and II.33f, respectively. The triviality of the Wilson loops together with the permutation-likeness of the sewing matrices proves that these filled bands indeed form a band representation.

Projected Symmetry Indicators to evaluate the Invariants The invariants by Kooi et al.[130] (cf. section II.8.2) can be evaluated using bands that are calculated using a PSO. To do so, we choose a $\mathring{\psi}_{\mathbf{k}}$ that produces a gauge in which the C_4 sewing matrix is block-diagonal and the TRS sewing matrix is block-off-diagonal. Such a $\mathring{\psi}_{\mathbf{k}}$ has to fulfil

$$\begin{aligned} \mathring{\psi}_{\mathbf{k}} &= \mathring{\psi}_{\mathbf{k}}^{\dagger}, \\ r_4 \mathring{\psi}_{\mathbf{k}} r_4^{\dagger} &= \mathring{\psi}_{R_4 \mathbf{k}}, \\ \mathcal{T} \mathring{\psi}_{\mathbf{k}} \mathcal{T}^{-1} &= -\mathring{\psi}_{-\mathbf{k}}. \end{aligned} \tag{II.161}$$

We can simply choose

$$\mathring{\psi}_{\mathbf{k}} = \begin{pmatrix} 1 & \\ & -1 \end{pmatrix} \tag{II.162}$$

when looking at the doubled models by Benalcazar et al.[133]. The resulting $\mathring{\Psi}$ band structures and Wilson loop spectra in the lower $\mathring{\Psi}$ bands are depicted in Fig. II.34 for $H_2^{(4)}(\mathbf{k}, t = 0.2)$ (Wyckoff position $1b$), $H_3^{(2)}(\mathbf{k}, t = 0.2)$ (Wyckoff position $2c$) and $H_3^{(2)}(\mathbf{k}, t = 1.2)$ (Wyckoff position $1a$). The calculation of the invariants and the needed quantities are listed in table II.3. They are straightforwardly evaluated, and lead to the correct number of electrons at each Wyckoff position, given by the numbers ν_{1a}^{I}, ν_{1b}^{I} and ν_{2c}^{I}, calculated using equations II.108.

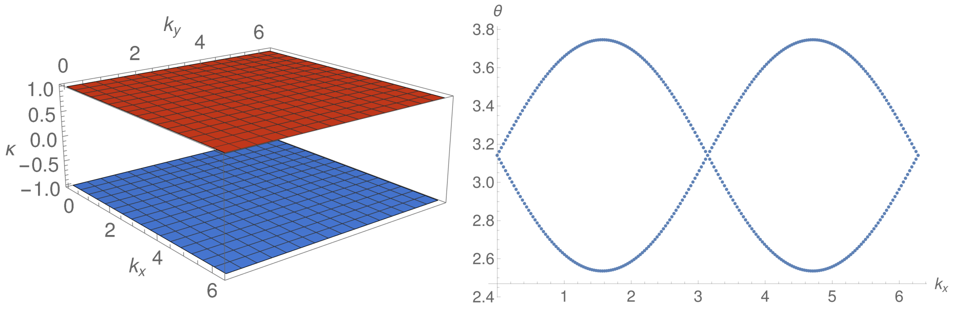

(a) $\mathring{\Psi}$ band structure (left) and Wilson loop spectrum in lower $\mathring{\Psi}$ bands (right) for $H_2^{(4)}(\mathbf{k}, t = 0.2)$. This Hamiltonian corresponds to Wyckoff position $1b$.

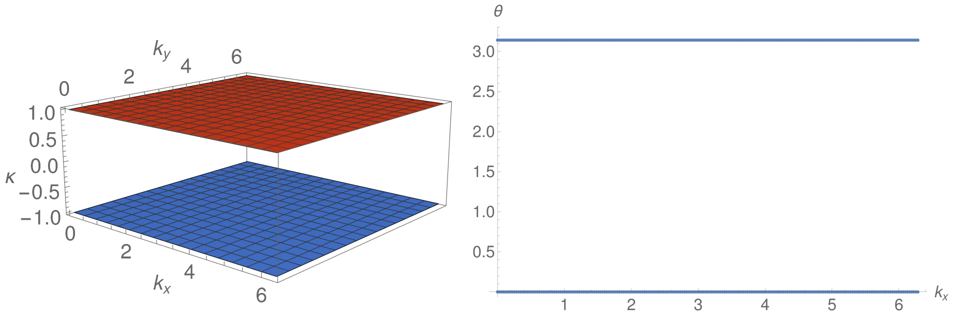

(b) $\mathring{\Psi}$ band structure (left) and Wilson loop spectrum in lower $\mathring{\Psi}$ bands (right) for $H_3^{(2)}(\mathbf{k}, t = 0.2)$. The occupied bands correspond to Wyckoff position $2c$.

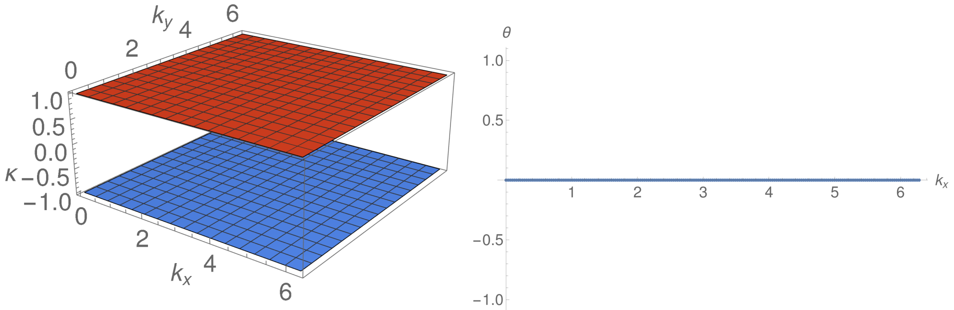

(c) $\mathring{\Psi}$ band structure (left) and Wilson loop spectrum in lower $\mathring{\Psi}$ bands (right) for $H_3^{(2)}(\mathbf{k}, t = 1.2)$. The occupied bands correspond to Wyckoff position $1a$.

Figure II.34.: On the left, $\mathring{\Psi}$ band structures to get a gauge that allows for the calculation of the invariants by Kooi et al.[130]. On the right, Wilson loop spectra in the lower bands of this gauge to read off the Chern number.

	$H_2^{(4)}(\mathbf{k}, t = 0.2)$	$H_3^{(2)}(\mathbf{k}, t = 0.2)$	$H_3^{(2)}(\mathbf{k}, t = 1.2)$
$\Gamma^I_{i\pi/4}$	1	1	1
$\Gamma^I_{-i\pi/4}$	0	0	0
$\Gamma^I_{3i\pi/4}$	0	0	0
$\Gamma^I_{-3i\pi/4}$	1	1	1
$M^I_{i\pi/4}$	1	0	1
$M^I_{-i\pi/4}$	0	1	0
$M^I_{3i\pi/4}$	0	1	0
$M^I_{-3i\pi/4}$	1	0	1
X^I_{-i}	2	1	0
X^I_{i}	0	1	2
C^I	0	0	0
ν^I_{1a}	0	0	-2
ν^I_{1b}	-2	0	0
ν^I_{2c}	0	-1	0

Table II.3.: Evaluation of the invariants by Kooi et al.[130] (cf. section II.8.2) for the primitive generators.

II.9.3.2. Case with C_6 and C_3 Symmetry

Next, we will study some cases with C_6 symmetry. The main focus herein will lie on the model $H_2^{(6)}(\mathbf{k}, t = 0.1)$. This section mainly deals with what we refer to as the problem of three-cycles. To understand the problem of three-cycles, look at the non-spin-degenerate model in Fig. II.35. It shows a lattice with C_6 symmetry, in which the electrons are situated on the edges of the unit cell as depicted on the right. There are three electrons per unit cell. One would like to split this three-band model with $\left\{\left|u^1_{\mathbf{k}}\right\rangle, \left|u^2_{\mathbf{k}}\right\rangle, \left|u^3_{\mathbf{k}}\right\rangle\right\}$ into three bands, each of which should have trivial Berry phase winding (Wilson loop spectrum without winding). Furthermore, the symmetries have to act as permutations on the bands. The obvious permutation in this situation is a permutation corresponding to cycling through the three electrons. In order to split them, one has to break C_3 symmetry, C_2 symmetry survives. The standard procedure to break, for example TRS or r_4 symmetry, is to have for a symmetry (s, S)

$$s\mathring{\psi}_{\mathbf{k}}s^{-1} = -\mathring{\psi}_{S\mathbf{k}}. \tag{II.163}$$

This procedure ensures that the symmetry acts as a permutation and the sewing matrix becomes

$$D^{mn}_{\mathbf{k}} = \langle u^m_{S\mathbf{k}}|s|u^n_{\mathbf{k}}\rangle \qquad \text{with } D_{\mathbf{k}} = \begin{pmatrix} 0 & * \\ * & 0 \end{pmatrix}. \tag{II.164}$$

The corresponding procedure for the case in Fig. II.35 is that the symmetry acts as a three-cycle. This translates into a sewing matrix of form

$$B^{mn}_{\mathbf{k}} = \left\langle u^m_{R_3\mathbf{k}}\middle|r_3\middle|u^n_{\mathbf{k}}\right\rangle \qquad \text{with } B_{\mathbf{k}} = \begin{pmatrix} 0 & * & 0 \\ 0 & 0 & * \\ * & 0 & 0 \end{pmatrix}. \tag{II.165}$$

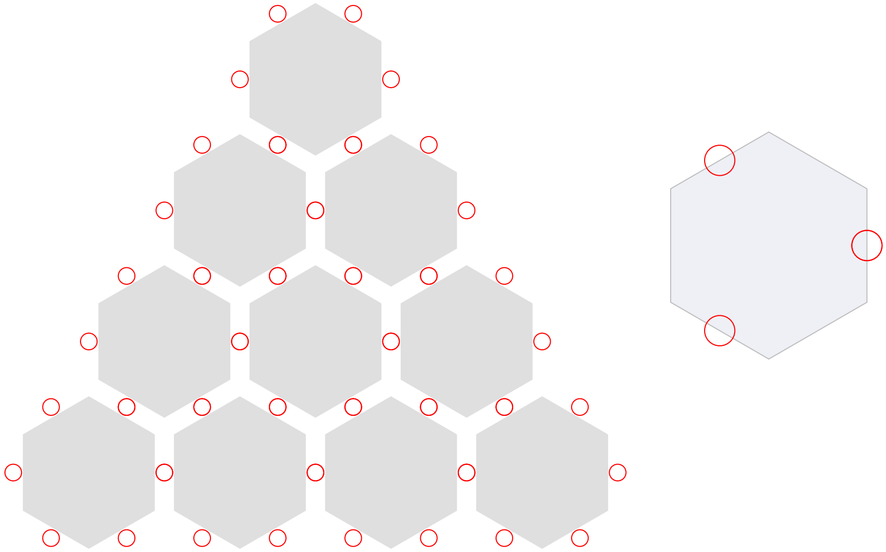

Figure II.35.: Lattice of a C_6-symmetric model with two (doubled model) or one (original model) electron situated at the $3c$ Wyckoff position.

This can be induced using a non-Hermitian $\mathring{\psi}$ with the property

$$r_3 \mathring{\psi}_{\mathbf{k}} r_3^\dagger = e^{\frac{i2\pi}{3}} \mathring{\psi}_{R_3\mathbf{k}} \tag{II.166}$$

that would have to exhibit a star gap. From the proof in section II.9.2.4 follows that the sewing matrices meet our conditions.

For the three-cycle solution to work when TRS is present, too, we need to use the $\mathcal{T}$ defined with the transpose. If we use the version with complex conjugation, we do not obtain a viable result. The reason for this is that we would require a $\mathring{\psi}$ fulfilling the following two conditions:

$$\begin{aligned} r_6 \mathring{\psi}_{\mathbf{k}} r_6^\dagger &= e^{\frac{4\pi i}{3}} \mathring{\psi}_{R_6\mathbf{k}} \\ \mathcal{T} \mathring{\psi}_{\mathbf{k}} \mathcal{T}^{-1} &= \mathring{\psi}_{-\mathbf{k}} \end{aligned} \tag{II.167}$$

Furthermore, we know that $[\mathcal{T}, r_6] = 0 \implies [\mathcal{T}^{-1}, r_6^\dagger] = 0$. Together this yields

$$\left.\begin{array}{ll} r_6 \mathcal{T} \mathring{\psi}_{\mathbf{k}} \mathcal{T}^{-1} r_6^\dagger & = \mathcal{T} r_6 \mathring{\psi}_{\mathbf{k}} r_6^\dagger \mathcal{T}^{-1} \\ = r_6 \mathring{\psi}_{-\mathbf{k}} r_6^\dagger & = \mathcal{T} e^{\frac{4\pi i}{3}} \mathring{\psi}_{R_6\mathbf{k}} \mathcal{T}^{-1} \\ = e^{\frac{4\pi i}{3}} \mathring{\psi}_{R_6^4\mathbf{k}} & = e^{\frac{-4\pi i}{3}} \mathring{\psi}_{R_6^4\mathbf{k}} \end{array}\right\} \implies \mathring{\psi}_{\mathbf{k}} = 0. \tag{II.168}$$

This problem does not appear if we instead define $\mathcal{T}$ using the transpose and require

$$\tau \mathring{\psi}_{\mathbf{k}}^T \tau^\dagger = \mathring{\psi}_{-\mathbf{k}}, \tag{II.169}$$

because then

$$\begin{array}{ll} r_6 \tau \alpha_{\mathbf{k}}^T \tau^\dagger r_6^\dagger & = \tau \left(r_6 \alpha_{\mathbf{k}} r_6^\dagger \right)^T \tau^\dagger \\ = r_6 \alpha_{-\mathbf{k}} r_6^\dagger & = \tau \left(e^{\frac{4\pi i}{3}} \alpha_{R_6\mathbf{k}} \right)^T \tau^\dagger \\ = e^{\frac{4\pi i}{3}} \alpha_{R_6^4\mathbf{k}} & = e^{\frac{4\pi i}{3}} \alpha_{R_6^4\mathbf{k}}. \end{array} \tag{II.170}$$

Thus this allows us to construct nice gauges on which the symmetries act as permutations. In the following, a few examples for such gauges are presented. To begin with we look at $H_2^{(6)}(\mathbf{k}, t = 0.1)$ and construct a gauge corresponding to a six-cycle in one step. The $\mathring{\psi}$ for such a gauge must carry the symmetries

$$\begin{aligned} r_6 \mathring{\psi}_{\mathbf{k}} r_6^\dagger &= e^{\frac{i\pi}{3}} \mathring{\psi}_{R_6 \mathbf{k}} \\ \tau \mathring{\psi}_{\mathbf{k}}^T \tau^\dagger &= -\mathring{\psi}_{-\mathbf{k}}. \end{aligned} \tag{II.171}$$

The TRS sewing matrix in this case must in addition be off-diagonal, because when cycling through the six electrons we cycle both through up- and down-spin electrons. The sewing matrices corresponding to this behaviour are

$$\begin{aligned} D_{r_6} &= \begin{pmatrix} & * & & & & \\ & & * & & & \\ & & & * & & \\ & & & & * & \\ & & & & & * \\ * & & & & & \end{pmatrix}, & D_{r_3} &= \begin{pmatrix} & & * & & & \\ & & & * & & \\ & & & & * & \\ & & & & & * \\ * & & & & & \\ & * & & & & \end{pmatrix}, \\ D_{r_2} &= \begin{pmatrix} & & & * & & \\ & & & & * & \\ & & & & & * \\ * & & & & & \\ & * & & & & \\ & & * & & & \end{pmatrix} \text{ and } & D_{\mathcal{T}} &= \begin{pmatrix} & & & * & & \\ & & & & * & \\ & & & & & * \\ * & & & & & \\ & * & & & & \\ & & * & & & \end{pmatrix}. \end{aligned} \tag{II.172}$$

The $\mathring{\psi}_{\mathbf{k}}$ we use in this case is a constant $\mathring{\psi}_{\mathbf{k}} = \mathring{\psi}$ constructed by symmetrising a random matrix $\mathring{\psi}_{\mathrm{r}}$. This symmetrisation procedure contains a C_6 and a TRS step. The C_6 step is given by

$$\mathring{\psi}_{C_6} = \mathring{\psi}_{\mathrm{r}} + e^{\frac{i\pi}{3}} r_6^\dagger \mathring{\psi}_{\mathrm{r}} r_6 + e^{\frac{2i\pi}{3}} r_6^{2\dagger} \mathring{\psi}_{\mathrm{r}} r_6^2 + e^{\frac{3i\pi}{3}} r_6^{3\dagger} \mathring{\psi}_{\mathrm{r}} r_6^3 + e^{\frac{4i\pi}{3}} r_6^{4\dagger} \mathring{\psi}_{\mathrm{r}} r_6^4 + e^{\frac{5i\pi}{3}} r_6^{5\dagger} \mathring{\psi}_{\mathrm{r}} r_6^5 \tag{II.173}$$

and the TRS step by

$$\mathring{\psi}_{\mathcal{T}} = \mathring{\psi}_{C_6} - \tau^\dagger \mathring{\psi}_{C_6}^T \tau. \tag{II.174}$$

By trimming the starting matrix $\mathring{\psi}_{\mathrm{r}}$, a $\mathring{\Psi}$ band structure with 6-star gap is found. The $\mathring{\psi}_{\mathcal{T}}$ that was used is given in equation II.262, appendix II.E. The band structure is depicted in Fig. II.36a (ring further outside). The inner ring with absolute value 1 consists of the eigenvalues of the unitary projection of $\mathring{\Psi}_{\mathbf{k}}$.

Fig. II.36b explains the meaning of the colors in the band structure plots. The colors represent a color-coded $\mathbf{k}$-space position. The three-dimensional impression in the figure of the $\mathring{\Psi}$ band structure results from the order in which different points are plotted and has no physical meaning. Without the colors, the band structure has sixfold rotational symmetry.

The Wilson loop spectra corresponding to the six single $\mathring{\Psi}$ bands are depicted in figures II.36c. All the Wilson loops are trivial, which shows that the occupied bands indeed corresponds to a BR.

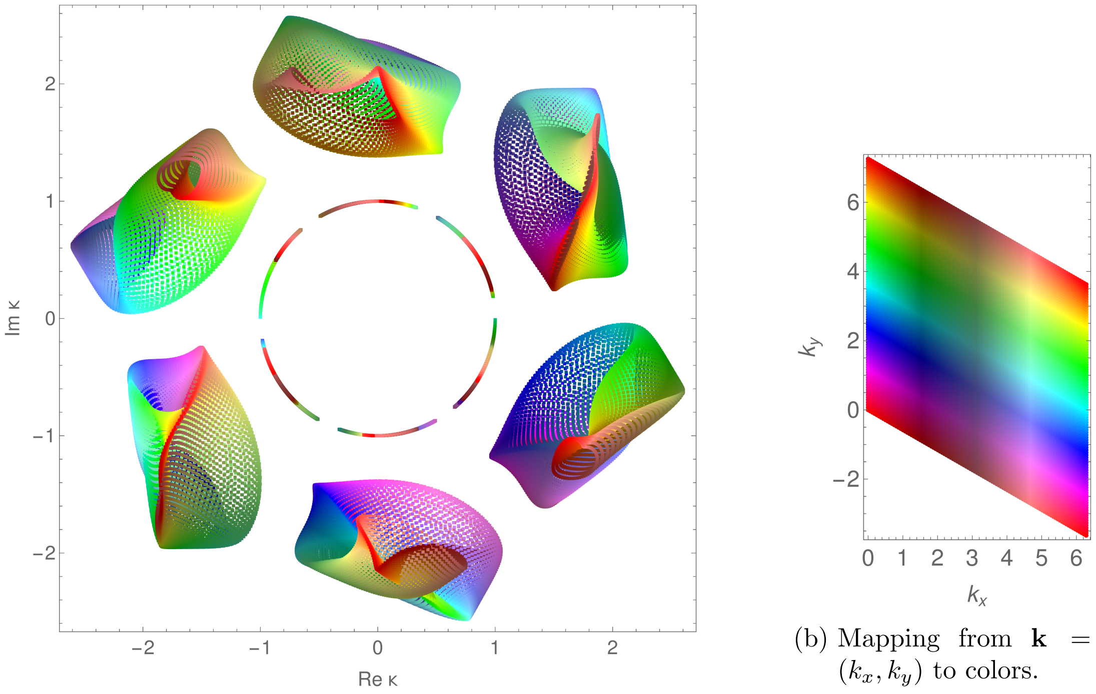

(a) Band structure of a $\mathring{\Psi}$ to get a 6-cycle gauge (outer). The ring with absolute value one consists of the eigenvalues of the unitary projection of the $\mathring{\Psi}$. The eigenvectors corresponding to this unitary projection form the new gauge. There is a 6-star gap.

(b) Mapping from $\mathbf{k} = (k_x, k_y)$ to colors.

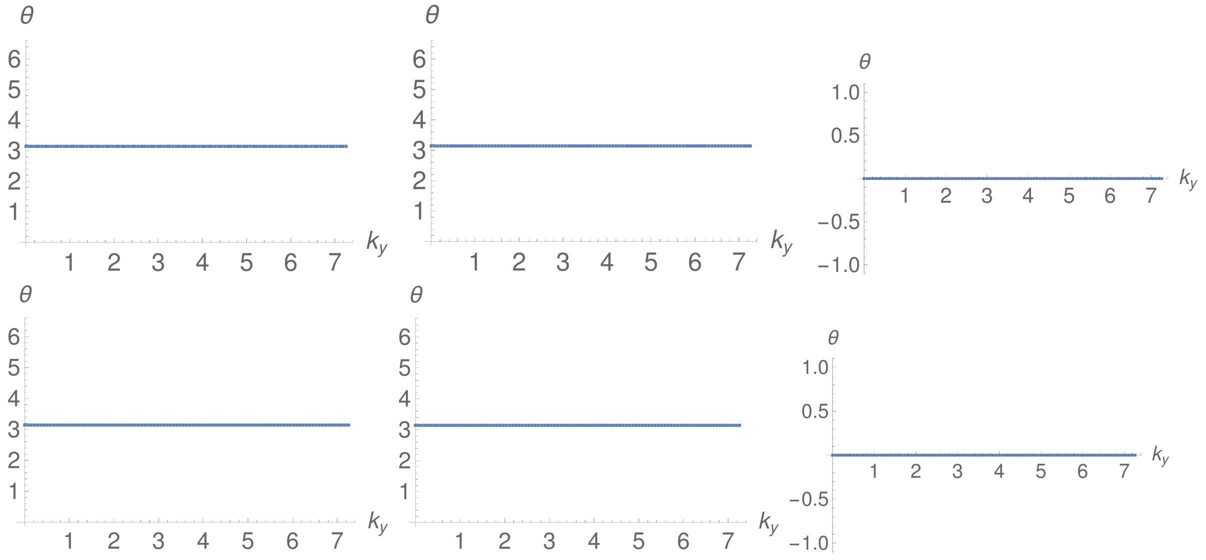

(c) Wilson loop spectra in the C_6-symmetric 6-cycle gauge.

Figure II.36.: $\mathring{\Psi}$ band structure and Wilson loop spectra for $H_2^{(6)}(t = 0.1)$ to get a 6-cycle gauge.

Next, we show two ways to construct a gauge with three-cycle behaviour in both the r_6 and the r_3 sewing matrices. This can either be done in one step or in two steps. With the one step procedure, we obtain the sewing matrices

$$\begin{aligned} D_{r_6} &= \begin{pmatrix} & & & & * & \\ & & & & & * \\ * & & & & & \\ & * & & & & \\ & & * & & & \\ & & & * & & \end{pmatrix}, & D_{r_3} &= \begin{pmatrix} , & & * & & & \\ & & & * & & \\ & & & & * & \\ & & & & & * \\ * & & & & & \\ & * & & & & \end{pmatrix}, \\ D_{r_2} &= \begin{pmatrix} * & & & & & \\ & * & & & & \\ & & * & & & \\ & & & * & & \\ & & & & * & \\ & & & & & * \end{pmatrix} \text{ and } & D_{\mathcal{T}} &= \begin{pmatrix} & & & * & & \\ & & & & * & \\ & & & & & * \\ * & & & & & \\ & * & & & & \\ & & * & & & \end{pmatrix}. \end{aligned} \tag{II.175}$$

The symmetrisations used to get these sewing matrices are

$$\mathring{\psi}_{C_6} = \mathring{\psi}_{\mathrm{r}} + e^{\frac{4\pi i}{3}} r_6^{\dagger} \mathring{\psi}_{\mathrm{r}} r_6 + e^{\frac{2i\pi}{3}} r_6^{2\dagger} \mathring{\psi}_{\mathrm{r}} r_6^2 + r_6^{3\dagger} \mathring{\psi}_{\mathrm{r}} r_6^3 + e^{\frac{4i\pi}{3}} r_6^{4\dagger} \mathring{\psi}_{\mathrm{r}} r_6^4 + e^{\frac{2i\pi}{3}} r_6^{5\dagger} \mathring{\psi}_{\mathrm{r}} r_6^5 \tag{II.176}$$

and

$$\mathring{\psi}_{\mathcal{T}} = \mathring{\psi}_{C_6} - \tau^{\dagger} \mathring{\psi}_{C_6}^{T} \tau. \tag{II.177}$$

It follows that

$$\tau \mathring{\psi}_{\mathcal{T}}^{T} \tau^{\dagger} = -\mathring{\psi}_{\mathcal{T}} \qquad \text{and} \qquad r_6 \mathring{\psi}_{\mathcal{T}} r_6^{\dagger} = e^{\frac{4\pi i}{3}} \mathring{\psi}_{\mathcal{T}}. \tag{II.178}$$

The $\mathring{\psi}_{\mathcal{T}}$ we used is given in equation II.263, appendix II.E. The $\mathring{\Psi}$ band structure as well as the eigenvalues of the unitary projection of $\mathring{\Psi}$ are depicted in Fig. II.37a. The mapping between **k** and the colors is again shown in Fig. II.37b. Fig. II.37c shows the Wilson loop spectra of the single bands. Their triviality together with the fact that the symmetries act as permutations on the bands proofs that the occupied bands form a BR.

If we construct the three-cycle gauge in two steps, we get the sewing matrices

$$\begin{aligned} D_{r_6} &= \begin{pmatrix} & & * & & & \\ * & & & & & \\ & * & & & & \\ & & & & & * \\ & & & * & & \\ & & & & * & \end{pmatrix}, & D_{r_3} &= \begin{pmatrix} & * & & & & \\ & & * & & & \\ * & & & & & \\ & & & & * & \\ & & & & & * \\ & & & * & & \end{pmatrix}, \\ D_{r_2} &= \begin{pmatrix} * & & & & & \\ & * & & & & \\ & & * & & & \\ & & & * & & \\ & & & & * & \\ & & & & & * \end{pmatrix} \text{ and } & D_{\mathcal{T}} &= \begin{pmatrix} & & & * & & \\ & & & & * & \\ & & & & & * \\ * & & & & & \\ & * & & & & \\ & & * & & & \end{pmatrix}. \end{aligned} \tag{II.179}$$

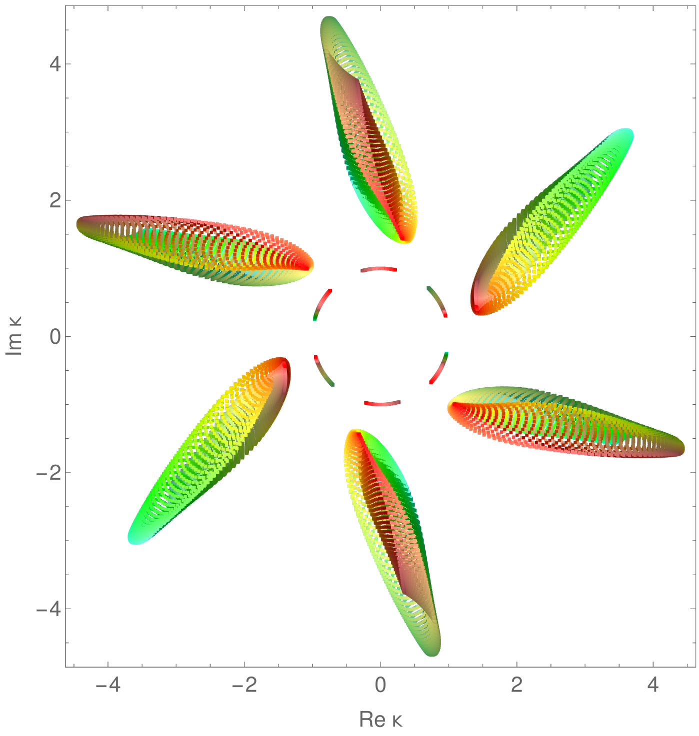

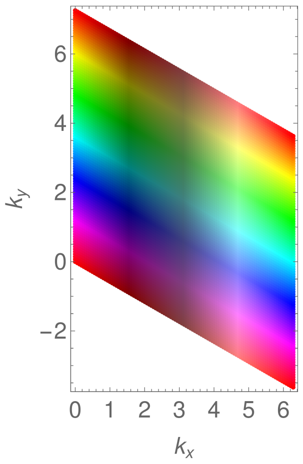

(b) Mapping from $\mathbf{k} = (k_x, k_y)$ to colors.

(a) Band structure of a $\mathring{\Psi}$ to get a three-cycle gauge (outer). The ring with absolute value 1 consists of the eigenvalues of the unitary projection of the $\mathring{\Psi}$. The eigenvectors corresponding to this unitary projection form the new gauge. There is a 6-star gap.

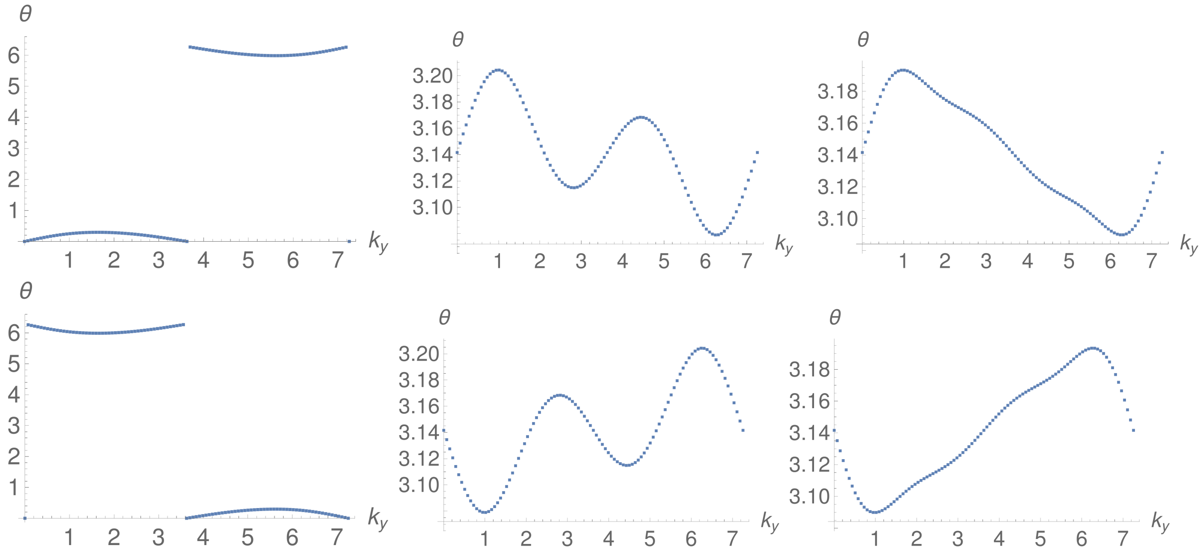

(c) Wilson loop spectra in the C_6-symmetric a three-cycle gauge, constructed in one go.

Figure II.37.: $\mathring{\Psi}$ band structures and Wilson loop spectra for $H_2^{(6)}(t = 0.1)$ to get three-cycles in one step.

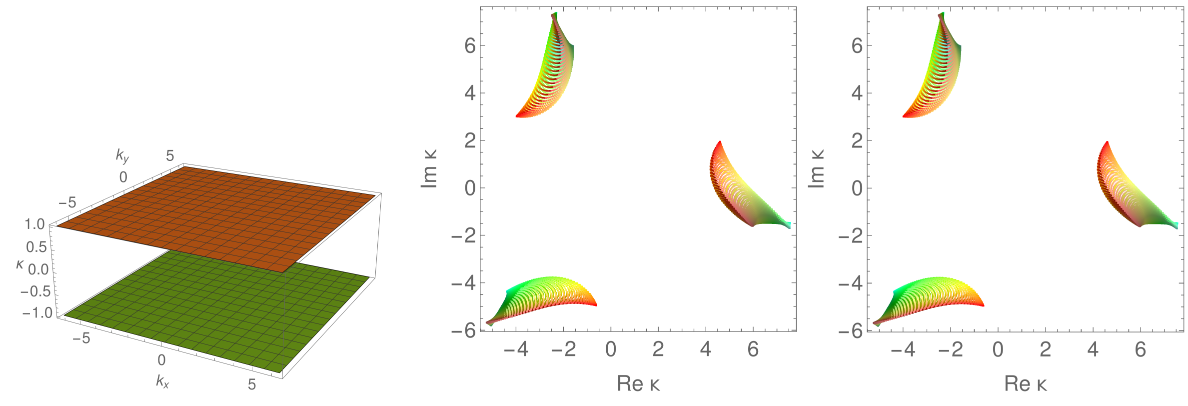

(a) $\mathring{\Psi}$ band structure to split the occupied subspace into two subspaces mapped onto each other by $\mathcal{T}$.

(b) $\mathring{\Psi}$ band structures to split the upper and the lower $\mathring{\Psi}$ bands into a gauge on which r_3 acts as a three-cycle. The mapping from $\mathbf{k}$ to colors is given in figure II.37b.

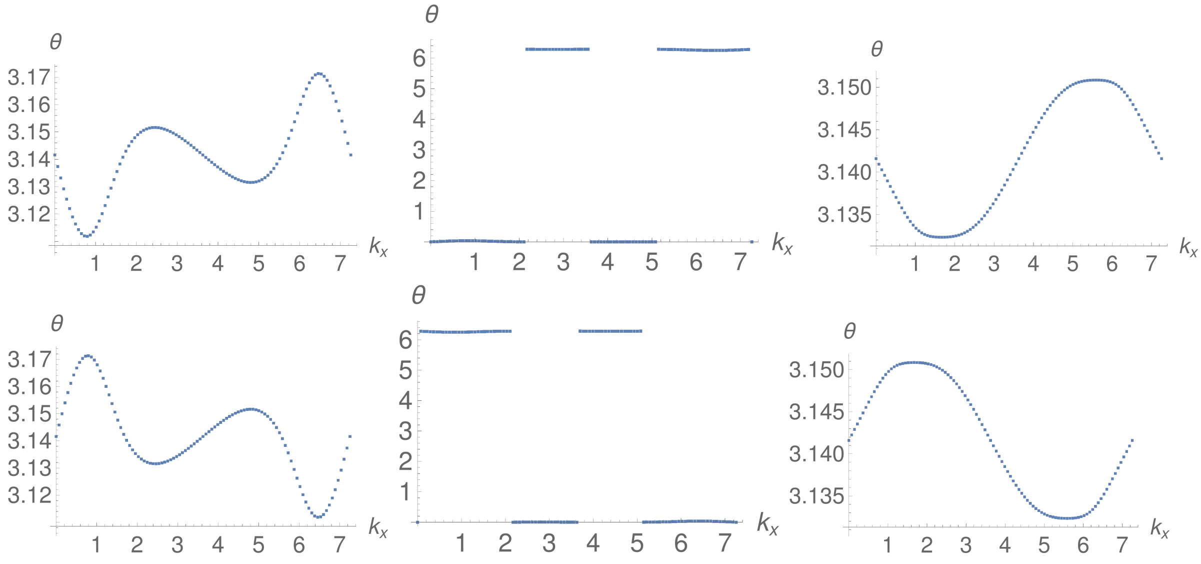

(c) Wilson loop spectra in the C_6-symmetric three-cycle gauge, constructed in two steps.

Figure II.38.: $\mathring{\Psi}$ band structures and Wilson loop spectra for $H_2^{(6)}(t = 0.1)$ to get three-cycles in two steps.

To construct this gauge, we first split the bands into “spin-up” and “spin-down“ bands, using a $\mathring{\psi}_{\mathbf{k}}$ with

$$\begin{aligned} \mathring{\psi}_{\mathbf{k}} &= \mathring{\psi}_{\mathbf{k}}^{\dagger}, \\ r_6 \mathring{\psi}_{\mathbf{k}} r_6^{\dagger} &= \mathring{\psi}_{R_6 \mathbf{k}}, \\ \tau \mathring{\psi}_{\mathbf{k}}^{T} \tau^{\dagger} &= -\mathring{\psi}_{-\mathbf{k}}. \end{aligned} \tag{II.180}$$

The operator we used for the first step is

$$\mathring{\psi}_{\mathbf{k}} = \begin{pmatrix} 1 & \\ & -1 \end{pmatrix}. \tag{II.181}$$

The $\mathring{\Psi}$ band structure for this first split is depicted in Fig. II.38a. Afterwards, the two three-band subspaces are treated separately and split to obtain three-cycles. For this we use a $\mathring{\psi}_{\mathbf{k}}$ constructed with respect to C_6 the same way as in equation II.176, but the time-reversal symmetrisation is chosen as

$$\mathring{\psi}_{\mathcal{T}} = \mathring{\psi}_{C_6} + \tau^{\dagger} \mathring{\psi}_{C_6}^{T} \tau, \tag{II.182}$$

such that the TRS sewing matrix is then diagonal within the block.

The $\mathring{\Psi}$ band structures of these two second splits are depicted in Fig. II.38b. Below, in Fig. II.38c, we show the corresponding Wilson loop spectra in the single bands. They are, as expected, trivial. The matrix used to split the bands into three-cycle single bands is given in appendix II.E, eq. II.264. It is often advantageous to perform such splits in several steps, because then the requirements on the operators used for splitting are less strict. As we have seen in the example, if we want to split the bands in one step, we need a 6-star gap; if we do it in two steps, we only need a 3-star gap. It is easier to find a matrix that has a open 3-star gap than a 6-star gap.

If the $\mathring{\psi}$ and the ground state of the Hamiltonian do not fit together, there are two possiblities: either the Wilson loop spectra show a winding behaviour, which means that the single bands have nonzero first Chern number; or it is not possible to construct a gauge that is symmetric and has smooth projectors, which means that all smooth functions $\mathring{\Psi}_{\mathbf{k}} : \mathbf{k} \to \mathring{\Psi}_{\mathbf{k}}$ that are smooth are gapless. Looking at the Hamiltonian $H_1^{(6)}(\mathbf{k})$, a Hamiltonian with eight occupied band corresponding to the Wyckoff position $4b$, and doing first a split breaking $\mathcal{T}$ to get “spin up” and “spin down” bands, we can split it further to get a three-cycle. The $\mathring{\Psi}$ band structure for this second split is shown in Fig. II.39; it is gapless, because the BR of the occupied bands does not fit to three-cycles.

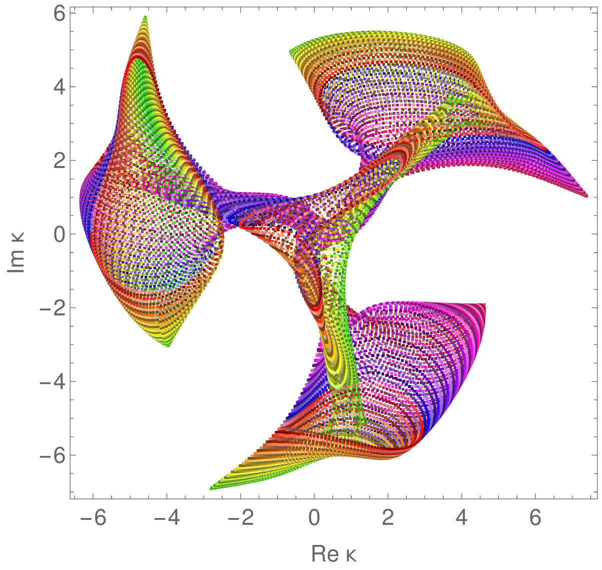

Figure II.39.: $\mathring{\Psi}$ band structures and Wilson loop spectra for $H_1^{(6)}(t = 0.0)$ to get three-cycles in one step. It is gapless because three-cycles are incompatible with the BR of the occupied bands of this Hamiltonian.

II.9.4. Construction of SOs based on Wyckoff Positions

In the previous section, we have described an unsystematic method to construct operators $\mathring{\psi}_{\mathbf{k}}$ to distinguish between different band representations corresponding to different Wyckoff positions. A next step might be to think about how to do this more systematically by linking the real space creation and annihilation operators to the **k**-space operators one might want to use to do the splits. The basic idea is to define an operator

$$\mathring{\psi}_{\mathbf{r}} = \sum_{\mathbf{R}} \hat{\mathring{\psi}}_{\mathbf{R}}, \tag{II.183}$$

where $\hat{\mathring{\psi}}_{\mathbf{R}}$ is a local operator. This operator is defined such that it assigns different values to different Wyckoff positions. For example, if we have a creation operator $d^{\dagger}_{\mathbf{R}}$ at a $1b$ Wyckoff position, then we would define

$$\hat{\mathring{\psi}}_{\mathbf{R}} = d_{1b,\mathbf{R}} d^{\dagger}_{1b,\mathbf{R}}. \tag{II.184}$$

This operator assigns a positive value to states situated at $1b$, and therefore we expect to be able to use it to split bands situated at $1b$ from other bands.

To make this concrete, we study the C_4 symmetric models by Benalcazar et al.[133]. They are defined on a quadratic lattice with four sites per unit cell, depicted in Fig. II.40. The version of the models studied here are the spin-degenerate ones, with one spin-up and one spin-down electron per site (black in the figure). The eight sites are then given by 1 ↑, 1 ↓, ..., 4 ↓. For each site i, the creation operator is $c^{\dagger}_{i\mathbf{R}}$, e.g. $c^{\dagger}_{1\uparrow(0,0)}$. We then define creation and annihilation operators centred at the Wyckoff position, which also correspond to specific C_4 eigenvalues. The first such operator is

$$d^{\dagger}_{1a\uparrow,\frac{3\pi}{4},\mathbf{R}} = -c^{\dagger}_{1\uparrow\mathbf{R}} + c^{\dagger}_{2\uparrow\mathbf{R}} - c^{\dagger}_{3\uparrow\mathbf{R}} + c^{\dagger}_{4\uparrow\mathbf{R}} \tag{II.185}$$

This operator has the property

$$\begin{aligned} r_4 d^\dagger_{1a\uparrow,\frac{3\pi}{4},\mathbf{R}} |0\rangle &= r_4 \left(-c^\dagger_{1\uparrow\mathbf{R}} + c^\dagger_{2\uparrow\mathbf{R}} - c^\dagger_{3\uparrow\mathbf{R}} + c^\dagger_{4\uparrow\mathbf{R}}\right)|0\rangle \\ &= e^{-\frac{i\pi}{4}} \left(-c^\dagger_{2\uparrow R_4\mathbf{R}} + c^\dagger_{3\uparrow R_4\mathbf{R}} - c^\dagger_{4\uparrow R_4\mathbf{R}} + c^\dagger_{1\uparrow R_4\mathbf{R}}\right)|0\rangle \\ &= e^{\frac{3i\pi}{4}} \left(-c^\dagger_{1\uparrow R_4\mathbf{R}} + c^\dagger_{2\uparrow R_4\mathbf{R}} - c^\dagger_{3\uparrow R_4\mathbf{R}} + c^\dagger_{4\uparrow R_4\mathbf{R}}\right)|0\rangle = e^{\frac{3i\pi}{4}} d^\dagger_{1a\uparrow,\frac{3\pi}{4},R_4\mathbf{R}} |0\rangle . \end{aligned} \tag{II.186}$$

This then implies that

$$r_4 \sum_{\mathbf{R}} d^\dagger_{1a\uparrow,\frac{3\pi}{4},\mathbf{R}} |0\rangle = e^{\frac{3i\pi}{4}} \sum_{\mathbf{R}} d^\dagger_{1a\uparrow,\frac{3\pi}{4},R_4\mathbf{R}} |0\rangle = e^{\frac{3i\pi}{4}} \sum_{\mathbf{R}} d^\dagger_{1a\uparrow,\frac{3\pi}{4},\mathbf{R}} |0\rangle , \tag{II.187}$$

which means that such a state has a well-defined C_4-eigenvalue of $e^{\frac{3i\pi}{4}}$.
The corresponding operators for the other eigenvalues are given by

$$\begin{aligned} d^\dagger_{1a\uparrow,\frac{3\pi}{4},\mathbf{R}} &= -c^\dagger_{1\uparrow\mathbf{R}} + c^\dagger_{2\uparrow\mathbf{R}} - c^\dagger_{3\uparrow\mathbf{R}} + c^\dagger_{4\uparrow\mathbf{R}}, \\ d^\dagger_{1a\uparrow,-\frac{3\pi}{4},\mathbf{R}} &= -ic^\dagger_{1\uparrow\mathbf{R}} - c^\dagger_{2\uparrow\mathbf{R}} + ic^\dagger_{3\uparrow\mathbf{R}} + c^\dagger_{4\uparrow\mathbf{R}}, \\ d^\dagger_{1a\uparrow,\frac{\pi}{4},\mathbf{R}} &= ic^\dagger_{1\uparrow\mathbf{R}} - c^\dagger_{2\uparrow\mathbf{R}} - ic^\dagger_{3\uparrow\mathbf{R}} + c^\dagger_{4\uparrow\mathbf{R}}, \\ d^\dagger_{1a\uparrow,-\frac{\pi}{4},\mathbf{R}} &= c^\dagger_{1\uparrow\mathbf{R}} + c^\dagger_{2\uparrow\mathbf{R}} + c^\dagger_{3\uparrow\mathbf{R}} + c^\dagger_{4\uparrow\mathbf{R}}, \\ d^\dagger_{1a\downarrow,\frac{3\pi}{4},\mathbf{R}} &= ic^\dagger_{1\downarrow\mathbf{R}} - c^\dagger_{2\downarrow\mathbf{R}} - ic^\dagger_{3\downarrow\mathbf{R}} + c^\dagger_{4\downarrow\mathbf{R}}, \\ d^\dagger_{1a\downarrow,-\frac{3\pi}{4},\mathbf{R}} &= -c^\dagger_{1\downarrow\mathbf{R}} + c^\dagger_{2\downarrow\mathbf{R}} - ic^\dagger_{3\downarrow\mathbf{R}} + c^\dagger_{4\downarrow\mathbf{R}}, \\ d^\dagger_{1a\downarrow,\frac{\pi}{4},\mathbf{R}} &= c^\dagger_{1\downarrow\mathbf{R}} + c^\dagger_{2\downarrow\mathbf{R}} + c^\dagger_{3\downarrow\mathbf{R}} + c^\dagger_{4\downarrow\mathbf{R}}, \\ d^\dagger_{1a\downarrow,-\frac{\pi}{4},\mathbf{R}} &= -ic^\dagger_{1\downarrow\mathbf{R}} - c^\dagger_{2\downarrow\mathbf{R}} + ic^\dagger_{3\downarrow\mathbf{R}} + c^\dagger_{4\downarrow\mathbf{R}}. \end{aligned} \tag{II.188}$$

r_4 has two eigenvectors for every eigenvalue, one for spin-up, one for spin-down. We define an operator that assigns positive eigenvalues to states located at the $1a, \pm\frac{3i\pi}{4}$ position by

$$\overset{\circ}{\psi}_{1a,\pm\frac{3\pi}{4}} = \sum_{\mathbf{R},s\in\{\uparrow,\downarrow\}} d^\dagger_{1as,\frac{3\pi}{4},\mathbf{R}} d_{1as,\frac{3\pi}{4},\mathbf{R}} + d^\dagger_{1as,\frac{-3\pi}{4},\mathbf{R}} d_{1as,\frac{-3\pi}{4},\mathbf{R}}. \tag{II.189}$$

The expectation is that the operator assigns zero eigenvalue to bands situated at other Wyckoff positions, like $1b$ or $2c$. After Fourier transformation using that $c^\dagger_{i\mathbf{R}} \propto \sum_{\mathbf{k}} e^{-i\mathbf{k}\cdot\mathbf{R}} c^\dagger_{i\mathbf{k}}$, we see that this operator has the properties

$$\begin{aligned} \overset{\circ}{\psi}{}^{1a\dagger}_{\mathbf{k}} &= \overset{\circ}{\psi}{}^{1a}_{\mathbf{k}}, \\ r_4 \overset{\circ}{\psi}{}^{1a}_{\mathbf{k}} r_4^\dagger &= \overset{\circ}{\psi}{}^{1a}_{R_4\mathbf{k}}, \\ \mathcal{T} \overset{\circ}{\psi}{}^{1a}_{\mathbf{k}} \mathcal{T}^{-1} &= \overset{\circ}{\psi}{}^{1a}_{-\mathbf{k}}, \end{aligned} \tag{II.190}$$

which are the properties needed in order to get a symmetric splitting with block-diagonality. Analogously one gets the operator for $1b$ by changing

$$\begin{aligned} c^\dagger_{1s\mathbf{R}} &\to c^\dagger_{1s\mathbf{R}}, \\ c^\dagger_{2s\mathbf{R}} &\to c^\dagger_{2s\mathbf{R}+(1,0)}, \\ c^\dagger_{3s\mathbf{R}} &\to c^\dagger_{3s\mathbf{R}+(1,1)}, \\ c^\dagger_{4s\mathbf{R}} &\to c^\dagger_{4s\mathbf{R}+(0,1)}. \end{aligned} \tag{II.191}$$

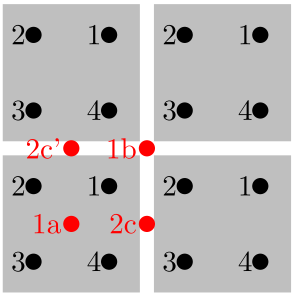

Figure II.40.: Unit cells for the Benalcazar model with C_4 symmetry, including high symmetry Wyckoff positions.

One might also want to to construct an operator for $2c$, to separate the two Kramers pairs at $2c$ and $2c'$. The problem in this case is that any such operator $\mathring{\psi}^{2c}$ can only carry the symmetries of the little group of $2c$, which is $\mathcal{T} \times C_2$. To ensure that the symmetry operators $\mathcal{T}$ and r_4 act as permutations on the bands, one must require that

$$\begin{aligned} \mathring{\psi}_{\mathbf{k}}^{2c\dagger} &= \mathring{\psi}_{\mathbf{k}}^{2c}, \\ r_4 \mathring{\psi}_{\mathbf{k}}^{2c} r_4^\dagger &= -\mathring{\psi}_{R_4\mathbf{k}}^{2c}, \\ \mathcal{T} \mathring{\psi}_{\mathbf{k}}^{2c} \mathcal{T}^{-1} &= \mathring{\psi}_{-\mathbf{k}}^{2c}. \end{aligned} \tag{II.192}$$

The important change here is the appearance of the minus in front of $\mathring{\psi}_{R_4\mathbf{k}}^{2c}$. One way to construct such an operator is to first define two operators, one of them by the replacement

$$\begin{aligned} c_{1s\mathbf{R}}^\dagger &\to c_{1s\mathbf{R}}^\dagger, \\ c_{2s\mathbf{R}}^\dagger &\to c_{2s\mathbf{R}+(1,0)}^\dagger, \\ c_{3s\mathbf{R}}^\dagger &\to c_{3s\mathbf{R}+(1,0)}^\dagger, \\ c_{4s\mathbf{R}}^\dagger &\to c_{4s\mathbf{R}}^\dagger, \end{aligned} \tag{II.193}$$

which we then refer to as $d_{2c}^\dagger$, and the other one by

$$\begin{aligned} c_{1s\mathbf{R}}^\dagger &\to c_{1s\mathbf{R}+(0,1)}^\dagger, \\ c_{2s\mathbf{R}}^\dagger &\to c_{2s\mathbf{R}+(0,1)}^\dagger, \\ c_{3s\mathbf{R}}^\dagger &\to c_{3s\mathbf{R}}^\dagger, \\ c_{4s\mathbf{R}}^\dagger &\to c_{4s\mathbf{R}}^\dagger, \end{aligned} \tag{II.194}$$

which we refer to as $d_{2c'}^\dagger$. There seems to be no obvious combination of the operators d_{2c} to obtain a gapless $\mathring{\psi}_{\mathbf{k}}$ for the position $2c$. Therfore, we are concerned with $1a$ and $1b$ Wyckoff positions in the remainder of the section.

To provide a few examples, we examine the case $H_2^{(4)}(\mathbf{k}, t = 0)$, which corresponds to the BR $1b \oplus 1b$. For this case, we define two operators to completely split the occupied bands to single

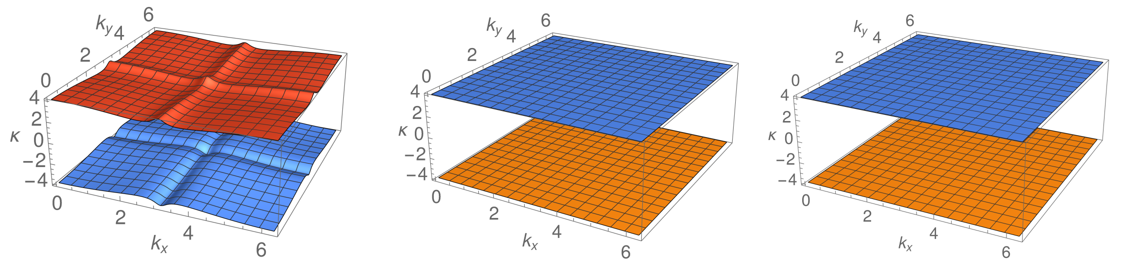

(a) $\mathring{\Psi}$ band structure of the model $H_3^{(2)}(\mathbf{k}, t = 1.2)$. Split to two 2-band-spaces using $\mathring{\psi}_{1a,(\frac{3\pi}{4}\leftrightarrow\frac{\pi}{4}),\mathbf{k}}$.

(b) $\tilde{\mathring{\Psi}}$ band structure within the lower (left) and upper (right) two bands, resp., using $\mathring{\psi}_{1a,(\uparrow\leftrightarrow\downarrow),\mathbf{k}}$.

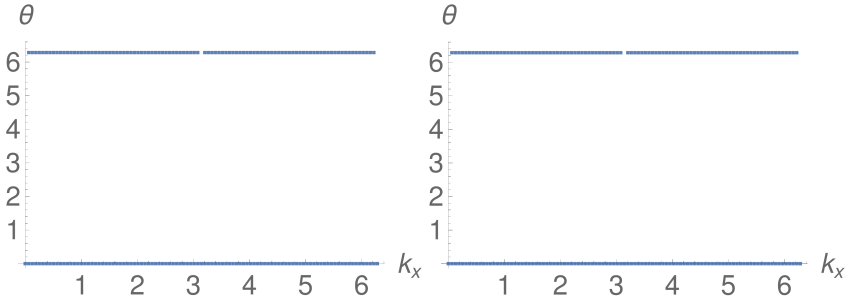

(c) Wilson loop spectrum in lower (left) and upper (right) $\mathring{\Psi}$ bands. We can see no winding.

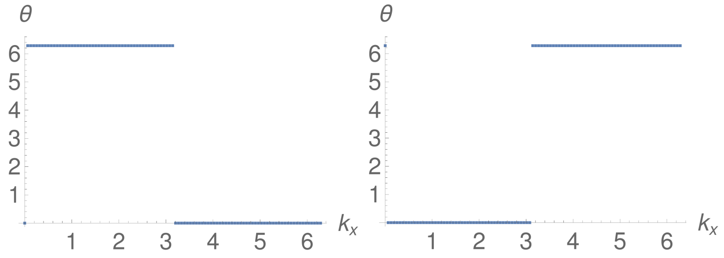

(d) Wilson loop spectrum in lower (left) and upper (right) $\tilde{\mathring{\Psi}}$ bands within the lower $\mathring{\Psi}$ band. These bands have zero first Chern number.

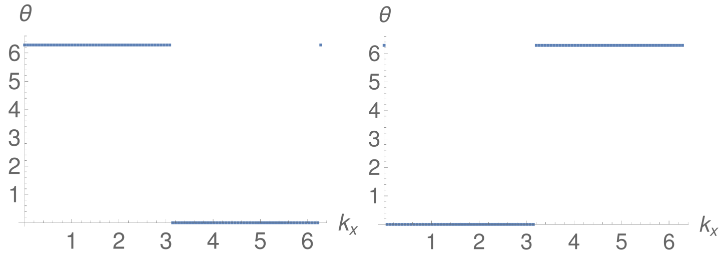

(e) Wilson loop spectrum in the lower (left) and upper (right) $\tilde{\mathring{\Psi}}$ bands within the upper $\mathring{\Psi}$ band. All these bands have zero first Chern number.

Figure II.41.: $\mathring{\Psi}$ band structures and Wilson loop spectra for $H_3^{(2)}(\mathbf{k}, t = 1.2)$ with a $\mathring{\psi}_{\mathbf{k}}$ that is compatible with Wyckoff position $1a$, constructed using creation operators.

bands. The first operator, defined as

$$\mathring{\psi}_{1b,\left(\frac{3\pi}{4}\leftrightarrow\frac{\pi}{4}\right)} = \sum_{\substack{\mathbf{R}\\ \sigma\in\{\uparrow,\downarrow\}\\ s\in\{+,-\}}} d^{\dagger}_{1b\sigma,s\frac{3\pi}{4},\mathbf{R}} d_{1b\sigma,s\frac{3\pi}{4},\mathbf{R}} - d^{\dagger}_{1b\sigma,s\frac{\pi}{4},\mathbf{R}} d_{1b\sigma,s\frac{\pi}{4},\mathbf{R}}, \tag{II.195}$$

splits the bands with $e^{\pm 3\pi i/4}$ eigenvalue at $1b$ from those with $e^{\pm \pi i/4}$ eigenvalues. Then we split bands with spin-up from those with spin-down by using the operator

$$\mathring{\psi}_{1b,(\uparrow\leftrightarrow\downarrow)} = \sum_{\substack{\mathbf{R}\\ \alpha\in\{\frac{\pi}{4},-\frac{\pi}{4},\frac{3\pi}{4},-\frac{3\pi}{4}\}}} d^{\dagger}_{1b\uparrow,\alpha,\mathbf{R}} d_{1b\uparrow,\alpha,\mathbf{R}} - d^{\dagger}_{1b\downarrow,\alpha,\mathbf{R}} d_{1b\downarrow,\alpha,\mathbf{R}}. \tag{II.196}$$

After Fourier transforming them, we simply obtain the operators for $1a$ instead $1b$ by setting

$$\begin{aligned} \mathring{\psi}_{1a,\left(\frac{3\pi}{4}\leftrightarrow\frac{\pi}{4}\right),\mathbf{k}} &= \mathring{\psi}_{1b,\left(\frac{3\pi}{4}\leftrightarrow\frac{\pi}{4}\right),\mathbf{k}=0}, \\ \mathring{\psi}_{1a,(\uparrow\leftrightarrow\downarrow),\mathbf{k}} &= \mathring{\psi}_{1b,(\uparrow\leftrightarrow\downarrow),\mathbf{k}=0}. \end{aligned} \tag{II.197}$$

The $\mathring{\Psi}$ band structure and the Wilson loop spectrum when using $\mathring{\psi}_{1b}$ on the occupied bands of $H_2^{(4)}(\mathbf{k}, t = 0.2)$ are shown in Fig. II.42. Figure II.42a shows the $\mathring{\Psi}$ band structure of the first split using $\mathring{\psi}_{1b,\left(\frac{3\pi}{4}\leftrightarrow\frac{\pi}{4}\right)}$. Figure II.42b shows the $\mathring{\Psi}$ band structure of the second split using $\mathring{\psi}_{1b,(\uparrow\leftrightarrow\downarrow)}$ within the two two-band subspaces obtained after the first split. These three $\mathring{\Psi}$ band structures are completely flat. The Wilson loop spectra in the two-band subspaces obtained after the first split are shown in Fig. II.42c. Interestingly, they resemble the Wilson loop spectra obtained for the whole occupied space. Figure II.42e shows the single-band Wilson loop spectra after the second split. All these bands have zero first Chern number. Therefore the occupied bands correspond to a band representation.

The $\mathring{\Psi}$ band structure when using $\mathring{\psi}_{1a}$, applied to the occupied bands of the Hamiltonian $H_3^{(2)}(\mathbf{k}, t = 1.2)$, is depicted in Fig. II.41. The occupied bands of this Hamiltonian correspond to Wyckoff position $1a$. Figure II.41a shows the $\mathring{\Psi}$ band structure for the first split using $\mathring{\psi}_{1a,\left(\frac{3\pi}{4}\leftrightarrow\frac{\pi}{4}\right)}$, Fig. II.41b shows the $\mathring{\Psi}$ band structure of $\mathring{\psi}_{1a,(\uparrow\leftarrow\downarrow)}$ within the two two-band subspaces of the previous split. The Wilson loop spectra in the two two-band subspaces are shown in Fig. II.41c. The Wilson loop spectra of the single bands, which all show trivial winding, are depicted in Figures II.41d and II.41e. This demonstrates that the occupied correspond to a band representation.

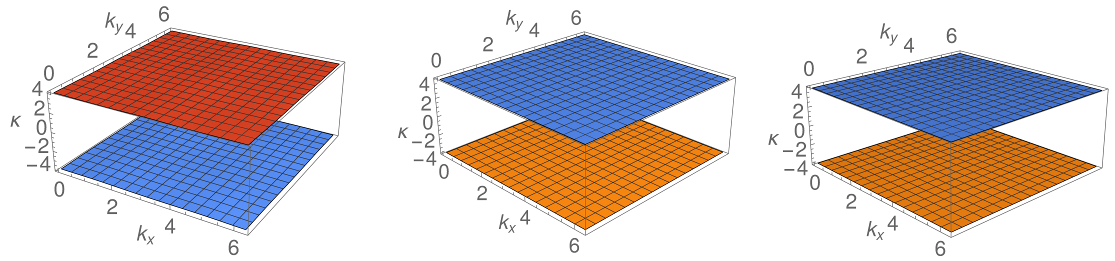

(a) $\mathring{\Psi}$ band structure of the model $H_2^{(4)}(\mathbf{k}, t = 0.2)$. Split to two 2-band spaces using $\mathring{\psi}_{1b,(\frac{3\pi}{4}\leftrightarrow\frac{\pi}{4}),\mathbf{k}}$.

(b) $\tilde{\mathring{\Psi}}$ band structure within the lower (left) and upper (right) two bands, resp., using $\mathring{\psi}_{1b,(\uparrow\leftrightarrow\downarrow),\mathbf{k}}$.

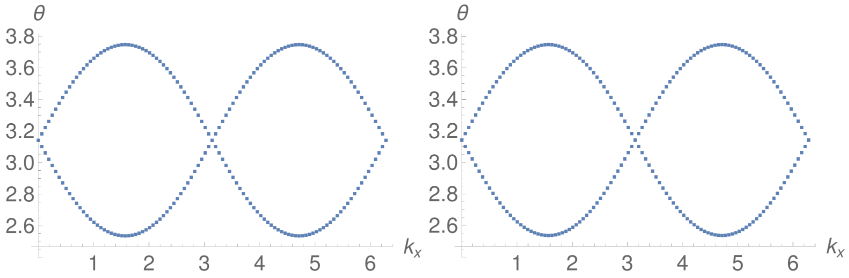

(c) Wilson loop spectrum in lower (left) and upper (right) $\mathring{\Psi}$ bands. We can see no winding.

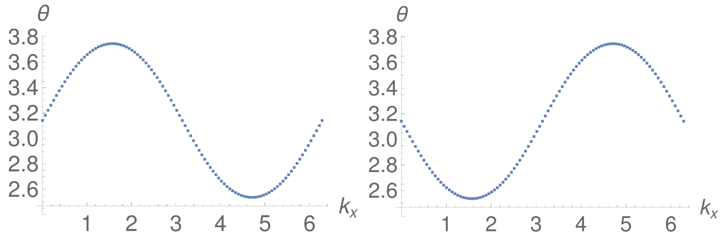

(d) Wilson loop spectrum in lower (left) and upper (right) $\tilde{\mathring{\Psi}}$ bands within the lower $\mathring{\Psi}$ band. These bands have zero first Chern number.

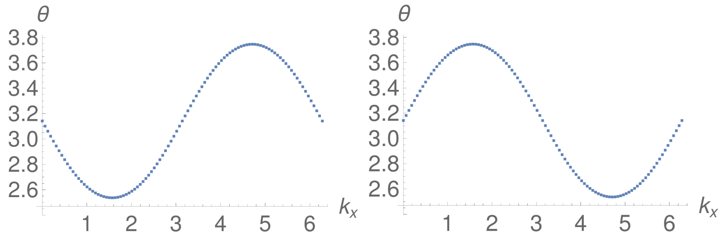

(e) Wilson loop spectrum in the lower (left) and upper (right) $\tilde{\mathring{\Psi}}$ bands within the upper $\mathring{\Psi}$ band. These bands have zero first Chern number.

Figure II.42.: $\mathring{\Psi}$ band structures and Wilson loop spectra for $H_2^{(4)}(\mathbf{k}, t = 0.2)$ with a $\mathring{\psi}_{\mathbf{k}}$ that is compatible with Wyckoff position $1b$, constructed using creation operators.

II.9.5. Degeneracies

In this section, degeneracies in the $\mathring{\Psi}$ band structure and their significance are investigated. For simplicity, we only look at the case of TRS- and C_4-symmetric Hamiltonians. Degeneracies can also arise in other cases, for example when trying to construct three-cycles. In general, degeneracies can arise either because the split one wants to perform is incompatible with the physical properties of the underlying bands, or accidentally. This section is structured as follows: In the first subsection II.9.5.1, we elucidate why single degeneracies cannot be gapped out. In the second subsection II.9.5.2, we explain the appearance of some degneracies that are enforced by the underlying bands, and can therefore not be gapped out. In the third subsection II.9.5.3, we explain from a Berry phase point of view, why pairs of degeneracies can be gapped out.

II.9.5.1. Protection of Degeneracies

This section tries to prove that the degeneracies in the spectrum of $\mathring{\Psi}^{mn}_{\mathbf{k}} = \left\langle u^m_{\mathbf{k}} \middle| \mathring{\psi}_{\mathbf{k}} \middle| u^n_{\mathbf{k}} \right\rangle$ cannot be gapped out individually, but only in pairs, if we have TRS and C_4-symmetry.
Because we are only interested in whether it is possible to gap out a degeneracy between two bands, it is sufficient to look at only these two bands. This means that $\mathring{\Psi}$ is a 2x2 matrix. Since $\mathring{\Psi}_{\mathbf{k}}$ and $\mathring{\psi}_{\mathbf{k}}$ are Hermitian, they are real linear combinations of the Pauli matrices

$$\mathring{\Psi}_{\mathbf{k}} = \sum_{i=0}^{3} A_i \sigma^i, \tag{II.198}$$

$$\mathring{\psi}_{\mathbf{k}} = \sum_{i=0}^{3} a_i \sigma^i. \tag{II.199}$$

Without loss of generality, we study the situation with $r_2\mathcal{T} = K$ as representation of the symmetry. In this situation, the allowed σ^i are σ^0, σ^1 and σ^3. σ^0 only shifts the degeneracies and therefore does not open a gap, thus it is not of interest. So what remains are two Pauli matrices, which give in a linearised regime

$$\tilde{\mathring{\Psi}}_{\mathbf{k}} \sim (a_1 + a_2 k_x + a_3 k_y)\sigma^1 + (b_1 + b_2 k_x + b_3 k_y)\sigma^3. \tag{II.200}$$

We have two parameters (k_x and k_y) to tune the positions of the degeneracies. The number of free parameters is insufficient to gap out the cones. This is because a change of prefactors only changes the position of the degeneracy in $\mathbf{k}$-space, but does not lead to its disappearance. This argumentation follows the precedent of the argumentation applied in similar cases by Schindler and Neupert [137, p. 49-50], Bernevig [10, p. 75] or Bradlyn et al.[76].

II.9.5.2. Appearance of Degeneracies

In this section, two aspects are showed:

1. that degeneracies at general positions always appear in sets of four at a time, situated at the position $R_4^i\mathbf{k}$, with $i \in [0, 1, 2, 3]$.
2. that the $\mathring{\Psi}$ band structure is degenerate at the TRIMs ($\mathbf{\Gamma}$, $\mathbf{M}$, $\mathbf{X}$, and $\mathbf{Y}$).

Degeneracies at general positions We know that the PSO at $R_4\mathbf{k}$ is given by

$$\mathring{\Psi}^{mn}_{R\mathbf{k}} = \left\langle u^m_{R\mathbf{k}} \middle| \mathring{\psi}_{R\mathbf{k}} \middle| u^n_{R\mathbf{k}} \right\rangle = \left\langle u^m_{\mathbf{k}} \middle| r_4^\dagger \left(r_4 \mathring{\psi}_{\mathbf{k}} r_4^\dagger \right) r_4 \middle| u^n_{\mathbf{k}} \right\rangle = \left\langle u^m_{\mathbf{k}} \middle| \mathring{\psi}_{\mathbf{k}} \middle| u^n_{\mathbf{k}} \right\rangle = \mathring{\Psi}^{mn}_{\mathbf{k}}. \tag{II.201}$$

This implies that a degeneracy at $\mathbf{k}$ also appears at $R_4^i\mathbf{k}$, which proves our statement. □

Degeneracies at TRIMs At TRIMs, $\mathbf{k} = -\mathbf{k}$, we observe that due to TRS there are two orthogonal eigenvectors $|b\rangle$ and $\left|\tilde{b}\right\rangle = \mathcal{T}\,|b\rangle = \tau\,|b\rangle^*$. This follows from

$$\left(\langle b|\mathcal{T}|b\rangle\right)^* = K \left\langle b \middle| K\tau^\dagger \mathcal{T}^2 \middle| b \right\rangle = \left\langle \tilde{b} \middle| \mathcal{T}^2 \middle| b \right\rangle = -\left\langle \tilde{b} \middle| \mathbb{1} \middle| b \right\rangle = -\left(\langle b|\mathcal{T}|b\rangle\right)^* \implies |b\rangle \perp \mathcal{T}\,|b\rangle\,. \tag{II.202}$$

Furthermore, we observe that if the $\left|b^M\right\rangle = \sum_n v_n^m\,|u^n\rangle$ is a basis of the occupied band, then the $\left|\tilde{b}^m\right\rangle = \sum_n v_n^{m*}\mathcal{T}\,|u^n\rangle$ also span the occupied space. The $\mathring{\Psi}$ in this basis is given by

$$\tilde{\mathring{\Psi}}_{mn} = \left(\langle u^m|\right)^* \tau^\dagger \mathring{\psi} \tau K\,|u^n\rangle = K \left\langle u^m \middle| \mathring{\psi} \middle| u^n \right\rangle, \tag{II.203}$$

which implies via

$$\mathring{\Psi}\vec{v} = \kappa\vec{v} \implies \mathring{\Psi}^*\vec{v}^* = \kappa\vec{v}^* \tag{II.204}$$

that the two vectors $\vec{v}$ and $\vec{v}^*$, which correspond to two orthogonal vectors $\left|b^i\right\rangle$ and $\left|\tilde{b}^i\right\rangle$, have the same eigenvalues (if $\mathring{\psi}$ Hermitian). We used the basis-indepedence of the vectors $|b^m\rangle$. It shows that there are two orthogonal vectors $|b^m\rangle$ corresponding to the same eigenvalues. Therefore, there is a degeneracy in the $\mathring{\Psi}$ band structure. If we imagine being in a four band situation, and closing a gap at a TRIM, we have to move two degenerate bands from below and above to a joint energy. This will give us a fourfold degeneracy.

II.9.5.3. Trivialisation of Degeneracies

It is also important to consider whether these degeneracies (Dirac cones) can always be gapped out. If we allow for a free choice of $\mathring{\psi}_{\mathbf{k}}$, and assume that there is a periodic smooth and block-wise symmetric gauge, then the possibility to remove them follows from the existence of a $\mathring{\psi}_{\mathbf{k}}$ with flat bands. But this argument makes a lot of assumptions, so we will not step there.
Also, we showed in the last chapter that some degeneracies cannot be gapped out without breaking symmetries.
Another way to see this is to look at the Berry phase (resp. the Wilson loop eigenvalues) of Wilson loops that encircle a degeneracy or double degeneracies. This is based on the observation that a single degeneracy contributes a Berry phase of π, which corresponds to Wilson loops eigenvalues $(\pi, 0)$. Degeneracies are regarded as trivialisable if the Wilson loops around them can be deformed to have trivial Wilson loop eigenvalues (e.g. $(0, 0)$). For this we first have a look at the Wilson loop around an arbitrary isolated cone. We are always only looking at the Wilson in the occupied occupied band (occupied bands of projected symmetric operator, subspace of occupied bands of Hamiltonian).
For this we assume that we have a basis of the occupied occupied space with $|\tilde{u}^n_{\mathbf{k}}\rangle = r_2\mathcal{T}\,|u^n_{\mathbf{k}}\rangle$. The $\tilde{u}$ are simply a different basis of the same space. The Wilson loop is then given by

$$W = \prod_{i=N}^{1} F(\mathbf{k}_i) \qquad \text{with } F_{mn}(\mathbf{k}_i) = \left\langle u^m_{\mathbf{k}_{i+1}} \middle| u^n_{\mathbf{k}_i} \right\rangle. \tag{II.205}$$

We observe that

$$F^*_{mn}(\mathbf{k}_i) = \left(\left\langle u^m_{\mathbf{k}_{i+1}} \middle| u^n_{\mathbf{k}_i}\right\rangle\right)^* = \left\langle \tilde{u}^m_{\mathbf{k}_{i+1}} \middle| \tau^\dagger r_2^\dagger r_2 \tau \middle| \tilde{u}^n_{\mathbf{k}_i}\right\rangle = \left\langle \tilde{u}^m_{\mathbf{k}_{i+1}} \middle| \tilde{u}^n_{\mathbf{k}_i}\right\rangle = \tilde{F}_{mn}(\mathbf{k}_i). \tag{II.206}$$

Because the Wilson loop eigenvalues are independent of reparametrisation of the basis, this means that

$$\text{Spectrum}(W) = \text{Spectrum}(W^*), \tag{II.207}$$

which implies that the eigenvalues must appear in complex conjugate pairs. If we only consider one cone, we can separate off the involved bands and only get one Wilson loop eigenvalue, which must be real. This then means that

$$\theta_{\text{single cone}} = 0, \pi. \tag{II.208}$$

The second eigenvalue is then simply trivial, so 0 as well. This gives us the Wilson loop eigenvalues of a single cone as $(0, \pi)$, we amass a Berry phase of π when circling around one cone.

Proof for trivialisability In this section, we argue that many degeneracies can be gapped out because the Berry phases of Wilson loops sourrounding the degeneracies are trivial. The fact that one cone contributes a phase of $(0, \pi)$ means that 4 cones together contribute only trivially. To have a closer look at this, we will look at a closed Wilson loop and its C_4-correspondent. A Wilson loop is given by

$$W = \prod_{\mathbf{k}_i = \mathbf{k}_N}^{\mathbf{k}_1} F(\mathbf{k}_i) \qquad \text{with } F_{mn}(\mathbf{k}_i) = \left\langle u^m_{\mathbf{k}_{i+1}} \middle| u^n_{\mathbf{k}_i}\right\rangle. \tag{II.209}$$

We then see that the Wilson loop at the position rotated by C_4 in k-space is given by

$$\begin{aligned}\tilde{W} &= \prod_{\mathbf{k}_i = C_4\mathbf{k}_N}^{C_4\mathbf{k}_1} F(\mathbf{k}_i) = \prod_{C_4^{-1}\mathbf{k}_i = \mathbf{k}_N}^{\mathbf{k}_1} F(\mathbf{k}_i) = \left\{\left\langle u^m_{C_4\mathbf{k}_{N+1}} \middle| u^n_{C_4\mathbf{k}_N}\right\rangle\right\} \cdots \left\{\left\langle u^m_{C_4\mathbf{k}_2} \middle| u^n_{C_4\mathbf{k}_1}\right\rangle\right\} \\ &= \left\{\left\langle u^m_{\mathbf{k}_{N+1}} \middle| r_4^\dagger r_4 \middle| u^n_{\mathbf{k}_N}\right\rangle\right\} \cdots \left\{\left\langle u^m_{\mathbf{k}_2} \middle| r_4^\dagger r_4 \middle| u^n_{\mathbf{k}_1}\right\rangle\right\} = \left\{\left\langle u^m_{\mathbf{k}_{N+1}} \middle| u^n_{\mathbf{k}_N}\right\rangle\right\} \cdots \left\{\left\langle u^m_{\mathbf{k}_2} \middle| u^n_{\mathbf{k}_1}\right\rangle\right\} = W.\end{aligned} \tag{II.210}$$

We see that the Wilson loops are the same. In this calculation we used that the C_4 sewing matrix is block-diagonal[75].

This can now be applied to the case of four degeneracies at general positions in the BZ (not at $\mathbf{\Gamma}$, $\mathbf{M}$, $\mathbf{X}$ or $\mathbf{Y}$). The joint Wilson loop W_c is then formed in C_4-symmetric way, such that four degeneracies are included. Its eigenvalue problem is then

$$W_c \vec{v} = W^4 \vec{v} = e^{4i\theta} \vec{v} = \vec{v}, \tag{II.211}$$

which is the case because the θ is 0 or π.

On the other hand, if we are at a high symmetry point of the BZ, which also happens to be TRIM for C_4 symmetric systems, our cones always appear in pairs. This then means that the total amassed Berry phase is $2\pi = 0$, which means that they can be gapped out.

II.10. Outlook

This section points out some possible directions of further research and describes a few ill-thought-through ideas I had. Maybe some of the ideas could be of use in the future and lead to interesting results.

II.10.1. Non-Hermitian Topology with Star-Gaps

Star-gaps are a (possibly) new phenomenon that appear when trying to construct gauges corresponding to n-cycle permutations. In the current research literature on non-Hermitian topology (cf. Ref. [95]) the only distinction seems to be between point gaps, which are gaps with one forbidden energy in the complex plane, and line gaps that are forbidden lines through the complex plane, which can be deformed to “real” gaps in the imaginary or real part of the energy spectrum. Star-like gaps are not mentioned. Therefore, it might be worthwhile to consider three questions:

- Are there physical systems that show such a star-like gap? If this is not the case, there is no reason to continue thinking about it.
- If yes, what is the topological classification of systems with such a gap?
- With which internal symmetries and/or space group symmetries are these gaps compatible? Is there any connection to C_n and/or screw-rotation symmetry?

II.10.2. PSO Method for Non-Hermitian Hamiltonians

It was shown in this part of the thesis that using an operator $\mathring{\psi}_{\mathbf{k}}$ and its projection onto the occupied subspace $\mathring{\Psi}_{\mathbf{k}}$ highly symmetric gauges can be constructed. Is there a corresponding method that also works for the occupied bands of non-Hermitian Hamiltonians?

What needs to be taken into account is that the eigenvectors of non-Hermitian matrices are in general not orthonormal, and therefore many of the proofs do not work anymore. Most probably, one has to work with left and right eigenvectors, maybe one could define

$$\mathring{\Phi}^{mn}_{\mathbf{k}} = \left\langle u^{Lm}_{\mathbf{k}} \middle| \mathring{\psi}_{\mathbf{k}} \middle| u^{Rn}_{\mathbf{k}} \right\rangle , \tag{II.212}$$

with the left eigenvectors $\left|u^{Lm}_{\mathbf{k}}\right\rangle$ and the right eigenvectors $\left|u^{Rm}_{\mathbf{k}}\right\rangle$.

II.10.3. Winding of Wilson Loops in the Occupied Bands

One question to adress is whether it is possible to prove that if the Wilson loop spectrum within the occupied subspace shows no winding, the bands correspond to a band representation. This statement can be phrased in two ways:

- If the Wilson spectrum shows no winding, the occupied bands are a band representation.
- If the occupied are not a band representation, the Wilson loop spectrum has non-trivial winding.

First, it was observed in a few instances that the Wilson loop before a split was exactly the overlay of the Wilson loop after a split using a $\mathring{\Psi}_{\mathbf{k}}$. This happened on the one hand for the two band case described in section II.6.2, but also when using a $\mathring{\psi}_{\mathbf{k}}$ constructed based on Wyckoff position $1b$ to split the occupied bands of $H_2^{(4)}$. If it were possible to prove that there is always a $\mathring{\psi}_{\mathbf{k}}$ that splits the bands and leaves the Wilson loop eigenvalues unchanged, this could be a pathway towards a proof.

II.11. Final Remarks

In the first part of the thesis, we have seen a quite universal method to construct gauges that respect specific conditions concerning smoothness of projectors and the action of symmetries. The method allows for a variety of different permutation patterns as sewing matrices and enforces smoothness if there is a well-defined gap. In comparison to the method proposed by Alexandradinata et al.[131] the main advantage of our method is that also n-cycle permutations with $n > 2$ can be constructed.

This method allows to characterise which atomic limit an occupied set of bands belongs to, by connecting it to the results of Kooi et al.[130] and their symmetry-indicator invariants. It is a mathematically easier method compared to the quite complicated parallel transport method by Kooi et al. and can be implemented straight-forwardly and easily. We are therefore now able to distinguish the obstructed atomic limit $1b|_{\pm\frac{\pi}{4}} \oplus 1b|_{\pm\frac{3\pi}{4}}$ from the trivial atomic limit.

Furthermore, we analysed in detail the behaviour of the $\mathring{\Psi}_{\mathbf{k}}$ band structures of Hamiltonians with TRS and C_4 symmetry.

II.A. Explicit Constructive Proof for the Existence of a SO in a Case with TRS and C_4 Symmetry

In this section, we prove for TRS and C_4-symmetric systems that if there is a smooth and symmetric gauge, then we can construct a $\mathring{\psi}$ that is TRS and C_4-symmetric and smooth. This is a direct constructive proof.

To prove the existence of an $\mathring{\psi}_{\mathbf{k}}$ that fulfills the conditions on symmetry and analyticity, we assume that there is a gauge $|u^n_{\mathbf{k}}\rangle$ that is smooth and respects all our symmetries. Such a gauge could for example be constructed along the lines of the method proposed by Winkler, Soluyanov and Troyer[147]. According to Alexandradinata et al.[131] the gauge exists if the bands correspond to a BR. As a consequence, for this gauge the states are orthonormal, the sewing matrices block-diagonal, and the gauge is smooth over the whole closed BZ. Due to the smoothness and the completely fulfilled symmetry requirements (block diagonal TRS and C_4 sewing matrices), the sectors $|u^n_{\mathbf{k}}\rangle$ can be uniquely assigned to the C_4 symmetry sectors. We refer to the states in the $e^{\pm i\pi/4}$ sector as $|v^n_{\mathbf{k}}\rangle$ and to those in the $e^{\pm 3i\pi/4}$ as $|w^m_{\mathbf{k}}\rangle$. We define the matrix-valued function

$$\beta_{\mathbf{k}} = \sqrt{2}\sum_n |v^n_{\mathbf{k}}\rangle\langle v^n_{\mathbf{k}}| - \sqrt{2}\sum_n |w^n_{\mathbf{k}}\rangle\langle w^n_{\mathbf{k}}| \,. \tag{II.213}$$

At the points $\mathbf{\Gamma}$ and $\mathbf{M}$, this matrix is obviously identical to $r_4+r_4^\dagger$, because $\beta_\Gamma\,|v^n_{\mathbf{k}}\rangle = \sqrt{2}\,|v^n_{\mathbf{k}}\rangle = \left(e^{+i\pi/4} + e^{-i\pi/4}\right)|v^n_{\mathbf{k}}\rangle = \left(r_4 + r_4^\dagger\right)|v^n_{\mathbf{k}}\rangle$ and analogously for $\mathbf{M}$, $|w^n_{\mathbf{k}}\rangle$.

The next step is to prove that $\beta_{\mathbf{k}}$ is smooth, gapped, Hermitian, and TRS and C_4-symmetric.

II.A.1. Smoothness and Gap

Smoothness $\beta_{\mathbf{k}}$ is smooth because the $|v^n_{\mathbf{k}}\rangle$ and $|w^n_{\mathbf{k}}\rangle$ are smooth, by assumption.

Gap Since the eigenvalues are basis independent, we can without any limitations use the basis spanned by $|v^n_{\mathbf{k}}\rangle$ and $|w^n_{\mathbf{k}}\rangle$. In this basis, $\mathring{\Psi}^{mn}_{\mathbf{k}} = \langle u^m_{\mathbf{k}}|\beta_{\mathbf{k}}|u^n_{\mathbf{k}}\rangle$ is diagonal with eigenvalues $\pm\sqrt{2}$. Therefore the $\mathring{\Psi}$ band structure is completely flat and gapped.

II.A.2. Symmetries

Hermiticity Hermiticity means that for any $|\varphi\rangle$ and $|\eta\rangle$

$$\langle\varphi,\beta_{\mathbf{k}}\eta\rangle = \langle\beta_{\mathbf{k}}\varphi,\eta\rangle \,. \tag{II.214}$$

Only the first term is explicitly evaluated as

$$\begin{aligned}
\langle\varphi,\beta_{\mathbf{k}}\eta\rangle &= \left\langle |\varphi\rangle\,, \sqrt{2}\sum_n |v^n_{\mathbf{k}}\rangle\langle v^n_{\mathbf{k}}|\eta\rangle \right\rangle = \sqrt{2}\sum_n \langle\varphi|u^n_{\mathbf{k}}\rangle\,\langle u^n_{\mathbf{k}}|\eta\rangle \\
&\qquad\qquad\qquad\qquad\qquad\qquad\qquad\qquad \shortparallel \\
\langle\beta_{\mathbf{k}}\varphi,\eta\rangle &= \left\langle \sqrt{2}\sum_n |u^n_{\mathbf{k}}\rangle\langle u^n_{\mathbf{k}}|\varphi\rangle\,, |\eta\rangle \right\rangle = \sqrt{2}\sum_n \langle u^n_{\mathbf{k}}|\eta\rangle\,\langle\varphi|u_{\mathbf{k}}\rangle\,,
\end{aligned} \tag{II.215}$$

which proves our claim. The other term follows analogously.

C_4 symmetry We want to prove that

$$\hat{r}\beta_{\mathbf{k}}\hat{r}^{\dagger} = \beta_{R\mathbf{k}} \Leftrightarrow \hat{r}\beta_{\mathbf{k}} = \beta_{R\mathbf{k}}\hat{r} \tag{II.216}$$

$$\Leftrightarrow \hat{r}\sum_n |v^n_{\mathbf{k}}\rangle\langle v^n_{\mathbf{k}}| - \hat{r}\sum_n |w^n_{\mathbf{k}}\rangle\langle w^n_{\mathbf{k}}| = \sum_n |v^n_{R\mathbf{k}}\rangle\langle v^n_{R\mathbf{k}}|\,\hat{r} - \sum_n |w^n_{R\mathbf{k}}\rangle\langle w^n_{R\mathbf{k}}|\,\hat{r}$$

This statement is true because it is true for every $|v^n_{\mathbf{k}}\rangle$, $|w^n_{\mathbf{k}}\rangle$ and $|s\rangle$, where $|s\rangle$ are vectors in the unoccupied subspace. These vectors together form an orthonormal basis. We exemplify this using $\left|v^1_{\mathbf{k}}\right\rangle$:

$$\hat{r}\sum_n |v^n_{\mathbf{k}}\rangle\langle v^n_{\mathbf{k}}|\,\left|v^1_{\mathbf{k}}\right\rangle - \hat{r}\sum_n |w^n_{\mathbf{k}}\rangle\langle w^n_{\mathbf{k}}|\,\left|v^1_{\mathbf{k}}\right\rangle = \sum_n |v^n_{R\mathbf{k}}\rangle\langle v^n_{R\mathbf{k}}|\,\hat{r}\,\left|v^1_{\mathbf{k}}\right\rangle - \sum_n |w^n_{R\mathbf{k}}\rangle\langle w^n_{R\mathbf{k}}|\,\hat{r}\,\left|v^1_{\mathbf{k}}\right\rangle .$$

This term can be simplified using the fact that the expressions with the projectors always act as identities on their respective subspaces and give 0 otherwise. With this simplification the term is reformulated as

$$\hat{r}\left|v^1_{\mathbf{k}}\right\rangle - 0 = \hat{r}\left|v^1_{\mathbf{k}}\right\rangle - 0, \tag{II.217}$$

which exemplifies the truth of the statement. The proof for the other terms is analogous.

TRS We have to prove that

$$\mathcal{T}\beta_{\mathbf{k}}\mathcal{T}^{-1} = \beta_{-\mathbf{k}} \Leftrightarrow \mathcal{T}\beta_{\mathbf{k}} = \beta_{-\mathbf{k}}\mathcal{T} \tag{II.218}$$

$$\Leftrightarrow \mathcal{T}\sum_n |v^n_{\mathbf{k}}\rangle\langle v^n_{\mathbf{k}}| - \mathcal{T}\sum_n |w^n_{\mathbf{k}}\rangle\langle w^n_{\mathbf{k}}| = \sum_n \left|v^n_{-\mathbf{k}}\right\rangle\left\langle v^n_{-\mathbf{k}}\right|\mathcal{T} - \sum_n \left|w^n_{-\mathbf{k}}\right\rangle\left\langle w^n_{-\mathbf{k}}\right|\mathcal{T}$$

The proof of this is analogous to the one for C_4 symmetry.

II.B. Explicit Proofs for the Block-(Off-)Diagonality of Sewing Matrices

In this section we present a few unnecessarily complicated proofs to show that certain sewing matrices become block-(off-)diagonal if we construct a smooth and symmetric gauge using certain specific $\mathring{\psi}$s. Much easier proofs for these statements are presented in the main part of the thesis (cf. section II.9.2.4). The proofs in the following demonstrate directly that certain vectors in the new basis $|b^n_{\mathbf{k}}\rangle = \sum_m v^m_{\mathbf{k},n}\,|u^m_{\mathbf{k}}\rangle$ are orthogonal to vectors at symmetry-transformed $\mathbf{k}$ space positions after being themselves subject to the symmetry transformation. They therefore show that certain elements of sewing matrices are zero. To show this, we first present a few useful lemmas. All of these proofs refer to the case with TRS and C_4 symmetry. The proofs are analogous to similar proofs in Appendix A of Ref. [75].

II.B.1. Lemmas

First, a connection between the eigenvalues and eigenvectors of $\mathring{\Psi}$ and a bra-ket expression.

$$\mathring{\Psi}\vec{v}_{\mathbf{k},n} = \kappa_{\mathbf{k},n}\vec{v}_{\mathbf{k},n} \Leftrightarrow \sum_l \mathring{\Psi}^{ml}_{\mathbf{k}} v^l_{\mathbf{k},n} = \kappa_{\mathbf{k},n}v^m_{\mathbf{k},n} = \sum_l \left\langle u^m_{\mathbf{k}}\middle|\mathring{\psi}_{\mathbf{k}}\middle|u^l_{\mathbf{k}}\right\rangle v^l_{\mathbf{k},n} = \left\langle u^m_{\mathbf{k}}\middle|\mathring{\psi}_{\mathbf{k}}\middle|b^n_{\mathbf{k}}\right\rangle$$

$$\implies \kappa_{\mathbf{k},n}v^m_{\mathbf{k},n} = \left\langle u^m_{\mathbf{k}}\middle|\mathring{\psi}_{\mathbf{k}}\middle|b^n_{\mathbf{k}}\right\rangle \tag{II.219}$$

Secondly, the proof that the rotation sewing matrix $\tilde{D}^{mn}_{\mathbf{k}} = \langle b^m_{R\mathbf{k}}|r|b^n_{\mathbf{k}}\rangle$ is unitary. For this we first express $\tilde{D}$ in terms of $D^{mn}_{\mathbf{k}} = \langle u^m_{R\mathbf{k}}|r|u^n_{\mathbf{k}}\rangle$:

$$\tilde{D}^{mn}_{\mathbf{k}} = \langle b^m_{R\mathbf{k}}|r|b^n_{\mathbf{k}}\rangle = \sum_{l\tilde{l}} v^{\tilde{l}*}_{R\mathbf{k},m} \left\langle u^{\tilde{l}}_{R\mathbf{k}} \middle| r \middle| u^l_{\mathbf{k}} \right\rangle v^l_{\mathbf{k},n} = \sum_{l\tilde{l}} v^{\tilde{l}*}_{R\mathbf{k},m} D^{\tilde{l}l}_{\mathbf{k}} v^l_{\mathbf{k},n} \tag{II.220}$$

This can then be used to prove the unitarity of $\tilde{D}$:

$$\begin{aligned}
\tilde{D}^{ml}_{\mathbf{k}} \left(\tilde{D}^{\dagger}_{\mathbf{k}}\right)^{ln} &= \sum_l \left(\sum_{a\tilde{a}} v^{\tilde{a}*}_{R\mathbf{k},m} D^{\tilde{a}a}_{\mathbf{k}} v^a_{\mathbf{k},l} \right) \left(\sum_{b\tilde{b}} v^{\tilde{b}*}_{R\mathbf{k},n} D^{\tilde{b}b}_{\mathbf{k}} v^b_{\mathbf{k},l} \right)^* \\
&= \sum_l \sum_{a\tilde{a}} \sum_{b\tilde{b}} v^{\tilde{a}*}_{R\mathbf{k},m} D^{\tilde{a}a}_{\mathbf{k}} v^a_{\mathbf{k},l} v^{\tilde{b}}_{R\mathbf{k},n} D^{\tilde{b}b*}_{\mathbf{k}} v^{b*}_{\mathbf{k},l} = \sum_{a\tilde{a}} \sum_{\tilde{b}} v^{\tilde{a}*}_{R\mathbf{k},m} D^{\tilde{a}a}_{\mathbf{k}} v^{\tilde{b}}_{R\mathbf{k},n} D^{\tilde{b}a*}_{\mathbf{k}} \qquad \text{(II.221)} \\
&= \sum_{\tilde{a}} \sum_{\tilde{b}} v^{\tilde{a}*}_{R\mathbf{k},m} v^{\tilde{b}}_{R\mathbf{k},n} \delta_{\tilde{a}\tilde{b}} = \delta_{mn} \implies
\end{aligned}$$

$$\tilde{D}^{ml}_{\mathbf{k}} \left(\tilde{D}^{\dagger}_{\mathbf{k}}\right)^{ln} = \delta_{mn} \Leftrightarrow \tilde{D}_{\mathbf{k}} \tilde{D}^{\dagger}_{\mathbf{k}} = \mathbb{1} \tag{II.222}$$

Here, the unitarity of the C_4 sewing matrix D, already known from Ref. [75], is used.

II.B.2. Proof that the C_4 Sewing Matrix $\tilde{D}$ is Block-Diagonal

We continue with the proof that the C_4 sewing matrix $\tilde{D}$ is block-diagonal. This proof follows along the lines of equations A6 to A8 of Schindler et al.[75], but is more involved due to the added complexity encountered dealing with special subspaces of the occupied space. The central element of the proof is that

$$\mathfrak{A} = \sum_m |b^m_{R\mathbf{k}}\rangle \, \tilde{D}^{mn}_{\mathbf{k}} \left[\kappa_{\mathbf{k},n} - \kappa_{R\mathbf{k},m}\right] = 0. \tag{II.223}$$

Due to the fact that $|b^m_{R\mathbf{k}}\rangle$ form a basis of the occupied space and the gap, which ensures that κ belonging to different C_4-spaces, the latter term $[\kappa_{\mathbf{k},n} - \kappa_{R\mathbf{k},m}]$ is always nonzero for different $\mathring{\Psi}$ bands. This ensures that $\tilde{D}^{mn}_{\mathbf{k}}$ is block-diagonal. The proof goes as follows.

$$\begin{aligned}
\mathfrak{A} = \sum_m |b^m_{R\mathbf{k}}\rangle \, \tilde{D}^{mn}_{\mathbf{k}} \left[\kappa_{\mathbf{k},n} - \kappa_{R\mathbf{k},m}\right] &= \sum_m |b^m_{R\mathbf{k}}\rangle \, \tilde{D}^{mn}_{\mathbf{k}} \kappa_{\mathbf{k},n} - \sum_m |b^m_{R\mathbf{k}}\rangle \, \tilde{D}^{mn}_{\mathbf{k}} \kappa_{R\mathbf{k},m}, \\
&= \kappa_{\mathbf{k},n} r \, |b^n_{\mathbf{k}}\rangle - \sum_m \kappa_{R\mathbf{k},m} \, |b^m_{R\mathbf{k}}\rangle \, \langle b^m_{R\mathbf{k}}|r|b^n_{\mathbf{k}}\rangle \,, \qquad \text{(II.224)} \\
&= \kappa_{\mathbf{k},n} r \, |b^n_{\mathbf{k}}\rangle - \sum_{ml} \kappa_{R\mathbf{k},m} v^l_{R\mathbf{k},m} \left| u^l_{R\mathbf{k}} \right\rangle \langle b^m_{R\mathbf{k}}|r|b^n_{\mathbf{k}}\rangle \,.
\end{aligned}$$

Then we apply equation II.219: $\left(\kappa_{\mathbf{k},n} v^m_{\mathbf{k},n} = \left\langle u^m_{\mathbf{k}} \middle| \mathring{\psi}_{\mathbf{k}} \middle| b^n_{\mathbf{k}} \right\rangle\right)$, to obtain

$$\mathfrak{A} = \kappa_{\mathbf{k},n} r \, |b^n_{\mathbf{k}}\rangle - \sum_{ml} \left\langle u^l_{R\mathbf{k}} \middle| \mathring{\psi}_{R\mathbf{k}} \middle| b^m_{R\mathbf{k}} \right\rangle \left| u^l_{R\mathbf{k}} \right\rangle \langle b^m_{R\mathbf{k}}|r|b^n_{\mathbf{k}}\rangle \tag{II.225}$$

We observe that $\sum_m |b^m_{R\mathbf{k}}\rangle\langle b^m_{R\mathbf{k}}|$ is a projector on the occupied subspace at the rotated position. We know from Ref. [75] that sewing matrices only connect states from the occupied/unoccupied subspace with each other. The projector therefore acts as an identity

$$\mathfrak{A} = \kappa_{\mathbf{k},n} r \left|b^n_{\mathbf{k}}\right\rangle - \sum_l \left\langle u^l_{R\mathbf{k}} \middle| \mathring{\psi}_{R\mathbf{k}} r \middle| b^n_{\mathbf{k}} \right\rangle \left|u^l_{R\mathbf{k}}\right\rangle . \tag{II.226}$$

Using that $r\mathring{\psi}_{\mathbf{k}} r^\dagger = \mathring{\psi}_{R\mathbf{k}} \implies r\mathring{\psi}_{\mathbf{k}} = \mathring{\psi}_{R\mathbf{k}} r$, we obtain

$$\mathfrak{A} = \kappa_{\mathbf{k},n} r \left|b^n_{\mathbf{k}}\right\rangle - r \sum_l r^\dagger \left|u^l_{R\mathbf{k}}\right\rangle \left\langle u^l_{R\mathbf{k}} \middle| r\mathring{\psi}_{\mathbf{k}} \middle| b^n_{\mathbf{k}} \right\rangle \tag{II.227}$$

is obtained. To proceed, we define another sewing matrix Q through

$$r^\dagger \left|u^l_{R\mathbf{k}}\right\rangle = \sum_m \left|u^m_{\mathbf{k}}\right\rangle \left\langle u^m_{\mathbf{k}}\right| r^\dagger \left|u^l_{R\mathbf{k}}\right\rangle = \sum_m \left|u^m_{\mathbf{k}}\right\rangle Q^{ml}_{\mathbf{k}} . \tag{II.228}$$

Q is unitary, since

$$\sum_l Q^{ml}_{\mathbf{k}} \left(Q^\dagger_{\mathbf{k}}\right)^{ln} = \left\langle u^m_{\mathbf{k}} \middle| r^\dagger \middle| u^l_{R\mathbf{k}} \right\rangle \left\langle u^l_{R\mathbf{k}} \middle| r \middle| u^n_{\mathbf{k}} \right\rangle = \delta_{mn} . \tag{II.229}$$

Setting this into the main equation, we obtain

$$\begin{aligned}
\mathfrak{A} &= \kappa_{\mathbf{k},n} r \left|b^n_{\mathbf{k}}\right\rangle - r \sum_l \sum_m \left|u^m_{\mathbf{k}}\right\rangle Q^{ml}_{\mathbf{k}} \sum_{\tilde{m}} Q^{\tilde{m}l*}_{\mathbf{k}} \left\langle u^{\tilde{m}}_{\mathbf{k}} \middle| \mathring{\psi}_{\mathbf{k}} \middle| b^n_{\mathbf{k}} \right\rangle , \\
&= \kappa_{\mathbf{k},n} r \left|b^n_{\mathbf{k}}\right\rangle - r \sum_{lm\tilde{m}} \left|u^m_{\mathbf{k}}\right\rangle Q^{ml}_{\mathbf{k}} \left(Q^\dagger_{\mathbf{k}}\right)^{l\tilde{m}} \left\langle u^{\tilde{m}}_{\mathbf{k}} \middle| \mathring{\psi}_{\mathbf{k}} \middle| b^n_{\mathbf{k}} \right\rangle , \\
&= \kappa_{\mathbf{k},n} r \left|b^n_{\mathbf{k}}\right\rangle - r \sum_m \left|u^m_{\mathbf{k}}\right\rangle \left\langle u^m_{\mathbf{k}} \middle| \mathring{\psi}_{\mathbf{k}} \middle| b^n_{\mathbf{k}} \right\rangle = \kappa_{\mathbf{k},n} r \left|b^n_{\mathbf{k}}\right\rangle - r \sum_m \left|u^m_{\mathbf{k}}\right\rangle \kappa_{\mathbf{k},n} v^m_{\mathbf{k},n} , \\
&= \kappa_{\mathbf{k},n} r \left|b^n_{\mathbf{k}}\right\rangle - r \kappa_{\mathbf{k},n} \left|b^n_{\mathbf{k}}\right\rangle = 0.
\end{aligned} \tag{II.230}$$

This proves that

$$\sum_m \left|b^m_{R\mathbf{k}}\right\rangle \tilde{D}^{mn}_{\mathbf{k}} \left[\kappa_{\mathbf{k},n} - \kappa_{R\mathbf{k},m}\right] = 0 \tag{II.231}$$

and therefore that $\tilde{D}$ is block-diagonal.
This is because the $\left|b^m_{R\mathbf{k}}\right\rangle$ are orthonormal, which means that each of the elements of the sum can be evaluated seperately, which implies that

$$\tilde{D}^{mn}_{\mathbf{k}} \left[\kappa_{\mathbf{k},n} - \kappa_{R\mathbf{k},m}\right] = 0, \tag{II.232}$$

which proves the block-diagonality. □

II.B.3. Proof that the C_4 Sewing Matrix is Block-Diagonal

The proof of the block-diagonality of the TRS sewing matrix largely follows the same lines as the proof for the C_4 sewing matrix, with a slight complication due to the antiunitary nature of the time reversal operator.
The time-reversal sewing matrix is defined as

$$\tilde{B}^{mn}_{\mathbf{k}} = \left\langle b^m_{-\mathbf{k}} \middle| \mathcal{T} \middle| b^n_{\mathbf{k}} \right\rangle = \left\langle b^m_{-\mathbf{k}} \middle| \tau K \middle| b^n_{\mathbf{k}} \right\rangle . \tag{II.233}$$

The corresponding operator on the original states, before applying $\mathring{\Psi}$, is

$$B_{\mathbf{k}}^{mn} = \left\langle u_{-\mathbf{k}}^{m} \middle| \mathcal{T} \middle| u_{\mathbf{k}}^{n} \right\rangle = \left\langle u_{-\mathbf{k}}^{m} \middle| \tau K \middle| u_{\mathbf{k}}^{n} \right\rangle . \tag{II.234}$$

TRS has the properties

$$\mathcal{T} = \tau K \qquad \mathcal{T}^{-1} = \mathcal{T}^{\dagger} = (\tau K)^{\dagger} = K \tau^{\dagger}. \tag{II.235}$$

In order to prove the block-diagonality of $\tilde{B}$, we want to prove that

$$\mathfrak{B} = \sum_{m} \left| b_{-\mathbf{k}}^{m} \right\rangle \tilde{B}_{\mathbf{k}}^{mn} \left[\kappa_{\mathbf{k},n} - \kappa_{-\mathbf{k},m} \right] = 0. \tag{II.236}$$

We procede as

$$\begin{aligned}
\mathfrak{B} &= \sum_{m} \left| b_{-\mathbf{k}}^{m} \right\rangle \tilde{B}_{\mathbf{k}}^{mn} \left[\kappa_{\mathbf{k},n} - \kappa_{-\mathbf{k},m} \right] = \sum_{m} \left| b_{-\mathbf{k}}^{m} \right\rangle \tilde{B}_{\mathbf{k}}^{mn} \kappa_{\mathbf{k},n} - \sum_{m} \left| b_{-\mathbf{k}}^{m} \right\rangle \tilde{B}_{\mathbf{k}}^{mn} \kappa_{-\mathbf{k},m}, \\
&= \kappa_{\mathbf{k},n} \sum_{m} \tilde{B}_{\mathbf{k}}^{mn} \left| b_{-\mathbf{k}}^{m} \right\rangle - \sum_{m} \left| b_{-\mathbf{k}}^{m} \right\rangle \tilde{B}_{\mathbf{k}}^{mn} \kappa_{-\mathbf{k},m}, \\
&= \kappa_{\mathbf{k},n} \sum_{m} \left\langle b_{-\mathbf{k}}^{m} \middle| \mathcal{T} \middle| b_{\mathbf{k}}^{n} \right\rangle \left| b_{-\mathbf{k}}^{m} \right\rangle - \sum_{m} \left| b_{-\mathbf{k}}^{m} \right\rangle \tilde{B}_{\mathbf{k}}^{mn} \kappa_{-\mathbf{k},m}, \\
&= \kappa_{\mathbf{k},n} \sum_{m} \left| b_{-\mathbf{k}}^{m} \right\rangle \left\langle b_{-\mathbf{k}}^{m} \middle| \mathcal{T} \middle| b_{\mathbf{k}}^{n} \right\rangle - \sum_{m} \left| b_{-\mathbf{k}}^{m} \right\rangle \tilde{B}_{\mathbf{k}}^{mn} \kappa_{-\mathbf{k},m}, \\
&= \kappa_{\mathbf{k},n} \mathcal{T} \left| b_{\mathbf{k}}^{n} \right\rangle - \sum_{m} \tilde{B}_{\mathbf{k}}^{mn} \kappa_{-\mathbf{k},m} \left| b_{-\mathbf{k}}^{m} \right\rangle = \kappa_{\mathbf{k},n} \mathcal{T} \left| b_{\mathbf{k}}^{n} \right\rangle - \sum_{m} \kappa_{-\mathbf{k},m} \left| b_{-\mathbf{k}}^{m} \right\rangle \left\langle b_{-\mathbf{k}}^{m} \middle| \mathcal{T} \middle| b_{\mathbf{k}}^{n} \right\rangle , \\
&= \kappa_{\mathbf{k},n} \mathcal{T} \left(\sum_{m} v_{\mathbf{k},n}^{m} \left| u_{\mathbf{k}}^{m} \right\rangle \right) - \sum_{m} \kappa_{-\mathbf{k},m} \sum_{j} v_{-\mathbf{k},m}^{j} \left| u_{-\mathbf{k}}^{j} \right\rangle \left\langle b_{-\mathbf{k}}^{m} \middle| \mathcal{T} \middle| b_{\mathbf{k}}^{n} \right\rangle .
\end{aligned} \tag{II.237}$$

In order to arrive at the next step, we use the Hermiticity of $\mathring{\Psi}_{\mathbf{k}}^{mn}$. We get

$$\mathfrak{B} = \mathcal{T} \left(\sum_{m} \kappa_{\mathbf{k},n} v_{\mathbf{k},n}^{m} \left| u_{\mathbf{k}}^{m} \right\rangle \right) - \sum_{mj} \kappa_{-\mathbf{k},m} v_{-\mathbf{k},m}^{j} \left| u_{-\mathbf{k}}^{j} \right\rangle \left\langle b_{-\mathbf{k}}^{m} \middle| \mathcal{T} \middle| b_{\mathbf{k}}^{n} \right\rangle \tag{II.238}$$

After that, we use equation II.219 to remove the v-components

$$\mathfrak{B} = \mathcal{T} \left(\sum_{m} \left\langle u_{\mathbf{k}}^{m} \middle| \mathring{\psi}_{\mathbf{k}} \middle| b_{\mathbf{k}}^{n} \right\rangle \left| u_{\mathbf{k}}^{m} \right\rangle \right) - \sum_{mj} \left\langle u_{-\mathbf{k}}^{j} \middle| \mathring{\psi}_{-\mathbf{k}} \middle| b_{-\mathbf{k}}^{m} \right\rangle \left\langle b_{-\mathbf{k}}^{m} \middle| \mathcal{T} \middle| b_{\mathbf{k}}^{n} \right\rangle \left| u_{-\mathbf{k}}^{j} \right\rangle , \tag{II.239}$$

and continue by using that $|b_k\rangle$ span the occupied subspace

$$\mathfrak{B} = \mathcal{T} \left(\sum_{m} \left\langle u_{\mathbf{k}}^{m} \middle| \mathring{\psi}_{\mathbf{k}} \middle| b_{\mathbf{k}}^{n} \right\rangle \left| u_{\mathbf{k}}^{m} \right\rangle \right) - \sum_{j} \left\langle u_{-\mathbf{k}}^{j} \middle| \mathring{\psi}_{-\mathbf{k}} \mathcal{T} \middle| b_{\mathbf{k}}^{n} \right\rangle \left| u_{-\mathbf{k}}^{j} \right\rangle , \tag{II.240}$$

and then using that $\mathcal{T}\mathring{\psi}_{\mathbf{k}}\mathcal{T}^{-1} = \mathring{\psi}_{-\mathbf{k}} \Leftrightarrow \mathcal{T}\mathring{\psi}_{\mathbf{k}} = \mathring{\psi}_{-\mathbf{k}}\mathcal{T}$ and perform a few manipulations

$$\begin{aligned}
\mathfrak{B} &= \mathcal{T}\left(\sum_m \left\langle u^m_{\mathbf{k}}\middle|\mathring{\psi}_{\mathbf{k}}\middle|b^n_{\mathbf{k}}\right\rangle \left|u^m_{\mathbf{k}}\right\rangle\right) - \mathcal{T}\mathcal{T}^{-1}\left(\sum_j \left\langle u^j_{-\mathbf{k}}\middle|\mathring{\psi}_{-\mathbf{k}}\mathcal{T}\middle|b^n_{\mathbf{k}}\right\rangle \left|u^j_{-\mathbf{k}}\right\rangle\right), \\
&= \mathcal{T}\left(\sum_m \left\langle u^m_{\mathbf{k}}\middle|\mathring{\psi}_{\mathbf{k}}\middle|b^n_{\mathbf{k}}\right\rangle \left|u^m_{\mathbf{k}}\right\rangle\right) - \mathcal{T}\left(K\tau^\dagger\left(\sum_j \left\langle u^j_{-\mathbf{k}}\middle|\mathring{\psi}_{-\mathbf{k}}\mathcal{T}\middle|b^n_{\mathbf{k}}\right\rangle \left|u^j_{-\mathbf{k}}\right\rangle\right)\right), \qquad \text{(II.241)} \\
&= \mathcal{T}\left(\sum_m \left\langle u^m_{\mathbf{k}}\middle|\mathring{\psi}_{\mathbf{k}}\middle|b^n_{\mathbf{k}}\right\rangle \left|u^m_{\mathbf{k}}\right\rangle\right) - \mathcal{T}\overline{\left(\sum_j \left\langle u^j_{-\mathbf{k}}\middle|\mathring{\psi}_{-\mathbf{k}}\mathcal{T}\middle|b^n_{\mathbf{k}}\right\rangle \tau^\dagger \left|u^j_{-\mathbf{k}}\right\rangle\right)},
\end{aligned}$$

to obtain

$$\mathfrak{B} = \mathcal{T}\left(\sum_m \left\langle u^m_{\mathbf{k}}\middle|\mathring{\psi}_{\mathbf{k}}\middle|b^n_{\mathbf{k}}\right\rangle \left|u^m_{\mathbf{k}}\right\rangle\right) - \mathcal{T}\left(\sum_j \overline{\left\langle u^j_{-\mathbf{k}}\middle|\mathcal{T}\mathring{\psi}_{\mathbf{k}}\middle|b^n_{\mathbf{k}}\right\rangle} K\tau^\dagger \left|u^j_{-\mathbf{k}}\right\rangle\right). \qquad \text{(II.242)}$$

In order to continue from here onwards, we make some helper calculations to elucidate the effects of the complex conjugation. These helper calculation are partly in component representation instead of the bra-ket formalism.

$$\begin{aligned}
\left\langle u^j_{-\mathbf{k}}\middle|\mathcal{T}\mathring{\psi}_{\mathbf{k}}\middle|b^n_{\mathbf{k}}\right\rangle &= \left\langle u^j_{-\mathbf{k}}\middle|\tau K\mathring{\psi}_{\mathbf{k}}\middle|b^n_{\mathbf{k}}\right\rangle = \left\langle u^j_{-\mathbf{k}}\right| \tau \left(\mathring{\psi}_{\mathbf{k}}\left|b^n_{\mathbf{k}}\right\rangle\right)^* \\
&= \left\langle u^j_{-\mathbf{k}}\right| \tau\mathring{\psi}^*_{\mathbf{k}}\left|b^n_{\mathbf{k}}\right\rangle^* = (\vec{u}^j_{-\mathbf{k}})^\dagger\tau\mathring{\psi}^*_{\mathbf{k}}\vec{b}^{n*}_{\mathbf{k}} \\
&\implies \overline{\left\langle u^j_{-\mathbf{k}}\middle|\mathcal{T}\mathring{\psi}_{\mathbf{k}}\middle|b^n_{\mathbf{k}}\right\rangle} = (\vec{u}^j_{-\mathbf{k}})^T\tau^*\mathring{\psi}_{\mathbf{k}}\vec{b}^n_{\mathbf{k}}. \qquad \text{(II.243)}
\end{aligned}$$

We also observe that

$$\begin{aligned}
\left((\vec{u}^j_{-\mathbf{k}})^T\tau^*\right)^\dagger &= \left(\tau^T\vec{u}^{j*}_{-\mathbf{k}}\right) = K\tau^\dagger\left|u^j_{-\mathbf{k}}\right\rangle = \sum_m \left|u^m_{\mathbf{k}}\right\rangle\left\langle u^m_{\mathbf{k}}\right| K\tau^\dagger\left|u^j_{-\mathbf{k}}\right\rangle \\
&= \sum_m \left|u^m_{\mathbf{k}}\right\rangle O^{mj}_{\mathbf{k}} = \left(\sum_m \left\langle u^m_{\mathbf{k}}\right| O^{mj*}_{\mathbf{k}}\right)^\dagger. \qquad \text{(II.244)}
\end{aligned}$$

This then allows us to find

$$\begin{aligned}
\overline{\left\langle u^j_{-\mathbf{k}}\middle|\mathcal{T}\mathring{\psi}_{\mathbf{k}}\middle|b^n_{\mathbf{k}}\right\rangle} &= (\vec{u}^j_{-\mathbf{k}})^T\tau^*\mathring{\psi}_{\mathbf{k}}\vec{b}^n_{\mathbf{k}} = \left(\left((\vec{u}^j_{-\mathbf{k}})^T\tau^*\right)^\dagger\right)^\dagger \mathring{\psi}_{\mathbf{k}}\vec{b}^n_{\mathbf{k}} \\
&= \left(\left(\sum_m \left\langle u^m_{\mathbf{k}}\right| O^{mj*}_{\mathbf{k}}\right)^\dagger\right)^\dagger \mathring{\psi}_{\mathbf{k}}\left|b^n_{\mathbf{k}}\right\rangle = \sum_m \left\langle u^m_{\mathbf{k}}\right| O^{mj*}_{\mathbf{k}}\mathring{\psi}_{\mathbf{k}}\left|b^n_{\mathbf{k}}\right\rangle. \qquad \text{(II.245)}
\end{aligned}$$

We then continue with the main calculation, using these helpful expressions, obtaining

$$\begin{aligned}
\mathfrak{B} &= \mathcal{T}\left(\sum_m \left\langle u^m_{\mathbf{k}}\middle|\mathring{\psi}_{\mathbf{k}}\middle|b^n_{\mathbf{k}}\right\rangle \left|u^m_{\mathbf{k}}\right\rangle\right) - \mathcal{T}\left(\sum_{jl}\sum_m \left\langle u^m_{\mathbf{k}}\right| O^{mj*}_{\mathbf{k}}\mathring{\psi}_{\mathbf{k}}\left|b^n_{\mathbf{k}}\right\rangle O^{lj}_{\mathbf{k}}\left|u^l_{\mathbf{k}}\right\rangle\right), \\
&= \mathcal{T}\left(\sum_m \left\langle u^m_{\mathbf{k}}\middle|\mathring{\psi}_{\mathbf{k}}\middle|b^n_{\mathbf{k}}\right\rangle \left|u^m_{\mathbf{k}}\right\rangle\right) - \mathcal{T}\left(\sum_{lm}\sum_j O^{lj}_{\mathbf{k}}\left(O^\dagger_{\mathbf{k}}\right)^{jm}\left\langle u^m_{\mathbf{k}}\right| \mathring{\psi}_{\mathbf{k}}\left|b^n_{\mathbf{k}}\right\rangle\left|u^l_{\mathbf{k}}\right\rangle\right),
\end{aligned} \qquad \text{(II.246)}$$

then using the unitarity of $O_{\mathbf{k}}^{mn}$, which can be proved as

$$\sum_j O_{\mathbf{k}}^{lj} \left(O_{\mathbf{k}}^{\dagger}\right)^{jm} = \sum_j \left\langle u_{\mathbf{k}}^{l} \middle| K\tau^{\dagger} \middle| u_{-\mathbf{k}}^{j} \right\rangle \left\langle u_{-\mathbf{k}}^{j} \middle| \tau K \middle| u_{\mathbf{k}}^{m} \right\rangle = \delta_{ml}, \tag{II.247}$$

to get

$$\begin{aligned} \mathfrak{B} &= \mathcal{T}\left(\sum_m \left\langle u_{\mathbf{k}}^{m} \middle| \mathring{\psi}_{\mathbf{k}} \middle| b_{\mathbf{k}}^{n} \right\rangle \left| u_{\mathbf{k}}^{m} \right\rangle\right) - \mathcal{T}\left(\sum_{lm} \delta_{ml} \left\langle u_{\mathbf{k}}^{m}\right| \mathring{\psi}_{\mathbf{k}} \left|b_{\mathbf{k}}^{n}\right\rangle \left| u_{\mathbf{k}}^{l} \right\rangle\right), \\ &= \mathcal{T}\left(\sum_m \left\langle u_{\mathbf{k}}^{m} \middle| \mathring{\psi}_{\mathbf{k}} \middle| b_{\mathbf{k}}^{n} \right\rangle \left| u_{\mathbf{k}}^{m} \right\rangle\right) - \mathcal{T}\left(\sum_{m} \left\langle u_{\mathbf{k}}^{m}\right| \mathring{\psi}_{\mathbf{k}} \left|b_{\mathbf{k}}^{n}\right\rangle \left| u_{\mathbf{k}}^{m} \right\rangle\right) = 0. \end{aligned} \tag{II.248}$$

Thus we have proved that

$$\sum_m \left| b_{-\mathbf{k}}^{m} \right\rangle \tilde{B}_{\mathbf{k}}^{mn} \left[\kappa_{\mathbf{k},n} - \kappa_{-\mathbf{k},m}\right] = 0. \tag{II.249}$$

As before, this implies that

$$\tilde{B}_{\mathbf{k}}^{mn} \left[\kappa_{\mathbf{k},n} - \kappa_{-\mathbf{k},m}\right] = 0 \tag{II.250}$$

and this implies that the $\tilde{B}_{\mathbf{k}}^{mn}$ is block-diagonal.

II.B.4. Further Splitting of Pairs of Bands

This section deals with two bands that cannot be further split with a $\mathring{\psi}_{\mathbf{k}}$ that satisfies $\mathcal{T}\mathring{\psi}_{\mathbf{k}}\mathcal{T}^{-1} = \mathring{\psi}_{-\mathbf{k}}$. In this case we break the $\mathcal{T}$-symemtry maximally and define $\mathring{\psi}_{\mathbf{k}}$ such that $\mathcal{T}\mathring{\psi}_{\mathbf{k}}\mathcal{T}^{-1} = -\mathring{\psi}_{-\mathbf{k}}$. In the case of two bands, the $\mathcal{T}$-sewing matrix is then off-diagonal and $\mathcal{T}$ maps one band onto the other.

The off-diagonality of the sewing matrix follows from the symmetric Wannier splitting theorem [131, p. 17].

Alternatively, it can be proved as follows. First, we examine the matrix $\mathring{\Psi}_{\mathbf{k}}^{mn} = \left\langle u_{\mathbf{k}}^{m} \middle| \mathring{\psi}_{\mathbf{k}} \middle| u_{\mathbf{k}}^{n} \right\rangle$ for different $\mathbf{k}$. We use that the occupied occupied space spanned by $\left|u_{\mathbf{k}}^{m}\right\rangle$ at $\mathbf{k}$ is spanned by $r\left|u_{\mathbf{k}}^{m}\right\rangle$ at $R\mathbf{k}$ as well as $\mathcal{T}\left|u_{\mathbf{k}}^{m}\right\rangle$ at $-\mathbf{k}$, and that the eigenvalues of $\mathring{\Psi}_{\mathbf{k}}^{mn}$ are independent of the choice of $\left|u_{\mathbf{k}}^{m}\right\rangle$. First, we observe that

$$\left\langle u_{R\mathbf{k}}^{m} \middle| \mathring{\psi}_{R\mathbf{k}} \middle| u_{R\mathbf{k}}^{n} \right\rangle = \left\langle u_{\mathbf{k}}^{m} \middle| r^{\dagger} r \mathring{\psi}_{\mathbf{k}} r^{\dagger} r \middle| u_{\mathbf{k}}^{n} \right\rangle = \left\langle u_{\mathbf{k}}^{m} \middle| \mathring{\psi}_{\mathbf{k}} \middle| u_{\mathbf{k}}^{n} \right\rangle \implies \mathring{\Psi}_{R\mathbf{k}} = \mathring{\Psi}_{\mathbf{k}}, \tag{II.251}$$

and for $r = r_2$,

$$\mathring{\Psi}_{-\mathbf{k}} = \mathring{\Psi}_{\mathbf{k}}, \tag{II.252}$$

which implies that the eigenvalues at $\mathbf{k}$ and $-\mathbf{k}$ are the same. Secondly, we realise that

$$\begin{aligned} \left\langle u_{-\mathbf{k}}^{m} \middle| \mathring{\psi}_{-\mathbf{k}} \middle| u_{-\mathbf{k}}^{n} \right\rangle &= -\left(\left\langle u_{\mathbf{k}}^{m}\right|\right)^{*} \tau^{\dagger}\tau K \mathring{\psi}_{\mathbf{k}} K \tau^{\dagger}\tau \left(\left|u_{\mathbf{k}}^{n}\right\rangle\right)^{*} = -\left(\left\langle u_{\mathbf{k}}^{m}\right|\right)^{*} \mathring{\psi}_{\mathbf{k}}^{*} \left(\left|u_{\mathbf{k}}^{n}\right\rangle\right)^{*} \\ &= -\left\langle u_{\mathbf{k}}^{m} \middle| \mathring{\psi}_{\mathbf{k}} \middle| u_{\mathbf{k}}^{n} \right\rangle^{*} = -\left\langle u_{\mathbf{k}}^{n} \middle| \mathring{\psi}_{\mathbf{k}} \middle| u_{\mathbf{k}}^{m} \right\rangle \implies \mathring{\Psi}_{-\mathbf{k}} = -\mathring{\Psi}_{\mathbf{k}}^{T} \end{aligned} \tag{II.253}$$

using that $\mathcal{T} = \tau K$, $\mathcal{T}^{-1} = K\tau^{\dagger}$ and the Hermiticity of $\mathring{\Psi}_{\mathbf{k}}$. Because the eigenvalues of a matrix and its transpose are the same, the eigenvalues of $\mathring{\Psi}_{-\mathbf{k}}$ are minus the eigenvalues of

$\mathring{\Psi}_{\mathbf{k}}$. Together with equation II.252 this implies that the bands have the C_n symmetry of the involved $\mathring{\psi}_{\mathbf{k}}$ and that the eigenvalues of $\mathring{\Psi}_{\mathbf{k}}$ appear in real pairs $\pm\kappa_n$, if we have C_2 symmetry. If we only have C_3 symmetry, the bands are C_3-symmetric and inversion symmetric with respect to the origin of the BZ. We now compare this with the situation in the previous proof of block(-off)-diagonality, taking the changes due to the different properties of $\mathring{\psi}_{\mathbf{k}}$ into account. The only change to the proof appears in equation II.242, where a minus appears in front of the second term. Following everything through, we get

$$\tilde{B}^{mn}_{\mathbf{k}} \left[\kappa_{\mathbf{k},n} + \kappa_{-\mathbf{k},m}\right] = 0. \tag{II.254}$$

For $m = n$, the term $[\kappa_{\mathbf{k},n} + \kappa_{-\mathbf{k},m}]$ is nonzero, therefore $\tilde{B}^{mn}$ has to vanish. On the contrary, for $m \neq n$, the term $[\kappa_{\mathbf{k},n} + \kappa_{-\mathbf{k},m}] = 0$ and therefore the $\tilde{B}^{mn}$ does not have to vanish. This proves the off-diagonality of the sewing matrix. For the case of C_3 symmetry, the required condition of the PSO-band structure is that it does not intersect zero at any point in the BZ. In other words, as Alexandradinata et al.[131] already observed , the $\mathcal{T}$ operator carries us from one band to the other.

II.C. Perturbation of $\mathring{\Psi}_{\mathbf{k}}$ Instead of $\mathring{\psi}_{\mathbf{k}}$

In this paragraph, we'll have a look at the effect of perturbations of $\mathring{\Psi}_{\mathbf{k}}$. More precisely, we'll have a short look at what happens if we directly perturb $\mathring{\Psi}_{\mathbf{k}}$ instead of perturbing $\mathring{\psi}_{\mathbf{k}}$. In principle, it's possible to perturb $\mathring{\Psi}_{\mathbf{k}}$ instead of $\mathring{\psi}_{\mathbf{k}}$, because for a perturbation $\tilde{\mathring{\psi}}_{\mathbf{k}} = \mathring{\psi}_{\mathbf{k}} + \delta\mathring{\psi}_{\mathbf{k}}$, the corresponding perturbation of $\mathring{\Psi}^{mn}_{\mathbf{k}}$ is $\left\langle u^m_{\mathbf{k}} \middle| \delta\mathring{\psi}_{\mathbf{k}} \middle| u^n_{\mathbf{k}} \right\rangle$. The problem with this term is that it is dependent on the gauge choice for $|u^m_{\mathbf{k}}\rangle$. If, like it is usually the case, the $|u^n_{\mathbf{k}}\rangle$ do not form a smooth gauge, the $\left\langle u^m_{\mathbf{k}} \middle| \delta\mathring{\psi}_{\mathbf{k}} \middle| u^n_{\mathbf{k}} \right\rangle$ is expected to dependent in a discontinuous way on $\mathbf{k}$. This makes the construction of a good perturbation of $\mathring{\Psi}_{\mathbf{k}}$ rather complicated, since constant terms as well smooth terms are normally forbidden. It is therefore much easier to perturb $\mathring{\psi}_{\mathbf{k}}$ instead of $\mathring{\Psi}_{\mathbf{k}}$.

In order to show the effects, we depict in Fig. II.43 the effect of a relatively big random Hermitian perturbation of $\mathring{\Psi}_{\mathbf{k}}$ to the time reversal symmetric Hamiltonian $H^{(2)}_3(\mathbf{k}, t = 0.2)$, where $\mathring{\Psi}_{\mathbf{k}}$ was calculated using $\mathring{\psi}_{\mathbf{k}} = r_4 + r_4^\dagger$. The perturbation is neither TRS nor C_4-symmetric, because this figure only serves to show that the continuity of the gauge is lost by perturbing $\mathring{\Psi}_{\mathbf{k}}$.

II.D. Calculation of Wilson Loop in Occupied $\mathring{\Psi}$ Bands Without Diagonalisation

One question one might ask is whether it is possible to obtain something similar to the Wilson loop in the occupied $\mathring{\Psi}$ bands without having to diagonalise the PSO $\mathring{\Psi}^{mn}_{\mathbf{k}} = \left\langle u^m_{\mathbf{k}} \middle| \mathring{\psi}_{\mathbf{k}} \middle| u^n_{\mathbf{k}} \right\rangle$. One way to do this is to work directly with eigenstates of the full occupied subspace. This can for example be done as follows. We first define the eigenvector $|v^n\rangle$ as the eigenvectors of $\mathring{\psi}_{\mathbf{\Gamma}}$. These eigenvectors come in two groups, at least in the case of $\mathring{\psi}_{\mathbf{\Gamma}} \approx r_4 + r_4^\dagger$, those with negative and those with positive real part of their eigenvalues. To look at one of the quantities

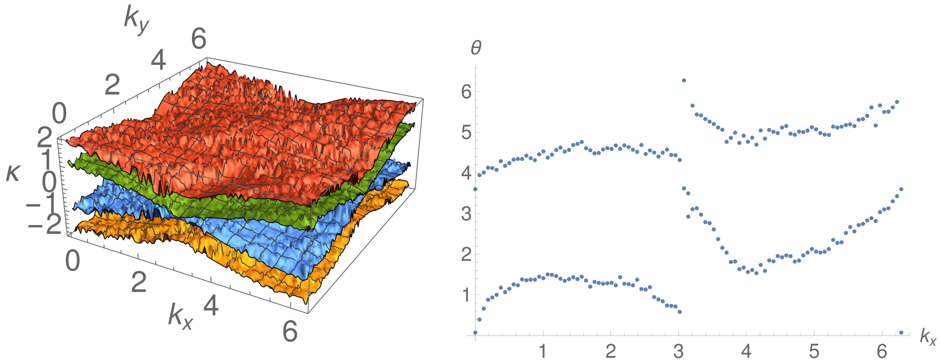

Figure II.43.: $\mathring{\Psi}$ band structure and Wilson loop spectrum of $H_3^{(2)}(\mathbf{k}, t = 0.2)$ with a quite strong Hermitian (but not TRS or C_4-symmetric) perturbation to $\mathring{\Psi}_{\mathbf{k}}$ (not to $\mathring{\psi}_{\mathbf{k}}$). Continuity is lost.

we're interested in, we choose for example, the $|v^n\rangle$ with negative eigenvalues. We then define the Wilson loop

$$\tilde{W}_{k_y} = \prod_{i=N}^{1} F^{\mathrm{sym}}_{i\Delta k_x, k_y} \tag{II.255}$$

with

$$F^{\mathrm{sym}}_{k_x,k_y,mn} = \left\langle v^m \middle| \left(\sum_m^{N_{\mathrm{occ}}} \left| u^m_{(k_x,k_y)} \right\rangle \left\langle u^m_{(k_x,k_y)} \right| \right) \middle| v^n \right\rangle . \tag{II.256}$$

Now the arguments of the biggest two eigenvalues of $\tilde{W}$ happen to show the same winding behaviour as the one seen before with the diagonalisation of $\mathring{\Psi}_{\mathbf{k}}$. But this is not always the case, and also does not seem to be reliable, as seen from the two plots in Fig. II.44. On the left-hand side, the figure shows this method applied to $H_{\mathbf{k}} = H_2^{(4)}(\mathbf{k}, t = 0.2)$. There it works nicely, as the arguments of the bigger two of the four eigenvalues show exactly the winding behaviour as seen also with diagonalizing $\mathring{\Psi}_{\mathbf{k}}$. On the right-hand side, the method is applied to $H_{\mathbf{k}} = H_2^{(4)}(\mathbf{k}, t = -0.2) + \frac{4}{5}\alpha_{4\text{ fold}}$, with $\alpha_{4\text{ fold}}$ given in equation II.257, Appendix II.E. In this case, the fourfold winding behaviour seen when diagonlizing $\mathring{\Psi}_{\mathbf{k}}$ is not reproduced. Therefore, we conclude that this method can in general not be applied.

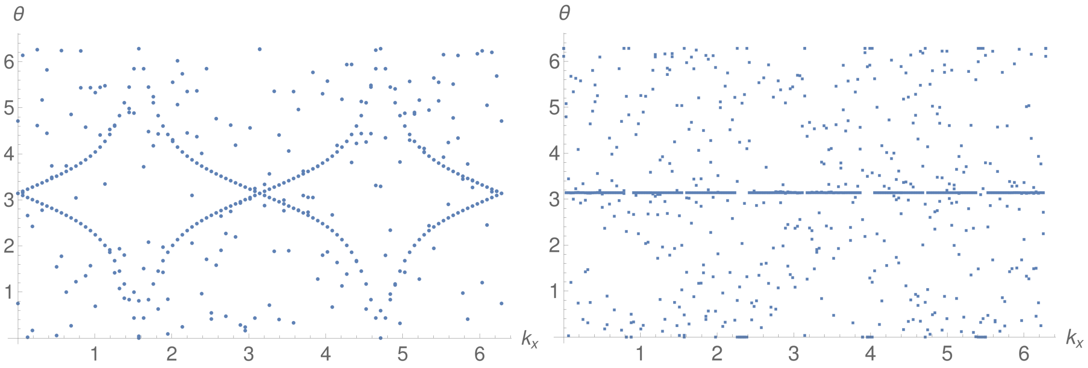

Figure II.44.: "Wilson loop spectrum" of $\tilde{W}_{k_x}$ for $H_2^{(4)}(\mathbf{k}, t = 0.2)$ ($H_\mathbf{k} = H_2^{(4)}(\mathbf{k}, t = -0.2) + \frac{4}{5}\alpha_{4\text{ fold}}$), respectively, when using a method that uses direct projection into the subspace of $r_4 + r_4^\dagger$ with eigenvalues with negative real part.

II.E. Matrices used

This section simply lists the matrices used earlier in the thesis. These are mainly random matrices that were symmetrised.

Perturbation matrix to add onto $H_2^{(4)}(\mathbf{k}, t=-0.2)$ to get fourfold winding, using $\mathring{\psi} = r_4 + r_4^\dagger$:

$$\alpha_{4\text{ fold}} = \begin{pmatrix} & & & & 0 & \frac{1}{2}-\frac{1}{2}i & \frac{1}{2} & \frac{1}{2}+\frac{1}{2}i \\ & & & & -\frac{1}{2}+\frac{1}{2}i & 0 & \frac{1}{2}+\frac{1}{2}i & \frac{1}{2}i \\ & & & & -\frac{1}{2} & -\frac{1}{2}-\frac{1}{2}i & 0 & -\frac{1}{2}+\frac{1}{2}i \\ & & & & -\frac{1}{2}-\frac{1}{2}i & -\frac{1}{2}i & \frac{1}{2}-\frac{1}{2}i & 0 \\ 0 & -\frac{1}{2}-\frac{1}{2}i & -\frac{1}{2} & -\frac{1}{2}+\frac{1}{2}i & & & & \\ \frac{1}{2}+\frac{1}{2}i & 0 & -\frac{1}{2}+\frac{1}{2}i & \frac{1}{2}i & & & & \\ \frac{1}{2} & \frac{1}{2}-\frac{1}{2}i & 0 & \frac{1}{2}+\frac{1}{2}i & & & & \\ \frac{1}{2}-\frac{1}{2}i & -\frac{1}{2}i & -\frac{1}{2}-\frac{1}{2}i & 0 & & & & \end{pmatrix} \tag{II.257}$$

Perturbation to add to $H_2^{(4)}(\mathbf{k})$ to get no winding $(t=0)$ (gauge compatible with $1b \oplus 1b$):

$$\beta = \begin{pmatrix} -1.17286 & 1.15227+1.12084i & 6.15019 & 1.15227-1.12084i & 0 & -0.0204446-1.05086i & -0.782216-0.448727i & 1.05086-0.0204446i \\ 1.15227-1.12084i & -1.17286 & 1.15227+1.12084i & 6.15019 & 0.0204446+1.05086i & 0 & 1.05086-0.0204446i & 0.448727-0.782216i \\ 6.15019 & 1.15227-1.12084i & -1.17286 & 1.15227+1.12084i & 0.782216+0.448727i & -1.05086+0.0204446i & 0 & 0.0204446+1.05086i \\ 1.15227+1.12084i & 6.15019 & 1.15227-1.12084i & -1.17286 & -1.05086+0.0204446i & -0.448727+0.782216i & -0.0204446-1.05086i & 0 \\ 0 & 0.0204446-1.05086i & 0.782216-0.448727i & -1.05086-0.0204446i & -1.17286 & 1.15227-1.12084i & 6.15019 & 1.15227+1.12084i \\ -0.0204446+1.05086i & 0 & -1.05086-0.0204446i & -0.448727-0.782216i & 1.15227+1.12084i & -1.17286 & 1.15227-1.12084i & 6.15019 \\ -0.782216+0.448727i & 1.05086+0.0204446i & 0 & -0.0204446+1.05086i & 6.15019 & 1.15227+1.12084i & -1.17286 & 1.15227-1.12084i \\ 1.05086+0.0204446i & 0.448727+0.782216i & 0.0204446-1.05086i & 0 & 1.15227-1.12084i & 6.15019 & 1.15227+1.12084i & -1.17286 \end{pmatrix} \tag{II.258}$$

The matrix α_{matadd} is given by

$$\alpha_{\text{matadd}} = \begin{pmatrix} -0.216335 & -0.0176005-0.0930735i & 0.0904765 & -0.0176005+0.0930735i & 0 & -0.0478227-0.0386695i & 0.0877777+0.254889i & 0.0386695-0.0478227i \\ -0.0176005+0.0930735i & -0.216335 & -0.0176005-0.0930735i & 0.0904765 & 0.0478227+0.0386695i & 0 & 0.0386695-0.0478227i & -0.254889+0.0877777i \\ 0.0904765 & -0.0176005+0.0930735i & -0.216335 & -0.0176005-0.0930735i & -0.0877777-0.254889i & -0.0386695+0.0478227i & 0 & 0.0478227+0.0386695i \\ -0.0176005-0.0930735i & 0.0904765 & -0.0176005+0.0930735i & -0.216335 & -0.0386695+0.0478227i & 0.254889-0.0877777i & -0.0478227-0.0386695i & 0 \\ 0 & 0.0478227-0.0386695i & -0.0877777+0.254889i & -0.0386695-0.0478227i & -0.216335 & -0.0176005+0.0930735i & 0.0904765 & -0.0176005-0.0930735i \\ -0.0478227+0.0386695i & 0 & -0.0386695-0.0478227i & 0.254889+0.0877777i & -0.0176005-0.0930735i & -0.216335 & -0.0176005+0.0930735i & 0.0904765 \\ 0.0877777-0.254889i & 0.0386695+0.0478227i & 0 & -0.0478227+0.0386695i & 0.0904765 & -0.0176005-0.0930735i & -0.216335 & -0.0176005+0.0930735i \\ 0.0386695+0.0478227i & -0.254889-0.0877777i & 0.0478227-0.0386695i & 0 & -0.0176005+0.0930735i & 0.0904765 & -0.0176005-0.0930735i & -0.216335 \end{pmatrix}. \tag{II.259}$$

Matrices to split $H_3^{(2)}$ to get single bands corresponding to $2c$ are given by

$$\alpha_{2c,\text{first split}} = \begin{pmatrix} -1.96682 & -0.142095-0.619812i & 1.05314 & 0.142095-0.619812i & 0 & -0.473943+1.35656i & 0.866529+0.183234i & 1.35656+0.473943i \\ -0.142095+0.619812i & 1.96682 & 0.142095+0.619812i & -1.05314 & 0.473943-1.35656i & 0 & 1.35656+0.473943i & 0.183234-0.866529i \\ 1.05314 & 0.142095-0.619812i & -1.96682 & -0.142095-0.619812i & -0.866529-0.183234i & -1.35656-0.473943i & 0 & 0.473943-1.35656i \\ 0.142095+0.619812i & -1.05314 & -0.142095+0.619812i & 1.96682 & -1.35656-0.473943i & -0.183234+0.866529i & -0.473943+1.35656i & 0 \\ 0 & 0.473943+1.35656i & -0.866529+0.183234i & -1.35656+0.473943i & -1.96682 & -0.142095+0.619812i & 1.05314 & 0.142095+0.619812i \\ -0.473943-1.35656i & 0 & -1.35656+0.473943i & -0.183234-0.866529i & -0.142095-0.619812i & 1.96682 & 0.142095-0.619812i & -1.05314 \\ 0.866529-0.183234i & 1.35656-0.473943i & 0 & -0.473943-1.35656i & 1.05314 & 0.142095+0.619812i & -1.96682 & -0.142095+0.619812i \\ 1.35656-0.473943i & 0.183234+0.866529i & 0.473943+1.35656i & 0 & 0.142095-0.619812i & -1.05314 & -0.142095-0.619812i & 1.96682 \end{pmatrix} \tag{II.260}$$

and

$$\alpha_{2c,\text{second split}} = \begin{pmatrix} 1.21201 & -1.02944+1.05569i & 0.0188021 & 1.02944+1.05569i & -3.07792-1.23006i & -0.518609-0.428424i & 0 & 0.428424-0.518609i \\ -1.02944-1.05569i & -1.21201 & 1.02944-1.05569i & -0.0188021 & -0.518609-0.428424i & -1.23006+3.07792i & -0.428424+0.518609i & 0 \\ 0.0188021 & 1.02944+1.05569i & 1.21201 & -1.02944+1.05569i & 0 & -0.428424+0.518609i & 3.07792+1.23006i & 0.518609+0.428424i \\ 1.02944-1.05569i & -0.0188021 & -1.02944-1.05569i & -1.21201 & 0.428424-0.518609i & 0 & 0.518609+0.428424i & 1.23006-3.07792i \\ -3.07792+1.23006i & -0.518609+0.428424i & 0 & 0.428424+0.518609i & -1.21201 & 1.02944+1.05569i & -0.0188021 & -1.02944+1.05569i \\ -0.518609+0.428424i & -1.23006-3.07792i & -0.428424-0.518609i & 0 & 1.02944-1.05569i & 1.21201 & -1.02944-1.05569i & 0.0188021 \\ 0 & -0.428424-0.518609i & 3.07792-1.23006i & 0.518609-0.428424i & -0.0188021 & -1.02944+1.05569i & -1.21201 & 1.02944+1.05569i \\ 0.428424+0.518609i & 0 & 0.518609-0.428424i & 1.23006+3.07792i & -1.02944-1.05569i & 0.0188021 & 1.02944-1.05569i & 1.21201 \end{pmatrix} \tag{II.261}$$

The matrix to get a 6-cycle split of $H_2^{(6)}$ is

$$\mathring{\psi}_{\mathcal{T}} = \frac{1}{4}\begin{pmatrix}
0.220879-1.00418i & -0.341746-1.92144i & 1.58215-0.411024i & 0.485391+1.94066i & 1.10887+3.10653i & -1.84079-0.946258i & 1.66506-8.69341i & -0.472119+1.54946i & -0.916067-0.948388i & -0.0869714+0.753145i & -0.916067-0.948388i & -0.472119+1.54946i \\
-1.73988+1.12104i & -0.759204-0.693376i & -1.83489-0.664759i & 0.435119-1.5757i & 1.92336+0.54997i & 3.24477+0.592953i & -0.472119+1.54946i & 1.66506-8.69341i & -0.472119+1.54946i & -0.916067-0.948388i & -0.0869714+0.753145i & -0.916067-0.948388i \\
2.1359-2.51358i & 0.100911+2.0673i & -0.980084+0.310802i & -1.49314+1.25668i & -1.14703-1.16467i & 1.43797-1.39069i & -0.916067-0.948388i & -0.472119+1.54946i & 1.66506-8.69341i & -0.472119+1.54946i & -0.916067-0.948388i & -0.0869714+0.753145i \\
-0.485391-1.94066i & -1.10887-3.10653i & 1.84079+0.946258i & -0.220879+1.00418i & 0.341746+1.92144i & -1.58215+0.411024i & -0.0869714+0.753145i & -0.916067-0.948388i & -0.472119+1.54946i & 1.66506-8.69341i & -0.472119+1.54946i & -0.916067-0.948388i \\
-0.435119+1.5757i & -1.92336-0.54997i & -3.24477-0.592953i & 1.73988-1.12104i & 0.759204+0.693376i & 1.83489+0.664759i & -0.916067-0.948388i & -0.0869714+0.753145i & -0.916067-0.948388i & -0.472119+1.54946i & 1.66506-8.69341i & -0.472119+1.54946i \\
1.49314-1.25668i & 1.14703+1.16467i & -1.43797+1.39069i & -2.1359+2.51358i & -0.100911-2.0673i & 0.980084-0.310802i & -0.472119+1.54946i & -0.916067-0.948388i & -0.0869714+0.753145i & -0.916067-0.948388i & -0.472119+1.54946i & 1.66506-8.69341i \\
5.15848+1.72281i & -0.223211-3.297i & 3.54336+1.75315i & -1.1781+0.36398i & -0.253413-3.94521i & 2.96689+1.4552i & -0.220879+1.00418i & 1.73988-1.12104i & -2.1359+2.51358i & 0.485391+1.94066i & 0.435119-1.5757i & -1.49314+1.25668i \\
-0.223211-3.297i & -1.08725-5.32878i & -2.74368+1.84181i & -0.253413-3.94521i & 0.904264+0.838272i & -3.28995+2.19207i & 0.341746+1.92144i & 0.759204+0.693376i & -0.100911-2.0673i & 1.10887+3.10653i & 1.92336+0.54997i & -1.14703-1.16467i \\
3.54336+1.75315i & -2.74368+1.84181i & -4.07124+3.60598i & 2.96689+1.4552i & -3.28995+2.19207i & 0.273832-1.20225i & -1.58215+0.411024i & 1.83489+0.664759i & 0.980084-0.310802i & -1.84079-0.946258i & 3.24477+0.592953i & 1.43797-1.39069i \\
-1.1781+0.36398i & -0.253413-3.94521i & 2.96689+1.4552i & 5.15848+1.72281i & -0.223211-3.297i & 3.54336+1.75315i & -0.485391-1.94066i & -0.435119+1.5757i & 1.49314-1.25668i & 0.220879-1.00418i & -1.73988+1.12104i & 2.1359-2.51358i \\
-0.253413-3.94521i & 0.904264+0.838272i & -3.28995+2.19207i & -0.223211-3.297i & -1.08725-5.32878i & -2.74368+1.84181i & -1.10887-3.10653i & -1.92336-0.54997i & 1.14703+1.16467i & -0.341746-1.92144i & -0.759204-0.693376i & 0.100911+2.0673i \\
2.96689+1.4552i & -3.28995+2.19207i & 0.273832-1.20225i & 3.54336+1.75315i & -2.74368+1.84181i & -4.07124+3.60598i & 1.84079+0.946258i & -3.24477-0.592953i & -1.43797+1.39069i & 1.58215-0.411024i & -1.83489-0.664759i & -0.980084+0.310802i
\end{pmatrix} \tag{II.262}$$

Matrix to get a three-cycle and TRS split in one go is

$$\alpha_{3\text{ cycle one go}} = \begin{pmatrix}
-2.68676-1.3736i & 0.851051-0.0670278i & 0.166029+0.933611i & -0.629777-1.13972i & 1.30772-1.20857i & -0.745043-0.441793i & 1.05536+2.26205i & 0.0139827-1.60405i & 0.880322-0.449631i & 0 & 0.880322-0.449631i & -0.0139827+1.60405i \\
0.755125-0.42433i & 2.53295-1.64001i & -0.367478+0.770545i & -0.891545-0.32302i & 1.30192+0.0244595i & 0.39279+1.7368i & 0.0139827-1.60405i & -1.05536-2.26205i & -0.0139827+1.60405i & -0.880322+0.449631i & 0 & -0.880322+0.449631i \\
-1.70051-0.528234i & -0.0100822+0.866123i & 0.153812+3.01361i & -0.483573-0.703518i & 0.725516-0.610591i & -0.672142+1.11526i & 0.880322-0.449631i & -0.0139827+1.60405i & 1.05536+2.26205i & 0.0139827-1.60405i & 0.880322-0.449631i & 0 \\
-0.629777-1.13972i & 1.30772-1.20857i & -0.745043-0.441793i & -2.68676-1.3736i & 0.851051-0.0670278i & 0.166029+0.933611i & 0 & -0.880322+0.449631i & 0.0139827-1.60405i & -1.05536-2.26205i & -0.0139827+1.60405i & -0.880322+0.449631i \\
-0.891545-0.32302i & 1.30192+0.0244595i & 0.39279+1.7368i & 0.755125-0.42433i & 2.53295-1.64001i & -0.367478+0.770545i & 0.880322-0.449631i & 0 & 0.880322-0.449631i & -0.0139827+1.60405i & 1.05536+2.26205i & 0.0139827-1.60405i \\
-0.483573-0.703518i & 0.725516-0.610591i & -0.672142+1.11526i & -1.70051-0.528234i & -0.0100822+0.866123i & 0.153812+3.01361i & -0.0139827+1.60405i & -0.880322+0.449631i & 0 & -0.880322+0.449631i & 0.0139827-1.60405i & -1.05536-2.26205i \\
-0.640278-0.563111i & 1.06887-0.0756659i & -0.264545-0.17639i & 0 & -0.0204858+0.317297i & 0.468908-0.963504i & 2.68676+1.3736i & -0.755125+0.42433i & 1.70051+0.528234i & 0.629777+1.13972i & 0.891545+0.32302i & 0.483573+0.703518i \\
1.06887-0.0756659i & 0.167529-0.836052i & 0.599965+0.887839i & 0.0204858-0.317297i & 0 & -0.285031+0.140907i & -0.851051+0.0670278i & -2.53295+1.64001i & 0.0100822-0.866123i & -1.30772+1.20857i & -1.30192-0.0244595i & -0.725516+0.610591i \\
-0.264545-0.17639i & 0.599965+0.887839i & 0.807807-0.272942i & -0.468908+0.963504i & 0.285031-0.140907i & 0 & -0.166029-0.933611i & 0.367478-0.770545i & -0.153812-3.01361i & 0.745043+0.441793i & -0.39279-1.7368i & 0.672142-1.11526i \\
0 & 0.0204858-0.317297i & -0.468908+0.963504i & 0.640278+0.563111i & -1.06887+0.0756659i & 0.264545+0.17639i & 0.629777+1.13972i & 0.891545+0.32302i & 0.483573+0.703518i & 2.68676+1.3736i & -0.755125+0.42433i & 1.70051+0.528234i \\
-0.0204858+0.317297i & 0 & 0.285031-0.140907i & -1.06887+0.0756659i & -0.167529+0.836052i & -0.599965-0.887839i & -1.30772+1.20857i & -1.30192-0.0244595i & -0.725516+0.610591i & -0.851051+0.0670278i & -2.53295+1.64001i & 0.0100822-0.866123i \\
0.468908-0.963504i & -0.285031+0.140907i & 0 & 0.264545+0.17639i & -0.599965-0.887839i & -0.807807+0.272942i & 0.745043+0.441793i & -0.39279-1.7368i & 0.672142-1.11526i & -0.166029-0.933611i & 0.367478-0.770545i & -0.153812-3.01361i
\end{pmatrix} \tag{II.263}$$

The matrix for three-cycle in two-step procedure (2nd step) is

$$\alpha_{3\text{ cycle two step}} = \begin{pmatrix}
6.70867-1.52874i & -2.0207+1.19094i & 1.62758-2.09224i & 0.993331-0.0775158i & 2.64819+0.154458i & -1.56217+1.40809i & 0 & 1.07933+0.516151i & -1.39616+0.170187i & 1.54235+4.23103i & 1.39616-0.170187i & 1.07933+0.516151i \\
-0.438359-2.05692i & -2.0304+6.57425i & -0.021034-2.34544i & 0.99815+2.45564i & -0.429535+0.899008i & -1.45786+2.21617i & -1.07933-0.516151i & 0 & -1.07933-0.516151i & 1.39616-0.170187i & -1.54235-4.23103i & -1.39616+0.170187i \\
-1.19033-2.37063i & 2.00053+0.648832i & -4.67826-5.0455i & 2.04173+1.15451i & -2.62572-0.363399i & -0.563796-0.821492i & 1.39616-0.170187i & 1.07933+0.516151i & 0 & 1.07933+0.516151i & -1.39616+0.170187i & 1.54235+4.23103i \\
0.993331-0.0775158i & 2.64819+0.154458i & -1.56217+1.40809i & 6.70867-1.52874i & -2.0207+1.19094i & 1.62758-2.09224i & -1.54235-4.23103i & -1.39616+0.170187i & -1.07933-0.516151i & 0 & -1.07933-0.516151i & 1.39616-0.170187i \\
0.99815+2.45564i & -0.429535+0.899008i & -1.45786+2.21617i & -0.438359-2.05692i & -2.0304+6.57425i & -0.021034-2.34544i & -1.39616+0.170187i & 1.54235+4.23103i & 1.39616-0.170187i & 1.07933+0.516151i & 0 & 1.07933+0.516151i \\
2.04173+1.15451i & -2.62572-0.363399i & -0.563796-0.821492i & -1.19033-2.37063i & 2.00053+0.648832i & -4.67826-5.0455i & -1.07933-0.516151i & 1.39616-0.170187i & -1.54235-4.23103i & -1.39616+0.170187i & -1.07933-0.516151i & 0 \\
0 & -2.51975-1.2566i & -0.0261832+0.962883i & 0.103073-0.686651i & -0.846973+0.458766i & 2.34812-1.55387i & 6.70867-1.52874i & -0.438359-2.05692i & -1.19033-2.37063i & 0.993331-0.0775158i & 0.99815+2.45564i & 2.04173+1.15451i \\
2.51975+1.2566i & 0 & -0.171628-2.81046i & -0.846973+0.458766i & 0.646193-0.254062i & -0.820789-0.504117i & -2.0207+1.19094i & -2.0304+6.57425i & 2.00053+0.648832i & 2.64819+0.154458i & -0.429535+0.899008i & -2.62572-0.363399i \\
0.0261832-0.962883i & 0.171628+2.81046i & 0 & 2.34812-1.55387i & -0.820789-0.504117i & 0.54312+0.432589i & 1.62758-2.09224i & -0.021034-2.34544i & -4.67826-5.0455i & -1.56217+1.40809i & -1.45786+2.21617i & -0.563796-0.821492i \\
-0.103073+0.686651i & 0.846973-0.458766i & -2.34812+1.55387i & 0 & 2.51975+1.2566i & 0.0261832-0.962883i & 0.993331-0.0775158i & 0.99815+2.45564i & 2.04173+1.15451i & 6.70867-1.52874i & -0.438359-2.05692i & -1.19033-2.37063i \\
0.846973-0.458766i & -0.646193+0.254062i & 0.820789+0.504117i & -2.51975-1.2566i & 0 & 0.171628+2.81046i & 2.64819+0.154458i & -0.429535+0.899008i & -2.62572-0.363399i & -2.0207+1.19094i & -2.0304+6.57425i & 2.00053+0.648832i \\
-2.34812+1.55387i & 0.820789+0.504117i & -0.54312-0.432589i & -0.0261832+0.962883i & -0.171628-2.81046i & 0 & -1.56217+1.40809i & -1.45786+2.21617i & -0.563796-0.821492i & 1.62758-2.09224i & -0.021034-2.34544i & -4.67826-5.0455i
\end{pmatrix} \tag{II.264}$$

III. Symmetry Indicator Invariants for Non-Hermitian Topological Materials

III.1. Abstract

In this work, symmetry indicator invariants for non-Hermitian Hamiltonians are described. In 1D with a point gap, the 1D winding number w_{1D} is determined modulo 2, in presence of pseudo-inversion symmetry ($\mathcal{I}\mathcal{H}_{\mathbf{k}}\mathcal{I}^{-1} = \mathcal{H}^{\dagger}_{-\mathbf{k}}$), using a symmetry indicator. In presence of inversion symmetry w_{1D} vanishes. In 2D with a line gap, the symmetry indicator invariants that are already known from Hermitian physics and allow for a determination of the Chern number are also valid for non-Hermitian systems. In 3D, symmetry indicators allow the determination of the 3D winding number modulo 2 (4; 8) in presence of pseudo-inversion (pseudo-inversion and TRS†; pseudo-inversion, TRS† and C_4 symmetry, respectively). If inversion symmetry is present, w_{3D} vanishes. In presence of TRS and pseudo-inversion symmetry, we can detect the nontrivial $\mathbb{Z}_2$ phase using a symmetry indicator invariant, instead of relying on the Chern-Simons invariant CS_3 with a specific gauge.

III.2. Introduction

In recent years, interest in the topological behaviour of non-Hermitian systems has been growing. While the topological properties of regular Hermitian Hamiltonians have already been investigated for a few decades[1–13] and there has been tremendous progress in understanding their physical behaviour as well as their topological classification[26], little interest had been paid to non-Hermitian system. This is due to the fact that regular quantum mechanical systems always possess a Hermitian Hamiltonian. By introducing loss or resistance, or by taking into account electron-electron interactions[88, 100, 120–129], Hermiticity-breaking terms can be added to a Hamiltonian. The resulting systems then show a behaviour that is distinctly different from Hermitian system in a topological phase, for example by showing a skin effect, which means that all the modes in a non-Hermitian system all shift towards one side of a sample, instead of a having only $\mathcal{O}(1)$ boundary localised modes like in Hermitian physics[88, 107, 109, 111, 112, 122, 128].

Currently, when striving to understand the topology of a concrete system, the approach is to calculate topological invariants, e.g. Chern or winding numbers, that are defined in terms of Brouillon zone (BZ) integrals. These calculations are computationally expensive. Therefore, in this part of the thesis, we propose to calculate symmetry indicator invariants, similar to those already being used to detect nontrivial topological phases in Hermitian systems, spearheaded by Fu et al.[154] and then extended, for instance, by Hughes et al.[37] and Fang et al.[41]. These invariants can be calculated knowing the symmetry eigenvalues of space group symmetries at high symmetry points of the BZ. We extend the concept of symmetry indicator invariants to some non-Hermitian systems with specific symmetries.

The structure of this part is as follows. In section III.3 the general properties of non-Hermitian

Hamiltonians are described. Different internal symmetries and space group symmetries are addressed and how they generalise the symmetries known from Hermitian physics. Furthermore, we define a pseudo-inversion symmetry. Next, the mapping between a Hamiltonian and its Hermitian double Hamiltonian and the flattening of Hamiltonians is described. The types of gaps that can appear in non-Hermitian systems, point and line gaps, are detailed. Subsequently, in section III.4, the winding number for 1D systems with point gap is analysed using a symmetry indicator in presence of inversion and pseudo-inversion symmetry. In section III.5, we use symmetry indicators to shed light onto the Chern number in two-dimensional systems with conventional inversion or rotational symmetry. We then turn to 3D systems. In section III.6, we first analyse the 3D winding number $w_{3\mathrm{D}}$ in the presence of inversion and pseudo-inversion symmetry using symmetry indicators. We also take into account reciprocity ($\mathrm{TRS}^{\dagger}$) and C_4-symmetry to obtain more information on $w_{3\mathrm{D}}$. Secondly, the non-trivial phase in the non-Hermitian AZ class AII is analysed using a symmetry indicator invariant in presence of pseudo-inversion.

III.3. General Properties of Non-Hermitian Systems

Non-Hermitian Hamiltonians do not possess many useful properties used in Hermitian physics to calculate properties of systems, like orthonormal eigensystems. In this section, we describe the spectrum, gaps and symmetries of non-Hermitian Hamiltonians.

III.3.1. Spectrum and Eigenspace of Non-Hermitian Systems

Non-Hermitian sytems, unlike Hermitian system, do not need to be diagonalisable and therefore do not necessarily have an eigenbasis. However, the number of matrices that cannot be diagonalised is vanishingly small, and thus we assume that the Hamiltonians we look at can be diagonalised everywhere except from a subset with vanishing measure $G \subset \mathrm{BZ} = \mathbb{T}^d$.
In general, the eigenvectors of non-Hermitian Hamiltonians are not orthonormal.

$$H(\mathbf{k}) |\varphi_n(\mathbf{k})\rangle = E_n(\mathbf{k}) |\varphi_n(\mathbf{k})\rangle \text{ with } \langle\varphi_m(\mathbf{k})|\varphi_n(\mathbf{k})\rangle \neq \delta_{mn}. \tag{III.1}$$

Instead, the eigenvectors of $H(\mathbf{k})$ and $H^{\dagger}(\mathbf{k}) \neq H(\mathbf{k})$ fulfill biorthogonality[95, 117]. This means that if

$$\begin{aligned} H(\mathbf{k}) |\varphi_n(\mathbf{k})\rangle &= E_n(\mathbf{k}) |\varphi_n(\mathbf{k})\rangle \text{ and} \\ H^{\dagger}(\mathbf{k}) |\chi_n(\mathbf{k})\rangle &= E_n^*(\mathbf{k}) |\chi_n(\mathbf{k})\rangle \end{aligned} \tag{III.2}$$

hold, then

$$\begin{aligned} \langle\chi_m(\mathbf{k})|\varphi_n(\mathbf{k})\rangle &= \delta_{mn} \text{ and} \\ \sum_n |\varphi_n(\mathbf{k})\rangle \langle\chi_n(\mathbf{k})| &= \mathbb{1}. \end{aligned} \tag{III.3}$$

Furthermore, the Hamiltonian has the spectral decompositon

$$H(\mathbf{k}) = \sum_n E_n(\mathbf{k}) |\varphi_n(\mathbf{k})\rangle \langle\chi_n(\mathbf{k})| . \tag{III.4}$$

Many quantities known in Hermitian physics, like the Wilson loop, can also be calculated using the right eigenvectors $|\varphi_n(\mathbf{k})\rangle$ and left eigenvectors $|\chi_n(\mathbf{k})\rangle$[105, 155, 156]. For the

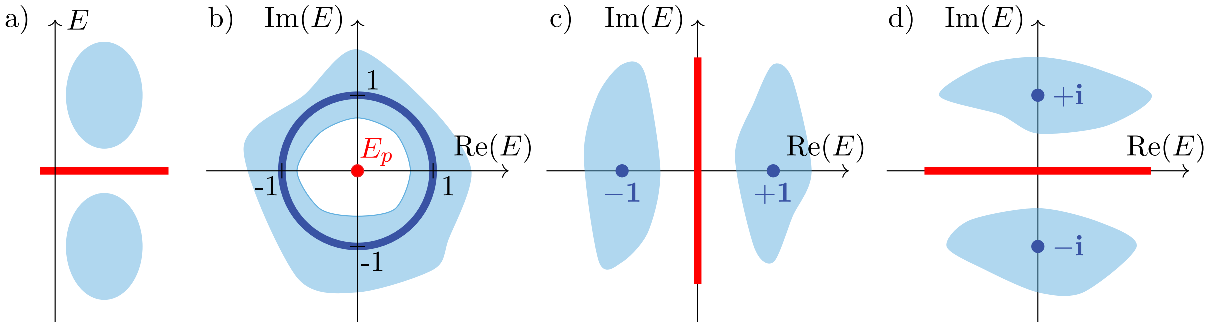

Figure III.1.: Overview over different types of gaps. In panel a), the conventional gap of a Hermitian Hamiltonian is depicted. The light blue areas are where the eigenvalues are found. Between the two areas, there is a gap (in red). In panel b), the spectrum of a non-Hermitian Hamiltonian with point gap is shown in light blue. The gap is indicated by the point E_p. The dark blue ring at absolute value 1 are the eigenvalues of the unitary projection of the Hamiltonian. Any non-Hermitian Hamiltonian with point gap can be deformed to a unitary matrix with eigenvalues of absolute value 1 (*unitary flattening*). Panel c) shows a real line gap. There is a line gap and the Hamiltonian can be flattened such that all the eigenvalues become ±1 (*Hermitian flattening*). In panel d) the spectrum of a Hamiltonian with imaginary line gap is depicted. In this situation, the eigenvalues can be flattened to $\pm i$[95].

Wilson loop, the projector known from Hermitian systems is simply replaced by the projector for non-Hermitian systems,

$$P(\mathbf{k}) = \sum_{n\in \text{occ.}} |\varphi_n(\mathbf{k})\rangle \langle \chi_n(\mathbf{k})| \,, \tag{III.5}$$

where we assumed a line gap and thus a distinction of “occupied” and “unoccupied” eigenstates is possible.

III.3.2. Gaps in Non-Hermitian Systems

The eigenvalues of Hermitian Hamiltonians are real, therefore the definition of a gap is unique. A gap is an energy E_G such that there is no momentum $\mathbf{k} \in$ BZ with an eigenvalue of $\mathcal{H}_\mathbf{k}$ equal to E_G, as shown in Fig. III.1a). If the Hamiltonian is non-Hermitian, its eigenvalues are not restricted to the real axis. The definition above therefore cannot be applied anymore. In non-Hermitian Physics, we distinguish two types of gaps (cf. Kawabata et al.[95]):

1. Point gaps are energy values $E_p \in \mathbb{C}$. We define that $\mathcal{H}_\mathbf{k}$ has a point gap if there is no crystal momentum $\mathbf{k} \in$ BZ such that $\mathcal{H}_\mathbf{k}$ has eigenvalue E_p. In this case the Hamiltonian can be flattened such that all eigenvalues are of unit absolute value. This situation is depicted in Fig. III.1b).

2. Line gaps are lines through the complex plane that are not intersected by the spectrum of the Hamiltonian. For the topological classification, one distinguishes between real and imaginary line gaps. The spectrum of Hamiltonians with real line gaps can be flattened to ±1 (depicted in Fig. III.1c); the spectrum of Hamiltonians with an imaginary line gap can be flattened to $\pm i$ (depicted in Fig. III.1d).

The topological classification depends on the type of gap and on the internal and crystalline symmetries.

For any non-Hermitian Hamiltonian $H(\mathbf{k})$ we define its Hermitian double as

$$H_{\mathrm{d}}(\mathbf{k}) = \begin{pmatrix} & H(\mathbf{k}) \\ H^{\dagger}(\mathbf{k}) & \end{pmatrix}. \tag{III.6}$$

If there is a vector $\vec{u} = (\vec{u}_1, \vec{u}_2)$ with $H_{\mathrm{d}}(\mathbf{k})\vec{u} = 0$, then this also implies that

$$H(\mathbf{k})\vec{u}_2 = 0 \quad \text{and} \quad H^{\dagger}(\mathbf{k})\vec{u}_1 = 0. \tag{III.7}$$

Therefore gaplessness of $H_{\mathrm{d}}(\mathbf{k})$ w.r.t. $E_G = 0$ implies gaplessness of $H(\mathbf{k})$ w.r.t. $E_p = 0$.

III.3.3. Symmetries in Non-Hermitian Systems

In this subsection, internal and space group symmetries of non-Hermitian systems are treated.

III.3.3.1. Internal Symmetries

Unlike in Hermitian systems, there are more than the 10 Altland-Zirnbauer internal symmetry classes[25] in non-Hermitian physics. The Hamiltonians are instead grouped into the 38 internal symmetry classes described by Kawabata et al.[95]. For non-Hermitian physics, we get $\mathcal{H}^{\dagger} \neq \mathcal{H}$ and $\mathcal{H}^{T} \neq \mathcal{H}^{*}$. Therefore, many of the symmetry classes known from Hermitian physics split into several symmetry classes when allowing non-Hermitian terms. For example, the Hermitian symmetry class AII is generalized to the non-Hermitian symmetry classes AII and AII†. The internal symmetries that appear in non-Hermitian physics are the following and their consequences for right (left) eigenvectors $|\varphi_m(\mathbf{k})\rangle$ ($|\chi_m(\mathbf{k})\rangle$) with $\mathcal{H}(\mathbf{k})\,|\varphi_m(\mathbf{k})\rangle = E_m(\mathbf{k})\,|\varphi_m(\mathbf{k})\rangle$ ($\mathcal{H}^{\dagger}(\mathbf{k})\,|\chi_m(\mathbf{k})\rangle = E_m^{*}(\mathbf{k})\,|\chi_m(\mathbf{k})\rangle$), are:

- Time reversal symmetry (TRS):

  $$\mathcal{T}_{+}\mathcal{H}^{*}(\mathbf{k})\mathcal{T}_{+}^{-1} = \mathcal{H}(-\mathbf{k}) \text{ with } \mathcal{T}_{+}\mathcal{T}_{+}^{*} = \pm 1 \tag{III.8}$$

  For an eigenvector $|\varphi_m(\mathbf{k})\rangle$ with eigenvalue $E_m(\mathbf{k})$, $|\varphi_m(-\mathbf{k})\rangle = \mathcal{T}_{+}\mathcal{K}\,|\varphi_m(\mathbf{k})\rangle$ is an eigenvector at $-\mathbf{k}$ with eigenvalue $E_m(-\mathbf{k}) = E_m^{*}(\mathbf{k})$. This implies that at time-reversal invariant momenta (TRIMs) the eigenvalues appear in complex-conjugate pairs.

- Particle hole symmetry (PHS):

  $$\mathcal{C}_{-}\mathcal{H}^{T}(\mathbf{k})\mathcal{C}_{-}^{-1} = -\mathcal{H}(-\mathbf{k}) \text{ with } \mathcal{C}_{-}\mathcal{C}_{-}^{*} = \pm 1 \tag{III.9}$$

  If $|\chi_m(\mathbf{k})\rangle$ is a left eigenvector with eigenvalue E_m^{*}, then $|\varphi_m(-\mathbf{k})\rangle = \mathcal{C}_{-}\,|\chi_m(\mathbf{k})\rangle^{*}$ is a right eigenvector at $-\mathbf{k}$ with eigenvalue $E_m(-\mathbf{k}) = -E_m(\mathbf{k})$. Therefore, at TRIMs, the eigenvalues come in pairs of $\pm E_m(\mathbf{k})$.

- "2nd" time reversal symmetry, reciprocity (TRS†):

  $$\mathcal{C}_{+}\mathcal{H}^{T}(\mathbf{k})\mathcal{C}_{+}^{-1} = \mathcal{H}(-\mathbf{k}) \text{ with } \mathcal{C}_{+}\mathcal{C}_{+}^{*} = \pm 1 \tag{III.10}$$

  $|\varphi_m(-\mathbf{k})\rangle = \mathcal{C}_{+}\,|\chi_m(\mathbf{k})\rangle^{*}$ is an eigenvector of $\mathcal{H}(-\mathbf{k})$ with the same eigenvalue $E_m(\mathbf{k})$.

- "2nd" particle hole symmetry (PHS†):

$$\mathcal{T}_- \mathcal{H}^*(\mathbf{k}) \mathcal{T}_-^{-1} = -\mathcal{H}(-\mathbf{k}) \text{ with } \mathcal{T}_+ \mathcal{T}_+^* = \pm 1 \tag{III.11}$$

  $|\varphi_m(-\mathbf{k})\rangle = \mathcal{T}_- |\varphi_m(\mathbf{k})\rangle^*$ is an eigenvector of $\mathcal{H}(-\mathbf{k})$ with eigenvalue $E_m(-\mathbf{k}) = -E_m^*(\mathbf{k})$.

- Chiral symmetry (CS):

$$\Gamma \mathcal{H}^\dagger(\mathbf{k}) \Gamma^{-1} = -\mathcal{H}(\mathbf{k}) \text{ with } \Gamma^2 = +1 \tag{III.12}$$

  If $|\chi_m(\mathbf{k})\rangle$ is a left eigenvector of $\mathcal{H}(\mathbf{k})$ with eigenvalue $E_m(\mathbf{k})$ (i.e. $\mathcal{H}^\dagger(\mathbf{k}) |\chi_m(\mathbf{k})\rangle = E_m^*(\mathbf{k}) |\chi_m(\mathbf{k})\rangle$), then $|\varphi_{\tilde{m}}(\mathbf{k})\rangle = \Gamma |\chi_m(\mathbf{k})\rangle$ is an eigenvector of $\mathcal{H}(\mathbf{k})$ with eigenvalue $E_{\tilde{m}}(\mathbf{k}) = -E_m^*(\mathbf{k})$.

- Sublattice symmetry (SLS):

$$\mathcal{S} H(\mathbf{k}) \mathcal{S}^{-1} = -H(\mathbf{k}) \text{ with } \mathcal{S}^2 = +1 \tag{III.13}$$

  If $|\varphi_m(\mathbf{k})\rangle$ is a right eigenvector of $\mathcal{H}(\mathbf{k})$ with eigenvalue $E_m(\mathbf{k})$, then $|\varphi_{\tilde{m}}(\mathbf{k})\rangle = \mathcal{S} |\varphi_m(\mathbf{k})\rangle$ is also a right eigenvector of $\mathcal{H}(\mathbf{k})$, but with eigenvalue $-E_m(\mathbf{k})$.

- Pseudo-Hermiticity:

$$\eta \mathcal{H}^\dagger(\mathbf{k}) \eta^{-1} = -\mathcal{H}(\mathbf{k}) \text{ with } \eta^2 = +1, \eta = \eta^\dagger, \eta\eta^\dagger = \mathbb{1} \tag{III.14}$$

  is a special variant of chiral symmetry, with the added condition that η must be Hermitian.

Mapping from internal symmetries of the Hamiltonian to the internal symmetries of its Hermitian double Hamiltonian If we have a non-Hermitian Hamiltonian $\mathcal{H}$ in one of the 38 symmetry classes, then we can determine which AZ symmetry class $\mathcal{H}_\mathrm{d}$ belongs to. $\mathcal{H}_\mathrm{d}$ is defined as

$$\mathcal{H}_\mathrm{d}(\mathbf{k}) = \begin{bmatrix} 0 & \mathcal{H}(\mathbf{k}) \\ \mathcal{H}^\dagger(\mathbf{k}) & 0 \end{bmatrix}. \tag{III.15}$$

The internal symmetries of $\mathcal{H}$ imply the following symmetries of $\mathcal{H}_\mathrm{d}$:

- TRS of $\mathcal{H}$ implies that $\mathcal{H}_\mathrm{d}$ has TRS with $\mathcal{T} = \begin{bmatrix} \mathcal{T}_+ & \\ & \mathcal{T}_+ \end{bmatrix}$.
- PHS of $\mathcal{H}$ implies that $\mathcal{H}_\mathrm{d}$ has PHS with $\mathcal{C} = \begin{bmatrix} & \mathcal{C}_- \\ \mathcal{C}_- & \end{bmatrix}$.
- TRS† of $\mathcal{H}$ implies that $\mathcal{H}_\mathrm{d}$ has TRS with $\mathcal{T} = \begin{bmatrix} & \mathcal{C}_+ \\ \mathcal{C}_+ & \end{bmatrix}$.
- PHS† of $\mathcal{H}$ implies that $\mathcal{H}_\mathrm{d}$ has PHS with $\mathcal{C} = \begin{bmatrix} \mathcal{T}_- & \\ & \mathcal{T}_- \end{bmatrix}$.
- CS of $\mathcal{H}$ implies that $\mathcal{H}_\mathrm{d}$ has SLS with $\mathcal{S} = \begin{bmatrix} & \Gamma \\ \Gamma & \end{bmatrix}$.

- SLS of $\mathcal{H}$ implies that $\mathcal{H}_\mathrm{d}$ has SLS with $\mathcal{S} = \begin{bmatrix} \mathcal{S} & \\ & \mathcal{S} \end{bmatrix}$.
- Pseudo-Hermiticity of $\mathcal{H}$ implies that $\mathcal{H}_\mathrm{d}$ has SLS with $\mathcal{S} = \begin{bmatrix} & \eta \\ \eta & \end{bmatrix}$.

Furthermore, $\mathcal{H}_\mathrm{d}$ always has SLS with

$$\mathcal{S} = \begin{bmatrix} \mathbb{1} & 0 \\ 0 & -\mathbb{1} \end{bmatrix}. \tag{III.16}$$

This means that the only allowed AZ classes for $\mathcal{H}_\mathrm{d}$ are AIII, BDI, DIII, CII and CI. Moreover, the existence of SLS together with TRS (PHS) implies PHS (TRS). Altogether these relations determine whether certain symmetries are present. In a concrete case the resulting AZ class of the Hermitian double depends on commutation relations between the symmetries of $\mathcal{H}$. If we look for example at a non-Hermitian Hamiltonian $\mathcal{H}$ in real AZ class AI, then the Hermitian double has TRS, SLS and PHS with $\mathcal{T}_\mathrm{d}^2 = +1$ and $\mathcal{S}_\mathrm{d}^2 = +1$, which means that it is either in AZ class BDI or CI. $\mathcal{T}_\mathrm{d}$ commutes with $\mathcal{S}_\mathrm{d}$, therefore $\mathcal{H}_\mathrm{d}$ is in AZ class BDI as

$$\begin{aligned} \mathcal{S}_\mathrm{d}\mathcal{T}_\mathrm{d} - \mathcal{T}_\mathrm{d}\mathcal{S}_\mathrm{d} &= \begin{bmatrix} 1 & \\ & -1 \end{bmatrix} \begin{bmatrix} \mathcal{T}_+ & \\ & \mathcal{T}_+ \end{bmatrix} - \begin{bmatrix} \mathcal{T}_+ & \\ & \mathcal{T}_+ \end{bmatrix} \begin{bmatrix} 1 & \\ & -1 \end{bmatrix} \\ &= \begin{bmatrix} \mathcal{T}_+ & \\ & -\mathcal{T}_+ \end{bmatrix} - \begin{bmatrix} \mathcal{T}_+ & \\ & -\mathcal{T}_+ \end{bmatrix} = 0 \implies \mathcal{C}_\mathrm{d}^2 = \mathcal{S}_\mathrm{d}\mathcal{T}_\mathrm{d}\mathcal{S}_\mathrm{d}\mathcal{T}_\mathrm{d} = \mathcal{S}_\mathrm{d}^2\mathcal{T}_\mathrm{d}^2 = \mathbb{1}, \end{aligned} \tag{III.17}$$

where we used that

$$\mathcal{C}_\mathrm{d} = \mathcal{S}_\mathrm{d}\mathcal{T}_\mathrm{d} \tag{III.18}$$

because

$$\mathcal{S}_\mathrm{d}\mathcal{T}_\mathrm{d}\mathcal{H}_\mathrm{d}^*(\mathbf{k}) \left(\mathcal{S}_\mathrm{d}\mathcal{T}_\mathrm{d}\right)^{-1} = \mathcal{S}_\mathrm{d}\mathcal{H}_\mathrm{d}(-\mathbf{k})\mathcal{S}_\mathrm{d}^{-1} = -\mathcal{H}_\mathrm{d}(-\mathbf{k}). \tag{III.19}$$

It is possible to proceed analogously for the other 37 non-Hermitian internal symmetry classes.

III.3.3.2. Space Group Symmetries

In Hermitian physics, space group symmetries are unitary operators acting on the Bloch Hamiltonian as

$$s\mathcal{H}_\mathbf{k}s^\dagger = \mathcal{H}_{S\mathbf{k}} \tag{III.20}$$

with s as representation of the symmetry on the orbitals and S is its action on crystal momenta. In non-Hermitian physics, $\mathcal{H}^\dagger \neq \mathcal{H}$, so there are two possibilities to generalise a symmetry of a Hermitian system to non-Hermitian physics:

- A real symmetry acts as in regular Hermitian physics

$$s\mathcal{H}_\mathbf{k}s^\dagger = \mathcal{H}_{S\mathbf{k}}. \tag{III.21}$$

- A pseudo-symmetry connects the Hamiltonian with its adjoint

$$s\mathcal{H}_\mathbf{k}^\dagger s^\dagger = \mathcal{H}_{S\mathbf{k}} \Leftrightarrow s\mathcal{H}_\mathbf{k}s^\dagger = \mathcal{H}_{S\mathbf{k}}^\dagger. \tag{III.22}$$

If a system has a real symmetry and $\mathbf{k} = S\mathbf{k}$, the symmetry commutes with the Hamiltonian. This allows for a joint diagonalisation of the symmetry and the Hamiltonian, which is not in general possible for pseudo-symmetries.
Both real and pseudo symmetries imply that the Hermitian double $\mathcal{H}_\mathrm{d}(\mathbf{k})$ also carries the same space group symmetry:

- If the Hamiltonian has a real symmetry $s\mathcal{H}_\mathbf{k}s^\dagger = \mathcal{H}_{S\mathbf{k}}$ then $\mathcal{H}_\mathrm{d}$ is symmetric with

$$s_\mathrm{d} = \begin{bmatrix} s & \\ & s \end{bmatrix} \quad \text{and} \quad s_\mathrm{d}\mathcal{H}_\mathrm{d}(\mathbf{k})s_\mathrm{d}^\dagger = \mathcal{H}_\mathrm{d}(S\mathbf{k}). \tag{III.23}$$

- If the Hamiltonian has the pseudo-symmetry $s\mathcal{H}_\mathbf{k}s^\dagger = \mathcal{H}_{S\mathbf{k}}^\dagger$, $\mathcal{H}_\mathrm{d}$ is symmetric with

$$s_\mathrm{d} = \begin{bmatrix} & s \\ s & \end{bmatrix} \quad \text{and} \quad s_\mathrm{d}\mathcal{H}_\mathrm{d}(\mathbf{k})s_\mathrm{d}^\dagger = \mathcal{H}_\mathrm{d}(S\mathbf{k}). \tag{III.24}$$

Inversion and pseudo-inversion A system is inversion-symmetric if there is a unitary operator $\mathcal{I}$ with $\mathcal{I}^2 = +1$ such that

$$\mathcal{I}\mathcal{H}_\mathbf{k}\mathcal{I}^{-1} = \mathcal{H}_{-\mathbf{k}}. \tag{III.25}$$

The inversion symmetry on the Hermitian double Hamiltonian is then represented as

$$\mathcal{I}_\mathrm{d} = \begin{pmatrix} \mathcal{I} & \\ & \mathcal{I} \end{pmatrix}. \tag{III.26}$$

If $\mathcal{H}_\mathbf{k}$ instead fulfills

$$\mathcal{I}\mathcal{H}_\mathbf{k}\mathcal{I}^{-1} = \mathcal{H}_{-\mathbf{k}}^\dagger. \tag{III.27}$$

it carries pseudo-inversion symmetry, which leads to an inversion symmetry of the Hermitian double with

$$\mathcal{I}_\mathrm{d} = \begin{pmatrix} & \mathcal{I} \\ \mathcal{I} & \end{pmatrix}. \tag{III.28}$$

III.4. One-Dimensional Systems

In this section, one-dimensional non-Hermitian systems with a point gap are treated. The winding numbers for odd-dimensional systems ($d \in 2\mathbb{Z}+1$) are

$$W_{2n+1} = \frac{n!}{(2\pi i)^{n+1}(2n+1)!} \int_{\mathrm{BZ}^d} \mathrm{Tr}\left[H^{-1}dH)\right]^{2n+1} . \tag{III.29}$$

These invariants have their origin in the $\mathbb{Z}$ winding number of Hermitian systems with chiral symmetry[26]. These are treated, for example, in the review by Chiu et al.[26]. There, these winding numbers are equivalently expressed in terms of the $\hat{Q}$-matrix given by $\hat{Q}_{\mathbf{k}} = 1 - P_{\mathbf{k}}$, where $P_{\mathbf{k}}$ is the projector into the occupied subspace at $\mathbf{k}$. If any Hermitian $H(\mathbf{k})$ has chiral symmetry, H and $\hat{Q}$ can be expressed as

$$H(\mathbf{k}) = \begin{pmatrix} 0 & D(\mathbf{k}) \\ D^\dagger(\mathbf{k}) & 0 \end{pmatrix} \qquad \hat{Q}(\mathbf{k}) = \begin{pmatrix} 0 & q(\mathbf{k}) \\ q^\dagger(\mathbf{k}) & 0 \end{pmatrix} . \tag{III.30}$$

The winding numbers for the Hermitian system are then given by

$$\begin{aligned} \nu_{2n+1}\left[q\right] &= \int_{\mathrm{BZ}^d \times \mathcal{M}^D} \omega_{2n+1}\left[q\right] , \\ \omega_{2n+1}\left[q\right] &= \frac{(-1)^n n!}{(2n+1)!} \left(\frac{i}{2\pi}\right)^{n+1} \mathrm{Tr}\left[\left(q^{-1}dq\right)^{2n+1}\right] , \end{aligned} \tag{III.31}$$

where $d+D$ is odd. For $(d,D) = (1,0)$ and $(3,0)$, resp.,

$$\begin{aligned} \nu_1 &= \frac{i}{2\pi} \int_{\mathrm{BZ}} dk \mathrm{Tr}\left[q^{-1}\partial_k q\right] , \\ \nu_3 &= \int_{\mathrm{BZ}} \frac{d^{\mathbf{k}}}{24\pi^2} \epsilon^{\mu\nu\rho} \mathrm{Tr}\left[(q^{-1}\partial_\mu q)(q^{-1}\partial_\nu q)(q^{-1}\partial_\rho q)\right] . \end{aligned} \tag{III.32}$$

D is a quantity connected to the co-dimension of defects, and therefore does not matter in our case, i.e. it is zero. These winding numbers from Hermitian physics also classify the non-Hermitian Hamiltonians with point gap and $\mathbb{Z}$ classification in AZ classes A and AII†.
In 1D, the winding number is

$$w_{1\mathrm{D}} = \int_{-\pi}^{+\pi} \frac{dk}{2\pi i} \partial_k \ln\det\left(H(k) - E\right) , \tag{III.33}$$

where E is the midgap energy (cf. Ref. [96]). This quantity can also be expressed as

$$w_{1\mathrm{D}} = -i \int_{\mathrm{BZ}} \frac{dk}{2\pi} \mathrm{Tr}\left[Q(k)\right] \text{ with } Q(k) = \left[H(k) - E\right]^{-1} \partial_k \left[H(k) - E\right] , \tag{III.34}$$

with $\mathrm{BZ} = [-\pi, \pi)$[100].
In the following, we study this winding number in presence of inversion symmetry. The final result of this endeavour is presented in Table III.1 below. It lists the symmetry indicators we found for 1D systems. If s is a real symmetry, $\bar{s}$ denotes the corresponding pseudo symmetry with $\bar{s}H_{\mathbf{k}}\bar{s}^{-1} = H^\dagger_{S\mathbf{k}}$. $\lambda_{k,j}$ is the j^{th} inversion eigenvalue at the TRIM k within the occupied bands of the Hermitian double Hamiltonian.

Int. Sym.	Point Group	Gap (L / P)	H / H_d	Symmetry indicator
-	$\mathcal{I}$	P	-	$w_{1\text{D}} = 0$
-	$\bar{\mathcal{I}}$	P	H_d	$(-1)^{w_{1\text{D}}} = \prod_{k\in\{0,\pi\},j\in\text{occ.}} \lambda_{k,j}$

Table III.1.: Symmetry indicators for non-Hermitian 1D systems.

III.4.1. (Pseudo-)Inversion Symmetry

If the Hamiltonian is inversion-symmetric, $w_{1\text{D}}$ vanishes. To prove this, we first observe that inversion symmetry implies that in any dimension

$$\begin{aligned}\mathcal{I}Q_j(\mathbf{k})\mathcal{I}^{-1} &= \mathcal{I}\left[H(\mathbf{k})-E\right]^{-1}\partial_{k_j}\left[H(\mathbf{k})-E\right]\mathcal{I}^{-1} \\ &= \mathcal{I}\left[H(\mathbf{k})-E\right]^{-1}\mathcal{I}^{-1}\mathcal{I}\partial_{k_j}\mathcal{I}^{-1}\mathcal{I}\left[H(\mathbf{k})-E\right]\mathcal{I}^{-1} = \left[H(-\mathbf{k})-E\right]^{-1}\partial_{k_j}\left[H(-\mathbf{k})-E\right] \\ &= -Q_j(-\mathbf{k}).\end{aligned} \tag{III.35}$$

This can then be used to evaluate $w_{1\text{D}}$

$$\begin{aligned}w_{1\text{D}} &= -i\int_\text{BZ}\frac{dk}{2\pi}\text{Tr}\left[Q(k)\right] = -i\int_\text{BZ}\frac{dk}{2\pi}\text{Tr}\left[\mathcal{I}Q(k)\mathcal{I}^{-1}\right] = -i\int_\text{BZ}\frac{dk}{2\pi}\text{Tr}\left[-Q(-k)\right] \\ &= +i\int_\text{BZ}\frac{d\tilde{k}}{2\pi}\text{Tr}\left[Q(\tilde{k})\right] = -w_{1\text{D}} \implies w_{1\text{D}} = 0 \text{ with } \tilde{k} = -k.\end{aligned} \tag{III.36}$$

This shows that $w_{1\text{D}}$ vanishes. □
Therefore, we do not consider this case any further.

If $H(\mathbf{k})$ instead carries pseudo-inversion symmetry, $w_{1\text{D}}$ is not always vanishing. In this case, we can use the connection between the eigenvalues of the Wilson loop and the inversion eigenvalues. This connection is described in the review of Chiu et al.[26]. For $\nu_1 = w_{1\text{D}}$ the property is

$$e^{\pi i \nu_1[q]} = e^{2\pi i \text{CS}_1[\mathcal{A}]} \tag{III.37}$$

with the first Chern Simons invariant CS_1

$$\text{CS}_1\left[\mathcal{A}\right] = \int_\text{BZ}\mathcal{Q}_1(\mathcal{A}) = \int_\text{BZ}\frac{i}{2\pi}\text{Tr}\left[\mathcal{A}\right] = \frac{i}{2\pi}\text{Tr}\left[\int_\text{BZ}\mathcal{A}\right]. \tag{III.38}$$

This then yields

$$e^{\pi i \nu_1[q]} = e^{-\text{Tr}\left[\int_\text{BZ}\mathcal{A}\right]} = \det e^{-\int_\text{BZ}\mathcal{A}} = \det W, \tag{III.39}$$

which holds in the specific gauge $\mathcal{A}_N = (1/2)q(\mathbf{k})dq^\dagger(\mathbf{k})$ and is expressed in terms of the Wilson loop W in the occupied bands of the Hermitian double Hamiltonian (cf. [137] for a definition of the Wilson loop).

Since both W and ν_1 are gauge-independent, the invariant $w_{1\text{D}} = \nu_1$ can be directly expressed via the determinant of the Wilson loop, with the expression for the Wilson loop from Ref. [137]. We use the mapping between inversion eigenvalues and Wilson loop eigenvalues from Ref. [140], and the mathematical fact that the product of the eigenvalues of a matrix is its determinant. In presence of inversion symmetry, $\det W = \pm 1$. The Wilson loop eigenvalues are either 1, -1, or appear in complex conjugate pairs with absolute value 1. The eigenvalues 1 do not contribute to the determinant and the complex conjugate pairs cancel each other. Therefore, only the eigenvalues -1 can flip the sign of $\det W$. If the number of -1 eigenvalues is odd, $\det W = -1$, in contrast if it is even, $\det W = +1$. We therefore want to prove that if the number of negative inversion eigenvalues is odd, then also the number of negative Wilson loop eigenvalues is odd. In order to do this, we look at the values of the quantities $\{n_\pm(\mathbf{k}_{\text{TRIM}}), n_s, k_s, \xi_s\}$. $n_\pm(\mathbf{k}_{\text{TRIM}})$ are the multiplicities of positive and negative inversion eigenvalues at the TRIMs. n_s is the smallest of these multiplicities, k_s is the momentum at which this smallest multiplicity occurs, and ξ_s is the inversion eigenvalue for which the smallest multiplicity occurs. Alexandradinata et al.[140] show that the spectrum of W consists of $[n_{(+)}(k_s+\pi) - n_s]$ eigenvalues $-\xi_s$, $[n_{(-)}(k_s+\pi) - n_s]$ eigenvalues $+\xi_s$, and n_s pairs of complex-conjugate eigenvalue pairs.

The following cases show that if the number of negative inversion eigenvalues, expressed as $n_-(\pi) + n_-(0)$, is odd, then the Wilson loop has a negative determinant.

First, we start with the case $n_s = n_+(0)$, $k_s = 0$, $\xi_s = +1$. In this case, the number of negative eigenvalues of W is given by

$$n_+(\pi) - n_+(0) = n_+(\pi) + n_+(0) - 2n_+(0) \in 2\mathbb{Z} + 1, \tag{III.40}$$

because $n_-(\pi) + n_-(0) \in 2\mathbb{Z} + 1$ implies that $n_+(\pi) + n_+(0) \in 2\mathbb{Z} + 1$.
Next, we look at the case $n_s = n_-(0)$, $k_s = 0$, $\xi_s = -1$. The number of negative Wilson eigenvalues is given by

$$n_-(\pi) - n_-(0) = n_-(\pi) + n_-(0) - 2n_-(0) \in 2\mathbb{Z} + 1. \tag{III.41}$$

Next, we look at the case $n_s = n_+(\pi)$, $k_s = \pi$, $\xi_s = 1$. The number of negative Wilson eigenvalues is given by

$$n_+(0) - n_+(\pi) = n_+(0) + n_+(\pi) - 2n_+(\pi) \in 2\mathbb{Z} + 1. \tag{III.42}$$

As a last step, we look at the case $n_s = n_-(\pi)$, $k_s = \pi$, $\xi_s = -1$. The number of negative Wilson eigenvalues is given by

$$n_-(0) - n_-(\pi) = n_-(0) + n_-(\pi) - 2n_-(\pi) \in 2\mathbb{Z} + 1. \tag{III.43}$$

These cases show that an odd number of negative inversion eigenvalues implies an odd number of negative -1 Wilson loop eigenvalues, showing that

$$(-1)^{w_{\text{1D}}} = \prod_{k\in\{0,\pi\}, j\in\text{occ.}} \lambda_{k,j}, \tag{III.44}$$

which completes our proof. □

III.5. Two-Dimensional Systems

In even spatial dimensions $d = 2n$ for systems with line gap, a good topological invariant is the n^{th} Chern number, defined as[95]

$$C_n = \frac{1}{n!}\left(\frac{i}{2\pi}\right)^n \int_{\text{BZ}} \text{Tr}\left[\mathcal{F}^n\right] = -\frac{1}{2^{2n+1}n!}\left(\frac{i}{2\pi}\right)^n \int_{\text{BZ}^d} \text{Tr}\left[Q_R(dQ_R)^{2n}\right] \tag{III.45}$$

with the non-Hermitian versions of the Berry curvature $\mathcal{F}$ and the Q matrix Q_R. The non-Abelian Berry connection and Berry curvature are defined as

$$\mathcal{A}_{lm}(\mathbf{k}) = \langle \chi_l(\mathbf{k}) | \partial_{\mathbf{k}} \varphi_m(\mathbf{k})\rangle \cdot d\mathbf{k} \tag{III.46}$$

and

$$\begin{aligned} &\mathcal{F} = d\mathcal{A} + \mathcal{A}^2, \\ &\mathcal{F}_{lm} = \langle \chi_l(\mathbf{k})| \left(1 - \sum_{n\in\text{occ}} |\varphi_n(\mathbf{k})\rangle \langle \chi_n(\mathbf{k})|\right) |\varphi_m(\mathbf{k})\rangle = \langle \chi_l(\mathbf{k})| \left(1 - \mathcal{P}_R\right) |\varphi_m(\mathbf{k})\rangle \end{aligned} \tag{III.47}$$

with

$$\mathcal{P}_R = \sum_{n\in\text{occ}} |\varphi_n(\mathbf{k})\rangle \langle \chi_n(\mathbf{k})| \,. \tag{III.48}$$

The Q matrix is given by

$$Q_R = 1 - 2\mathcal{P}_R. \tag{III.49}$$

We find the first Chern number

$$C_1 = \frac{i}{2\pi}\int_{\text{BZ}} \text{Tr}\left[\mathcal{F}\right]. \tag{III.50}$$

The first Chern number gives a $\mathbb{Z}$ classification of two-dimensional phases with line gaps. The Chern number is the same, independently of whether it is calculated using left and right eigenstates, or only left or only right eigenstates[157].

Systems in the non-Hermitian AZ class A (without any internal symmetries) indeed have a $\mathbb{Z}$ topological classification[95]. Such systems with a line gap can be flattened to Hermitian Hamiltonians with eigenvalues ±1[95]. If this can also be demonstrated while respecting the symmetries, we obtain an easy proof for the validity of the symmetry indicators known from Hermitian physics for the non-Hermitian case. The description of the Hermitian flattening can be found, for example, in Ref. [95]. It consists of two step:

1. First, the Hamiltonian can always be written as

$$H(\mathbf{k}) = R(\mathbf{k}) \begin{pmatrix} E_1(\mathbf{k}) & & & \\ & E_2(\mathbf{k}) & & \\ & & \ddots & \\ & & & E_N(\mathbf{k}) \end{pmatrix} R(\mathbf{k})^{-1}, \tag{III.51}$$

   where $R_{\mathbf{k}}$ is the matrix with the eigenvectors of $H(\mathbf{k})$ as column vectors. We then flatten the spectrum of $H(\mathbf{k})$ to reduce the eigenvalues to ±1. We do this by simply continuously moving all eigenvalues on one side of the line gap to +1, and all eigenvalues on the other side to −1. The result is a non-Hermitian matrix with eigenvalues ±1, still respecting the symmetries.

2. In a second step, the matrix is hermitised by changing $R(\mathbf{k}) \to U_R(\mathbf{k})$, where $U_R(\mathbf{k})$ is a unitary matrix defined as

$$R(\mathbf{k}) = \Lambda_R(\mathbf{k}) U_R(\mathbf{k}) \qquad \text{with } \Lambda_R(\mathbf{k}) = \Big[R(\mathbf{k}) R^\dagger(\mathbf{k})\Big]^{1/2}. \tag{III.52}$$

In this expression, the square root of $R(\mathbf{k})R^\dagger(\mathbf{k})$ is given through

$$\begin{aligned} R(\mathbf{k})R^\dagger(\mathbf{k}) &= V(\mathbf{k}) \begin{pmatrix} \lambda_1^2(\mathbf{k}) & \\ & \ddots \end{pmatrix} V^\dagger(\mathbf{k}) \\ &\implies \Big[R(\mathbf{k})R^\dagger(\mathbf{k})\Big]^{1/2} = V(\mathbf{k}) \begin{pmatrix} \lambda_1(\mathbf{k}) & \\ & \ddots \end{pmatrix} V^\dagger(\mathbf{k}). \end{aligned} \tag{III.53}$$

This is possible because $R(\mathbf{k})R^\dagger(\mathbf{k})$ is positive definite. $U_R(\mathbf{k})$ can then be calculated using $U_R(\mathbf{k}) = \Lambda_R^{-1}(\mathbf{k})R(\mathbf{k})$. The deformation $R(\mathbf{k}) \to U_R(\mathbf{k})$ is performed by moving all $\lambda_i \to 1$, which implies that $\Lambda_R(\mathbf{k}) = \mathbb{1}$, and therefore only $U_R(\mathbf{k})$ remains.

III.5.1. Hermitian Flattening and Rotational Symmetry

In this section, we prove that the procedure described in the previous section maintains the rotational symmetry at every step along the path from the non-Hermitian Hamiltonian to its Hermitian projection. We only have the look at the part acting on the eigenstates, because the move to eigenvalues ±1 can obviously be executed in a C_n-symmetric way.

The path of $H_\varphi(\mathbf{k})$ is a function

$$H_\varphi(\mathbf{k}) : \varphi \in [0,1] \to H_\varphi(\mathbf{k}) \tag{III.54}$$

given by the path followed by $\lambda_i(\varphi, \mathbf{k})$, which is, for instance,

$$\lambda_i(\varphi, \mathbf{k}) = \lambda_i(\mathbf{k}) + \varphi\left(1 - \lambda_i(\mathbf{k})\right). \tag{III.55}$$

In the following, we will prove that

$$r_n H_\varphi(\mathbf{k}) r_n^\dagger = H_\varphi(R_n\mathbf{k}) \qquad \forall \varphi. \tag{III.56}$$

If $H(\mathbf{k})$ is rotationally symmetric,

$$r_n H(\mathbf{k}) r_n^\dagger = H(R_n\mathbf{k}) \Leftrightarrow r_n H(\mathbf{k}) = H(R_n\mathbf{k}) r_n, \tag{III.57}$$

which translates into the condition that if $\left|u_{\mathbf{k}}^i\right\rangle$ is an eigenvector of $H(\mathbf{k})$, then $r_n \left|u_{\mathbf{k}}^i\right\rangle$ is an eigenvector of $H(R_n\mathbf{k})$. This then implies that

$$\begin{aligned} &R(R_n\mathbf{k}) = r_n R(\mathbf{k}) \\ &\implies R(R_n\mathbf{k}) = \Lambda_R(R_n\mathbf{k}) U_R(R_n\mathbf{k}) = r_n R(k) = r_n \Lambda_R(\mathbf{k}) r_n^\dagger r_n U_R(\mathbf{k}). \end{aligned} \tag{III.58}$$

On the other hand,

$$\Lambda_R(R_n\mathbf{k}) = \Big[R(R_n\mathbf{k}) R^\dagger(R_n\mathbf{k})\Big]^{1/2} = r_n V(\mathbf{k}) \begin{pmatrix} \lambda_1(\mathbf{k}) & \\ & \ddots \end{pmatrix} V^\dagger(\mathbf{k}) r_n^\dagger, \tag{III.59}$$

so we get

$$\begin{aligned}\Lambda_R(R_n\mathbf{k}) &= r_n\Lambda_R(\mathbf{k})r_n^\dagger,\\ U_R(R_n\mathbf{k}) &= r_nU_R(\mathbf{k}).\end{aligned}\tag{III.60}$$

Setting all this together, taking into consideration that all φ dependence is within $\Lambda_R(\varphi,\mathbf{k})$, and that this dependence does not change eq. III.60, we can write

$$\begin{aligned}r_nH_\varphi(\mathbf{k})r_n^\dagger = r_nR_\varphi(\mathbf{k})\begin{pmatrix}1 & \\ & -1\end{pmatrix}R_\varphi(\mathbf{k})^{-1}r_n^\dagger &= r_n\Lambda_R(\varphi,\mathbf{k})U_R(\mathbf{k})\begin{pmatrix}1 & \\ & -1\end{pmatrix}U_R^\dagger(\mathbf{k})\Lambda_R^{-1}(\varphi,\mathbf{k})r_n^\dagger\\ &= r_n\Lambda_R(\varphi,\mathbf{k})r_n^\dagger r_nU_R(\mathbf{k})\begin{pmatrix}1 & \\ & -1\end{pmatrix}U_R^\dagger(\mathbf{k})r_n^\dagger r_n\Lambda_R^{-1}(\varphi,\mathbf{k})r_n^\dagger\\ &= \Lambda_R(\varphi,R_n\mathbf{k})U_R(R_n\mathbf{k})\begin{pmatrix}1 & \\ & -1\end{pmatrix}U_R^\dagger(R_n\mathbf{k})\Lambda_R^{-1}(\varphi,R_n\mathbf{k}) = H_\varphi(R_n\mathbf{k}),\end{aligned}\tag{III.61}$$

which proves that $H_\varphi(\mathbf{k})$ remains rotationally symmetric along the flattening path.

Topological invariants do not change under smooth transformations that respect the symmetries. Thus as the path for the flattening respects the symmetries and maintains smoothness, the topological invariants of the Hamiltonian before and after Hermitian flattening are the same. Respect of internal symmetries was shown by Kawabata et al.[95].

If the Hamiltonian has rotational symmetry or inversion symmetry, we can write at the high symmetry point (HSP) $\mathbf{k}^*$ of the BZ that

$$sH(\mathbf{k}^*) - H(\mathbf{k}^*)s = 0,\tag{III.62}$$

with a symmetry operator s. s can be an inversion or rotation symmetry operator. Inversion is equivalent to a C_2 rotational symmetry, but always with $\mathcal{I}^2 = +1$. Because $H(\mathbf{k}^*)$ commutes with the unitary symmetry operator, the joint eigenvectors have the property that the eigensectors of different symmetry eigenvalues are orthogonal to each other. We observe, using that the columns of $R(\mathbf{k})$ are eigenvectors of r_n, that

$$(rR)_{ij}(\mathbf{k}) = \alpha_jR_{ij}(\mathbf{k}) \text{ and } (R^\dagger(\mathbf{k})r_n^\dagger)_{jk} = (r_nR(\mathbf{k}))^*_{kj} = \alpha_j^*R^*_{kj}(\mathbf{k}).\tag{III.63}$$

We can therefore write

$$\Big(rR(\mathbf{k})R^\dagger(\mathbf{k})r^\dagger\Big)_{ik} = \alpha_jR_{ij}(\mathbf{k})\alpha_j^*R^*_{jk}(\mathbf{k}) = R_{ij}(\mathbf{k})R^*_{kj}(\mathbf{k}) = \Big(R(\mathbf{k})R^\dagger(\mathbf{k})\Big)_{ik},\tag{III.64}$$

which then implies

$$\begin{aligned}\left[\Lambda_R^2(\mathbf{k}), r_n\right] = \Big[R(\mathbf{k})R^\dagger(\mathbf{k}), r_n\Big] &= R(\mathbf{k})R^\dagger(\mathbf{k})r_n - r_nR(\mathbf{k})R^\dagger(\mathbf{k}) = 0\\ &\Leftrightarrow R(\mathbf{k})R^\dagger(\mathbf{k}) - r_nR(\mathbf{k})R^\dagger(\mathbf{k})r_n^\dagger = 0.\end{aligned}\tag{III.65}$$

From this we get the identity

$$\left[\Lambda_R^2(\mathbf{k}), r_n\right] = \Lambda_R(\mathbf{k})\left[\Lambda_R(\mathbf{k}), r_n\right] + \left[\Lambda_R(\mathbf{k}), r_n\right]\Lambda_R(\mathbf{k}) = 0 \implies \left[\Lambda_R(\mathbf{k}), r_n\right] = 0,\tag{III.66}$$

Int. Sym.	Point Group	Gap (L / P)	Symmetry indicator
-	$\mathcal{I}$	L	$(-1)^C = \prod_{\mathbf{k}\in\text{TRIMs},j\in\text{occ.}} \lambda_j(\mathbf{k})$
-	C_2	L	$(-1)^C = \prod_{i\in\text{occ.}} \zeta_i(\Gamma)\zeta_i(X)\zeta_i(Y)\zeta_i(M)$
-	C_4	L	$i^C = \prod_{n\in\text{occ.}} \xi_n(\Gamma)\xi_n(M)\zeta_n^{-1}(Y)$
-	C_3	L	$e^{i2\pi C/3} = \prod_{i\in\text{occ.}} (-1)^F \theta_i(\Gamma)\theta_i(K)\theta_i(K')$
-	C_6	L	$e^{i\pi C/3} = \prod_{i\in\text{occ.}} (-1)^F \eta_i(\Gamma)\theta_i(K)\zeta_i(K')$

Table III.2.: Symmetry indicator invariants to limit the allowed values for the Chern number[37][41] in 2D with line gap.

which then leads to

$$rU_R(\mathbf{k}) = r\Lambda_R^{-1}(\mathbf{k})R(\mathbf{k}) = \Lambda_R^{-1}(\mathbf{k})rR(\mathbf{k}) \tag{III.67}$$

and we finally evaluate it only for the first column, getting

$$r_n\vec{u}_{R1} = \Lambda_R^{-1}(\mathbf{k})r_n\vec{r}_1 = \Lambda_R^{-1}(\mathbf{k})\beta^1\vec{r}_1 = \beta^1\vec{u}_{R1}, \tag{III.68}$$

with the rotational eigenvalue β_1 of the first column vector of $R(\mathbf{k})$. This calculation shows that the column vectors of $U_R(\mathbf{k})$ are eigenvectors of r_n with the same eigenvalues as the original joint eigenvectors of $\mathcal{H}(\mathbf{k})$ and r_n. Therefore, we can calculate the symmetry eigenvalues of the Hermitian projection by evaluating the symmetry eigenvalues of the original Hamiltonian.

This means that the flattening procedure does not change the symmetry eigenvalues at the HSPs. We further know that the topological invariants are unchanged. Therefore, any symmetry indicator invariant can be calculated in the Hermitian flattened system by using the symmetry eigenvalues of the non-Hermitian system. Also, the symmetry indicator from the Hermitian case works in the non-Hermitian case as well. The symmetry indicators, as found by Fang et al.[41] and Hughes et al.[37], are listed in Table III.2.

In this table $\lambda_j(\mathbf{k})$ is the jth inversion eigenvalue at $\mathbf{k}$, ζ is the C_2 eigenvalue, ξ the C_4 eigenvalue, θ the C_3 eigenvalue, and η the C_6 eigenvalue. F is given by $C_2^2 = (-1)^F$.

III.6. Three-Dimensional Systems

This chapter dedicated to the symmetry-indicated topological classification of 3D non-Hermitian systems. Two aspects are treated:

1. Determination of the 3D winding number $w_{3\mathrm{D}}$ using symmetry indicators in presence of space group symmetries, for systems are in class A and AII†. In class A, no internal symmetries are present, in class AII†, a TRS† symmetry is present. In these classes, there is a $\mathbb{Z}$ topological classification with invariant $w_{3\mathrm{D}}$[95] whose value can be constrained using symmetry indicators.

2. In non-Hermitian AZ class AII, there is a topological $\mathbb{Z}_2$ classification[95]. A symmetry indicator invariant for this classification in presence of pseudo-inversion symmetry is presented. This invariant is easier to calculate than the invariant currently used, the Chern-Simons invariant CS$_3$ in a special gauge.

III.6.1. Model of the Exceptional Topological Insulator

In the whole chapter, we will base our discussion on a model taken from a paper by Denner et al.[100] about Exceptional Topological Insulators (ETIs). Therefore, this section starts with a short discussion of the ETI model.

III.6.1.1. Hamiltonian and Symmetries

The model for the ETI[100] is given as

$$\mathcal{H}(\mathbf{k}) = \left(\sum_{j=x,y,z} \cos k_j - M \right) \tau_z \sigma_0 + \lambda \sum_{j=x,y,z} \sin k_j \tau_x \sigma_j + \left[\sin \alpha \tau_0 + \cos \alpha \tau_z \right] (\mathbf{B} \cdot \sigma) + i \delta \tau_x \sigma_0. \quad \text{(III.69)}$$

The spectra of this Hamiltonian for $\lambda = 1$, $\delta = 0.5$ and $M = 2$, 2.5 and 3 are shown in Fig. III.2. For this set of parameters, the gap closes at $M = 2.5$; at this value the system transitions from the non-trivial ETI-phase with a point gap around $E_p = \epsilon = 0$ to a trivial phase without point gap around $E_p = \epsilon = 0$. The Hamiltonian has pseudo-inversion symmetry with $\mathcal{I} = \tau_z \sigma_0$. The

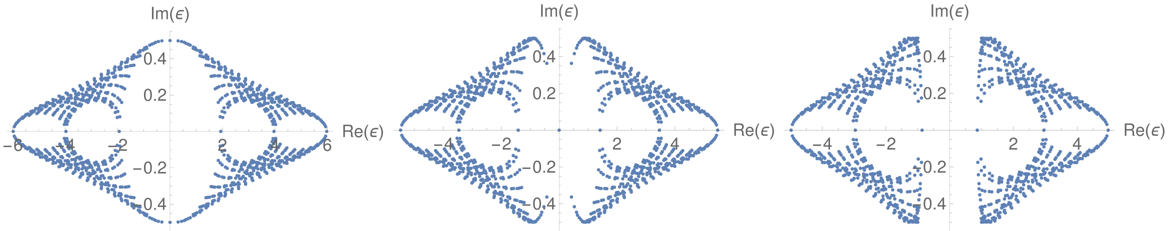

(a) $M = 3.0$ (b) $M = 2.5$ (c) $M = 2.0$

Figure III.2.: Spectrum of the ETI with periodic boundary conditions for $\lambda = 1$, $\delta = \frac{1}{2}$, $M = 2$, 2.5, 3. On the left, the ETI-phase, in the middle the transition between the ETI-phase and the trivial pahse, on the right in the trivial phase.

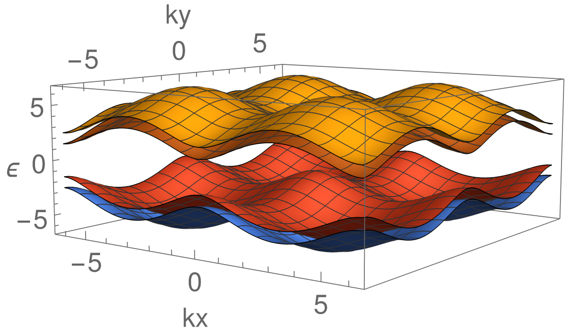

Figure III.3.: Band structure of the Hermitian double Hamiltonian of the ETI Hamiltonian model by Denner et al.[100] for $\lambda = 1$, $\delta = 0.5$, $M = 3$ on the plane (k_x, k_y, π). The band structure is gapped.

Hermitian double of $\mathcal{H}$ is defined as

$$\mathcal{H}_{\mathrm{d}}(\mathbf{k}) = \begin{bmatrix} 0 & \mathcal{H}(\mathbf{k}) \\ \mathcal{H}^{\dagger}(\mathbf{k}) & 0 \end{bmatrix}. \tag{III.70}$$

$\mathcal{H}_{\mathrm{d}}$ has an additional sublattice symmetry (SLS) with the symmetry representation $\mathcal{S}$

$$\mathcal{S}\mathcal{H}_{\mathrm{d}}(\mathbf{k})\mathcal{S}^{-1} = -\mathcal{H}_{\mathrm{d}}(\mathbf{k}), \qquad \mathcal{S} = \begin{bmatrix} \tau_0\sigma_0 & 0 \\ 0 & -\tau_0\sigma_0 \end{bmatrix}. \tag{III.71}$$

The spectrum of the Hermitian double Hamiltonian on the plane (k_x, k_y, π) is shown in Fig. III.3. The pseudo-inversion of $\mathcal{H}$ becomes a normal inversion symmetry of $\mathcal{H}_{\mathrm{d}}$:

$$\begin{bmatrix} 0 & \mathcal{I} \\ \mathcal{I} & 0 \end{bmatrix} \begin{bmatrix} 0 & \mathcal{H}(\mathbf{k}) \\ \mathcal{H}^{\dagger}(\mathbf{k}) & 0 \end{bmatrix} \begin{bmatrix} 0 & \mathcal{I} \\ \mathcal{I} & 0 \end{bmatrix} = \begin{bmatrix} 0 & \mathcal{I}\mathcal{H}^{\dagger}(\mathbf{k})\mathcal{I} \\ \mathcal{I}\mathcal{H}(\mathbf{k})\mathcal{I} & 0 \end{bmatrix} = \begin{bmatrix} 0 & \mathcal{H}(-\mathbf{k}) \\ \mathcal{H}(-\mathbf{k})^{\dagger} & 0 \end{bmatrix}. \tag{III.72}$$

In addition, the ETI-Hamiltonian happens to have a TRS† symmetry (reciprocity) with $\mathcal{C}_{+} = \tau_0\sigma_y$. This symmetry leads to a TRS of the Hermitian double represented by

$$\mathcal{T} = \begin{bmatrix} & \tau_0\sigma_y \\ \tau_0\sigma_y & \end{bmatrix}. \tag{III.73}$$

III.6.1.2. Topological Classification

The ETI with or without TRS† symmetry has a $\mathbb{Z} \times \mathbb{Z}^3$ classification. Such non-Hermitian 3D systems with point gaps are characterised by two different types of invariants. Firstly, there are three weak 1D invariants for the three crystallographic directions[100] (for the $\mathbb{Z}^3$), given by

$$w_{1\mathrm{D},j} = -i \int_{\mathrm{BZ}} \frac{d^3\mathbf{k}}{(2\pi)^3} \mathrm{Tr}\left[Q_j(\mathbf{k})\right] \in \mathbb{Z} \tag{III.74}$$

and secondly an intrinsically 3D integer winding number invariant (for the remaining $\mathbb{Z}$ classification)

$$w_{3\mathrm{D}} = -\int_{\mathrm{BZ}} \frac{d^3\mathbf{k}}{24\pi^2} \epsilon_{ijk} \mathrm{Tr}\left[Q_i(\mathbf{k})Q_j(\mathbf{k})Q_k(\mathbf{k})\right] \in \mathbb{Z}. \tag{III.75}$$

Nonzero $w_{\mathrm{1D},j}$ implies the appearance of non-Hermitian skin effect[106, 107]. If $w_{\mathrm{3D}} = \pm 1$ and $w_{\mathrm{1D},j} = 0 \; \forall j$, the system is in the ETI phase[100].

The 3D invariant is inherited, similarly to the 1D invariant, from an invariant for Hermitian systems with chiral symmetry. The corresponding invariant, ν_3, is also the winding number of the Hermitian double. Expressed in the style of Chiu et al.[26], it is written as

$$\nu_3 = \int_{\mathrm{BZ}} \frac{d^3\mathbf{k}}{24\pi^2} \epsilon^{\mu\nu\rho} \mathrm{Tr}\left[(q^{-1}\partial_\mu q)(q^{-1}\partial_\nu q)(q^{-1}\partial_\rho q) \right] . \tag{III.76}$$

This quantity is directly connected to the magnetoelectric polarisability and the "θ" angle, as

$$e^{i\theta} = e^{2\pi i \int_{\mathrm{BZ}^3} \mathcal{Q}_3[\mathcal{A}]} = e^{2\pi i \mathrm{CS}_3[\mathcal{A}]} = W_3\left[\mathcal{A}\right] = e^{\pi i \nu_3[q]} \implies \theta \mod 2\pi = \pi\nu_3[q] \mod 2\pi . \tag{III.77}$$

The Chern-Simons (CS) form $\mathcal{Q}_3$ is given by

$$\mathcal{Q}_3(\mathcal{A}) = -\frac{1}{8\pi^2} \mathrm{Tr}\left[\mathcal{A} d\mathcal{A} + \frac{2}{3}\mathcal{A}^3 \right] , \tag{III.78}$$

which holds in the specific gauge $\mathcal{A}_N = (1/2) q(\mathbf{k}) dq^\dagger(\mathbf{k})$[26].

Thus we can easily characterise the topology of a system by calculating $w_{\mathrm{1D},j}$ and w_{3D}. But these calculations are computationally costly. Therefore symmetry indicator invariants that can be calculated using only eigenstates at the high-symmetry points would be preferable.

III.6.2. Symmetry Indicators for w_{3D} and $w_{\mathrm{1D},j}$

The properties of $w_{\mathrm{1D},j}$ are inherited from the 1D case. Without loss of generality, we study $w_{\mathrm{1D},x}$ in a cubic BZ. It is

$$w_{\mathrm{1D},x} = -i \int_{\mathrm{BZ}} \frac{d^3\mathbf{k}}{(2\pi)^3} \mathrm{Tr}\left[Q_x(\mathbf{k})\right] = \int \frac{dk_y dk_z}{(2\pi)^2} \underbrace{\left(-i \int_{\mathrm{1D\ BZ}} \frac{dk_x}{2\pi} \mathrm{Tr}\left[Q_j(\mathbf{k})\right] \right)}_{w_{\mathrm{1D}}} . \tag{III.79}$$

The expression in the brackets is the 1D winding number in one dimension. Because the system is gapped, the 1D invariant cannot change as function of the momenta k_y and k_z. If w_{1D} would change, this would imply that the bulk gap is closed at the point (k_x, k_y) where w_{1D} changes. Together with the quantisation of w_{1D}, we observe that $w_{\mathrm{1D},x}$ can be evaluated by evaluated along any line in k_x direction. If we choose a high symmetry line, the symmetry indicators from section III.4.1 can be applied.

Therefore, we are mostly concerned with the 3D invariant w_{3D}. This section is structured as follows: First we describe why systems with real inversion symmetry have vanishing w_{3D}. In the remainder of the section, we are concerned having systems with pseudo-inversion symmetry. First we look at systems with only pseudo-inversion symmetry, then at systems with pseudo-inversion and TRS† symmetry, and finally at systems with pseudo-inversion, TRS† and C_4 symmetry. For all these cases, symmetry indicator formulae are provided.

III.6.2.1. Real Inversion

If a system obeys inversion symmetry, which means that

$$\mathcal{I}\mathcal{H}_{\mathbf{k}}\mathcal{I}^{-1} = \mathcal{H}_{-\mathbf{k}} \tag{III.80}$$

then

$$w_{\mathrm{1D},j} = 0 \text{ and } w_{\mathrm{3D}} = 0. \tag{III.81}$$

$w_{\mathrm{1D},j} = 0$ follows from the 1D calculation, see section III.4.1. On the other hand, for the 3D invariant, we obtain

$$\begin{aligned} w_{\mathrm{3D}} &= -\int_{\mathrm{BZ}} \frac{d^3\boldsymbol{k}}{24\pi^2} \epsilon_{ijk} \mathrm{Tr}[Q_i(\boldsymbol{k})Q_j(\boldsymbol{k})Q_k(\boldsymbol{k})], \\ &= -\int_{\mathrm{BZ}} \frac{d^3\boldsymbol{k}}{24\pi^2} \epsilon_{ijk} \mathrm{Tr}[\mathcal{I}Q_i(\boldsymbol{k})\mathcal{I}^{-1}\mathcal{I}Q_j(\boldsymbol{k})\mathcal{I}^{-1}\mathcal{I}Q_k(\boldsymbol{k})\mathcal{I}^{-1}], \\ &= +\int_{\mathrm{BZ}} \frac{d^3\boldsymbol{k}}{24\pi^2} \epsilon_{ijk} \mathrm{Tr}[Q_i(-\boldsymbol{k})Q_j(-\boldsymbol{k})Q_k(-\boldsymbol{k})], \\ &= +\int_{\mathrm{BZ}} \frac{d^3\boldsymbol{k}}{24\pi^2} \epsilon_{ijk} \mathrm{Tr}[Q_i(\boldsymbol{k})Q_j(\boldsymbol{k})Q_k(\boldsymbol{k})] = -w_{\mathrm{3D}}, \end{aligned} \tag{III.82}$$

which directly implies that

$$w_{\mathrm{3D}} = 0. \tag{III.83}$$

III.6.2.2. Pseudo-Inversion

The more interesting case for us is the one with pseudo-inversion symmetry, defined as

$$\mathcal{I}\mathcal{H}_{\mathbf{k}}\mathcal{I}^{-1} = \mathcal{H}^{\dagger}_{-\mathbf{k}}. \tag{III.84}$$

In this case, both w_{1D} and w_{3D} can be nonvanishing. $w_{\mathrm{1D},j}$ is obtained like in the 1D case (cf. section III.4.1). The symmetry indicator formula is

$$w_{\mathrm{1D},j} \mod 2 = \prod_{n \in \mathrm{occ.}} \lambda_{\mathbf{k}^*,n} \lambda_{\mathbf{k}^* + \pi \hat{k}_j, n} \mod 2, \tag{III.85}$$

where the $\lambda_{\mathbf{k},n}$ is the n^{th} inversion eigenvalue in the occupied bands of the Hermitian double Hamiltonian at the TRIM $\mathbf{k}$, and $\hat{k}_j$ is the unit vector in k_j direction.

w_{3D} is obtained as

$$(-1)^{\frac{\mu_1}{2}} = (-1)^{w_{\mathrm{3D}}} \qquad \text{with } \frac{\mu_1}{2} = \frac{1}{4} \sum_{\mathbf{k} \in \mathrm{TRIMs}} \left(n^+_{\mathbf{k}} - n^-_{\mathbf{k}}\right) \in \mathbb{Z}. \tag{III.86}$$

First, we show that $\frac{\mu_1}{2}$ is integer. We assume that we start with a system having only +1 inversion eigenvalues. If we flip one of them, we have $\mu_1 \to \mu_1 - 1$, if we flip two of them, we have that $\mu_1 \to \mu_1 - 2$. We study the gap of the Hermitian double Hamiltonian under flipping of inversion eigenvalues. If we flip only one of the eigenvalues, and if it was gapped before, we change the Chern-Number of the Hermitian double one of two opposite planes. The change of the Chern number from one plane to the other requires a gap closing[38]. This is depicted in Fig. III.4.

If the gap of the Hermitian double closes, the gap of the $H(\mathbf{k})$ closes as well. Therefore it is not allowed to flip only one eigenvalue; thus we have to change two at once, which changes μ_1 by two. Therefore $\frac{\mu_1}{2} \in \mathbb{Z}$. We also know that $\frac{\mu_1}{2}$ is a topological invariant from Ref. [36]. It

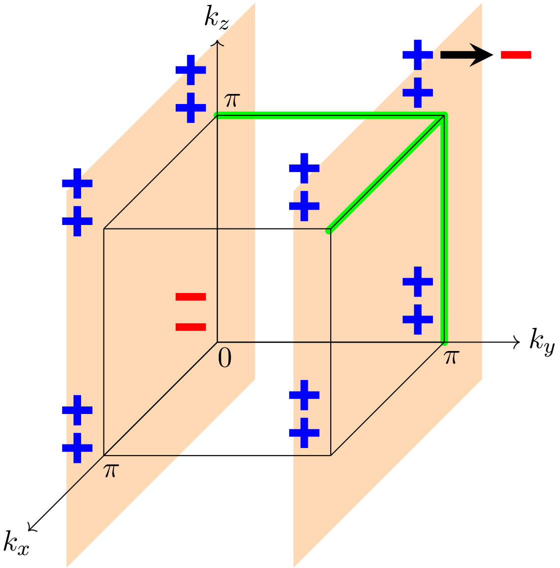

Figure III.4.: If the overall number of negative inversion eigenvalues is odd, the Hamiltonian is gapless. This can be seen by looking at the Hermitian double, starting with an even number of negative eigenvalues. Then the parity of the Chern number of two high symmetry planes (orange planes) in the BZ is the same, because the number of inversion values is either odd on both planes or even on both planes. If we flip one inversion eigenvalue, the Chern number on one of the planes changes. The change of the Chern number from one plane to the other necessitates a gap closure. Another way to see this is by looking at the invariant w_{1D}. We know that for the system not to show a skin effect, w_{1D} has to vanish along all the edges of the cube in the figure. If we flip an eigenvalue, w_{1D} necessarily becomes nonvanishing along three lines, which is forbidden. Thus, flipping only one inversion eigenvalue is forbidden.

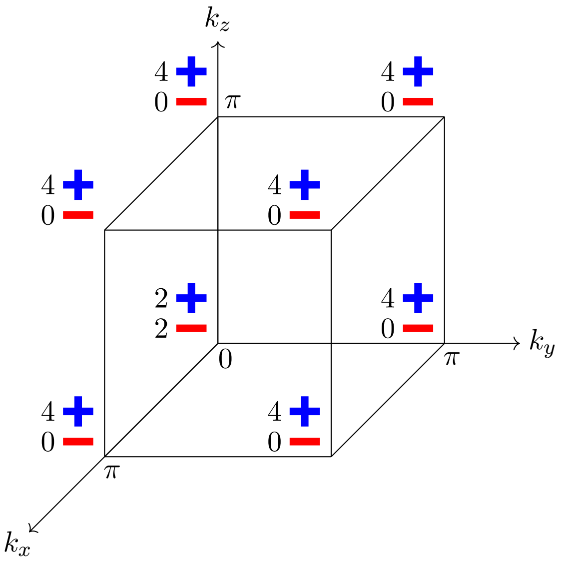

Figure III.5.: Inversion eigenvalues of the Hermitian double Hamiltonian of the ETI model by Denner et al.[100] in the topologically nontrivial phase with $w_{\mathrm{3D}} = 1$. We indicate the number of negative and positive inversion eigenvalues at the TRIMs.

remains to show that $(-1)^{\frac{\mu_1}{2}} = (-1)^{w_{\mathrm{3D}}}$.

Fig. III.5 shows the inversion eigenvalues of the Hermitian double of the ETI model by Denner et al.[100] in the nontrivial phase with $w_{\mathrm{3D}} = 1$. Using these eigenvalues, we can evaluate $\mu_1/2$ to be

$$\frac{\mu_1}{2} = \frac{1}{4} \sum_{\mathbf{k} \in \mathrm{TRIMs}} \left(n_{\mathbf{k}}^{+} - n_{\mathbf{k}}^{-}\right) = \frac{7 \times 4}{4} = 7 \implies (-1)^{\mu_1/2} = -1 = (-1)^{w_{\mathrm{3D}}}. \tag{III.87}$$

Therefore, we conclude that in this specific example the symmetry indicator invariant indeed works.

To prove this connection, we take an in-depth look at the magnetic polarisability in inversion-symmetric insulators. Such systems have been studied from a symmetry indicator point-of-view by Hughes et al.[37] and Turner et al.[38]. Wang et al.[158], Hosur et al.[159] and Deng et al.[31] have studied chiral systems and their properties in detail from a more practical perspective of numerics and tight-binding models. Topological insulators with inversion symmetry were studied by Turner et al.[160] from the point of view of their entanglement spectrum. The main result we use from Turner et al.[38] is that the magnetoelectric polarisability is, for systems with zero Hall conductance, given by the symmetry indicator formula

$$\frac{\theta}{\pi} = \frac{1}{2} \sum_{\mathbf{k} \in \mathrm{TRIMs}} n_o(\mathbf{k}), \tag{III.88}$$

where $n_o(\mathbf{k})$ is the number of negative inversion eigenvalues in the occupied bands at $\mathbf{k}$. This formula holds if the Hall conductance vector $\mathbf{G}_H$ is zero. The allowed values for the vector can be limited using the symmetry indicator formula

$$e^{\frac{i}{2}G_{H_i}} = \prod_{\substack{\mathbf{k}\in\text{TRIMs}\\ \mathbf{k}\cdot\mathbf{R}_i=0}} \prod_{\alpha}^{N_{\text{occ}}} \lambda_{\mathbf{k}}^{\alpha}, \qquad i \in \{x, y, z\}. \tag{III.89}$$

The Hall conductance vector components are even or odd multiples of 2π. This means that the Hall conductance is non-zero if there is a plane with an odd number of negative inversion eigenvalues. If there is such a plane, we can find a line along one of the edges of the plane with an odd number of inversion eigenvalues. Along this line, $w_{1\text{D}} \neq 0$. This entails that the condition $w_{1\text{D}} = 0$ is already a sufficient condition to establish that the Hall conductance vector components must be even multiples of 2π. Using equation III.77, we obtain, under condition of vanishing Hall conductance, that

$$e^{\frac{i\pi}{2}\sum_{\mathbf{k}\in\text{TRIMs}} n_o(\mathbf{k})} = e^{i\theta} = e^{\pi i \nu_3[q]} \implies i^{\left(\sum_{\mathbf{k}\in\text{TRIMs}} n_o(\mathbf{k})\right)} = (-1)^{w_{3\text{D}}}. \tag{III.90}$$

As $\sum_{\mathbf{k}\in\text{TRIMs}} n_o(\mathbf{k})$ is always even for insulators, this gives a well-defined expression for $w_{3\text{D}}$, which coincides with the former expression, by looking at

$$\begin{aligned} i^{\left(\sum_{\mathbf{k}\in\text{TRIMs}} n_{\mathbf{k}}^{-}\right)} &= (-1)^{\frac{1}{2}\left(\sum_{\mathbf{k}\in\text{TRIMs}} n_{\mathbf{k}}^{-}\right)} = (-1)^{\frac{1}{4}\left(\sum_{\mathbf{k}\in\text{TRIMs}} n_{\mathbf{k}}^{-}-n_{\mathbf{k}}^{+}\right)}(-1)^{\frac{1}{4}\left(\sum_{\mathbf{k}\in\text{TRIMs}} N_{\text{occ}}\right)} \\ &= (-1)^{\frac{1}{4}\left(\sum_{\mathbf{k}\in\text{TRIMs}} n_{\mathbf{k}}^{+}-n_{\mathbf{k}}^{-}\right)}(-1)^{\left(\frac{8}{4}N_{\text{occ}}\right)} = (-1)^{\frac{1}{4}\left(\sum_{\mathbf{k}\in\text{TRIMs}} n_{\mathbf{k}}^{+}-n_{\mathbf{k}}^{-}\right)}. \end{aligned} \tag{III.91}$$

This reasoning proves that the symmetry indicator invariant indeed works, given vanishing Hall conductance of the Hermitian double. There is another approach to this issue, based on surface Hamiltonians and their eigenstates. In the following we will describe this point of view as well.

Argumentation using surface Hamiltonians We know that the Hermitian double Hamiltonian is an axion insulator[63, 161] (as it has inversion symmetry) with an additional chiral symmetry (SLS symmetry).

In principle, an axion insulator without chiral symmetry has hinge states, which stem from surface states that are gapped out[63]. If there is an additional chiral symmetry, gapping out the surface states is forbidden, and therefore there are surface states forming a Dirac cone.

This axion insulator can be detected using the symmetry indicator invariant by Ono et al.[36], μ_1.

We will now make this more concrete by calculating the surface states of the ETI given by Hamiltonian in eq. III.69. This surface Hamiltonian should then be gapless and and there should be no allowed constant mass term that gaps it out.

Before proceeding, we will haphazardly choose a surface Hamiltonian and show that it cannot be gapped out. More concretely, if we have a surface Hamiltonian with a Dirac-like kinetic part

$$\mathcal{H}_{\text{kin}}(k_x, k_y) = k_x \tau_z \sigma_x + k_y \tau_z \sigma_y, \tag{III.92}$$

where τ stands for the side of the sample, and σ for the local degree of freedom. This Hamiltonian has inversion symmetry with $\mathcal{I} = \tau_x \sigma_0$ and sublattice symmetry with $\mathcal{S} = \tau_y \sigma_0$. A mass term that gaps out the Hamiltonian has to anticommute with the kinetic term, it has to anticommute with sublattice symmetry and it has to commute with inversion symmetry. Furthermore, it has to be local. The only term fulfilling all the symmetry requirements is

$$\mathcal{H}_{\text{mass}}(k_x, k_y) = m \tau_x \sigma_0. \tag{III.93}$$

This term is not local, and is therefore no allowed mass term. This shows that if there is a gapless Dirac cone-like state on the surface, it cannot be gapped out. The symmetry indicators in the Hermitian class AIII are the same as in class A[36], in principle one gets, with inversion, a $\mathbb{Z}_4$ classification through the symmetry indicator μ_1. Since we have already showed that that only even μ_1 are allowed, we get a $\mathbb{Z}_2$ classification. For $\mu_1 = 2$, a system in class A would be a HOTI with chiral hinge modes. These chiral hinge modes come into existence by gapping out the surface states. Due to CS, these chiral hinge modes are forbidden in class AIII, and the only allowed phases are those with either a gapless surface state or a gapless bulk[36]. Since we assume a gapless bulk, the surface must be gapless. Thus, we have written down an argumentation for the existence of a gapless surface state for odd $\mu_1/2$.
It is known that the number of gapless surface states of the Hermitian double Hamiltonian is in one-to-one correspondence to $w_{3\mathrm{D}}$[100]. Thus, we get that $w_{3\mathrm{D}} \mod 2$ is obtained by calculating $\mu_1/2 \mod 2$.
In the next paragraph, we will make this argument more precise by explicitly calculating the surface Hamiltonian of the Hermitian double of the ETI Hamiltonian by Denner et al.[100].

More precise version using the surface Hamiltonian To make the argument using the surface Hamiltonian more precise, we try to derive it from the bulk Hamiltonian. The Bulk Hamiltonian can be expanded in small $\mathbf{k}$ as

$$\mathcal{H}_{\mathrm{D}}(\mathbf{k}) = (3 - M)\,\tau_z\sigma_0 + \lambda \sum_{j=x,y,z} k_j\tau_x\sigma_j + i\delta\tau_x\sigma_0, \tag{III.94}$$

where we set $\mathbf{B} = 0$. If $\delta = 0$ and $M = 3$, the Hamiltonian is gapless. We then calculate the surface Hamiltonian of the Hermitian double and show that it cannot be gapped out. The methodology of this procedure is based on Schindler[162].
The linearised Hermitian double of $\mathcal{H}_{\mathrm{D}}$ is given by

$$\mathcal{H}_{\mathrm{Dd}}(\mathbf{k}) = (3 - M)\eta_x\tau_z\sigma_0 + \lambda \sum_{j=x,y,z} k_j\eta_x\tau_x\sigma_j - \delta\eta_y\tau_x\sigma_0. \tag{III.95}$$

The system is topologically nontrivial with $w_{3\mathrm{D}} = +1$ for $M = 3$, $\delta = \frac{1}{2}$, therefore this case is studied. The sign of δ determines the sign of $w_{3\mathrm{D}}$, the spectrum is gapless for $\delta = 0$. Therefore, in order to look at a x-dependent transition from the trivial to the non-trivial phase, M is varied. For $M = 3$, the system is in a non-trivial phase with point gap around $E = 0$ (compare Fig. III.2). For $M = 3 - \delta$, this gap closes and the spectrum is gapless. At $M < 3 - \delta$, the system is again gapped, but with a line-gap, such that $w_{3\mathrm{D}}$ w.r.t. $E_p = 0$ vanishes. Therefore, we look at an x-dependent Hamiltonian, with fixed $\delta = \frac{1}{2}$, $\lambda = 1$ and a varying $M(x) = \frac{5}{2} - mx$. For small negative (positive) x, the system is in the topological (trivial) phase, respectively. So, we look at the Hamiltonian

$$\mathcal{H}_{\mathrm{Dd'}}(\mathbf{k}) = \left(\frac{1}{2} + mx\right)\eta_x\tau_z\sigma_0 + \left(-i\frac{\partial}{\partial x}\eta_x\tau_x\sigma_x + \sum_{j=y,z} k_j\eta_x\tau_x\sigma_j\right) - \frac{1}{2}\eta_y\tau_x\sigma_0. \tag{III.96}$$

Reordering and writing it out as $\mathcal{H}_{\mathrm{Hd'}}(\mathbf{k})\,|\Psi\rangle = 0$ to get boundary states with zero energy, we find at $k_y = k_z = 0$ that

$$i\eta_x\tau_x\sigma_x\frac{\partial}{\partial x}\,|\Psi\rangle = \frac{1}{2}\left(\eta_x\tau_z\sigma_0 - \eta_y\tau_x\sigma_0\right)|\Psi\rangle + mx\eta_x\tau_z\sigma_0\,|\Psi\rangle\,. \tag{III.97}$$

We search for zero-energy surface states at $k_y = k_z = 0$. To this end we use the ansatz

$$|\Psi\rangle = e^{\alpha x^2+\beta x}\,|\Psi_0\rangle\,, \tag{III.98}$$

with a constant vector $|\Psi_0\rangle$. Putting this in the differential equation III.97 from above, we get

$$\begin{aligned} i\eta_x\tau_x\sigma_x(2\alpha x+\beta)e^{\alpha x^2+\beta x}\,|\Psi_0\rangle &= \frac{1}{2}\left(\eta_x\tau_z\sigma_0-\eta_y\tau_x\sigma_0\right)e^{\alpha x^2+\beta x}\,|\Psi_0\rangle + mx\eta_x\tau_z\sigma_0 e^{\alpha x^2+\beta x}\,|\Psi_0\rangle \\ \Leftrightarrow i\eta_x\tau_x\sigma_x(2\alpha x+\beta)\,|\Psi_0\rangle &= \frac{1}{2}\left(\eta_x\tau_z\sigma_0-\eta_y\tau_x\sigma_0\right)|\Psi_0\rangle + mx\eta_x\tau_z\sigma_0\,|\Psi_0\rangle\,. \end{aligned} \tag{III.99}$$

We observe that the solutions of this equation are given by the intersection of the kernel of $2\alpha i\eta_x\tau_x\sigma_x - m\eta_x\tau_z\sigma_0$ with the kernel of $\beta i\eta_x\tau_x\sigma_x - \frac{1}{2}\left(\eta_x\tau_z\sigma_0-\eta_y\tau_x\sigma_0\right)$. β and α are free parameters, but we would like that $\alpha < 0$ for reasons of normalisation. For a kernel to be nontrivial, the determinant of the matrix must vanish. Therefore, first, we solve the equation

$$\det\left(2\alpha i\eta_x\tau_x\sigma_x - m\eta_x\tau_z\sigma_0\right) = \left(m^2-4\alpha^2\right)^4 = 0 \implies \alpha = \pm\frac{m}{2}. \tag{III.100}$$

Then we choose $\alpha = -\frac{m}{2}$ to find

$$\operatorname{Ker}\left(-mi\eta_x\tau_x\sigma_x - m\eta_x\tau_z\sigma_0\right) = \left\langle \begin{pmatrix}0\\0\\0\\0\\-i\\0\\0\\1\end{pmatrix}, \begin{pmatrix}0\\0\\0\\0\\0\\-i\\1\\0\end{pmatrix}, \begin{pmatrix}-i\\0\\0\\1\\0\\0\\0\\0\end{pmatrix}, \begin{pmatrix}0\\-i\\1\\0\\0\\0\\0\\0\end{pmatrix} \right\rangle \tag{III.101}$$

and

$$\operatorname{Ker}\left(\beta i\eta_x\tau_x\sigma_x - \frac{1}{2}\left(\eta_x\tau_z\sigma_0-\eta_y\tau_x\sigma_0\right)\right) = \left\langle \begin{pmatrix}0\\0\\0\\0\\0\\-i\\0\\1\end{pmatrix}, \begin{pmatrix}0\\0\\0\\0\\-i\\0\\1\\0\end{pmatrix}, \begin{pmatrix}0\\i\\0\\1\\0\\0\\0\\0\end{pmatrix}, \begin{pmatrix}i\\0\\1\\0\\0\\0\\0\\0\end{pmatrix} \right\rangle \tag{III.102}$$

for $\beta = 0$. The intersection of these two spaces is given by

$$\left\langle(-i,i,-1,1,0,0,0,0)^T,(0,0,0,0,-i,-i,1,1)^T\right\rangle. \tag{III.103}$$

So we have

$$|\Psi_1(x)\rangle = \frac{1}{\mathcal{N}}e^{-\frac{1}{2}mx^2}\begin{pmatrix}-i\\i\\-1\\1\\0\\0\\0\\0\end{pmatrix} \qquad \text{and} \qquad |\Psi_2(x)\rangle = \frac{1}{\mathcal{N}}e^{-\frac{1}{2}mx^2}\begin{pmatrix}0\\0\\0\\0\\-i\\-i\\1\\1\end{pmatrix}. \tag{III.104}$$

The surface Hamiltonian is then given by the matrix elements of $\mathcal{H}_{Dd'}(\mathbf{k})$ in the basis of $\{|\Psi_1(x)\rangle, |\Psi_2(x)\rangle\}$

$$\mathcal{H}_{\mathrm{surf}}(x,k_y,k_z) = \begin{pmatrix} 0 & 4(k_y - ik_z) \\ 4(k_y + ik_z) & 0 \end{pmatrix} = 4k_y\sigma_x + 4k_z\sigma_y \propto k_y\sigma_x + k_z\sigma_y. \tag{III.105}$$

This Hamiltonian has the sublattice symmetry $\mathcal{S} = \sigma_z$, which can be obtained from $\mathcal{S}_{mn} \propto \langle\Psi_m(x)|\mathcal{S}_{\mathrm{d}}|\Psi_n(x)\rangle$. There is no allowed mass term because there is no allowed Hermitian term that anticommutes with $\mathcal{S}$ and the kinetic part of the Hamiltonian.
There are also two-additional zero-energy states of $\mathcal{H}_{Dd'}$ with an x-dependence $e^{-\frac{1}{2}mx^2-x}$. These states are artefacts of the choice of x-dependence of $M(x) = \frac{5}{2} - mx$, which means that $\mathcal{H}_{D'}$ passes twice from the topological to the trivial phase: at $M = 5/2$ and $M = 7/2$. These states can therefore be discarded.
The fact that the surface Hamiltonian of the Hermitian double cannot be gapped out entails that there are surface states with vanishing energy. These surface states can be analysed using symmetry indicator invariants (cf. Ref. [36]). The concrete calculation here has shown that these states indeed stem from an ETI with $w_{\mathrm{3D}} = \pm 1$ and that the number of gapless surface states is equal to $|w_{\mathrm{3D}}|$. By topology, this then also applies to other systems with the same symmetries that can be smoothly transformed to this Hamiltonian while respecting the symmetries.

III.6.2.3. Pseudo-Inversion and TRS†

In this section, systems with TRS† and pseudo-inversion symmetry are treated. An example of such a system is the one described by the ETI Hamiltonian (cf. Eq. III.69). Symmetry indicators then allow a $\mathbb{Z}_4$ determination of w_{3D}. If $w_{\mathrm{3D}} = \pm 2$, we get a state with two Dirac cones on each surface, immune to being gapped out by constant mass terms. In the following, we argue, using a surface Hamiltonian argument, that indeed the addition of TRS† gives us a more complete tool to determine w_{3D}.

A TRS† symmetry of the Hamiltonian implies a TRS of the Hermitian double Hamiltonian, which appears in addition to the already existing $\mathcal{I}$ and $\mathcal{S}$ symmetries. We first write down an argument using an invented surface Hamiltonian for the Hermitian double. We want to show that a surface Hamiltonian with two gapless states (a double Dirac cone) cannot be gapped out. If the surface of a system is in addition TR-symmetric, we have, for example,

$$\mathcal{H}_{\mathrm{kin}}(k_x,k_y) = k_x\rho_z\tau_z\sigma_x + k_y\rho_z\tau_z\sigma_y \tag{III.106}$$

with the symmetries

$$\begin{aligned} \mathcal{T} &= \rho_0\tau_0\sigma_y\mathcal{K} \\ \mathcal{I} &= \rho_0\tau_x\sigma_0 \\ \mathcal{S} &= \rho_0\tau_y\sigma_0. \end{aligned} \tag{III.107}$$

In this situation a potential mass term has to commute with $\mathcal{T}$ and $\mathcal{I}$ and anticommute with $\mathcal{S}$ and the kinetic part. The only terms fulfilling the syemmtry requirements are

$$\begin{aligned} \mathcal{H}_{\mathrm{mass}}(k_x,k_y) &= m\rho_0\tau_x\sigma_0, \\ \mathcal{H}_{\mathrm{mass}}(k_x,k_y) &= m\rho_z\tau_x\sigma_0, \\ \mathcal{H}_{\mathrm{mass}}(k_x,k_y) &= m\rho_y\tau_x\sigma_z. \end{aligned} \tag{III.108}$$

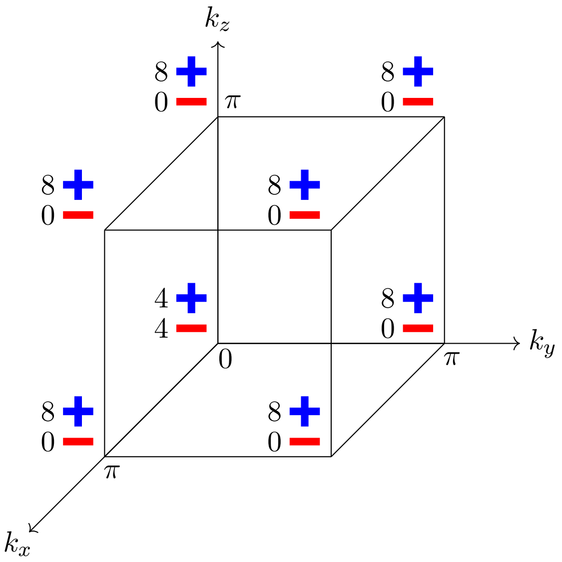

Figure III.6.: Inversion eigenvalues of the Hermitian double of TRS†-doubled ETI model by Denner et al.[100].

Unfortunately, these terms are non-local, so they cannot serve as mass terms. The fact that a mass term is forbidden shows that there is indded a $\mathbb{Z}_4$ symmetry indicator, which allows the determination of the number of gapless surfaces states. As the number of gapless surface states of the Hamiltonian and its Hermitian double are identical, and as in addition w_{3D} gives the number of gapless surface states, we get a $\mathbb{Z}_4$ characterisation of w_{3D}. Next, we show that we get an analogous result by starting with the ETI Hamiltonian.

Surface states of the Hermitian double Now, we study the doubled ETI with TRS†, such that $w_{\text{3D}} = 2$. This Hamiltonian is given by

$$\mathcal{H} = \mathcal{H}_{\text{ETI}} \oplus \mathcal{H}_{\text{ETI}}. \tag{III.109}$$

The inversion eigenvalues of this Hamiltonian are depicted in Fig. III.6 and numerically we can check that it has $w_{\text{3D}} = 2$. Using the inversion eigenvalues, we evaluate the symmetry indicator as

$$\frac{\mu_1}{2} = \sum_{\mathbf{k}\in\text{TRIMs}} \left(n^+_{\mathbf{k}} - n^-_{\mathbf{k}}\right) = \frac{7\times 8}{4} = 14 \implies w_{\text{3D}} \mod 4 = \frac{\mu_1}{2} \mod 4. \tag{III.110}$$

This is in agreement with the claimed $\mathbb{Z}_4$ determination of w_{3D} using this symmetry indicator. We now calculate the surface states of the Hermitian double. We start by expanding $\mathcal{H}$ in small momenta around $\mathbf{k} = 0$; we get

$$\mathcal{H}_{\text{Dd}}(\mathbf{k}) = (3-M)\eta_x\rho_0\tau_z\sigma_0 + \lambda \sum_{j=x,y,z} k_j\eta_x\rho_0\tau_x\sigma_j - \delta\eta_y\rho_0\tau_x\sigma_0. \tag{III.111}$$

We then look at the phase transition around $M = \frac{5}{2}$ with $\delta = \frac{1}{2}$ and $\lambda = 1$. Furthermore, we use x as a real space variable. Then, we obtain

$$\mathcal{H}_{\text{Dd'}}(\mathbf{k}) = \left(\frac{1}{2} + mx\right) \eta_x \rho_0 \tau_z \sigma_0 + \left(-i\frac{\partial}{\partial x}\eta_x \rho_0 \tau_x \sigma_x + \sum_{j=y,z} k_j \eta_x \rho_0 \tau_x \sigma_j\right) - \frac{1}{2}\eta_y \rho_0 \tau_x \sigma_0. \tag{III.112}$$

Searching again for the zero-energy states with the ansatz $|\Psi\rangle = e^{\alpha x^2 + \beta x} |\Psi_0\rangle$, we get $\alpha = -\frac{m}{2}$ and $\beta \in \{-1, 0, +1\}$. The vectors with $\beta = 0$ are then given by

$$\begin{aligned}
|\Psi_1(x)\rangle &= e^{-\frac{m}{2}x^2} \left(-i, i, -1, 1, 0, 0, 0, 0, 0, 0, 0, 0, 0, 0, 0, 0\right)^T, \\
|\Psi_2(x)\rangle &= e^{-\frac{m}{2}x^2} \left(0, 0, 0, 0, -i, i, -1, 1, 0, 0, 0, 0, 0, 0, 0, 0\right)^T, \\
|\Psi_3(x)\rangle &= e^{-\frac{m}{2}x^2} \left(0, 0, 0, 0, 0, 0, 0, 0, i, i, -1, -1, 0, 0, 0, 0\right)^T, \\
|\Psi_4(x)\rangle &= e^{-\frac{m}{2}x^2} \left(0, 0, 0, 0, 0, 0, 0, 0, 0, 0, 0, 0, i, i, -1, -1\right)^T.
\end{aligned} \tag{III.113}$$

The surface Hamiltonian has then the form

$$\begin{aligned}
\mathcal{H}_{\text{surf}}(x, k_y, k_z) &= -4e^{-mx^2} \begin{pmatrix} 0 & 0 & (k_y + ik_z) & 0 \\ 0 & 0 & 0 & (k_y + ik_z) \\ (k_y - ik_z) & 0 & 0 & 0 \\ 0 & (k_y - ik_z) & 0 & 0 \end{pmatrix} \\
&\propto k_y \tau_x \sigma_0 - k_z \tau_y \sigma_0,
\end{aligned} \tag{III.114}$$

if we only use the states centred at $x = 0$ (i.e. $\beta = 0$). The symmetries on the surface are then time reversal symmetry with

$$\mathcal{T} = \tau_y \sigma_x \tag{III.115}$$

and sublattice symmetry with

$$\mathcal{S} = \tau_z \sigma_0. \tag{III.116}$$

There is no constant mass term $\tau_\mu \sigma_\nu$ that anticommutes with $\mathcal{S}$ and with the kinetic term and that commutes with $\mathcal{T}$. Therefore the surface cannot be gapped out, and the symmetry indicator invariant indeed works.

III.6.2.4. Pseudo-Inversion, TRS† and C_4

Next, we evaluate the case where the Hamiltonian has an additional C_4 symmetry. The concrete symmetrisation for our model is described below. If we start with the Hamiltonian $\mathcal{H}_{\text{ETI}}(\mathbf{k})$, then we get the C_4 symmetric Hamiltonian as

$$\mathcal{H}(\mathbf{k}) = \mathcal{H}_{\text{ETI}}(\mathbf{k}) \oplus r_4^\dagger \mathcal{H}_{\text{ETI}}(R\mathbf{k}) r_4 \oplus r_4^{\dagger 2} \mathcal{H}_{\text{ETI}}(R^2\mathbf{k}) r_4^2 \oplus r_4^{\dagger 3} \mathcal{H}_{\text{ETI}}(R^3\mathbf{k}) r_4^3. \tag{III.117}$$

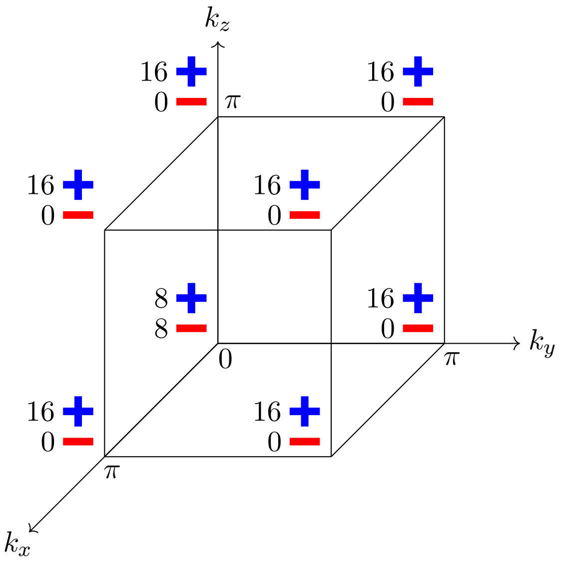

Figure III.7.: Inversion eigenvalues of the Hermitian double of the C_4-symmetrised ETI model by Denner et al.[100].

This Hamiltonian has four times the dimension of $\mathcal{H}_{\mathrm{ETI}}$ and has the symmetries

$$\begin{aligned}\tilde{r}_4 &= \begin{bmatrix} & r_4 & & \\ & & r_4 & \\ & & & r_4 \\ r_4 & & & \end{bmatrix},\\ \tilde{\mathcal{I}} &= \mathbb{1}_4 \otimes \mathcal{I},\\ \tilde{\tau} &= \mathbb{1}_4 \otimes \tau,\\ &, \end{aligned} \tag{III.118}$$

which act as

$$\begin{aligned}\tilde{r}_4 \mathcal{H}(\mathbf{k}) \tilde{r}_4^\dagger &= \mathcal{H}(R_4\mathbf{k}),\\ \tilde{\mathcal{I}} \mathcal{H}(\mathbf{k}) \tilde{\mathcal{I}}^\dagger &= \mathcal{H}^\dagger(-\mathbf{k}),\\ \tilde{\tau} \mathcal{H}^T(\mathbf{k}) \tilde{\tau}^\dagger &= \mathcal{H}(-\mathbf{k}).\end{aligned} \tag{III.119}$$

The symmetries are constructed using the operators with dimensionality of $\mathcal{H}_{\mathrm{ETI}}$, $\mathcal{I} = \tau_z\sigma_0$, $\tau = \tau_0\sigma_y$ and

$$r_4 = \begin{bmatrix} e^{i\pi/4} & & & \\ & e^{-i\pi/4} & & \\ & & e^{3i\pi/4} & \\ & & & e^{-3i\pi/4} \end{bmatrix}. \tag{III.120}$$

The choice of r_4 is quite arbitrary, as long as it fullfills $r_4^4 = -1$, $\tilde{\mathcal{I}}\tilde{r}_4 - \tilde{r}_4\tilde{\mathcal{I}} = 0$ and $\tilde{\tau}\mathcal{K}\tilde{r}_4 - \tilde{r}_4\tilde{\tau}\mathcal{K} = 0$. The Hamiltonian has $w_{\mathrm{3D}} = 4$ and its inversion eigenvalues are shown in Fig. III.7.
A symmetry indicator for the doubled Hamiltonian is (cf. Ref. [33]),

$$\Delta = \kappa_1 - 2\kappa_4, \tag{III.121}$$

where

$$\kappa_1 = \frac{1}{4} \sum_{\mathbf{k} \in \mathrm{TRIMs}} \left(n_{\mathbf{k}}^{+} - n_{\mathbf{k}}^{-} \right) \tag{III.122}$$

and

$$\kappa_4 = \frac{1}{2\sqrt{2}} \sum_{\mathbf{k} \in K_4} \sum_{\alpha} e^{i(\alpha\pi/4)} n_{\mathbf{k}}^{\alpha} \in \mathbb{Z} \text{ with } \alpha = 1, 3, 5, 7 \tag{III.123}$$

and

$$K_4 = \{(0,0,0), (\pi,\pi,0), (0,0,\pi), (\pi,\pi,\pi)\} \tag{III.124}$$

for primitive lattice systems, as well as

$$K_4 = \{(0,0,0), (0,0,2\pi), (\pi,\pi,-\pi), (\pi,\pi,\pi)\} \tag{III.125}$$

for body-centred systems.
The claim here is then that

$$\Delta \mod 8 = \kappa_1 - 2\kappa_2 \mod 8 = w_{\mathrm{3D}} \mod 8. \tag{III.126}$$

If we evaluate this invariant on our example Hamiltonian $\mathcal{H}(\mathbf{k})$, we get

$$\begin{aligned} \kappa_1 &= \frac{1}{4} \sum_{\mathbf{k} \in \mathrm{TRIMs}} \left(n_{\mathbf{k}}^{+} - n_{\mathbf{k}}^{-} \right) = \frac{16 \times 7}{4} = 28, \\ \kappa_4 &= 0, \\ &\implies \Delta = \kappa_1 - 2\kappa_4 = 28, \end{aligned} \tag{III.127}$$

where we used that at all $\mathbf{k} \in K_4$ each C_4 eigenvalue $e^{i\alpha/4}$, $\alpha \in \{1,3,5,7\}$ appears four times. Thus, the symmetry indicator formula holds for this example.
In order to prove that it holds in general, we look at the surface Hamiltonian of the Hermitian double Hamiltonian.

Surface states of the Hermitian double First, we expand the Hamiltonian for small $\mathbf{k}$ and then double it. For that, we expand it around $\mathbf{k} = 0$ at $\mathbf{B} = 0$.

$$\mathcal{H}_{\mathrm{ETI}}(\mathbf{k}) = (\delta + mx)\, \tau_z \sigma_0 + \lambda \sum_{j=x,y,z} k_j \tau_x \sigma_j + i\delta \tau_x \sigma_0. \tag{III.128}$$

The C_4-symmetrised expression is then

$$\mathcal{H}_{C_4\mathrm{ETI}} = (\delta + mx)\, A + \lambda \sum_{j=x,y,z} k_j \Gamma_j + i\delta\Delta \tag{III.129}$$

with

$$\begin{aligned} A &= (\tau_z\sigma_0) \oplus r_4^{\dagger} (\tau_z\sigma_0) r_4 \oplus r_4^{\dagger 2} (\tau_z\sigma_0) r_4^2 \oplus r_4^{\dagger 3} (\tau_z\sigma_0) r_4^3, \\ \Gamma_x &= (\tau_x\sigma_x) \oplus r_4^{\dagger} (\tau_x\sigma_y) r_4 \oplus r_4^{\dagger 2} (-\tau_x\sigma_x) r_4^2 \oplus r_4^{\dagger 3} (-\tau_x\sigma_y) r_4^3, \\ \Gamma_y &= (\tau_x\sigma_y) \oplus r_4^{\dagger} (-\tau_x\sigma_x) r_4 \oplus r_4^{\dagger 2} (-\tau_x\sigma_y) r_4^2 \oplus r_4^{\dagger 3} (\tau_x\sigma_x) r_4^3, \\ \Gamma_z &= (\tau_x\sigma_z) \oplus r_4^{\dagger} (\tau_x\sigma_z) r_4 \oplus r_4^{\dagger 2} (\tau_x\sigma_z) r_4^2 \oplus r_4^{\dagger 3} (\tau_x\sigma_z) r_4^3, \\ \Delta &= (\tau_x\sigma_0) \oplus r_4^{\dagger} (\tau_x\sigma_0) r_4 \oplus r_4^{\dagger 2} (\tau_x\sigma_0) r_4^2 \oplus r_4^{\dagger 3} (\tau_x\sigma_0) r_4^3. \end{aligned} \tag{III.130}$$

The Hermitian double Hamiltonian, expressed as a function of $\mathbf{k} = (k_x, k_y, k_z)$ is then

$$\mathcal{H}_d(\mathbf{k}) = (\delta + m x_i)\, A_\mathrm{d} + \lambda k_x \Gamma_{x\mathrm{d}} + \lambda k_y \Gamma_{y\mathrm{d}} + \lambda k_z \Gamma_{z\mathrm{d}} - \delta \Delta_\mathrm{d}, \tag{III.131}$$

with

$$\begin{aligned} A_\mathrm{d} &= \eta_x \otimes A, \\ \Gamma_{x\mathrm{d}} &= \eta_x \otimes \Gamma_x, \\ \Gamma_{y\mathrm{d}} &= \eta_x \otimes \Gamma_y, \\ \Gamma_{z\mathrm{d}} &= \eta_x \otimes \Gamma_z, \\ \Delta_\mathrm{d} &= \eta_y \otimes \Delta \end{aligned} \tag{III.132}$$

and $x_i \in \{x, y, z\}$.
We now solve the equation at $k_y = k_z = 0$, which is

$$\left[(\delta + mx)\, A_\mathrm{d} + \lambda \Gamma_{x\mathrm{d}} \left(-i\frac{\partial}{\partial x}\right) - \delta \Delta_\mathrm{d}\right] |\Psi(x)\rangle = 0. \tag{III.133}$$

With the ansatz $|\Psi(x)\rangle = e^{\alpha x^2 + \beta x} |\Psi_0\rangle$, we get

$$(\delta + mx)\, A_\mathrm{d} e^{\alpha x^2 + \beta x} |\Psi_0\rangle - i\lambda \Gamma_{x\mathrm{d}} \left((2\alpha x + \beta) e^{\alpha x^2 + \beta x} |\Psi_0\rangle\right) - \delta \Delta_\mathrm{d} e^{\alpha x^2 + \beta x} |\Psi_0\rangle = 0, \tag{III.134}$$

which is equivalent to

$$(\delta A_\mathrm{d} - \delta \Delta_\mathrm{d} - i\beta\lambda \Gamma_{x\mathrm{d}})\, |\Psi_0\rangle + (mx A_\mathrm{d} - 2i\lambda\alpha x \Gamma_{x\mathrm{d}})\, |\Psi_0\rangle = 0. \tag{III.135}$$

Subsequently, we search for the intersection of the kernels of $(\delta A_\mathrm{d} - \delta\Delta_\mathrm{d} - i\beta\lambda\Gamma_{x\mathrm{d}})$ and $(m A_\mathrm{d} - 2i\lambda\alpha\Gamma_{x\mathrm{d}})$. The kernels are nontrivial if $\alpha = \pm m/2\lambda$ and $\beta \in \{0, +2\delta/\lambda, -2\delta/\lambda\}$. We presume that $\lambda > 0$ and $\delta > 0$. Therefore, $\alpha = -m/2\lambda$ and the intersection of the kernels is empty for $\beta = 2\delta/\lambda$. We use the values for $\beta = 0$, because the states for $\beta = -2\delta/\lambda$ merely stem from our choice of $m(x)$. The vectors $|\Psi(x)\rangle$ are

$$\begin{aligned}
|\Psi_1(x)\rangle &= e^{-\frac{m}{2\lambda}x^2}(-i, i, -1, 1, 0, 0, 0, 0, 0, 0, 0, 0, 0, 0, 0, 0, 0, 0, 0, 0, 0, 0, 0, 0, 0, 0, 0, 0, 0, 0, 0, 0)^T, \\
|\Psi_2(x)\rangle &= e^{-\frac{m}{2\lambda}x^2}(0, 0, 0, 0, 1, 1, -1, 1, 0, 0, 0, 0, 0, 0, 0, 0, 0, 0, 0, 0, 0, 0, 0, 0, 0, 0, 0, 0, 0, 0, 0, 0)^T, \\
|\Psi_3(x)\rangle &= e^{-\frac{m}{2\lambda}x^2}(0, 0, 0, 0, 0, 0, 0, 0, i, -i, -1, 1, 0, 0, 0, 0, 0, 0, 0, 0, 0, 0, 0, 0, 0, 0, 0, 0, 0, 0, 0, 0)^T, \\
|\Psi_4(x)\rangle &= e^{-\frac{m}{2\lambda}x^2}(0, 0, 0, 0, 0, 0, 0, 0, 0, 0, 0, 0, -1, -1, -1, 1, 0, 0, 0, 0, 0, 0, 0, 0, 0, 0, 0, 0, 0, 0, 0, 0)^T, \\
|\Psi_5(x)\rangle &= e^{-\frac{m}{2\lambda}x^2}(0, 0, 0, 0, 0, 0, 0, 0, 0, 0, 0, 0, 0, 0, 0, 0, i, i, -1, -1, 0, 0, 0, 0, 0, 0, 0, 0, 0, 0, 0, 0)^T, \\
|\Psi_6(x)\rangle &= e^{-\frac{m}{2\lambda}x^2}(0, 0, 0, 0, 0, 0, 0, 0, 0, 0, 0, 0, 0, 0, 0, 0, 0, 0, 0, 0, -1, 1, -1, -1, 0, 0, 0, 0, 0, 0, 0, 0)^T, \\
|\Psi_7(x)\rangle &= e^{-\frac{m}{2\lambda}x^2}(0, 0, 0, 0, 0, 0, 0, 0, 0, 0, 0, 0, 0, 0, 0, 0, 0, 0, 0, 0, 0, 0, 0, 0, -i, -i, -1, -1, 0, 0, 0, 0)^T, \\
|\Psi_8(x)\rangle &= e^{-\frac{m}{2\lambda}x^2}(0, 0, 0, 0, 0, 0, 0, 0, 0, 0, 0, 0, 0, 0, 0, 0, 0, 0, 0, 0, 0, 0, 0, 0, 0, 0, 0, 0, 1, -1, -1, -1)^T.
\end{aligned} \tag{III.136}$$

By evaluating

$$\mathcal{H}_\mathrm{surf}(x, k_y, k_z)_{mn} = \langle \Psi_m(x) | \mathcal{H}_\mathrm{d} | \Psi_n(x) \rangle\,, \tag{III.137}$$

we get

$$
\begin{aligned}
&\mathcal{H}_{\mathrm{surf}}(x,k_y,k_z) = -4\lambda e^{-\frac{m}{\lambda}x^2}\times \\
&\begin{pmatrix}
0 & 0 & 0 & 0 & k_y+ik_z & 0 & 0 & 0 \\
0 & 0 & 0 & 0 & 0 & k_y+ik_z & 0 & 0 \\
0 & 0 & 0 & 0 & 0 & 0 & k_y+ik_z & 0 \\
0 & 0 & 0 & 0 & 0 & 0 & 0 & k_y+ik_z \\
k_y-ik_z & 0 & 0 & 0 & 0 & 0 & 0 & 0 \\
0 & k_y-ik_z & 0 & 0 & 0 & 0 & 0 & 0 \\
0 & 0 & k_y-ik_z & 0 & 0 & 0 & 0 & 0 \\
0 & 0 & 0 & k_y-ik_z & 0 & 0 & 0 & 0
\end{pmatrix} \\
&= -4\lambda e^{-\frac{m}{\lambda}x^2}\left(k_y\xi_x\zeta_0\sigma_0 - k_z\xi_y\zeta_0\sigma_0\right). \quad \text{(III.138)}
\end{aligned}
$$

This surface Hamiltonian has a sublattice symmetry with $\mathcal{S}=\xi_z\zeta_0\sigma_0$ and time-reversal symmetry with $\tau=\xi_y\zeta_0\sigma_0$. In this case, there is also no constant mass term that would meet the conditions

$$
\begin{aligned}
\tau\mathcal{H}^*_{\mathrm{mass}}(\mathbf{k})\tau^\dagger - \mathcal{H}_{\mathrm{mass}}(-\mathbf{k}) &= 0, \\
\mathcal{S}\mathcal{H}_{\mathrm{mass}}(\mathbf{k})\mathcal{S}^\dagger + \mathcal{H}_{\mathrm{mass}}(\mathbf{k}) &= 0, \\
\mathcal{H}_{\mathrm{surf}}(\mathbf{k})\mathcal{H}_{\mathrm{mass}}(\mathbf{k}) + \mathcal{H}_{\mathrm{mass}}(\mathbf{k})\mathcal{H}_{\mathrm{surf}}(\mathbf{k}) &= 0.
\end{aligned} \quad \text{(III.139)}
$$

Therefore we conclude that the surface degeneracies cannot be gapped out.
Repeating the same procedure in y yields

$$
\begin{aligned}
&\mathcal{H}_{\mathrm{surf}}(k_x,y,k_z) = 4\lambda e^{-\frac{m}{\lambda}y^2}\times \\
&\begin{pmatrix}
0 & 0 & 0 & 0 & k_x-ik_z & 0 & 0 & 0 \\
0 & 0 & 0 & 0 & 0 & k_x-ik_z & 0 & 0 \\
0 & 0 & 0 & 0 & 0 & 0 & k_x-ik_z & 0 \\
0 & 0 & 0 & 0 & 0 & 0 & 0 & k_x-ik_z \\
k_x+ik_z & 0 & 0 & 0 & 0 & 0 & 0 & 0 \\
0 & k_x+ik_z & 0 & 0 & 0 & 0 & 0 & 0 \\
0 & 0 & k_x+ik_z & 0 & 0 & 0 & 0 & 0 \\
0 & 0 & 0 & k_x+ik_z & 0 & 0 & 0 & 0
\end{pmatrix} \\
&= 4\lambda e^{-\frac{m}{\lambda}y^2}\left(k_x\xi_x\zeta_0\sigma_0 + k_z\xi_y\zeta_0\sigma_0\right), \quad \text{(III.140)}
\end{aligned}
$$

with TRS with $\tau=i\xi_y\zeta_0\sigma_0$ and sublattice symmetry with $\mathcal{S}=\xi_z\zeta_0\sigma_0$. It is again impossible to find a mass term compatible with the conditions laid down in eq. III.139.

The procedure in z direction yields

$$
\begin{aligned}
&\mathcal{H}_{\mathrm{surf}}(k_x, k_y, z) = 2\lambda e^{-\frac{m}{\lambda}z^2} \times \\
&\begin{pmatrix}
0 & 0 & 0 & 0 & k_y - ik_x & 0 & 0 & 0 \\
0 & 0 & 0 & 0 & 0 & k_y - ik_x & 0 & 0 \\
0 & 0 & 0 & 0 & 0 & 0 & k_y - ik_x & 0 \\
0 & 0 & 0 & 0 & 0 & 0 & 0 & k_y - ik_x \\
k_y + ik_x & 0 & 0 & 0 & 0 & 0 & 0 & 0 \\
0 & k_y + ik_x & 0 & 0 & 0 & 0 & 0 & 0 \\
0 & 0 & k_y + ik_x & 0 & 0 & 0 & 0 & 0 \\
0 & 0 & 0 & k_y + ik_x & 0 & 0 & 0 & 0
\end{pmatrix} \\
&= 2\lambda e^{-\frac{m}{\lambda}z^2} \left(k_x \xi_y \zeta_0 \sigma_0 + k_y \xi_x \zeta_0 \sigma_0 \right). \qquad \text{(III.141)}
\end{aligned}
$$

This surface Hamiltonian has r_4, $\mathcal{T}$ and $\mathcal{S}$ symmetries, whose matrix representations are given by

$$
\begin{aligned}
\mathcal{S} &= \xi_z \zeta_0 \sigma_0, \\
\tau &= -\xi_y \zeta_0 \sigma_0, \\
r_4 &= \begin{pmatrix}
0 & e^{-\frac{3i\pi}{4}} & 0 & 0 & 0 & 0 & 0 & 0 \\
0 & 0 & e^{-\frac{3i\pi}{4}} & 0 & 0 & 0 & 0 & 0 \\
0 & 0 & 0 & e^{-\frac{3i\pi}{4}} & 0 & 0 & 0 & 0 \\
e^{-\frac{3i\pi}{4}} & 0 & 0 & 0 & 0 & 0 & 0 & 0 \\
0 & 0 & 0 & 0 & 0 & e^{\frac{3i\pi}{4}} & 0 & 0 \\
0 & 0 & 0 & 0 & 0 & 0 & e^{\frac{3i\pi}{4}} & 0 \\
0 & 0 & 0 & 0 & 0 & 0 & 0 & e^{\frac{3i\pi}{4}} \\
0 & 0 & 0 & 0 & e^{\frac{3i\pi}{4}} & 0 & 0 & 0
\end{pmatrix}.
\end{aligned} \tag{III.142}
$$

There is again no allowed constant mass term of the form $\xi_\mu \zeta_\nu \sigma_\omega$ that satisfies all the conditions from equation III.139. Interestingly, it is not necessary to make any use of fourfold rotational symmetry.
This shows that the symmetry is indeed a $\mathbb{Z}_8$ invariant for $w_{3\mathrm{D}}$. Further this calculation has showed that a $\mathcal{H}$ with $w_{3\mathrm{D}} = 4$ indeed corresponds to a system with four gapless surface states that can be analysed with the symmetry indicator invariant in eq. III.126.

Calculating the invariant using SVD The symmetry indicator invariant can also be calculated without using the Hermitian double Hamiltonian, but instead using the Singular Value Decomposition (SVD) of the Hamiltonian

$$H(\mathbf{k}) = U(\mathbf{k})\Sigma(\mathbf{k})V^\dagger(\mathbf{k}), \tag{III.143}$$

where U and V are unitary and Σ is a diagonal matrix with non-negative real entries. Any matrix can be decomposed in this form.
Then

$$H(\boldsymbol{k})V(\boldsymbol{k}) = U(\boldsymbol{k})\Sigma(\boldsymbol{k}), \quad H(\boldsymbol{k})^\dagger U(\boldsymbol{k}) = V(\boldsymbol{k})\Sigma(\boldsymbol{k}), \tag{III.144}$$

which implies that

$$\frac{1}{\sqrt{2}}\begin{bmatrix}U(\boldsymbol{k}) & U(\boldsymbol{k})\\ V(\boldsymbol{k}) & -V(\boldsymbol{k})\end{bmatrix}^{\dagger}\begin{bmatrix}0 & H(\boldsymbol{k})\\ H(\boldsymbol{k})^{\dagger} & 0\end{bmatrix}\begin{bmatrix}U(\boldsymbol{k}) & U(\boldsymbol{k})\\ V(\boldsymbol{k}) & -V(\boldsymbol{k})\end{bmatrix}\frac{1}{\sqrt{2}}=\begin{bmatrix}\Sigma(\boldsymbol{k}) & 0\\ 0 & -\Sigma(\boldsymbol{k})\end{bmatrix}. \tag{III.145}$$

The corresponding matrix whose eigenvalues allow us to calculate the invariant are

$$I_{\mathrm{occ}}(\boldsymbol{k})=\frac{1}{\sqrt{2}}\begin{bmatrix}U(\boldsymbol{k})\\ -V(\boldsymbol{k})\end{bmatrix}^{\dagger}\begin{bmatrix}0 & \mathcal{I}\\ \mathcal{I} & 0\end{bmatrix}\begin{bmatrix}U(\boldsymbol{k})\\ -V(\boldsymbol{k})\end{bmatrix}\frac{1}{\sqrt{2}}=-\frac{1}{2}\left[V(\boldsymbol{k})^{\dagger}\mathcal{I}U(\boldsymbol{k})+U(\boldsymbol{k})^{\dagger}\mathcal{I}V(\boldsymbol{k})\right]. \tag{III.146}$$

The only advantage is that instead of having to calculate the eigenvectors of $\mathcal{H}_{\mathrm{d}}$ at the TRIMs, we can calculate I_{occ}.

III.6.3. Symmetry Indicators for Class AII

In this section Hamiltonians carrying pseudo-inversion symmetry and TRS with complex conjugation are studied. They belong to the non-Hermitian AZ class AII. Consequently, there are two unitary operators τ and $\mathcal{I}$ such that

$$\begin{aligned}\mathcal{I}\mathcal{H}_{\mathbf{k}}\mathcal{I}^{\dagger}&=\mathcal{H}^{\dagger}_{-\mathbf{k}}\text{ with }\mathcal{I}^2=+1,\\ \tau\mathcal{H}^{*}_{\mathbf{k}}\tau^{\dagger}&=\mathcal{H}_{-\mathbf{k}}\text{ with }\tau\tau^{*}=-1.\end{aligned} \tag{III.147}$$

The Hermitian double Hamiltonian has PHS, TRS, SLS and inversion symmetry and is in symmetry class CII. According to Schnyder et al.[29], Dirac cones on the surfaces of insulators in class CII are at least twofold degenerate. Thus, the Hermitian double of a non-Hermitian insulator in class AII in its topologically nontrivial phase has an even multiple of two surface Dirac cones. Such surface states can be detected with the symmetry indicator invariant μ_1[33], as the symmetry indicators in AZ classes AII and CII are the same[36].

But first, before continuing, we study the invariant w_{3D} with TRS. w_{3D} is always defined with respect to a point gap energy E_p. Because TRS implies that energies appear in pairs (E_p, E_p^*), we assume that E_p is real. $Q_j(\mathbf{k})$ then has the property that

$$\begin{aligned}\tau Q_j^{*}(\mathbf{k})\tau^{\dagger}&=\tau\left[\left(H(\mathbf{k})-E_p\right)^{-1}\partial_{k_j}\left(H(\mathbf{k})-E_p\right)\right]^{*}\tau^{\dagger},\\ &=\tau\left[\left(H(\mathbf{k})-E_p\right)^{-1}\right]^{*}\tau^{\dagger}\tau\partial^{*}_{k_j}\tau^{\dagger}\tau\left[\left(H(\mathbf{k})-E_p\right)\right]^{*}\tau^{\dagger},\\ &=\left(H(-\mathbf{k})-E_p^{*}\right)^{-1}\left(\tau\partial^{*}_{k_j}\tau^{\dagger}\right)\left(H(-\mathbf{k})-E_p^{*}\right),\\ &=\left(H(-\mathbf{k})-E_p^{*}\right)^{-1}\partial_{k_j}\left(H(-\mathbf{k})-E_p^{*}\right)=-Q_j(-\mathbf{k}),\end{aligned} \tag{III.148}$$

using that $E_p=E_p^*$ and $\left[\left(H(\mathbf{k})-E_p\right)^{-1}\right]^{*}=\left(H^{*}(\mathbf{k})-E_p^{*}\right)^{-1}$. For w_{3D}, we can then find the identity

$$\begin{aligned}
w_{\mathrm{3D}}^{*} &= -\int_{\mathrm{BZ}} \frac{d^3\mathbf{k}}{24\pi^2}\epsilon_{ijk}\mathrm{Tr}\left[Q_i(\mathbf{k})Q_j(\mathbf{k})Q_k(\mathbf{k})\right]^*, \\
&= -\int_{\mathrm{BZ}} \frac{d^3\mathbf{k}}{24\pi^2}\epsilon_{ijk}\mathrm{Tr}\left[Q_i^*(\mathbf{k})Q_j^*(\mathbf{k})Q_k^*(\mathbf{k})\right], \\
&= -\int_{\mathrm{BZ}} \frac{d^3\mathbf{k}}{24\pi^2}\epsilon_{ijk}\mathrm{Tr}\left[\tau Q_i^*(\mathbf{k})\tau^\dagger\tau Q_j^*(\mathbf{k})\tau^\dagger\tau Q_k^*(\mathbf{k})\tau^\dagger\right], \\
&= -\int_{\mathrm{BZ}} \frac{d^3\mathbf{k}}{24\pi^2}\epsilon_{ijk}\mathrm{Tr}\left[(-Q_i^*(-\mathbf{k}))(-Q_j^*(-\mathbf{k}))(-Q_k^*(-\mathbf{k}))\right], \\
&= +\int_{\mathrm{BZ}} \frac{d^3\mathbf{k}}{24\pi^2}\epsilon_{ijk}\mathrm{Tr}\left[Q_i(-\mathbf{k})Q_j(-\mathbf{k})Q_k(-\mathbf{k})\right], \\
&= +\int_{\mathrm{BZ}} \frac{d^3\mathbf{k}}{24\pi^2}\epsilon_{ijk}\mathrm{Tr}\left[Q_i(\mathbf{k})Q_j(\mathbf{k})Q_k(\mathbf{k})\right] = -w_{\mathrm{3D}}.
\end{aligned} \tag{III.149}$$

Using that w_{3D} is a winding number and therefore has to be real, we obtain the result

$$w_{\mathrm{3D}} = -w_{\mathrm{3D}} \implies w_{\mathrm{3D}} = 0. \tag{III.150}$$

Thus, it is shown that the winding number w_{3D} is not able to serve as an invariant for the $\mathbb{Z}_2$ classification present in the symmetry class AII with point gap[95]. According to Kawabata et al.[95], the right invariant to use is the $\mathbb{Z}_2$ invariant for chiral Hermitian systems in class CII. This invariant, also referred to as the second descendant of the winding number[26], is the Chern-Simons invariant with with a specific gauge choice[26]. It is calculated in terms of the Hermitian double Hamiltonian. The Chern-Simons invariant CS_3 is

$$\mathrm{CS}_3 = \int_{\mathrm{BZ}^d} \mathcal{Q}_3 \text{ with } \mathcal{Q}_3(\mathcal{A}) = -\frac{1}{8\pi^2}\mathrm{Tr}\left[\mathcal{A}d\mathcal{A} + \frac{2}{3}\mathcal{A}^3\right], \tag{III.151}$$

in terms of the Chern-Simons curvature $\mathcal{Q}_3$. To obtain the invariant for class CII, the gauge condition

$$\int_{\partial\mathrm{BZ}^3_{1/2}} \mathrm{Tr}\left[(XdX^\dagger)^2\right] = 0 \tag{III.152}$$

has to be enforced, where $X(\mathbf{k}) = (u^1, ..., u^N, v^1, ..., v^N)$ is the unitary matrix formed by the eigenstates of the Hermitian double Hamiltonian. $\partial\mathrm{BZ}^d_{1/2}$ is half the BZ, and obtained by limiting one of the crystal momenta, e.g. k_x, to only run between 0 andπ. The $\mathbb{Z}_2$ invariant is trivial for even CS_3 and nontrivial for odd CS_3. Due to the gauge condition, it is quite cumbersome to evaluate it, and since CS_3 is a BZ integral it is anyway computationally costly. Therefore, we propose to use a symmetry indicator invariant instead.

To investigate this type of system more in detail, we study a doubled version of the ETI model by Denner et al.[100]. The original ETI Hamiltonian by Denner et al.[100] is

$$H_\delta(\mathbf{k}) = \left(\left[\sum_{i\in\{x,y,z\}} \cos k_i\right] - 3\right)\tau_z\sigma_0 + \sum_{i\in\{x,y,z\}} \sin(k_i)\tau_x\sigma_i + \delta i\tau_x\sigma_0, \tag{III.153}$$

with $M = 3$, $\lambda = 1$ and $\mathbf{B} = 0$.

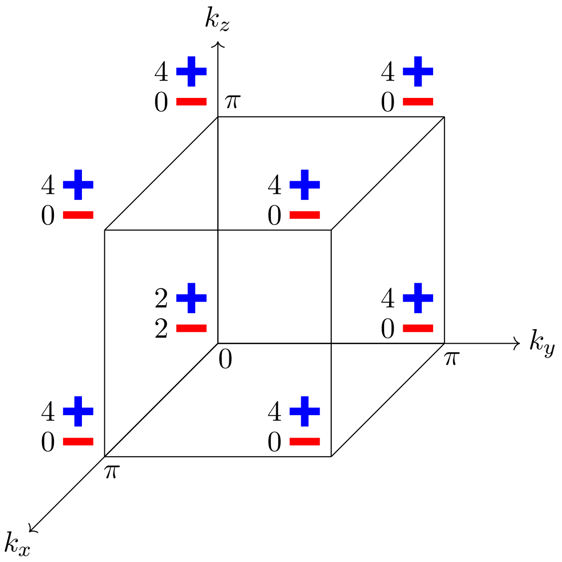

Figure III.8.: Inversion eigenvalues of the Hermitian double of the time reversal doubled Hamiltonian $H_{\mathcal{T}}$, based on the ETI Hamiltonian by Denner et al.[100].

The Hamiltonian is then doubled to obtain

$$H_{\mathcal{T}}(\mathbf{k}) = H_{+1/2}(\mathbf{k}) \oplus H_{-1/2}(\mathbf{k}) = \begin{bmatrix} H_{+1/2}(\mathbf{k}) & \\ & H_{-1/2}(\mathbf{k}) \end{bmatrix}. \tag{III.154}$$

$H_{\mathcal{T}}(\mathbf{k})$ has $w_{3\mathrm{D}} = 0$ and its symmetries are

1. a pseudo-inversion symmetry $\mathcal{I} H_{\mathcal{T}}(\mathbf{k}) \mathcal{I}^{-1} = H_{\mathcal{T}}^{\dagger}(-\mathbf{k})$ with

$$\mathcal{I} = \rho_0 \tau_z \sigma_0, \tag{III.155}$$

2. and a TRS $\tau H_{\mathcal{T}}^{*}(\mathbf{k}) \tau^{\dagger} = H_{\mathcal{T}}(-\mathbf{k})$ with

$$\tau = \rho_x \tau_0 \sigma_y. \tag{III.156}$$

The Hamiltonian $H_{\mathcal{T}}$ carries all the sought symmetries.
Its Hermitian double has an additional sublattice symmetry, and the representations of the symmetries are

$$\begin{aligned} \mathcal{I}_{\mathrm{d}} &= \eta_1 \rho_0 \tau_z \sigma_0, \\ \tau_{\mathrm{d}} &= \eta_0 \rho_x \tau_0 \sigma_y, \\ \mathcal{S}_{\mathrm{d}} &= \eta_z \rho_0 \tau_0 \sigma_0. \end{aligned} \tag{III.157}$$

These operators are indeed compatible with the Hermitian AZ class CII. In the nontrivial phase, it has the inversion eigenvalues depicted in Fig. III.8 and the symmetry indicator is $\mu_1/2 = 2$. This is compatible with the claim that the system is in the topologically nontrivial phase for odd $\mu_1/4$. Furthermore, we checked numerically that indeed $w_{3\mathrm{D}} = 0$.

Due to the fact that $\mu_1/2 = 2$, taking into account the correspondence between the Hermitian double and the non-Hermitian Hamiltonian, there need to be gapless surface states. Therefore, we expect a phase with two gapless surface states. To further investigate the surface of this system, we take four steps:

1. Study the surface states of the Hermitian double Hamiltonian.
2. Study the system in a slab geometry with open boundary conditions (OBC) in one direction. We check that the system is indeed gapless.
3. Check quite generically for two-band Hamiltonians with TRS that there cannot be a point- or line-gap in the spectrum of a linearized non-Hermitian Hamiltonian.
4. Furthermore, deliberate briefly about the properties of exceptional points that might arise on the surface.

III.6.3.1. Surface States of the Hermitian Double

We study the linearised Hermitian double Hamiltonian, given by

$$\mathcal{H}_{\mathrm{d}}(\mathbf{k}) = (\delta + mx)\,\eta_x\rho_0\tau_z\sigma_0 + \lambda \sum_{j\in\{x,y,z\}} k_j\eta_x\rho_0\tau_x\sigma_j - \delta\eta_y\rho_z\tau_x\sigma_0. \tag{III.158}$$

Setting $k_y = k_z = 0$, we have to solve

$$\begin{aligned}&\mathcal{H}_{\mathrm{d}}(\mathbf{k})\,|\Psi(x)\rangle \\ &= (\delta + mx)\,\eta_x\rho_0\tau_z\sigma_0\,|\Psi(x)\rangle + \lambda\eta_x\rho_0\tau_x\sigma_x\left(-i\frac{\partial}{\partial x}\right)|\Psi(x)\rangle - \delta\eta_y\rho_z\tau_x\sigma_0\,|\Psi(x)\rangle = 0\end{aligned} \tag{III.159}$$

using the ansatz $e^{\alpha x^2+\beta x}\,|\Psi_0\rangle$. This leads to the equation

$$\begin{aligned}&(\delta + mx)\,\eta_x\rho_0\tau_z\sigma_0 e^{\alpha x^2+\beta x}\,|\Psi_0\rangle - i\lambda\eta_x\rho_0\tau_x\sigma_x\,(2\alpha x + \beta)\,e^{\alpha x^2+\beta x}\,|\Psi_0\rangle \\ &\qquad - \delta\eta_y\rho_z\tau_x\sigma_0 e^{\alpha x^2+\beta x}\,|\Psi_0\rangle = 0 \Leftrightarrow \\ &(mx\eta_x\rho_0\tau_z\sigma_0 - 2\alpha x i\lambda\eta_x\rho_0\tau_x\sigma_x)\,|\Psi_0\rangle + (\delta\eta_x\rho_0\tau_z\sigma_0 - \beta i\lambda\eta_x\rho_0\tau_x\sigma_x - \delta\eta_y\rho_z\tau_x\sigma_0)\,|\Psi_0\rangle = 0.\end{aligned} \tag{III.160}$$

The relevant values of α and β are $\alpha = -m/2\lambda$ and $\beta = 0$. Repeating the procedure seen in the previous secton III.6.2.2, we obtain the eigenstates

$$\begin{aligned}|\Psi_1(x)\rangle &= e^{-\frac{m}{2\lambda}x^2}(-i, i, -1, 1, 0, 0, 0, 0, 0, 0, 0, 0, 0, 0, 0, 0)^T, \\ |\Psi_2(x)\rangle &= e^{-\frac{m}{2\lambda}x^2}(0, 0, 0, 0, i, i, -1, -1, 0, 0, 0, 0, 0, 0, 0, 0)^T, \\ |\Psi_3(x)\rangle &= e^{-\frac{m}{2\lambda}x^2}(0, 0, 0, 0, 0, 0, 0, 0, i, i, -1, -1, 0, 0, 0, 0)^T, \\ |\Psi_4(x)\rangle &= e^{-\frac{m}{2\lambda}x^2}(0, 0, 0, 0, 0, 0, 0, 0, 0, 0, 0, 0, -i, i, -1, 1)^T.\end{aligned} \tag{III.161}$$

The surface Hamiltonian is

$$\begin{aligned}\mathcal{H}_{\mathrm{surf}}(x, k_y, k_z) &= -4\lambda e^{-\frac{m}{\lambda}x^2}\begin{pmatrix} 0 & 0 & k_y + ik_z & 0 \\ 0 & 0 & 0 & k_y - ik_z \\ k_y - ik_z & 0 & 0 & 0 \\ 0 & k_y + ik_z & 0 & 0 \end{pmatrix} \\ &= -4\lambda e^{-\frac{m}{\lambda}x^2}\left(k_y\xi_x\zeta_0 - k_z\xi_y\zeta_z\right).\end{aligned} \tag{III.162}$$

This Hamiltonian has SLS with $\mathcal{S} = \xi_z\zeta_0$ and TRS with $\tau = i\xi_z\zeta_y$. Therefore, the only symmetry-allowed constant terms are

$$\begin{aligned} \mathcal{H}_{\text{mass}} &= \xi_1\zeta_1, \\ \mathcal{H}_{\text{mass}} &= \xi_1\zeta_2, \\ \mathcal{H}_{\text{mass}} &= \xi_1\zeta_3, \\ \mathcal{H}_{\text{mass}} &= \xi_2\zeta_0. \end{aligned} \tag{III.163}$$

All these terms do not anticommute with the surface Hamiltonian. Therefore, no allowed mass term exists for the surface of the Hermitian double Hamiltonian. This further implies that the Hamiltonian itself must also have zero-energy surface states.

III.6.3.2. Slab Spectrum

In this paragraph, the behaviour of the system $H_{\mathcal{T}}(\mathbf{k})$ from the point of view of its slab spectrum is described[100]. The slab spectrum is calculated as follows: First, one defines a $H_{\text{hop}}(k_1, k_2)$ as

$$H_{\text{hop}}(h, k_1, k_2) = \frac{1}{L} \sum_{k \in k_{\text{BZ}}} e^{-ikh} H_{\mathcal{T}}(k, k_1, k_2), \quad k_{\text{BZ}} = \{0, \frac{2\pi}{L}, ..., (L-1)\frac{2\pi}{L}\}. \tag{III.164}$$

The slab Hamiltonian is then defined as

$$H_{\text{slab}}(k_1, k_2)_{ij} = \begin{cases} H_{\text{hop}}(0, k_1, k_2), & \text{for } i = j, \\ H_{\text{hop}}(1, k_1, k_2) & \text{for } j = i+1, \\ H_{\text{hop}}(-1, k_1, k_2) & \text{for } i = j+1. \end{cases} \tag{III.165}$$

This matrix of matrices is flattened to get a matrix of complex numbers. The spectra of the Hamiltonian $H_{\mathcal{T}}$ with periodic boundary conditions and H_{slab} with open boundary conditions are depicted in Fig. III.9. With periodic boundary conditions, the spectrum has a point gap. With open boundary conditions this gap is filled. It must be stressed that in the OBC case, the eigenvalues at $\text{Im}(\epsilon) = 0$ do not stem from one mode that spans over the whole BZ. Instead these states stem from four TRIMs, from $\mathbf{k}^* = (0,0), (\pi,0), (0,\pi), (\pi,\pi)$. The eigenvalues near the edge, with $\text{Re}(\epsilon) \in ((-6,-3.96) \cup (3.96, 6))$, are from $\mathbf{k}^* = (\pi,\pi)$. The eigenvalues with real part $\text{Re}(\epsilon) \in ((-3.96,-1.9) \cup (1.9, 3.96))$ are from $\mathbf{k}^* = (\pi, 0)$ and $\mathbf{k}^* = (0,\pi)$. The eigenvalues with real part $\text{Re}(\epsilon) \in (-1.9, 1.9)$ are from $\mathbf{k}^* = (0,0)$.

Now, from the plot with open boundary conditions, one might get the impression that new gaps open below and above the line at $\text{Im}(\epsilon) = 0$. This impression is misleading, as can be verified by looking at Fig. III.10 that shows the OBC plot zoomed in by a factor of 10000 around $\mathbf{k} = \vec{0}$ ($\mathbf{k} \in \left(-\frac{\pi}{10000}, +\frac{\pi}{10000}\right)^2$). It can be seen clearly that the gap closes, though it seems that the eigenvalues approach the real axis only exponentionally slowly.

After having established that the spectrum itself is gapless, the next step would be to show that no perturbation of $H_{\mathcal{T}}$ that is compatible with $\mathcal{T}$ and pseudo-inversion can open a gap. This has been checked: it is indeed impossible to open a gap by adding a perturbation to the bulk Hamiltonian, though often the crystal momentum for which the gap closes is quite hard to find. If a constant mass term added to $H_{\mathcal{T}}$ has the form $\rho_\mu\tau_\nu\sigma_\lambda$, the allowed values

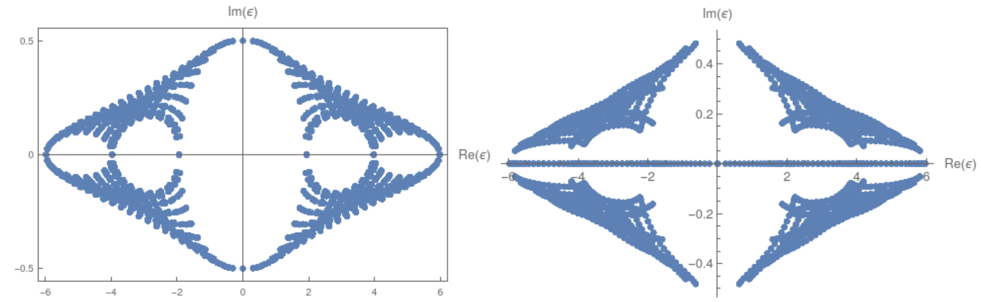

Figure III.9.: Spectrum of $H_{\mathcal{T}}$ with periodic (left) and open (right) boundary conditions.

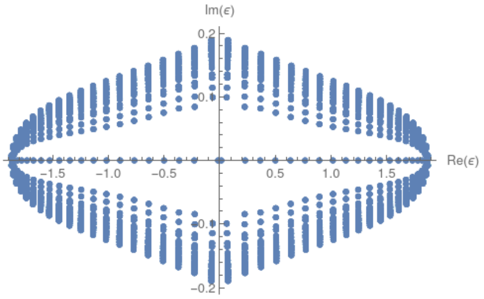

Figure III.10.: Spectrum of $H_{\mathcal{T}}$ with open boundary conditions in the area near $\mathbf{k} = 0$.

for (μ, ν, λ) are {(0,0,0),(0,3,0),(1,0,0), (1,3,0), (2,0,0), (2,3,0), (3,0,1), (3,0,2), (3,0,3), (3,3,1), (3,3,2), (3,3,3)}. If instead the constant mass term has the form $i\rho_\mu \tau_\nu \sigma_\lambda$, the allowed values of (μ, ν, λ) are {(0,1,1), (0,1,2), (0,1,3), (0,2,0), (1,1,1), (1,1,2), (1,1,3), (1,2,0), (2,1,1), (2,1,2), (2,1,3), (2,2,0), (3,1,0), (3,2,1), (3,2,2), (3,2,3)}. All of these possibilities were checked and none of them lead to the appearance of a gap. This was done without and with a B-Field of form $H_B = \cos(\alpha) \sum_i \rho_3 \tau_3 \sigma_i + \cos(\alpha) \rho_3 \tau_0 \sigma_i$ with $\alpha = \pi/2$ and $\alpha = 0$.

The eigenvalues that fill the gap and reach the point $\epsilon = 0$ are often away from $(k_x, k_y) = (0, 0)$. As an example, the PBC spectrum of $H_{\mathcal{T}}$ with an added magnetic field $0.01 H_B$ and a perturbation of the form $0.15 \rho_1 \tau_0 \sigma_0$ is shown in Fig. III.11. The gap remains open. Fig. III.12 shows the OBC spectrum of the same Hamiltonian both in the whole BZ as well as in the region $(-\pi/10, +\pi/10)^2$ around the origin. In the plot of the region around the origin, we can see that the gap is actually closed.

III.6.3.3. Precise Calculations in 2-Band Systems

In this section, we try to model the surface of such an insulator. To this end we simply assume a "Dirac-like" two-band Hamiltonian with linear dispersion that is compatible with TRS.

Surface states by assuming a form of $\mathcal{T}$ We study the surface Hamiltonian, respecting time reversal symmetry with complex conjugation with the representation

$$\mathcal{T} = i\sigma_y \mathcal{K}. \tag{III.166}$$

We can then write the kinetic part of the Hamiltonian around a degeneracy as

$$ik_j \sigma_0 \text{ and } k_j \sigma_l \forall l \in \{x, y, z\}. \tag{III.167}$$

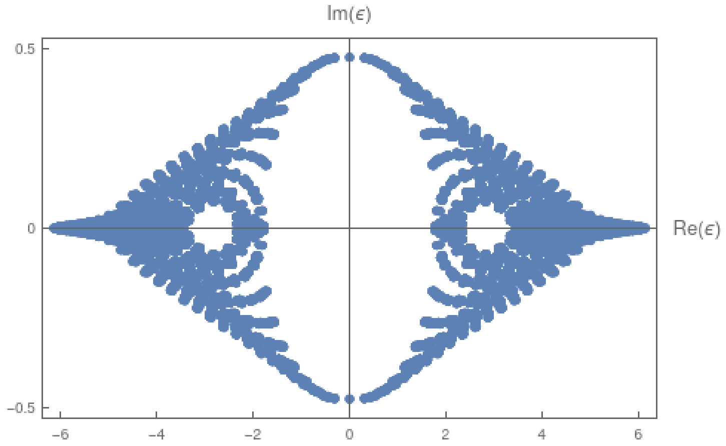

Figure III.11.: Periodic boundary condition spectrum of a perturbed $H_{\mathcal{T}}$.

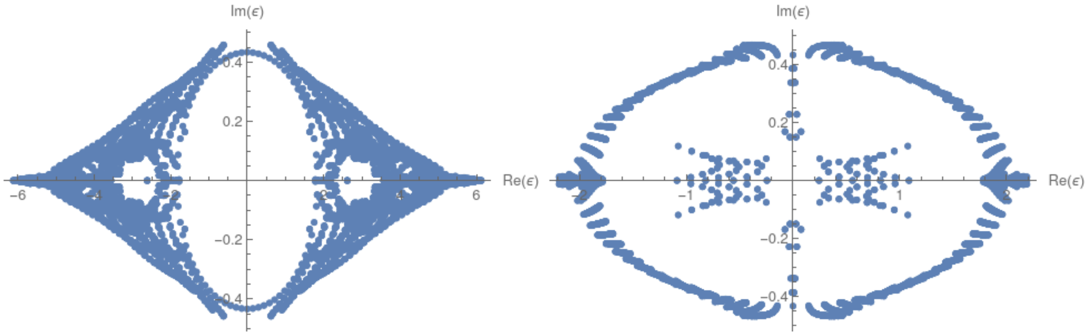

Figure III.12.: Slab Hamiltonian spectrum of a perturbed $H_{\mathcal{T}}$. On the left, the whole BZ, on the right only an excerpt of size $(-\pi/10, +\pi/10)^2$ around the origin of the BZ. We can see that the gap is closed.

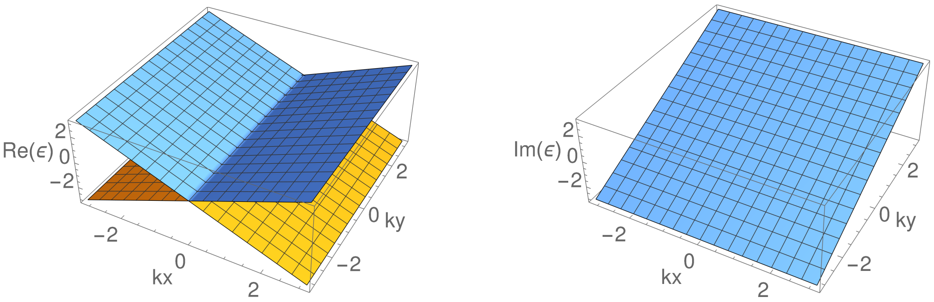

Figure III.13.: Real (left) and imaginary (right) part of the band structure of $\mathcal{H}_{\text{kin}}$. No gap is present.

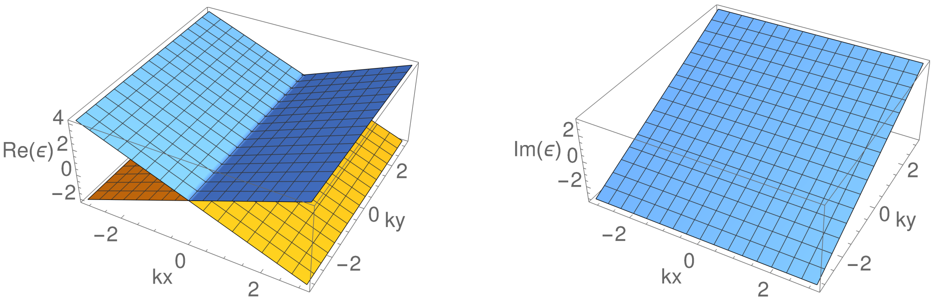

Figure III.14.: Real (left) and imaginary (right) part of the band structure of $\mathcal{H}_{\text{kin}} + \sigma_0$. No gap is present.

We therefore write down the local 2-band Hamiltonian

$$\mathcal{H}_{\text{kin}}(\mathbf{k}) = k_x \sigma_x + k_y i \sigma_0. \tag{III.168}$$

This is the TRS-compatible doubling of the surface states with dispersion $k_x + ik_y$ appearing in the ETI (cf. Denner et al.[100]). The real and imaginary band structure of this Hamiltonian are depicted in Fig. III.13. TRS allows constant mass terms of the form $i\sigma_j$, for $j \in \{x, y, z\}$, and σ_0. To get a feeling for the band structures of these surface Hamiltonians, we plot the real and imaginary part of the eigenvalues as functions of $\mathbf{k} = (k_x, k_y)$ for the four different allowed mass terms. In none of the cases any gap appears. Figure III.14 shows the band structure with a σ_0-mass. Figures III.15 (III.16, III.17) show the band structure with a mass of form $i\sigma_x$ ($i\sigma_y$, $i\sigma_z$).

Precise thinking about why there cannot be a point- or line-gap To think precisely about why a point or line gap cannot exist, we solve the eigenvalue problem of the surface Hamiltonian exactly. Our surface Hamiltonian is characterised by the 12 real parameters $\alpha^\mu = (\alpha^0, \vec{\alpha})$, $\beta^\mu = (\beta^0, \vec{\beta})$ and $\gamma^\mu = (\gamma^0, \vec{\gamma})$, which act as prefactors to the allowed kinetic terms $\sigma_\mu^{\text{kin}} = (\sigma_0^{\text{kin}}, \vec{\sigma}^{\text{kin}})$ and $\sigma_\mu^{\text{mass}} = (\sigma_0^{\text{mass}}, \vec{\sigma}^{\text{mass}})$. The allowed terms are

$$\sigma_0^{\text{mass}} = \sigma_0, \qquad \sigma_1^{\text{mass}} = i\sigma_x, \qquad \sigma_2^{\text{mass}} = i\sigma_y, \qquad \sigma_3^{\text{mass}} = i\sigma_z, \tag{III.169}$$

and

$$\sigma_0^{\text{kin}} = i\sigma_0, \qquad \sigma_1^{\text{kin}} = \sigma_x, \qquad \sigma_2^{\text{kin}} = \sigma_y, \qquad \sigma_3^{\text{kin}} = \sigma_z. \tag{III.170}$$

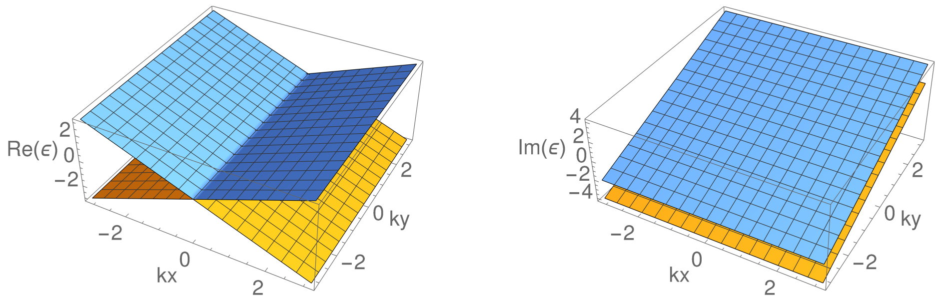

Figure III.15.: Real (left) and imaginary (right) part of the band structure of $\mathcal{H}_{\text{kin}} + i\sigma_x$. No gap is present.

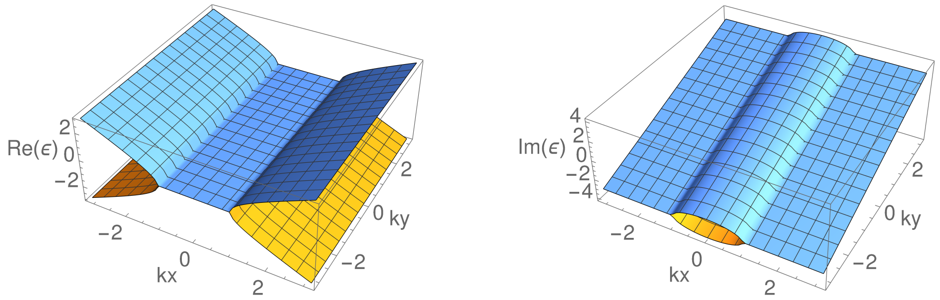

Figure III.16.: Real (left) and imaginary (right) part of the band structure of $\mathcal{H}_{\text{kin}} + i\sigma_y$. No gap is present.

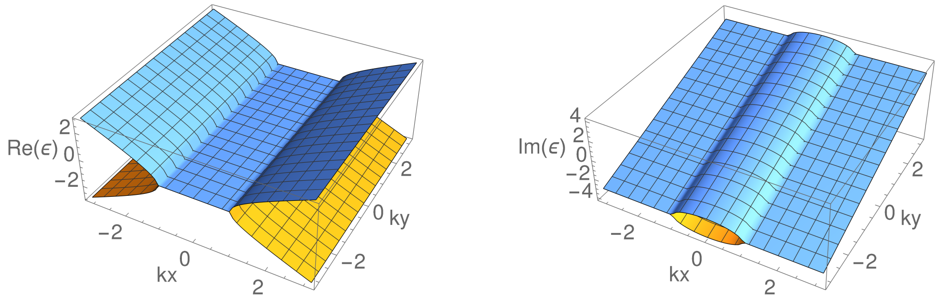

Figure III.17.: Real (left) and imaginary (right) part of the band structure of $\mathcal{H}_{\text{kin}} + i\sigma_z$. No gap is present.

The two-band Dirac Hamiltonian is then, in full generality, given by

$$\mathcal{H}(k_x, k_y) = k_x \alpha^\mu \sigma_\mu^{\text{kin}} + k_y \beta^\mu \sigma_\mu^{\text{kin}} + \gamma^\mu \sigma_\mu^{\text{mass}}, \tag{III.171}$$

with summation over repeated indices. The eigenvalues of this Hamiltonian are

$$E_\pm = \gamma^0 + i\alpha^0 k_x + i\beta^0 k_y \pm \sqrt{(\vec{\alpha} k_x + \vec{\beta} k_y + i\vec{\gamma})^2}. \tag{III.172}$$

Non-existence of a line gap First, we want to prove that there is no real line gap. To do this, we prove that there are states continuously from ∞ real part to $-\infty$ real part. We study $k_x = 0$ and obtain

$$\begin{aligned} k_x = 0, k_y = 0 \qquad & \implies E_\pm = \gamma^0 \pm i\,|\vec{\gamma}|\,, \\ k_x = 0, k_y \to \pm_1 \infty \qquad & \implies E_{\pm_2} \approx i\beta^0 k_y \pm_2 k_y \left|\vec{\beta}\right|. \end{aligned} \tag{III.173}$$

Here, we see that E_+ covers the real range $[\gamma_0, \infty]$ and E_- covers the real range $[-\infty, \gamma_0]$. This means that there is no line gap parallel to the imaginary axis.
To gain further insights, we explicitly show that for any $E \in \mathbb{R}$ we can find a (k_x, k_y) with this eigenvalue. The energies appearing in the spectrum are eigenvalues of the Hamiltonian

$$\begin{aligned} \mathcal{H}(k_x, k_y) = k_x & \begin{pmatrix} \alpha^3 + i\alpha^0 & \alpha^1 - i\alpha^2 \\ \alpha^1 + i\alpha^2 & -\alpha^3 + i\alpha^0 \end{pmatrix} \\ & + k_y \begin{pmatrix} \beta^3 + i\beta^0 & \beta^1 - i\beta^2 \\ \beta^1 + i\beta^2 & -\beta^3 + i\beta^0 \end{pmatrix} + \begin{pmatrix} \gamma^0 + i\gamma^3 & i\gamma^1 + \gamma^2 \\ i\gamma^1 - \gamma^2 & \gamma^0 - i\gamma^3 \end{pmatrix}. \end{aligned} \tag{III.174}$$

We can write an equation for the eigenvalues $E = x + iy + \gamma^0$, which is

$$\begin{aligned} + 2i\alpha^0 k_x x - 2\alpha^0 k_x y - \alpha_\mu \alpha^\mu k_x^2 - 2\alpha_\mu \beta^\mu k_x k_y - \beta_\mu \beta^\mu k_y^2 \\ + 2i\vec{\alpha}\cdot\vec{\gamma} k_x + 2i\vec{\beta}\cdot\vec{\gamma} k_y + 2i\beta^0 k_y x - 2\beta^0 k_y y \\ + \vec{\gamma}\cdot\vec{\gamma} + (x + iy)^2 = 0. \end{aligned} \tag{III.175}$$

Setting $y = 0$, looking at states with zero imaginary value, we get states on the real axis. Then we can first solve the condition that $\text{Re}(0) = 0$ and $\text{Im}(0) = 0$. This yields the two equations

$$(\alpha^0 x + \vec{\alpha}\cdot\vec{\gamma}) k_x + (\beta^0 x + \vec{\beta}\cdot\vec{\gamma}) k_y = 0 \tag{III.176}$$

for the imaginary part and

$$\vec{\gamma}\cdot\vec{\gamma} - \alpha_\mu \alpha^\mu k_x^2 - 2\alpha_\mu \beta^\mu k_x k_y - \beta_\mu \beta^\mu k_y^2 + x^2 = 0 \tag{III.177}$$

for the real part. For generic parameters, we get

$$k_y = -\frac{\alpha^0 x + \vec{\alpha}\cdot\vec{\gamma}}{\beta^0 x + \vec{\beta}\cdot\vec{\gamma}} k_x \tag{III.178}$$

and by setting this into equation III.177

$$k_x = \pm\sqrt{\frac{\vec{\gamma}^2 + x^2}{\left((\beta^0\vec{\alpha} - \alpha^0\vec{\beta})x + (\vec{\alpha}(\vec{\beta}\cdot\vec{\gamma}) - \vec{\beta}(\vec{\alpha}\cdot\vec{\gamma}))\right)^2 + \left(\beta^0\vec{\alpha}\cdot\vec{\gamma} - \alpha^0\vec{\beta}\cdot\vec{\gamma}\right)^2}}, \tag{III.179}$$

which yields a solution because it is a positive quantity under a square root. To check that it really works, we have to ensure that that the cases for which the denominator in Eq. III.178 vanishes are also covered. If $\beta^0 x + \vec{\beta}\cdot\vec{\gamma} = 0$, then there are two cases:

1. If $\beta^0 = 0 = \vec{\beta}\cdot\vec{\gamma}$, the denominator vanishes for all x and we have $(\alpha^0 x + \vec{\alpha}\cdot\vec{\gamma})k_x = 0$. If the first term vanishes, k_x is arbitrary. This means that the system of equations is underdefined, and there is a solution for k_x, k_y such that we get x. This follows from the fact that the paralleloid spanned by equation III.177 cuts through the zero plane: for $k_x = k_y = 0$, it is at $x^2 + \vec{\gamma}\cdot\vec{\gamma}$, for $k_x = 0, k_y \to \infty$ (or vice versa), it drops to $-\infty$. The only exception to this is if $\alpha_\mu = \beta_\mu = 0$, which would not be a Dirac-like Hamiltonian, so it can also be excluded. If the second term vanishes, then $k_x = 0$, and the remaining equation becomes $\vec{\gamma}\cdot\vec{\gamma} + x^2 = \beta_\mu\beta^\mu k_y^2$, which also has real solutions.
2. If $\beta^0 \neq 0$, the problem only arises for one very specific value of x. Therefore, by continuity, there is no issue.

Thus, for any real Energy $E = x + \gamma^0$, there is a corresponding $\mathbf{k} = (k_x, k_y)$ with eigenvalue E. This excludes the possiblity of having a real gap, as long as we have a Dirac-like Hamiltonian that is not a constant matrix.

Arbitrary prefactors The next step is to contemplate how the spectrum away from the real axis looks like. To do so, the energy spectrum with constant real part is studied, with $E = x + iy + \gamma^0 \in \mathbb{C}$. The values for (k_x, k_y) are then given as functions of the parameters α^μ, β^μ, γ^μ and x, y. Within the formula, a square root expression arises, which limits the allowed values of x, y. Therefore we can write

$$\begin{aligned} k_x &= F_x(x, y, \alpha^\mu, \beta^\mu, \gamma^\mu, \mathfrak{f}(x, y, \alpha^\mu, \beta^\mu, \gamma^\mu)), \\ k_y &= F_y(x, y, \alpha^\mu, \beta^\mu, \gamma^\mu, \mathfrak{f}(x, y, \alpha^\mu, \beta^\mu, \gamma^\mu)), \end{aligned} \tag{III.180}$$

where $\mathfrak{f}$ limits the range for y at fixed x. It is given by

$$\begin{aligned} \mathfrak{f}^2 = 4y^2 &\left((a^0\vec{\beta}\cdot\vec{\beta}x^2 - b^0\vec{\alpha}\cdot\vec{\beta}x^2 - \vec{\beta}\cdot\vec{\gamma}(\beta^0\vec{\alpha}\cdot\vec{\gamma} - \alpha^0\vec{\beta}\cdot\vec{\gamma}) + \vec{\alpha}\cdot\vec{\gamma}\vec{\beta}\cdot\vec{\beta}x - \vec{\alpha}\cdot\vec{\beta}\vec{\beta}\cdot\vec{\gamma}x)\right)^2 \\ &\qquad - 4\left(-(\beta^0\vec{\alpha}\cdot\vec{\gamma} - \alpha^0\vec{\beta}\cdot\vec{\gamma})^2 - ((\alpha^0\vec{\beta} - \beta^0\vec{\alpha})x - (\vec{\alpha}\vec{\beta}\cdot\vec{\gamma} - \vec{\alpha}\cdot\vec{\gamma}\vec{\beta}))^2\right) \\ &\qquad \times \left(-\vec{\beta}\cdot\vec{\beta}x^2y^2 - \vec{\beta}\cdot\vec{\gamma}\vec{\beta}\cdot\vec{\gamma}y^2 + (\vec{\beta}\cdot\vec{\gamma} + \beta^0 x)^2(\vec{\gamma}\cdot\vec{\gamma} + x^2)\right) \\ = 4(\vec{\beta}\cdot\vec{\gamma} &+ \beta^0 x)^2(\vec{\gamma}^2 + x^2)\left(\left[\beta^0\vec{\alpha}\cdot\vec{\gamma} - \alpha^0\vec{\beta}\cdot\vec{\gamma}\right]^2 + \left[(\alpha^0\vec{\beta} - \beta^0\vec{\alpha}) - ((\vec{\beta}\cdot\vec{\gamma})\vec{\alpha} - (\vec{\alpha}\cdot\vec{\gamma})\vec{\beta})\right]^2\right) \\ &\qquad - 4y^2\left((\vec{\beta}\cdot\vec{\gamma} + \beta^0 x)^2\left[(\vec{\alpha}\times\vec{\beta})^2 x^2 + (\alpha(\vec{\beta}\cdot\vec{\gamma}) - (\vec{\alpha}\cdot\vec{\gamma})\vec{\beta})^2\right]\right). \end{aligned} \tag{III.181}$$

For fixed x it has the form

$$\mathfrak{f} = \sqrt{\mathrm{Const}_1 - \mathrm{Const}_2 y^2}, \tag{III.182}$$

which yields the maximum imaginary value. As a result, we can directly calculate the (k_x, k_y) for all the values of y between 0 and $y_{\max} = \sqrt{\mathrm{Const}_1/\mathrm{Const}_2}$. $y_{\max}$ is a smooth function of its parameters. This implies that there cannot be any point gap.

Simple Hamiltonian from the beginning For the sake of completeness, we return to the beginning of this section and study the case of the very specific kinetic part given by

$$\mathcal{H}_{\mathrm{kin}}(k_x, k_y) = k_x\sigma_x + ik_y\sigma_0, \tag{III.183}$$

to which we add an arbitrary mass term of form

$$\mathcal{H}_{\text{mass}}(k_x,k_y)=\gamma^\mu\sigma_\mu^{\text{mass}}. \tag{III.184}$$

The eigenvalues of this Hamiltonian are given by the equation

$$0=\gamma^\mu\gamma_\mu-k_x^2-k_y^2-2\gamma^0z+z^2+2i(\gamma^0k_y-\gamma^1k_x-k_yz). \tag{III.185}$$

Setting $z=x+iy$ with $x,y\in\mathbb{R}$, we obtain

$$k_x^2=\vec{\gamma}^2+(\gamma^0-x)^2-(k_y-y)^2 \text{ and } -\gamma^1k_x+(\gamma^0-x)(k_y-y)=0. \tag{III.186}$$

To check for which values of (x,y) there is a solution (k_x,k_y), we first look at the case $(\gamma^0-x)\neq 0$. Then we have

$$k_y-y=\frac{\gamma^1k_x}{\gamma^0-x}\implies\left(1+\left(\frac{\gamma^1}{\gamma^0-x}\right)^2\right)k_x^2=\vec{\gamma}^2+(\gamma^0-x)^2. \tag{III.187}$$

Since $\left(1+\left(\frac{\gamma^1}{\gamma^0-x}\right)^2\right)\neq 0$, the equations yield two real solutions k_x, each of which permits a calculation of k_y. On the other hand, if $\gamma^0-x=0$, we get the two equations

$$k_x^2=\vec{\gamma}^2-(k_y-y)^2 \text{ and } -\gamma^1k_x=0. \tag{III.188}$$

We choose $k_x=0$ in order to satisfy the second equation, and get

$$(k_y-y)^2=\vec{\gamma}^2. \tag{III.189}$$

This equation can be solved for k_y for any choice of y. Therefore, we get the result $(k_x,k_y)=(0,y\pm|\vec{\gamma}|)$.

Thus, we have shown that for every point on the complex plane we can find a momentum (k_x,k_y) such that the Hamiltonian has the complex number $E=x+iy$ as its eigenvalue.

Case of Two Exceptional Points The case of two Exceptional Points (EPs) can be modelled with the 2-band Hamiltonian

$$\mathcal{H}(k_x,k_y)=k_x\sigma_x+k_y\sigma_z+i\sigma_x. \tag{III.190}$$

This is an interesting situation because we know from Ref. [100] that one of the possible surface states of an ETI is a state with an EP. Physically, one of the possible expected states of a time reversal doubled ETI is therefore a state with two EPs.
The band structure of the Hamiltonian is depicted in Fig. III.18 and its complex spectrum in Fig. III.19. There are two Exceptional Points at $\mathbf{k}=(0,\pm1)$. At the EP at $\mathbf{k}=(0,1)$, there is only one eigenvector, $(-\frac{1}{\sqrt{2}},\frac{1}{\sqrt{2}})$, with eigenvalue 0. This non-existence of two distinct eigenvectors signals that it is indeed an EP. The same phenomenon also appears at $\mathbf{k}=(0,-1)$. Expressed as a generic Hamiltonian, the parameters are $\alpha^1=1$, $\beta^3=1$, $\gamma^1=1$ (cf. equation III.171). For simplicity, we omit $i\sigma_x$, which we are allowed to do since it is anyway

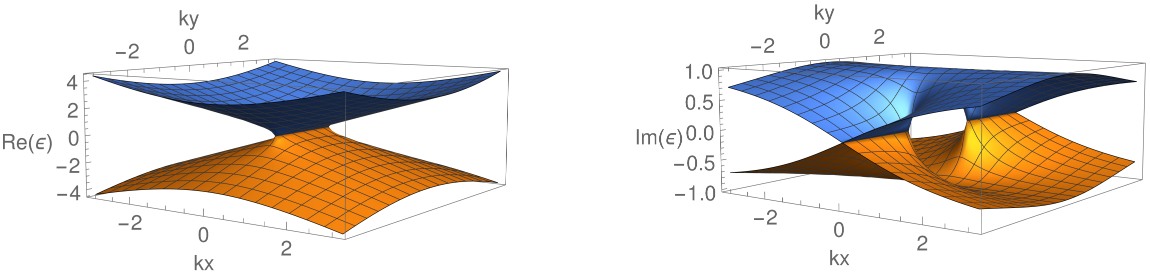

Figure III.18.: Real (left) and imaginary (right) part of the band structure of the Hamiltonian in eq. III.190 with two Exceptional Points at $\mathbf{k} = (0, \pm 1)$.

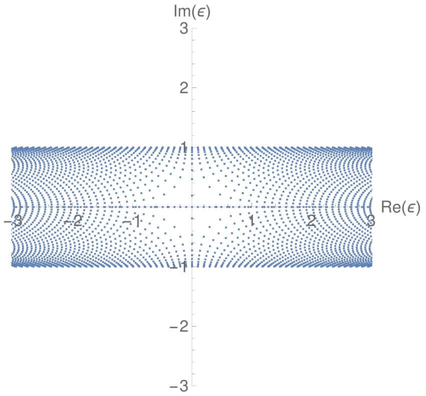

Figure III.19.: Complex spectrum of the Hamiltonian III.190 with two Exceptional Points. The spectrum is gapless, but does not reach every point in the complex plane.

a symmetry-allowed mass. Now, we check whether $k_x\sigma_x + k_y\sigma_z$ can be gapped out by adding an arbitrary mass. The equations for k_x, k_y, given the eigenvalue $E = x + iy$, are

$$\begin{aligned} \gamma_\mu\gamma^\mu - k_x^2 - k_y^2 - 2\gamma^0 x + x^2 - y^2 = 0, \\ -\gamma^1 k_x - \gamma^3 k_y - \gamma^0 y + xy = 0. \end{aligned} \tag{III.191}$$

As we know that $\gamma^1 \approx 1$, we can solve the second equation for k_x, which is

$$k_x = \frac{1}{\gamma^1}\left(xy - \gamma^0 y - \gamma^3 k_y\right). \tag{III.192}$$

This can then be used to calculate k_y, given as

$$k_y = \pm\frac{\sqrt{\vec{\gamma}\cdot\vec{\gamma} + (\gamma^0 - x)^2}}{\sqrt{1 + \frac{(\gamma^3)^2}{(\gamma^1)^2}}} \tag{III.193}$$

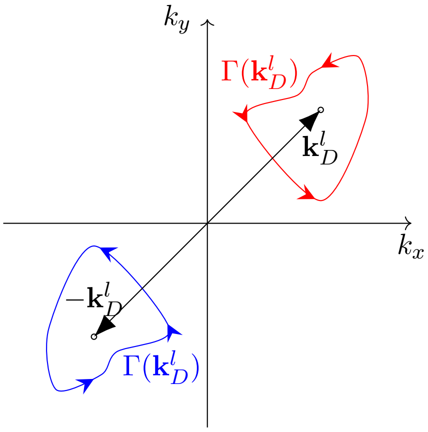

Figure III.20.: Paths around two Exceptional points situated at $\mathbf{k}_D^l$ and $-\mathbf{k}_D^l$, which are mapped onto each under time reversal.

if $y = 0$, which always yields a result. If $y \neq 0$, we get

$$\begin{aligned} k_y = &\frac{\gamma^3 x - \gamma^0\gamma^3}{(\gamma^1)^2 + (\gamma^3)^2} y \pm \frac{(\gamma^1)}{(\gamma^1)^2 + (\gamma^3)^2}\sqrt{\mathfrak{g}(x, y, \gamma^\mu)} \\ &\text{with } \mathfrak{g}(x, y, \gamma^\mu) = ((\gamma^1)^2 + (\gamma^3)^2)^2 + (\gamma^2)^2((\gamma^3)^2 + (\gamma^1)^2) + (\gamma^0\gamma^1 - \gamma^1 x)^2 \\ &\qquad\qquad + (\gamma^0\gamma^3 - \gamma^3 x)^2 - ((\gamma^1)^2 + (\gamma^3)^2 + (\gamma^0 - x)^2)y^2 \\ &\qquad\quad = \mathrm{Const}_1 - \mathrm{Const}_2 y^2. \end{aligned} \tag{III.194}$$

Due to the positivity of these constants, the spectrum is gapless, and therefore the two EPs represent a surface state protected against being gapped out.

III.6.3.4. Surface Exceptional Points and their Discriminant Numbers

In this section we study Exceptional Points from the point of view the discriminant number[163], which is an integral quantity that counts the number of EPs in the area encircled by a closed path. It is given by

$$\nu(\mathbf{k}_D^l) = \frac{i}{2\pi}\oint_{\Gamma(\mathbf{k}_D^l)} d\mathbf{k} \cdot \nabla_{\mathbf{k}} \ln \mathrm{Disc}_E[\mathcal{H}](\mathbf{k}) \tag{III.195}$$

with

$$\mathrm{Disc}_E[\mathcal{H}](\mathbf{k}) = \prod_{i<j} [E_i(\mathbf{k}) - E_j(\mathbf{k})]^2 . \tag{III.196}$$

Here, $\mathbf{k}_D^l$ is the location of the lth degeneracy (here Exceptional Point) and $\Gamma(\mathbf{k}_D^l)$ is a path around it. If $\nu(\mathbf{k}_D^l)$ does not vanish, it guarantees the stability against a gap opening of the degeneracy encircled by the path. In the following, the behaviour of this invariant under time reversal is studied. If there is an eigenstate $|u\rangle$ at $\mathbf{k}$ with eigenvalue $E_i(\mathbf{k})$, there is an eigenstates $\tau\mathcal{K}|u\rangle$ at $-\mathbf{k}$ with eigenvalue $E_i^*(\mathbf{k})$. The discriminant at $-\mathbf{k}$ is

$$\mathrm{Disc}_E[\mathcal{H}](-\mathbf{k}) = \prod_{i<j} \left[E_i^*(\mathbf{k}) - E_j^*(\mathbf{k})\right]^2 = (\mathrm{Disc}_E[\mathcal{H}](\mathbf{k}))^* . \tag{III.197}$$

The contour integral around $-\mathbf{k}_D^l$ is

$$\nu(-\mathbf{k}_D^l) = \frac{i}{2\pi} \oint_{\Gamma(-\mathbf{k}_D^l)} d\mathbf{k} \cdot \nabla_{\mathbf{k}} \ln \mathrm{Disc}_E[\mathcal{H}](\mathbf{k}), \tag{III.198}$$

where $\Gamma(-\mathbf{k}_D^l)$ is the path around the EP at $-\mathbf{k}_D^l$. If $\Gamma(\mathbf{k}_D^l) : t \to \mathbf{k}(t)$ is the path around $\mathbf{k}_D^l$, then $\Gamma(-\mathbf{k}_D^l)$ is given by $t \to -\mathbf{k}(t)$ (situation depicted in Fig. III.20). If $\Gamma(\mathbf{k}_D^l)$ has positive mathematical direction, $\Gamma(-\mathbf{k}_D^l)$ has as well. Explicitly evaluated, we get

$$\begin{aligned}
\nu(-\mathbf{k}_D^l) &= \frac{i}{2\pi} \oint_{\Gamma(-\mathbf{k}_D^l)} d\mathbf{k} \cdot \nabla_{\mathbf{k}} \ln \mathrm{Disc}_E[\mathcal{H}](\mathbf{k}) \\
&= \frac{i}{2\pi} \int_0^1 dt \frac{\partial(-\mathbf{k}(t))}{\partial t} \cdot \nabla_{-\mathbf{k}(t)} \ln \mathrm{Disc}_E[\mathcal{H}](-\mathbf{k}(t)) \\
&= \frac{i}{2\pi} \int_0^1 dt \frac{\partial(\mathbf{k}(t))}{\partial t} \cdot \nabla_{\mathbf{k}(t)} \left[\ln \mathrm{Disc}_E[\mathcal{H}](\mathbf{k}(t))\right]^* \\
&= \frac{i}{2\pi} \oint_{\Gamma(\mathbf{k}_D^l)} d\mathbf{k} \cdot \nabla_{\mathbf{k}} \left[\ln \mathrm{Disc}_E[\mathcal{H}](\mathbf{k})\right]^* \\
&= -\nu(\mathbf{k}_D^l),
\end{aligned} \tag{III.199}$$

where we used in the last line that the integral as whole is imaginary, and therefore the complex conjugation acts by flipping the sign. This means that if there is an EP at $+\mathbf{k}_D^l$, there is also an EP at $-\mathbf{k}_D^l$ with flipped discriminant number. In other words, Exceptional Points in time reversal symmetric systems appear in pairs at momenta $\pm\mathbf{k}_D$, and since they have opposite discriminant numbers, they can be annihilated by bringing them together. Therefore the state with two EPs is not a separate phase, but can be continuously transformed into a state with Dirac-cone-like degeneracies.

III.6.4. Summary Table

In the following, all the symmetry indicators for 3D systems are collected in table III.3. Here, $\lambda_{\mathbf{k}}^i$ is the i^{th} inversion eigenvalue of the Hermitian double at $\mathbf{k}$. $n_{\mathbf{k}}^{\pm}$ is the number of ±1 inversion eigenvalues of the Hermitian double at $\mathbf{k}$. $n_{\mathbf{k}}^{\alpha}$ is the number of $e^{i(\alpha\pi/4)}$ C_4 eigenvalues of the Hermitian double at $\mathbf{k}$.

Int. Sym.	Point Group	Gap (L / P)	H / H_d	Symmetry indicator
-	$\mathcal{I}$	P	-	$w_{1\mathrm{D},j} = 0$
-	$\bar{\mathcal{I}}$	P	H_d	$(-1)^{w_{1\mathrm{D},j}} = \prod_{i\in\mathrm{occ.}} \lambda_{\mathbf{0}}^i \lambda_{\pi\hat{\mathbf{j}}}^i$
-	$\mathcal{I}$	P	-	$w_{3\mathrm{D}} = 0$
-	$\bar{\mathcal{I}}$	P	H_d	$(-1)^{w_{3\mathrm{D}}} = (-1)^{\frac{1}{4}\sum_{\mathbf{k}\in\mathrm{TRIMs}}\left(n_{\mathbf{k}}^+ - n_{\mathbf{k}}^-\right)}$
-	$\bar{\mathcal{I}}$	P	H_d	$(-1)^{w_{3\mathrm{D}}} = (-1)^{\frac{1}{4}\sum_{\mathbf{k}\in\mathrm{TRIMs}}\left(n_{\mathbf{k}}^+ - n_{\mathbf{k}}^-\right)}$
TRS†	$\bar{\mathcal{I}}$	P	H_d	$i^{w_{3\mathrm{D}}} = i^{\frac{1}{4}\sum_{\mathbf{k}\in\mathrm{TRIMs}}\left(n_{\mathbf{k}}^+ - n_{\mathbf{k}}^-\right)}$
TRS†	$\bar{\mathcal{I}}$, C_4	P	H_d	$\left(e^{i\pi/4}\right)^{w_{3\mathrm{D}}} = \left(e^{i\pi/4}\right)^{\frac{1}{4}\sum_{\mathbf{k}\in\mathrm{TRIMs}}\left(n_{\mathbf{k}}^+ - n_{\mathbf{k}}^-\right)}$ $\times(-i)^{\frac{1}{2\sqrt{2}}\sum_{\mathbf{k}\in K_4}\sum_\alpha e^{i(\alpha\pi/4)} n_{\mathbf{k}}^\alpha}$
TRS	$\bar{\mathcal{I}}$	P	-	$w_{3\mathrm{D}} = 0$
TRS	$\bar{\mathcal{I}}$	P	H_d	$(-1)^{\mathrm{CS}_3} = (-1)^{\frac{1}{8}\sum_{\mathbf{k}\in\mathrm{TRIMs}}\left(n_{\mathbf{k}}^+ - n_{\mathbf{k}}^-\right)}$

Table III.3.: Symmetry indicator invariants for 3D non-Hermitian systems.

III.7. Outlook

The approach of using symmetry indicator invariants to detect nontrivial topological phases can be extended to more non-Hermitian AZ classes. One could simply graze through all the classes listed in Ref. [95]. Furthermore, one might also be able to detect non-Hermitian topological phases that go beyond the classification in this table, requiring space group symmetry to protect their surface states. These would then be non-Hermitian topological crystalline insulators.

III.8. Final Remarks

In this part, some symmetry indicator invariants for non-Hermitian were presented. In 1D, the 1D winding number w_{1D} for systems with point gap can be determined up to modulus 2 using a symmetry indicator invariant in presence of pseudo-inversion symmetry. In presence of inversion symmetry, w_{1D} vanishes. In 2D, when there is a line gap and conventional rotation or inversion symmetry, the symmetry indicator invariants known from Hermitian systems can be used. In 3D, the allowed values of the 3D winding number w_{3D} can be limited using symmetry indicator invariants in presence of pseudo-inversion symmetry. In presence of pseudo-inversion, it can be determined modulo 2, in presence of pseudo-inversion and TRS† modulo 4, and in presence of pseudo-inversion, TRS† and C_4 symmetry modulo 8. If a system has TRS symmetry, the classification is $\mathbb{Z}_2$. In presence of pseudo-inversion symmetry, we are able to detect the non-trivial phase using a symmetry indicator invariant.

IV. General Conclusion

In this thesis, two aspects of topological matter in presence of space group symmetries were elucidated. In the first part, the focus was on OAL of C_4 symmetric spin-orbit coupled 2D materials. A method to construct highly symmetric gauges, the *projected symmetric operator* method, was in detail analysed and its applications to the problem are showed.
This method, together with the invariants by Kooi et al.[130], represent an easy method to determine to which band representation a set of occupied bands corresponds.

In the second part, symmetry indicator invariants for non-Hermitian Hamiltonians were treated. In 1D and 3D, the values of the winding numbers $w_{1\mathrm{D},j}$ and $w_{3\mathrm{D}}$ were bounded using symmetry indicator in presence of inversion, $\mathrm{TRS}^{\dagger}$ and C_4 symmetry. In 3D in presence of inversion and TRS symmetry, a new phase with two Exceptional Points or a degeneracy on the surface was discovered. In 2D, the validity of symmetry indicators already known from the Hermitian case was proven for the non-Hermitian situation. These symmetry indicators make the detection of topologically nontrivial phases in non-Hermitian physics much easier. They could pave the way to the development of many more symmetry indicator invariants for different non-Hermitian phases, and thereby lead towards a systematic search for new non-Hermitian topological phases using automatised searches.

Bibliography

[1] M Zahid Hasan and Charles L Kane. “Colloquium: topological insulators”. In: *Reviews of modern physics* 82.4 (2010), p. 3045.

[2] T Senthil. “Symmetry-protected topological phases of quantum matter”. In: *Annu. Rev. Condens. Matter Phys.* 6.1 (2015), pp. 299–324.

[3] Jing Wang and Shou-Cheng Zhang. “Topological states of condensed matter”. In: *Nature materials* 16.11 (2017), pp. 1062–1067.

[4] Xiao-Gang Wen. “Colloquium: Zoo of quantum-topological phases of matter”. In: *Reviews of Modern Physics* 89.4 (2017), p. 041004.

[5] F Duncan M Haldane. “Nobel lecture: Topological quantum matter”. In: *Reviews of Modern Physics* 89.4 (2017), p. 040502.

[6] Arun Bansil, Hsin Lin, and Tanmoy Das. “Colloquium: Topological band theory”. In: *Reviews of Modern Physics* 88.2 (2016), p. 021004.

[7] Barry Bradlyn et al. “Topological quantum chemistry”. In: *Nature* 547.7663 (2017), pp. 298–305.

[8] Stephan Rachel. “Interacting topological insulators: a review”. In: *Reports on Progress in Physics* 81.11 (2018), p. 116501.

[9] Xiao-Liang Qi and Shou-Cheng Zhang. “Topological insulators and superconductors”. In: *Reviews of Modern Physics* 83.4 (2011), p. 1057.

[10] B Andrei Bernevig and Taylor L Hughes. *Topological insulators and topological superconductors.* Princeton university press, 2013.

[11] Michel Fruchart and David Carpentier. “An introduction to topological insulators”. In: *Comptes Rendus Physique* 14.9-10 (2013), pp. 779–815.

[12] Shun-Qing Shen. *Topological insulators.* Vol. 174. Springer, 2012.

[13] Joel E Moore. “An introduction to topological phases of electrons”. In: *Topological Aspects of Condensed Matter Physics: Lecture Notes of the Les Houches Summer School: Volume 103, August 2014* 103 (2017), p. 1.

[14] K v Klitzing, Gerhard Dorda, and Michael Pepper. “New method for high-accuracy determination of the fine-structure constant based on quantized Hall resistance”. In: *Physical Review Letters* 45.6 (1980), p. 494.

[15] Robert B Laughlin. “Anomalous quantum Hall effect: an incompressible quantum fluid with fractionally charged excitations”. In: *Physical Review Letters* 50.18 (1983), p. 1395.

[16] Hongming Weng et al. “Quantum anomalous Hall effect and related topological electronic states”. In: *Advances in Physics* 64.3 (2015), pp. 227–282.

[17] F Duncan M Haldane. “Model for a quantum Hall effect without Landau levels: Condensed-matter realization of the” parity anomaly””. In: *Physical review letters* 61.18 (1988), p. 2015.

[18] David J Thouless et al. “Quantized Hall conductance in a two-dimensional periodic potential”. In: *Physical review letters* 49.6 (1982), p. 405.

[19] Mikio Nakahara. *Geometry, topology and physics.* CRC Press, 2003.

[20] David J Griffiths. *Introduction to quantum mechanics.* Prentice Hall, second edi, 2005.

[21] Michael Victor Berry. “Quantal phase factors accompanying adiabatic changes”. In: *Proceedings of the Royal Society of London. A. Mathematical and Physical Sciences* 392.1802 (1984), pp. 45–57.

[22] Emil Prodan. “Robustness of the spin-Chern number”. In: *Physical Review B* 80.12 (2009), p. 125327.

[23] Cui-Zu Chang et al. “Experimental observation of the quantum anomalous Hall effect in a magnetic topological insulator”. In: *Science* 340.6129 (2013), pp. 167–170.

[24] Charles L Kane and Eugene J Mele. “Quantum spin Hall effect in graphene”. In: *Physical review letters* 95.22 (2005), p. 226801.

[25] Alexander Altland and Martin R Zirnbauer. “Nonstandard symmetry classes in mesoscopic normal-superconducting hybrid structures”. In: *Physical Review B* 55.2 (1997), p. 1142.

[26] Ching-Kai Chiu et al. “Classification of topological quantum matter with symmetries”. In: *Reviews of Modern Physics* 88.3 (2016), p. 035005.

[27] Alexei Kitaev. “Periodic table for topological insulators and superconductors”. In: *AIP conference proceedings.* Vol. 1134. 1. American Institute of Physics. 2009, pp. 22–30.

[28] Andreas P Schnyder et al. “Classification of topological insulators and superconductors”. In: *AIP Conference Proceedings.* Vol. 1134. 1. American Institute of Physics. 2009, pp. 10–21.

[29] Andreas P Schnyder et al. “Classification of topological insulators and superconductors in three spatial dimensions”. In: *Physical Review B* 78.19 (2008), p. 195125.

[30] Andreas WW Ludwig. “Topological phases: classification of topological insulators and superconductors of non-interacting fermions, and beyond”. In: *Physica Scripta* 2016.T168 (2015), p. 014001.

[31] D-L Deng, S-T Wang, and L-M Duan. “Systematic construction of tight-binding Hamiltonians for topological insulators and superconductors”. In: *Physical Review B* 89.7 (2014), p. 075126.

[32] Liang Fu and Charles L Kane. “Topological insulators with inversion symmetry”. In: *Physical Review B* 76.4 (2007), p. 045302.

[33] Eslam Khalaf et al. “Symmetry indicators and anomalous surface states of topological crystalline insulators”. In: *Physical Review X* 8.3 (2018), p. 031070.

[34] Hoi Chun Po, Ashvin Vishwanath, and Haruki Watanabe. “Symmetry-based indicators of band topology in the 230 space groups”. In: *Nature communications* 8.1 (2017), pp. 1–9.

[35] Feng Tang et al. “Efficient topological materials discovery using symmetry indicators”. In: *Nature Physics* 15.5 (2019), pp. 470–476.

[36] Seishiro Ono and Haruki Watanabe. "Unified understanding of symmetry indicators for all internal symmetry classes". In: *Physical Review B* 98.11 (2018), p. 115150.

[37] Taylor L Hughes, Emil Prodan, and B Andrei Bernevig. "Inversion-symmetric topological insulators". In: *Physical Review B* 83.24 (2011), p. 245132.

[38] Ari M Turner et al. "Quantized response and topology of magnetic insulators with inversion symmetry". In: *Physical Review B* 85.16 (2012), p. 165120.

[39] Hoi Chun Po. "Symmetry indicators of band topology". In: *Journal of Physics: Condensed Matter* 32.26 (2020), p. 263001.

[40] Sander H Kooi, Guido van Miert, and Carmine Ortix. "Hybrid-order topology of weak topological insulators". In: *Physical Review B* 102.4 (2020), p. 041122.

[41] Chen Fang, Matthew J Gilbert, and B Andrei Bernevig. "Bulk topological invariants in noninteracting point group symmetric insulators". In: *Physical Review B* 86.11 (2012), p. 115112.

[42] Terry A Loring. "K-theory and pseudospectra for topological insulators". In: *Annals of Physics* 356 (2015), pp. 383–416.

[43] Luuk Stehouwer et al. "Classification of crystalline topological insulators through K-theory". In: *arXiv preprint arXiv:1811.02592* (2018).

[44] Yuan-Ming Lu and Dung-Hai Lee. "Inversion symmetry protected topological insulators and superconductors". In: *arXiv preprint arXiv:1403.5558* (2014).

[45] N Read. "Compactly supported Wannier functions and algebraic K-theory". In: *Physical Review B* 95.11 (2017), p. 115309.

[46] Xiao-Liang Qi, Taylor L Hughes, and Shou-Cheng Zhang. "Topological field theory of time-reversal invariant insulators". In: *Physical Review B* 78.19 (2008), p. 195424.

[47] Andrei Bernevig and Titus Neupert. "Topological superconductors and category theory". In: *Lecture Notes of the Les Houches Summer School: Topological Aspects of Condensed Matter Physics* (2017), pp. 63–121.

[48] Liang Fu. "Topological crystalline insulators". In: *Physical Review Letters* 106.10 (2011), p. 106802.

[49] Andreas P Schnyder and Shinsei Ryu. "Topological phases and surface flat bands in superconductors without inversion symmetry". In: *Physical Review B* 84.6 (2011), p. 060504.

[50] Chen Fang and Liang Fu. "New classes of topological crystalline insulators having surface rotation anomaly". In: *Science advances* 5.12 (2019), eaat2374.

[51] Sander H Kooi, Guido van Miert, and Carmine Ortix. "Classification of crystalline insulators without symmetry indicators: Atomic and fragile topological phases in twofold rotation symmetric systems". In: *Physical Review B* 100.11 (2019), p. 115160.

[52] Alexander Lau, Jeroen van den Brink, and Carmine Ortix. "Topological mirror insulators in one dimension". In: *Physical Review B* 94.16 (2016), p. 165164.

[53] Aris Alexandradinata and B Andrei Bernevig. "Berry-phase description of topological crystalline insulators". In: *Physical Review B* 93.20 (2016), p. 205104.

[54] Ian Mondragon-Shem and Taylor L Hughes. “Robust topological invariants of topological crystalline phases in the presence of impurities”. In: *arXiv preprint arXiv:1906.11847* (2019).

[55] A Alexandradinata, Zhijun Wang, and B Andrei Bernevig. “Topological insulators from group cohomology”. In: *Physical Review X* 6.2 (2016), p. 021008.

[56] Robert-Jan Slager et al. “The space group classification of topological band-insulators”. In: *Nature Physics* 9.2 (2013), pp. 98–102.

[57] Jorrit Kruthoff et al. “Topological classification of crystalline insulators through band structure combinatorics”. In: *Physical Review X* 7.4 (2017), p. 041069.

[58] Y Tanaka et al. “Experimental realization of a topological crystalline insulator in SnTe”. In: *Nature Physics* 8.11 (2012), pp. 800–803.

[59] P Dziawa et al. “Topological crystalline insulator states in Pb 1- x Sn x Se”. In: *Nature materials* 11.12 (2012), pp. 1023–1027.

[60] Xiaoting Zhou et al. “Topological crystalline insulator states in the Ca 2 As family”. In: *Physical Review B* 98.24 (2018), p. 241104.

[61] Nicodemos Varnava and David Vanderbilt. “Surfaces of axion insulators”. In: *Physical Review B* 98.24 (2018), p. 245117.

[62] Chang Liu et al. “Robust axion insulator and Chern insulator phases in a two-dimensional antiferromagnetic topological insulator”. In: *Nature materials* 19.5 (2020), pp. 522–527.

[63] Eslam Khalaf. “Higher-order topological insulators and superconductors protected by inversion symmetry”. In: *Physical Review B* 97.20 (2018), p. 205136.

[64] Frank Wilczek. “Two applications of axion electrodynamics”. In: *Physical review letters* 58.18 (1987), p. 1799.

[65] Masatoshi Sato and Yoichi Ando. “Topological superconductors: a review”. In: *Reports on Progress in Physics* 80.7 (2017), p. 076501.

[66] B Béri. “Topologically stable gapless phases of time-reversal-invariant superconductors”. In: *Physical Review B* 81.13 (2010), p. 134515.

[67] Anastasiia Skurativska, Titus Neupert, and Mark H Fischer. “Atomic limit and inversion-symmetry indicators for topological superconductors”. In: *Physical Review Research* 2.1 (2020), p. 013064.

[68] Xiao-Liang Qi, Taylor L Hughes, and Shou-Cheng Zhang. “Chiral topological superconductor from the quantum Hall state”. In: *Physical Review B* 82.18 (2010), p. 184516.

[69] Jin-Peng Xu et al. “Artificial topological superconductor by the proximity effect”. In: *Physical Review Letters* 112.21 (2014), p. 217001.

[70] Jennifer Cano and Barry Bradlyn. “Band Representations and Topological Quantum Chemistry”. In: *Annual Review of Condensed Matter Physics* 12 (2020).

[71] Jennifer Cano et al. “Building blocks of topological quantum chemistry: Elementary band representations”. In: *Physical Review B* 97.3 (2018), p. 035139.

[72] Jennifer Cano et al. “Topology of disconnected elementary band representations”. In: *Physical review letters* 120.26 (2018), p. 266401.

[73] J Zak. “Symmetry specification of bands in solids”. In: *Physical Review Letters* 45.12 (1980), p. 1025.

[74] J Zak. “Band representations and symmetry types of bands in solids”. In: *Physical Review B* 23.6 (1981), p. 2824.

[75] Frank Schindler et al. “Fractional corner charges in spin-orbit coupled crystals”. In: *Physical Review Research* 1.3 (2019), p. 033074.

[76] Barry Bradlyn et al. “Disconnected elementary band representations, fragile topology, and Wilson loops as topological indices: An example on the triangular lattice”. In: *Physical Review B* 99.4 (2019), p. 045140.

[77] Hoi Chun Po, Haruki Watanabe, and Ashvin Vishwanath. “Fragile topology and wannier obstructions”. In: *Physical review letters* 121.12 (2018), p. 126402.

[78] Zhi-Da Song et al. “Fragile phases as affine monoids: classification and material examples”. In: *Physical Review X* 10.3 (2020), p. 031001.

[79] Zhi-Da Song, Luis Elcoro, and B Andrei Bernevig. “Twisted bulk-boundary correspondence of fragile topology”. In: *Science* 367.6479 (2020), pp. 794–797.

[80] DJ Thouless. “Wannier functions for magnetic sub-bands”. In: *Journal of Physics C: Solid State Physics* 17.12 (1984), p. L325.

[81] Alexey A Soluyanov and David Vanderbilt. “Wannier representation of Z 2 topological insulators”. In: *Physical Review B* 83.3 (2011), p. 035108.

[82] A Alexandradinata and J Höller. “No-go theorem for topological insulators and high-throughput identification of Chern insulators”. In: *Physical Review B* 98.18 (2018), p. 184305.

[83] Christian Brouder et al. “Exponential localization of Wannier functions in insulators”. In: *Physical review letters* 98.4 (2007), p. 046402.

[84] JC Budich et al. “Search for localized Wannier functions of topological band structures via compressed sensing”. In: *Physical Review B* 90.11 (2014), p. 115110.

[85] Frank Schindler et al. “Higher-order topological insulators”. In: *Science advances* 4.6 (2018), eaat0346.

[86] Guido Van Miert and Carmine Ortix. “Higher-order topological insulators protected by inversion and rotoinversion symmetries”. In: *Physical Review B* 98.8 (2018), p. 081110.

[87] Akishi Matsugatani and Haruki Watanabe. “Connecting higher-order topological insulators to lower-dimensional topological insulators”. In: *Physical Review B* 98.20 (2018), p. 205129.

[88] Linhu Li, Ching Hua Lee, and Jiangbin Gong. “Topological switch for non-Hermitian skin effect in cold-atom systems with loss”. In: *Physical Review Letters* 124.25 (2020), p. 250402.

[89] Wladimir A Benalcazar, B Andrei Bernevig, and Taylor L Hughes. “Quantized electric multipole insulators”. In: *Science* 357.6346 (2017), pp. 61–66.

[90] Wladimir A Benalcazar, B Andrei Bernevig, and Taylor L Hughes. “Electric multipole moments, topological multipole moment pumping, and chiral hinge states in crystalline insulators”. In: *Physical Review B* 96.24 (2017), p. 245115.

[91] Shang Ren, Ivo Souza, and David Vanderbilt. “Quadrupole moments, edge polarizations, and corner charges in the Wannier representation”. In: *arXiv preprint arXiv:2010.13862* (2020).

[92] Christopher W Peterson et al. “A quantized microwave quadrupole insulator with topologically protected corner states”. In: *Nature* 555.7696 (2018), pp. 346–350.

[93] Frank Schindler et al. “Higher-order topology in bismuth”. In: *Nature physics* 14.9 (2018), pp. 918–924.

[94] Moon Jip Park et al. “Higher-order topological insulator in twisted bilayer graphene”. In: *Physical Review Letters* 123.21 (2019), p. 216803.

[95] Kohei Kawabata et al. “Symmetry and topology in non-Hermitian physics”. In: *Physical Review X* 9.4 (2019), p. 041015.

[96] Zongping Gong et al. “Topological phases of non-Hermitian systems”. In: *Physical Review X* 8.3 (2018), p. 031079.

[97] Huitao Shen, Bo Zhen, and Liang Fu. “Topological band theory for non-Hermitian Hamiltonians”. In: *Physical review letters* 120.14 (2018), p. 146402.

[98] Daniel Leykam et al. “Edge modes, degeneracies, and topological numbers in non-Hermitian systems”. In: *Physical review letters* 118.4 (2017), p. 040401.

[99] Shunyu Yao and Zhong Wang. “Edge states and topological invariants of non-Hermitian systems”. In: *Physical review letters* 121.8 (2018), p. 086803.

[100] M Michael Denner et al. “Exceptional Topological Insulators”. In: *arXiv preprint arXiv:2008.01090* (2020).

[101] Kohei Kawabata, Ken Shiozaki, and Shinsei Ryu. “Topological Field Theory of Non-Hermitian Systems”. In: *arXiv preprint arXiv:2011.11449* (2020).

[102] Jong Yeon Lee et al. “Topological correspondence between Hermitian and non-Hermitian systems: Anomalous dynamics”. In: *Physical review letters* 123.20 (2019), p. 206404.

[103] Kazuki Yokomizo and Shuichi Murakami. “Non-bloch band theory of non-Hermitian systems”. In: *Physical review letters* 123.6 (2019), p. 066404.

[104] Rui Chen et al. “Finite-size effects in non-Hermitian topological systems”. In: *Physical Review B* 99.15 (2019), p. 155431.

[105] Xi-Wang Luo and Chuanwei Zhang. “Higher-order topological corner states induced by gain and loss”. In: *Physical Review Letters* 123.7 (2019), p. 073601.

[106] Kai Zhang, Zhesen Yang, and Chen Fang. “Correspondence between winding numbers and skin modes in non-hermitian systems”. In: *Physical Review Letters* 125.12 (2020), p. 126402.

[107] Nobuyuki Okuma et al. “Topological origin of non-Hermitian skin effects”. In: *Physical review letters* 124.8 (2020), p. 086801.

[108] Dan S Borgnia, Alex Jura Kruchkov, and Robert-Jan Slager. “Non-Hermitian boundary modes and topology”. In: *Physical review letters* 124.5 (2020), p. 056802.

[109] Fei Song, Shunyu Yao, and Zhong Wang. “Non-Hermitian skin effect and chiral damping in open quantum systems”. In: *Physical review letters* 123.17 (2019), p. 170401.

[110] Tao Liu et al. “Second-order topological phases in non-Hermitian systems”. In: *Physical review letters* 122.7 (2019), p. 076801.

[111] Ryo Okugawa, Ryo Takahashi, and Kazuki Yokomizo. “Second-order topological non-Hermitian skin effects”. In: *Physical Review B* 102.24 (2020), p. 241202.

[112] Kohei Kawabata, Masatoshi Sato, and Ken Shiozaki. “Higher-order non-Hermitian skin effect”. In: *Physical Review B* 102.20 (2020), p. 205118.

[113] Elisabet Edvardsson, Flore K Kunst, and Emil J Bergholtz. “Non-Hermitian extensions of higher-order topological phases and their biorthogonal bulk-boundary correspondence”. In: *Physical Review B* 99.8 (2019), p. 081302.

[114] HC Wu, L Jin, and Z Song. “Inversion symmetric non-Hermitian Chern insulator”. In: *Physical Review B* 100.15 (2019), p. 155117.

[115] Mark R Hirsbrunner, Timothy M Philip, and Matthew J Gilbert. “Topology and observables of the non-Hermitian Chern insulator”. In: *Physical Review B* 100.8 (2019), p. 081104.

[116] Shunyu Yao, Fei Song, and Zhong Wang. “Non-hermitian chern bands”. In: *Physical review letters* 121.13 (2018), p. 136802.

[117] Kohei Kawabata, Ken Shiozaki, and Masahito Ueda. “Anomalous helical edge states in a non-Hermitian Chern insulator”. In: *Physical Review B* 98.16 (2018), p. 165148.

[118] C Yuce and H Ramezani. “Topological states in a non-Hermitian two-dimensional Su-Schrieffer-Heeger model”. In: *Physical Review A* 100.3 (2019), p. 032102.

[119] Simon Lieu. “Topological phases in the non-Hermitian Su-Schrieffer-Heeger model”. In: *Physical Review B* 97.4 (2018), p. 045106.

[120] Jiacheng Bao et al. “Topoelectrical circuit octupole insulator with topologically protected corner states”. In: *Physical Review B* 100.20 (2019), p. 201406.

[121] Motohiko Ezawa. “Non-Hermitian higher-order topological states in nonreciprocal and reciprocal systems with their electric-circuit realization”. In: *Physical Review B* 99.20 (2019), p. 201411.

[122] Tobias Hofmann et al. “Reciprocal skin effect and its realization in a topolectrical circuit”. In: *Physical Review Research* 2.2 (2020), p. 023265.

[123] Motohiko Ezawa. “Electric circuits for non-Hermitian Chern insulators”. In: *Physical Review B* 100.8 (2019), p. 081401.

[124] Shuo Liu et al. “Gain-and Loss-Induced Topological Insulating Phase in a Non-Hermitian Electrical Circuit”. In: *Physical Review Applied* 13.1 (2020), p. 014047.

[125] Jien Wu et al. “Observation of corner states in second-order topological electric circuits”. In: *Physical Review B* 102.10 (2020), p. 104109.

[126] Zhuangzhuang Li et al. “Bound state in the continuum in topological inductor–capacitor circuit”. In: *Applied Physics Letters* 116.26 (2020), p. 263501.

[127] Julia M Zeuner et al. “Observation of a topological transition in the bulk of a non-Hermitian system”. In: *Physical review letters* 115.4 (2015), p. 040402.

[128] Henning Schomerus. “Nonreciprocal response theory of non-Hermitian mechanical metamaterials: Response phase transition from the skin effect of zero modes”. In: *Physical Review Research* 2.1 (2020), p. 013058.

[129] Ananya Ghatak et al. “Observation of non-Hermitian topology and its bulk–edge correspondence in an active mechanical metamaterial”. In: *Proceedings of the National Academy of Sciences* 117.47 (2020), pp. 29561–29568.

[130] Sander H Kooi, Guido van Miert, and Carmine Ortix. “Bulk-corner correspondence of time-reversal symmetric insulators: deduplicating real-space invariants”. In: *arXiv preprint arXiv:2008.07345* (2020).

[131] A Alexandradinata et al. “Crystallographic splitting theorem for band representations and fragile topological photonic crystals”. In: *arXiv preprint arXiv:1908.08541* (2019).

[132] Shinsei Ryu et al. “Topological insulators and superconductors: tenfold way and dimensional hierarchy”. In: *New Journal of Physics* 12.6 (2010), p. 065010.

[133] Wladimir A Benalcazar, Tianhe Li, and Taylor L Hughes. “Quantization of fractional corner charge in C n-symmetric higher-order topological crystalline insulators”. In: *Physical Review B* 99.24 (2019), p. 245151.

[134] Felix Bloch. “Über die Quantenmechanik der Elektronen in Kristallgittern”. In: *Zeitschrift für Physik* 52.7-8 (1929), pp. 555–600.

[135] E Dobardžić, M Dimitrijević, and MV Milovanović. “Generalized bloch theorem and topological characterization”. In: *Physical Review B* 91.12 (2015), p. 125424.

[136] Charles Kittel, Paul McEuen, and Paul McEuen. *Introduction to solid state physics*. Vol. 8. Wiley New York, 1996.

[137] Dario Bercioux et al. *Topological Matter: Lectures from the Topological Matter School 2017*. Vol. 190. Springer, 2018.

[138] Zhida Song, Zhong Fang, and Chen Fang. “(d- 2)-dimensional edge states of rotation symmetry protected topological states”. In: *Physical review letters* 119.24 (2017), p. 246402.

[139] Adrien Bouhon, Annica M Black-Schaffer, and Robert-Jan Slager. “Wilson loop approach to fragile topology of split elementary band representations and topological crystalline insulators with time-reversal symmetry”. In: *Physical Review B* 100.19 (2019), p. 195135.

[140] A Alexandradinata, Xi Dai, and B Andrei Bernevig. “Wilson-loop characterization of inversion-symmetric topological insulators”. In: *Physical Review B* 89.15 (2014), p. 155114.

[141] Daniel Arovas. *UCSD Physics 220: Group Theory*. 2016. URL: `https://courses.physics.ucsd.edu/2016/Spring/physics220/LECTURES/CH07.pdf`.

[142] Wolfram Research Inc. *Mathematica, Version 12.1*. Champaign, IL, 2020. URL: `https://www.wolfram.com/mathematica`.

[143] Brian Hall. *Lie groups, Lie algebras, and representations: an elementary introduction*. Vol. 222. Springer, 2015.

[144] Gianluca Panati. “Triviality of bloch and bloch–dirac bundles”. In: *Annales Henri Poincaré*. Vol. 8. 5. Springer. 2007, pp. 995–1011.

[145] János K Asbóth, László Oroszlány, and András Pályi. “A short course on topological insulators”. In: *Lecture notes in physics* 919 (2016), pp. 997–1000.

[146] Alexey A Soluyanov and David Vanderbilt. “Smooth gauge for topological insulators”. In: *Physical Review B* 85.11 (2012), p. 115415.

[147] Georg W Winkler, Alexey A Soluyanov, and Matthias Troyer. “Smooth gauge and Wannier functions for topological band structures in arbitrary dimensions”. In: *Physical Review B* 93.3 (2016), p. 035453.

[148] Armin Rainer. “Quasianalytic multiparameter perturbation of polynomials and normal matrices”. In: *Transactions of the American Mathematical Society* 363.9 (2011), pp. 4945–4977.

[149] Armin Rainer. “Perturbation theory for normal operators”. In: *Transactions of the American Mathematical Society* 365.10 (2013), pp. 5545–5577.

[150] Jerry L Kazdan. “Matrices A (t) depending on a Parameter t”. In: *unpublished note* (1995).

[151] Anne Greenbaum, Ren-cang Li, and Michael L Overton. “First-order perturbation theory for eigenvalues and eigenvectors”. In: *SIAM review* 62.2 (2020), pp. 463–482.

[152] Günter Gramlich. *Anwendungen der linearen Algebra: mit MATLAB; mit 68 Beispielen und 41 Aufgaben*. Hanser Verlag, 2004.

[153] Kanti Bhushan Datta. *Matrix and linear algebra*. Prentice-Hall of India New Delhi, India, 1991.

[154] Liang Fu and C. L. Kane. “Topological insulators with inversion symmetry”. In: *Phys. Rev. B* 76 (4 July 2007), p. 045302. DOI: `10.1103/PhysRevB.76.045302`. URL: `https://link.aps.org/doi/10.1103/PhysRevB.76.045302`.

[155] Junpeng Hou, Ya-Jie Wu, and Chuanwei Zhang. “Non-Hermitian topological phase transitions for quantum spin Hall insulators”. In: *arXiv preprint arXiv:1910.14606* (2019).

[156] Haiping Hu and Erhai Zhao. “Knots and Non-Hermitian Bloch Bands”. In: *arXiv preprint arXiv:2007.09311* (2020).

[157] Ananya Ghatak and Tanmoy Das. “New topological invariants in non-Hermitian systems”. In: *Journal of Physics: Condensed Matter* 31.26 (2019), p. 263001.

[158] S-T Wang et al. “Quantized electromagnetic response of three-dimensional chiral topological insulators”. In: *Physical Review B* 91.3 (2015), p. 035108.

[159] Pavan Hosur, Shinsei Ryu, and Ashvin Vishwanath. “Chiral topological insulators, superconductors, and other competing orders in three dimensions”. In: *Physical Review B* 81.4 (2010), p. 045120.

[160] Ari M Turner, Yi Zhang, and Ashvin Vishwanath. “Entanglement and inversion symmetry in topological insulators”. In: *Physical Review B* 82.24 (2010), p. 241102.

[161] Benjamin J Wieder and B Andrei Bernevig. “The axion insulator as a pump of fragile topology”. In: *arXiv preprint arXiv:1810.02373* (2018).

[162] Frank Schindler. “Dirac equation perspective on higher-order topological insulators”. In: *Journal of Applied Physics* 128.22 (2020), p. 221102.

[163] Zhesen Yang et al. “Fermion doubling theorems in 2D non-Hermitian systems for Fermi points and exceptional points”. In: *arXiv preprint arXiv:1912.02788* (2019).

List of Figures

II.1. Visualisation of fractional corner charges. 11
II.2. C_4-symmetric 2D Brouillon zone. 12
II.3. Wyckoff positions in 2D C_4-symmetric systems. 12
II.4. Lattice model $H_1^{(2)}$ by Benalcazar et al.[133] 16
II.5. Lattice model $H_2^{(4)}$ by Benalcazar et al.[133]. 16
II.6. Lattice model $H_3^{(2)}$ by Benalcazar et al.[133]. 17
II.7. Lattice model $H_4^{(2)}$ by Benalcazar et al.[133]. 18
II.8. Lattice model $H_1^{(6)}$ by Benalcazar et al.[133]. 19
II.9. Lattice model $H_2^{(6)}$ by Benalcazar et al.[133]. 20
II.10. Lattice models $H_1^{(3)}$ and $H_2^{(3)}$ by Benalcazar et al.[133]. 20
II.11. Band structure of the model by Song et al.[138] 22
II.12. Symmetrisation procedure to get perturbations for the Hamiltonian or symmetric operators. 23
II.13. Brouillon zones of C_2-, C_4-, C_3- and C_6-symmetric systems with HSPs. 25
II.14. Wyckoff positions in C_2-, C_4-, C_3- and C_6-symmetric 2D unit cells. 25
II.15. Wyckoff positions in quadratic system with C_4 symmetry. 26
II.16. Intuitive calculation of the Wilson loop in 1D. 28
II.17. Wilson loop spectra of the models used in part I. 31
II.18. Brouillon zone with paths used in the arguments about the effects of symmetries on the Wilson loop spectrum. 33
II.19. Path $\overline{\mathbf{\Gamma M \Gamma}}$ in the BZ. 37
II.20. Components of a smooth vector along the line $\overline{\mathbf{\Gamma M \Gamma M \Gamma}}$. 40
II.21. Effective BZ (EBZ) defined by Kooi et al.[130]. 42
II.22. Types of gaps relevent for the construction of gauges using PSOs. 45
II.23. $\mathring{\Psi}$ band structures calculated using $\mathring{\psi} = r_4 + r_4^\dagger$ for the models $H_2^{(4)}(\mathbf{k}, t = 0)$ and $H_3^{(2)}(\mathbf{k}, t = 0)$. 51
II.24. A typical function $t_\mathbf{k}$ with r_4 symmetry. 51
II.25. $\mathring{\Psi}$ band structures and Wilson loop spectra for $H_2^{(4)}(\mathbf{k}, t = 0)$, perturbed $\mathring{\psi}$. . . 53
II.26. $\mathring{\Psi}$ band structures and Wilson loop spectra for $H_3^{(2)}(\mathbf{k}, t = 0)$, perturbed $\mathring{\psi}$. . . 54
II.27. $\mathring{\Psi}$ band structures and Wilson loop spectra for $H_2^{(4)}(\mathbf{k}, t = -0.2) + \frac{4}{5}\alpha_{4\text{ fold}}$, using $\mathring{\psi}_\mathbf{k} = r_4 + r_4^\dagger$. 55
II.28. $\mathring{\Psi}$ band structures and Wilson loop spectra for $H_2^{(4)}(t = 0.2) + \frac{4}{5}\alpha_\text{matadd}$ using $\mathring{\psi}_\mathbf{k} = H_2^{(4)}(\mathbf{k}, t = 0.2) + \alpha_\text{matadd}$. 56
II.29. $\mathring{\Psi}$ band structures and Wilson loop spectra for $H_2^{(4)}(t = 0.2) + \alpha_\text{matadd}$ using $\mathring{\psi} = r_4 + r_4^\dagger$. 57
II.30. $\mathring{\Psi}$ band structures and Wilson loop spectra for $H_\text{double TI}$. 58

II.31. $\mathring{\Psi}$ band structures and Wilson loop spectra for $H_2^{(4)}(\mathbf{k}, t = 0)$, calculated using $\mathring{\psi} = (r_4 + r_4^\dagger)(1 + \cos k_x + \cos k_y) + t_{\mathbf{k}}\beta$. 60
II.32. $\mathring{\Psi}$ band structures and Wilson loop spectra for $H_2^{(4)}(\mathbf{k}, t = 0)$ using $\mathring{\psi}_{\mathbf{k}} = (r_4 + r_4^\dagger) + t_{\mathbf{k}}\sigma_0 \otimes \sigma_1 \otimes \sigma_0$. 61
II.33. $\mathring{\Psi}$ band structures and Wilson loop spectra for $H_3^{(2)}(\mathbf{k}, t = 0.2)$ using a $\mathring{\psi}_{\mathbf{k}}$ that is compatible with Wyckoff position $2c$. 62
II.34. $\mathring{\Psi}$ band structures and Wilson loop spectra in calculation to evaluate invariant by Kooi et al.[130]. 64
II.35. Lattice of a C_6-symmetric model with two (doubled model) or one (original model) electron situated at the $3c$ Wyckoff position. 66
II.36. $\mathring{\Psi}$ band structure and Wilson loop spectra for $H_2^{(6)}(t = 0.1)$ to get a 6-cycle gauge. 68
II.37. $\mathring{\Psi}$ band structures and Wilson loop spectra for $H_2^{(6)}(t = 0.1)$ to get three-cycles in one step. 70
II.38. $\mathring{\Psi}$ band structures and Wilson loop spectra for $H_2^{(6)}(t = 0.1)$ to get three-cycles in two steps. 71
II.39. Gapless $\mathring{\Psi}$ band structure in procedure to get three-cycle gauge. 73
II.40. Unit cells for the Benalcazar model with C_4 symmetry, including high symmetry Wyckoff positions. 75
II.41. $\mathring{\Psi}$ band structures and Wilson loop spectra for $H_3^{(2)}(\mathbf{k}, t = 1.2)$ with a $\mathring{\psi}_{\mathbf{k}}$ that is compatible with Wyckoff position $1a$, constructed using creation operators. 76
II.42. $\mathring{\Psi}$ band structures and Wilson loop spectra for $H_2^{(4)}(\mathbf{k}, t = 0.2)$ with a $\mathring{\psi}_{\mathbf{k}}$ that is compatible with Wyckoff position $1b$, constructed using creation operators. 78
II.43. $\mathring{\Psi}$ band structure and Wilson loop spectrum of $H_3^{(2)}(\mathbf{k}, t = 0.2)$ when perturbing $\mathring{\Psi}_{\mathbf{k}}$ instead of $\mathring{\psi}_{\mathbf{k}}$. 92
II.44. Direct calculation of Wilson loop spectrum in occupied $\mathring{\Psi}$ bands by modification of formula for the Wilson loop. 93

III.1. Gaps in non-Hermitian physics. 98
III.2. Spectrum of the ETI with periodic boundary conditions for $\lambda = 1$, $\delta = \frac{1}{2}$, $M = 2, 2.5, 3$. 110
III.3. Band structure of the Hermitian double Hamiltonian of the ETI Hamiltonian model by Denner et al.[100] for $\lambda = 1$, $\delta = 0.5$, $M = 3$ on the plane (k_x, k_y, π). 111
III.4. Argumentation why the number of negative inversion eigenvalues must be evne for gapped 3D Hamiltonians. 114
III.5. Inversion eigenvalues of the Hermitian double Hamiltonian of the ETI model by Denner et al.[100] in the topologically nontrivial phase with w_{1D}. 115
III.6. Inversion eigenvalues of the Hermitian double of TRS†-doubled ETI model by Denner et al.[100]. 120
III.7. Inversion eigenvalues of the Hermitian double of the C_4-symmetrised ETI model by Denner et al.[100]. 122
III.8. Inversion eigenvalues of the Hermitian double of the time reversal doubled Hamiltonian $H_{\mathcal{T}}$, based on the ETI Hamiltonian by Denner et al.[100]. 129
III.9. Spectrum of $H_{\mathcal{T}}$ with periodic and open boundary conditions. 132
III.10. Spectrum of $H_{\mathcal{T}}$ with open boundary conditions in the area near $\mathbf{k} = 0$. 132

III.11. Periodic boundary condition spectrum of a perturbed $H_{\mathcal{T}}$. 133
III.12. Slab Hamiltonian spectrum of a perturbed $H_{\mathcal{T}}$. 133
III.13. Real and imaginary part of the band structure of $\mathcal{H}_{\text{kin}}$. 134
III.14. Real and imaginary part of the band structure of $\mathcal{H}_{\text{kin}} + \sigma_0$. 134
III.15. Real and imaginary part of the band structure of $\mathcal{H}_{\text{kin}} + i\sigma_x$. 135
III.16. Real and imaginary part of the band structure of $\mathcal{H}_{\text{kin}} + i\sigma_y$. 135
III.17. Real and imaginary part of the band structure of $\mathcal{H}_{\text{kin}} + i\sigma_z$. 135
III.18. Real and imaginary part of the band structure of the surface Hamiltonian with two Exceptional Points. 139
III.19. Complex spectrum of a Hamiltonian with two Exceptional Points. 139
III.20. Paths around two Exceptional points situated at $\mathbf{k}_D^l$ and $-\mathbf{k}_D^l$, which are mapped onto each under time reversal. 140

List of Tables

I.1. Altland-Zirnbauer symmetry classes and the tenfold classification of topological insulators and superconductors with bulk gap. 6

II.1. Electronic corner charge, polarisation and topological invariants for the different primitive generators for C_4-symmetric spinless systems. 11
II.2. EBRs, topological invariants and corner charges for spin-orbit coupled C_4-symmetric systems 12
II.3. Evaluation of the invariants by Kooi et al.[130] for the models by Benalcazar et al.[133]. 65

III.1. Symmetry indicators for non-Hermitian 1D systems. 104
III.2. Symmetry indicators for non-Hermitian 2D systems 109
III.3. Symmetry indicators for non-Hermitian 3D systems 141